SYNTHESIS, CHARACTERIZATION AND APPLICATIONS OF SEMICONDUCTING METAL OXIDE NANOMATERIALS

Thesis submitted
to the University of Calicut for the
adjudge of the degree of

DOCTOR OF PHILOSOPHY IN CHEMISTRY

SHAHNAS BEEGAM. M

DEPARTMENT OF CHEMISTRY
UNIVERSITY OF CALICUT
KERALA- 673635
INDIA
JANUARY-2018

CERTIFICATE

This is to certify that the thesis entitled "SYNTHESIS, CHARACTERIZATION AND APPLICATIONS OF SEMICONDUCTING METAL OXIDE NANOMATERIALS" submitted by Mrs. Shahnas Beegam. M to the University of Calicut for the award for the degree of Doctor of Philosophy in Chemistry is a record of precise research work carried out at the department of Chemistry, University of Calicut under my guidance and supervision. The contents of the thesis have been checked for plagiarism using the software 'Urkund' and similarity index falls under permissible limit. I further certify that the thesis or part has not previously formed the basis for the award of any degree, diploma, fellowship, associateship or any other similar title of any other universities or institutions. Certified that all the modifications suggested by the examiners have been incorporated in the thesis.

Calicut University
August 2018

Dr. Pradeepan Periyat

DECLARATION

It is hereby declared that the thesis entitled "SYNTHESIS, CHARACTERIZATION AND APPLICATIONS OF SEMICONDUCTING METAL OXIDE NANOMATERIALS" submitted herewith is an authentic record of the research work carried out by me under the supervision of Dr. Pradeepan Periyat, Assistant Professor, Department of Chemistry, University of Calicut, in partial fulfillment of the requirements for the award of the degree of Doctor of Philosophy in Chemistry under the Faculty of Sciences, University of Calicut, Kerala. The contents of this thesis have not been submitted to any other institute or University for the award of any degree or diploma.

Shahnas Beegam. M

ACKNOWLEDGEMENT

First of all let me thank Lord Almighty for showering enormous grace upon me, blessing me with a lot of well-wishers to support and motivate me, and for providing me enough facilities to do my work, thereby enabling me to complete the work in time.

It would not have been possible to write this doctoral thesis without the help and support of the kind people around me. It is a pleasure to convey my gratitude to them all in my humble acknowledgment. Although it should be relatively simple, this part is not the easiest part of my thesis. At the moment of approaching the finish line of my PhD study, I am very grateful for all help I have received throughout these years. After finishing the above thesis, I might forget to mention a few people…but certainly they are not forgotten and they are in my mind and memories.

First and foremost I would like to thank Dr. Pradeepan Periyat, my supervisor whose stimulating motivation and support made my dream come true. I express my heartfelt thanks to him for his valuable advices, constant encouragement and timely corrections. His knowledge, support and enthusiasm has been exceptional and the major factor in the success of this work. I will always remember his efforts.

I would like to thank all my teachers, Prof. P. Raveendran (Head, Department of Chemistry), Prof. K. Muraleedharan (former Head, Department of Chemistry),

Prof. V. M. Abdul Mujeeb, Prof. Aravindakshan, Prof. Purushothaman, Prof. Abraham Joseph, Dr. Yahya Ismail, Dr. N. K. Renuka, Dr. Ramesan and all the non-teaching staff of the Department of Chemistry.

This thesis would have remained a distant dream had it not been for the unconditional support of my family. I extend my deepest and loving thanks to my father (late) and mother for their spiritual support and belief in my abilities to excel, my mother-in-law to always shower her blessings and pray for my success. My heartfelt thanks also go to my sister, brothers, sister-in-laws and brother-in-law for always being there for me and motivating me endlessly. Finally I dedicate this thesis to my dear son, Abdul Hannan (Abi), he suffered a lot during the period of my phD work.

I extend my deepest gratitude to my loving and understanding husband Anwar Sadique for his unconditional support in all the phases of my Ph.D tenure. Without his care, love, support and motivation, this journey towards a doctorate degree would not have been smooth, fruitful, and even possible. His professional expertise in computer came to my rescue each time I got stuck up with computer glitches. He helped me selflessly in my work, and ensured that it is completed successfully.

I am happy to acknowledge my research group colleagues Binu Naufal, Jithesh, Dhinesh and Sanjay with whom I've had the pleasure to work during all these years, for all the good times we've had together in the lab and outside of it and for every wonderful day we've spent together. The peaceful and loving moments shared by my friends

Rajeena pathoor, Thasneem, Sangeetha, Soufeena, Jaseela, Nibila, Jyothi, Sumitha, Shamseera, Shainy, Anupama, Revathy, Ramya and all other research scholars in the department of chemistry for always be a relaxation during the continuous hours spent in the lab. I take this opportunity to thank all them. A special thanks to Soumya B.N, Central University, Kerala for her valuable suggestions and help.

I am thankful to Prof. Suresh Pillai (Institute of Technology, Sligo, Ireland) and Mr. Sarath (AIMS, Kochi) for the XPS facility. I also thank STIC Cochin, King Abdul Azeez University, NIST Trivandrum, Departments of Physics and nanotechnology, University of Calicut for their instrumental facility.

I gratefully acknowledge UGC, for providing financial support to complete my Ph D work.

Any omission in this brief acknowledgement doesn't mean lack of gratitude.

Shahnas Beegam.M

CONTENTS

ABSTRACT

Semiconductor photocatalysis attracted much attention during the last two three decades due to their low environmental impact. Among various semiconductors, titania (TiO_2) paves more attention due to its non-toxicity, low cost, stability and better catalytic activity. However, due to its large band gap, the spectral response is in the UV region which constitutes only 4-5% of the sun light. Of the three common polymorphs of TiO_2, anatase is a widely accepted catalyst mostly towards photocatalytic applications. However, it is transformed into rutile at a temperature range of 400-500 °C. In order for TiO_2 to be utilized in wider areas, it is necessary that anatase can be stable at higher temperatures. In the present work, a co-doping technique is used for the modification of TiO_2 to improve its overall material properties including spectral response and photocatalytic activity. This thesis work achieved the improvement in high temperature stability of anatase TiO_2 and higher photocatalytic activity of TiO_2 by using various non-metal modifiers. Using the visible region of the electromagnetic spectrum, the prepared catalysts were successfully employed for the removal of a dye, methylene blue which can be considered as a model contaminant in this thesis.

In the first part of the present thesis, as prepared TiO_2samples were modified using non-metallic and low cost precursors such as thiourea, thiosemicarbazide, sulfanilic acid, cysteine, ammonium fluoride are studied. Modifiers are selected in such a way that they contain non-metallic element as dopant nitrogen, sulfur and fluorine. All these

modifiers were improved the anatase phase stability and photocatalytic activity of TiO_2. The high temperature treatment of modified TiO_2 resulted in high crystallinity, higher amount of hydroxyl radical on the surface of TiO_2 and higher surface area, which are the important factors that contributed to photocatalytic activity of anatase TiO_2. Therefore using this chemical modification process achieved a dual aim *i.e.* high temperature anatase stability and higher photocatalytic activity. The thermal stability of N, F-codoped TiO_2 sample exhibit 100% anatase phase even at temperature of 1000°C and displayed better photocatalytic property than that of undoped TiO_2 at the same temperature.

Second major aim of this thesis work is to achieve selectivity in the photocatalytic activity of TiO_2. Generally photocatalytic degradation by TiO_2 follows free radical mechanism and which follows complete mineralization of pollutant non-selectively. This non-selectivity / poor selectivity limit its application to differentiate between highly toxic contaminants and the compounds to be recovered, in an effluent. In this thesis, high temperature stable nanocrystalline TiO_2 for the selective photocatalytic degradation of ionic dyes from an aqueous mixture of methyl orange (MO) and methylene blue (MB) under UV light (Ref. M. S. Beegam, S. G. Ullattil, P. Periyat, Solar Energy, 2018, 160, 10) were synthesized. TiO_2 samples (TNF500 & TNF700) selectively degraded cationic methylene blue (MB) over anionic methyl orange (MO) from an aqueous mixture of MB and MO dye. The selective photocatalysis was well accounted by surface charge

obtained from zeta potential measurements as well as the presence of (001) facets as obtained from TEM analysis of TNF samples.

Tuning of the photocatalytic selectivity of N, F codoped sample by adding various concentrations of Mn ion (Ref. M. S. Beegam, S. B. Narendranath and P. Periyat, Solar Energy, 2017, 158, 774-781) was also achieved. The selective photocatalysis was tested by measuring the rate of degradation of aqueous dye mixture of methyl orange (MO) and methylene blue (MB), and the rate of selective degradation of the dye mixture was tuned by varying the surface charge on the TiO_2. The surface charge was probed with zeta (ζ) potential measurements. The ζ-potential measurement showed that the selectivity of dye degradation depends on the surface charge present on TiO_2 nanomaterial.

CHAPTER 1
INTRODUCTION

CONTENTS

1.1. Introduction to nanomaterials, nanoscience and nanotechnology

Nanomaterials are cornerstones of nanoscience and nanotechnology. Nanoscience and technology is an interdisciplinary area of research and development activity that has been growing explosively worldwide in the past few years.

The term nanotechnology comes from the combination of two words: the Greek numerical prefix 'nanos' means dwarf referring to one billionth of a meter and the word technology.[1] The concept nanotechnology was introduced by Richard Feynman in his pioneering lecture "There's plenty of the room at the bottom" held at California institute of technology in 1959. Invention of scanning tunneling microscope (STM) in 1981 had excelled the popularization of nanotechnology and provides better understanding about atoms and bonds. Theory behind the role of individual atom in nanotechnology was successfully conceptualized after the development of STM in 1989.

A basic definition has been given to nanotechnology is that: it is the engineering of functional systems at the molecular scale or the ability to construct objects from the bottom up. The field of nanotechnology is rapidly growing and faces numerous challenges to its further growth and development. Nanotechnology promises the possibility of creating nanostructures having properties including superconductivity and magnetism. Another very important aspect of nanotechnology is the miniaturization of current and new instruments, sensors and machines

that will greatly impact the world we live in. Examples of possible miniaturization are computers with infinitely great power that compute algorithms to mimic human brains, biosensors that warn us at the early stage of the onset of disease and preferably at the molecular level and target specific drugs that automatically attack the diseased cells on site, nanorobots that can repair internal damage and remove chemical toxins in human bodies, nanoscaled electronics that constantly monitor our local environment. The evolution and future implication of nanotechnology has been summarized in Figure 1.1.

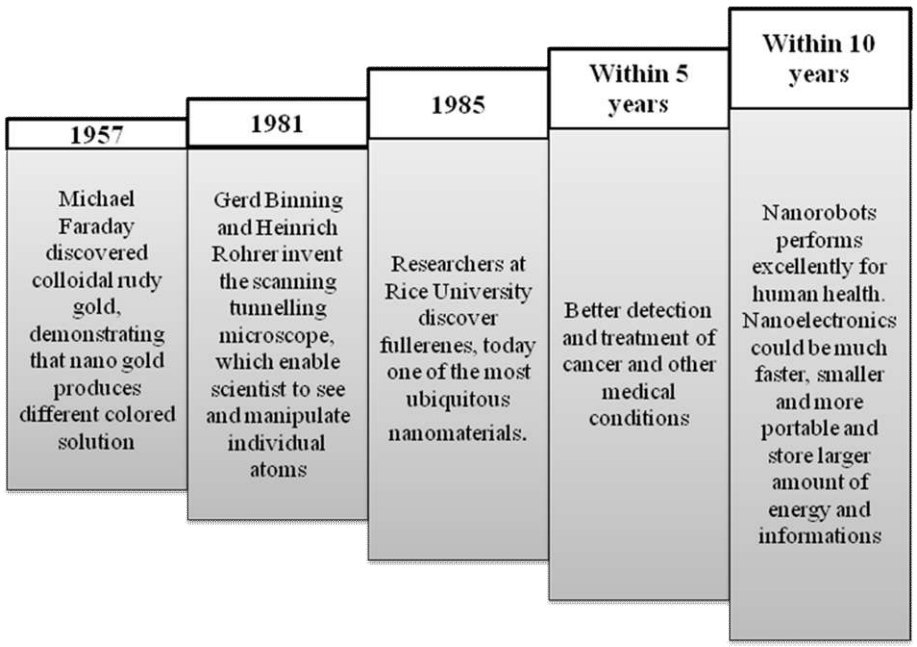

Figure 1.1: Development of nanotechnology over the years[2]

1.1.1. What are nanomaterials?

Nanomaterials are single or multi-phased polycrystalline particles of organic or inorganic materials having a size of few nanometers,

typically in the range of 1-100 nm.[3] A nanometer is one billionth of a meter - approximately 100,000 times smaller than the diameter of a human hair. Nanomaterials are of interest because at the nanometer scale unique optical, electrical, magnetic, and other properties emerge. These emerged properties have the potential for great impacts in electronics, medicine, and other fields.

Two general methods exist concerning the controlled synthesis and arrangement of nanoparticles: top-down and bottom-up methods (Figure 1.2). Top-down methods involve the creation of nanoscale objects/devices from larger ones, or the physical manipulation of nanoscale objects with larger ones. On the other hand, bottom-up synthesis (assembly techniques) rely on smaller interactions between nanomaterials to guide their self-assembly. Using chemical bottom up approach, different nanocrystals having properties such as narrow size distribution, desired particle size over the largest possible range, good crystallinity, high luminescent quantum yield, controllable surface functionalization, *etc.* can be obtained on a gram scale and handled like ordinary chemical substances. However, top-down techniques are currently more common, time consuming, expensive, not for practical scale up and commercialization. The bottom-up methods are desirable because they are more easily scalable, and thus cheaper than top-down options. The bottom-up techniques once properly mastered, allow for the economic scale up of nanomaterial synthesis and nanodevice production.

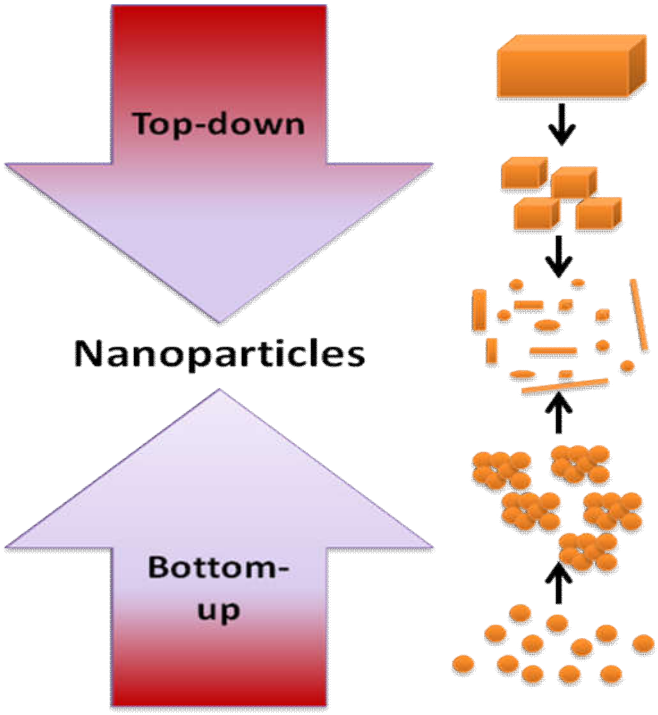

Figure 1.2. Schematic representation of the preparative methods of nanoparticles

Nanomaterials often can be distinguished from bulk materials by the following means:

- Electromagnetic forces dominate gravitational forces.
- Nanoscaled materials exhibit quantum effects-Unique surface properties of nanomaterials amplify light intensity, shows unexpected optical properties.
- Larger surface area to volume ratios.
- Enhanced diffusivity.
- Exhibit Brownian movement.

It is seen that the properties of nanomaterials are quite sensitive to their sizes.[4] Nanomaterial having size range of 1-20 nm have become a major interdisciplinary area of research and their extremely small size has the potential for wide range of applications in electronic, industrial and biomedical fields. This is partly connected with the fact that surfaces and interfaces are very important for nanomaterials, but in the case of bulk materials, relatively small percentage of atoms will be present at or near the surface or interface.[5] In nanomatrials, small size ensures that many number of atoms, probably half or more in some cases will be near at the surface and high percentage of surface atoms introduce many size dependent phenomena. High surface area is an important feature of nanosized and nanoporous materials.[5] Surface properties of a material, such as electronic structure, energy levels and reactivity can be quite different from interior states and results quite different material properties. Summarizing, the optimization of structure, morphology, optical, mechanical and electronic properties of nanometer sized systems have the fundamental importance in the design of nanostructures with favorable properties.

1.1.2. Classification of nanomaterials:

Depending on the dimensionality of nanomaterilas in which the size effect on the resultant property, the nanomaterials can be classified as zerodimensional (e.g. quantum dots) in which the electronic movement is confined in all the three dimensions, one-dimensional (e.g. quantum wires, nanorods, nanoneedle) in which the electrons can move freely in one direction (say. X-direction), two-dimensional (thin films, strands) in which the free electron can move in X-Y plane, or three dimensional

(nanostructured material built of nanoparticles as building blocks) in which the free electron can move in any of the direction i.e. in X, Y and Z direction (Figure 1.3).

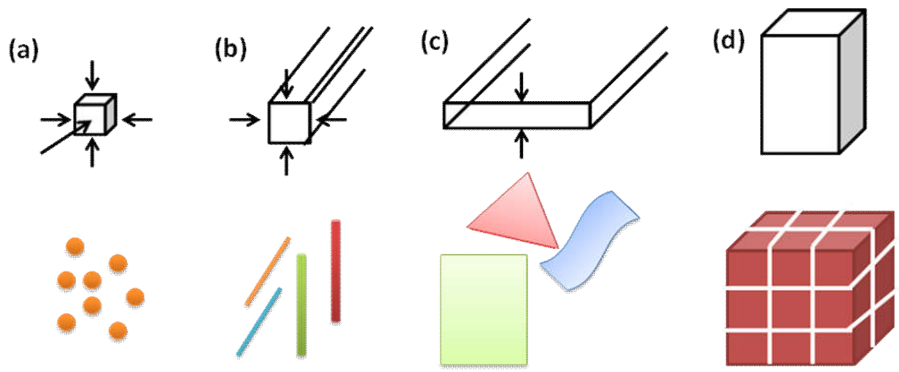

Figure 1.3. Classification of nanomaterials (a) 0 dimensional spheres or clusters, (b) 1 dimensional nanofibers, wires or rods, (c) 2 dimensional films or plates and (d) 3 dimensional nanomaterials.

Nanoparticles (NPs) further divided into various categories based on their morphology, size and chemical properties. Some of the well known classes coming under this scheme are carbon based NPs (e.g. carbon nanotube and fullerenes), Metal NPs (e.g. Cu, Ag and Au NPs), Semiconductor NPs, Polymeric NPs, Lipid based NPs etc.[6]

1.2. Semiconductor nanomaterials

Semiconductor materials possess properties in between metals and insulators and due to this property they found various applications in different fields. Currently, semiconductor nanomaterials and devices are still in the research stage, but they are promising for applications in many fields, such as solar cells, nanoscale electronic devices, light-

emitting nano devices, laser technology, photocatalysis, waveguide, chemicals and biosensors.[7,8,9] Further development of nanotechnology will lead to significant breakthroughs in the semiconductor industry.

Semiconductors can act as sensitizers for the light induced redox processes due to electronic structure of the metal atoms in chemical combinations with other atom such as oxygen, which is characterized by a filled valence band and an empty conduction band.[10,11] By absorbing suitable radiations, valence band electrons get promoted to conduction band leaving behind a hole. Either the holes react with electron donors such as hydroxide ions or electrons react with oxygen molecules to produce powerful oxidizing species like hydroxide and superoxide radicals respectively. These radicals are highly reactive and can be used for many applications. Subsequent to the initial charge separation, electron-hole recombinations will results which must be prevented as much as possible.

Among all the semiconductor materials in photoinduced applications, TiO_2 materials are expected to play an important role in helping to solve many serious environmental and pollution challenges. TiO_2 also bears tremendous hope in helping ease the energy crisis through effective utilization of solar energy based on photovoltaic and water-splitting devices.[12,13,14,15] Though TiO_2 has the disadvantage of not being activated by visible light, but by UV light, it has advantageous over the others in that it is photoctalytically stable, chemically and biologically inert, able to efficiently catalyze reactions, relatively easy to produce and use, cheap and can handle without risks to human and environment.[10]

1.3. Titanium dioxide

Titanium dioxide is the naturally occurring oxide of titanium at atmospheric pressure. It was discovered in England in 1791 by Reverend William Gregor, who identified a new element in ilmenite. German chemist, Heinrich Klaporth rediscovered it in rutile ore after several years and named Titans, mythological first son of the goddess Ge (Earth in Greek mythology). Normally TiO_2 occurs in different minerals like rutile, ilmenite, anatase, brookite, leucoxene, perovskite and spene. Among these rutile, anatase and brookite are the most important crystalline forms of titania.[16,17] The crystal structures of rutile (tetragonal), anatase (tetragonal) and brookite (orthorhombic) are assembled by connecting TiO_6 octahedral in different ways. In anatase phase each octahedral unit is connected by their edges, vertices are connected in rutile and both vertices and edges are connected in brookite phase (Figure 1.4).

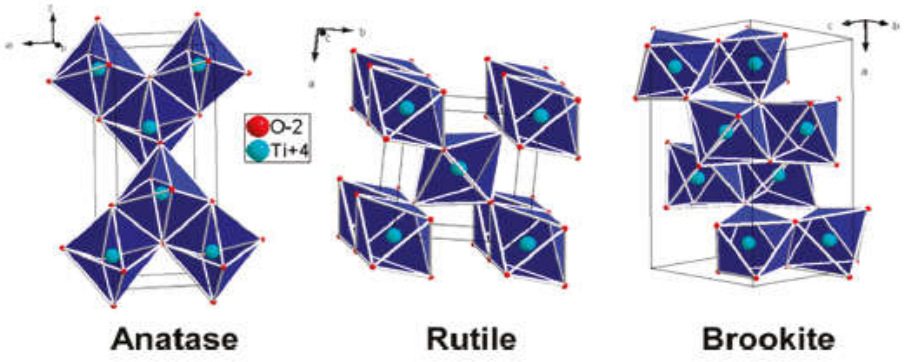

Figure 1.4. Crystal structure of anatase, rutile and brookite phases of TiO_2.[18]

It is well known that Rutile is the most stable form and primary source of titanium dioxide and was discovered by Werner in 1803. The name rutile is derived from the Latin word rutilus, red due to deep red colour as observed through the transmitted light in most specimens. It is commonly reddish brown but is also sometimes yellowish, bluish or violet, being transparent to opaque. Rutile ore usually contains up to 10% iron, and also other impurities such as tantalum, niobium, chromium, vanadium, and tin in small quantities. It is associated with minerals such as hematite, silicates and quartz. Notable occurrences include Brazil, Swiss Alps, the USA and African countries.[19] Effective light scattering property, high refractive index and chemical inertness of rutile phase make its usage in pigment industry in larger amount. Rutile is stable at most temperatures and Zhang *et al* showed that anatase and brookite phases are irreversibly transformed to the rutile phase after attaining a definite particle size and rutile phase is more stable than anatase for particle size higher than 14 nm.

Brookite phase was discovered by A. Levy in 1825 and was named in honour of English mineralogist, H. J. Brooke. Its crystals are dark brown to greenish black opaque. Associated minerals are rutile, quartz, feldspar, and hematite. Notable occurrences include those in the USA, Austria, Russia and Switzerland.[19] Because of the difficulty in the preparation of metastable brookite phase, only limited reports are available based on the applications of this TiO_2 polymorph.[20]

Anatase was named by R. J. Hauy in 1801 from the Greek word anatasis meaning extension, due to its longer vertical axis than that of rutile. It is associated with rock crystal often found in feldspar and

mica schist in France or associated with the walls of crevices in the gneiss rocks of the Swiss Alps.[19] Muscat *et al* predict that anatase is more stable than the rutile at 0K, but the difference in energy between these two phases is small (approximately 2 to 10 kJ/mol).[21] Thermodynamically rutile is the most stable form, although anatase phase forms at lower temperatures.

Titanium dioxide is an n-type semiconductor, that has a band gap of 3 eV for rutile and 3.0 eV for both anatase and brookite phases.[22,23,24,25,26,27] TiO_2 is the most widely investigated photocatalyst due to its strong oxidative properties, non-toxicity, low cost, chemical and thermal stability.[28] Anatase and rutile phases of TiO_2 are the most researched polymorphs, since these are more useful for practical applications.[19,12 ,29] Their properties are summarised in Table1.1.

Table 1.1. Physical and structural properties of anatase and rutile.[30]

Property	Anatase	Rutile
Molecular weight (g/mol)	79.88	79.88
Melting point (°C)	1825	
Specific gravity	3.9	4.0
Light absorption (nm)	< 390	< 415
Mohr's Hardness	5.5	6.5-7.0
Refractive index	2.55	2.75
Dielectric constant	48	114
Crystal structure	Tetragonal	Tetragonal
Lattice constants (Å)	a =b= 3.78 c = 9.52	a = b=4.59 c = 2.96
Density (g/cm3)	3.79	4.13

1.4. Synthesis technique

Nanocrystalline materials, which are the combinations of ultrafine crystals with dimensions are in the range of one to hundred nanometers, are currently receiving much attention on account of their special mechanical, physical and chemical properties, which are suited for various applications. There are many methods for synthesizing nanocrystalline metallic oxide materials, such as sol-gel method, hydrothermal, microwave synthesis,[31,32] chemical vapour deposition,[33,34] physical vapour deposition,[35,36,37]solvothermal method[38,39] and micelle and inverse micelle method.[40] This research chose sol-gel technique for synthesizing nanotitania, which will be discussed in greater details.

1.5. Sol-gel methods

The sol-gel process is a versatile method, used for the fabrication of various oxide materials. It can be considered as a wet chemical technique and involves the transition of a system from a colloidal liquid sol into a solid gel phase.[30,12 ,41] A sol is a stable colloidal suspension of small solid particles in a liquid medium.[42] Sols can be classified as lyophilic if the interaction between solvent and particle are relatively strong and lyophobic if the interaction is relatively weak.[43,44] Repulsive force between the particles will stabilize the formation of sol. The sol can be prepared by the hydrolysis and polycondensation reactions of the suitable precursor. Metal alkoxide and metal chlorides are commonly used precursor in sol-gel method. Based on the chemical nature of the precursor used, the sol gel method can be classified into two

1. Non-alkoxide method: precursor used are :-$TiOCl_2$,$TiCl_4$, $SiCl_4$, $TiOSO_4$, etc.[45, 46,47]

2. Alkoxide method: precursor used are :-$Ti(OC_3H_7)_4$, $Ce(NO_3)_3 \cdot 6H_2O$, $Ti(OC4H9)_4$, *etc.*[48,49,50,51,52]

In Non-alkoxide route, removal of the inorganic anion is necessary to produce the required oxide.[46] However, halides often remain in the final oxide material and are difficult to remove.[53] Therefore the alkoxide route is used throughout this thesis.

After complete polymerisation, the removal of the solvent molecule results the transition of liquid sol into solid wet gel and the process can be termed as gelation. The gel is simply defined as a non-fluid three dimensional continuous network, which extends through a fluid phase.[54] Further drying of these wet gels through different track can result various products with diverse functional properties. If the gel is dried by evaporation, then the gel network will collapse and results xerogel having humongous surface area, small pore size and high porosity.[54,55] If the drying process is performed under supercritical conditions, the structure of the gel network may retain and results aerogel with low density and highly porous material (Figure 1.5).[54,56] Number of studies follows sol-gel method for the synthesis of nanocrystalline materials for different applications because of its interesting advantages in sol-gel field and they are

1. The method requires simple processing steps and simple equipment.[43]

2. Cost effective method.

3. Sol-gel preparation needed room temperature.[43]

4. Chemical homogeneity of the sol-gel product is possible with high purity. [43]

5. Able to get small sized materials having high surface area and porosity.[57]

6. Sol-gel method can be used to make ceramic and glassy materials in the form of powders, fibers, or thin films.[43,58]

7. Easily get variety of products such as fibers, films, powders with suitable properties.[59]

8. Easy to do coatings for films.

9. Metal (inorganic) – organic nano composites can easily got through sol-gel method.

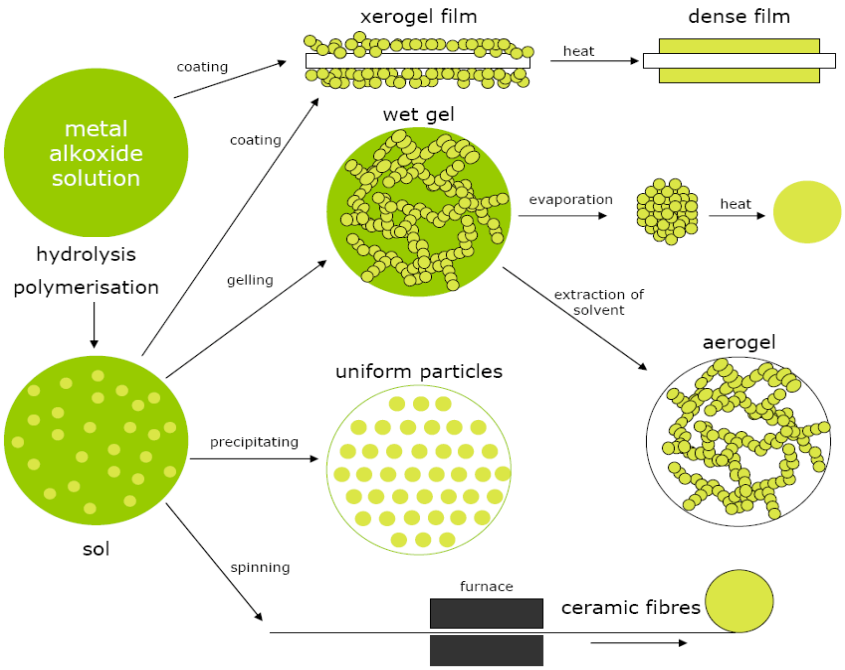

Figure 1.5. Schematic representation of sol-gel process.

1.6. Sol-gel synthesis of titanium dioxide

The mostly used precursor for the synthesis of titanium dioxide in metal alkoxide route are Ti $(OR)_4$, where R=-OC_3H_7 (isopropoxide), -OC_4H_9 (butoxide) and -OC_2H_5 (ethoxide). The entire thesis uses only titanium isopropoxide as precursor for the synthesis of nano TiO_2 by sol-gel technique. Normally, the sol-gel method involves hydrolysis and condensation of metal alkoxide pursued by heat treatment at required temperatures, which results polymerised metal oxide framework.[60] In general, the lower electronegativity and corresponding oxidation state of transition metals are lower than their coordination number in the oxide network. So, expansion of the coordination sphere spontaneously occurs upon reaction with water (hydrolysis) or other nucleophilic reagents by accepting lone pair of electrons from these reagents to increase the coordination number of the titanium metal from 4 to 6.[61] Also the coordination expansion is quiet easy in the case of titanium metal due to its vacant d orbitals.

In addition, metal alkoxides contain metal-oxygen bond, highly electronegative alkoxide group and electrophilic transition metals, which make the molecules highly polar and reactive. Therefore it is necessary to control the reaction condition to produce materials having nano size, consistent structure and shape even though the controlling of the conditions to be difficult. Different steps involved in sol-gel process are

1.6.1. Hydrolysis

Hydrolysis of titanium alkoxide proceeds through nucleophilic substitution reaction.[62] In the nucleophilic addition of water molecule to the titanium precursor, titanium can accept lone pair of electrons from water molecule through oxygen. –OR group was reported as better leaving group, so which can be easily replaced by an –OH group. The leaving alkoxide group can easily protonated within the transition state from water molecule and removed as alcohol (scheme 1.1).

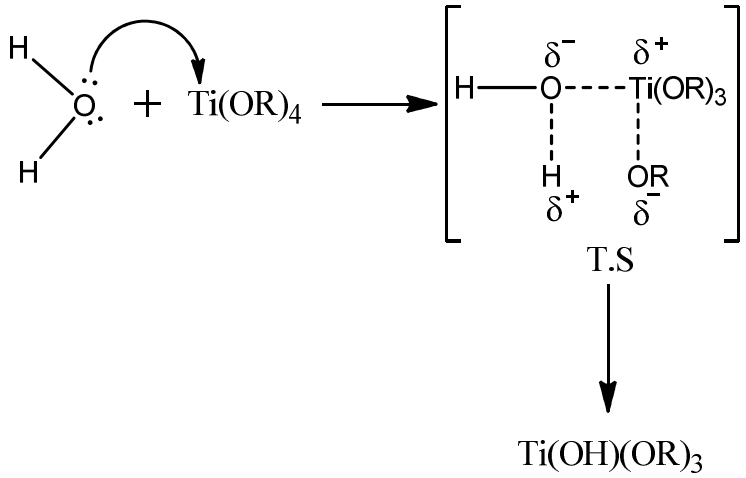

Scheme 1.1: Mechanism for the hydrolysis of titanium alkoxide

1.6.2. Condensation

Condensation reaction can form large chains of molecules through polymerization. Condensation can proceed via two routes: either through alcoxolation or through oxolation reaction. In both these processes an oxo bridge (M-O-M) is formed in between the metals as seen in the scheme 1.2 and 1.3, but leaving group differs. Alcoxolation

is the process of removal of alcohol when a partially hydrolysed metal alkoxide combine with another metal alkoxide molecule and form an oxo bridge between the two metal atoms (scheme 1.2). However, oxolation happened when two partially hydrolysed metal alkoxide molecules link together by nucleophilic addition reaction to form the same oxo bridge as in alcoxolation, but the only difference is that the leaving group is water in place of alcohol (scheme 1.3).

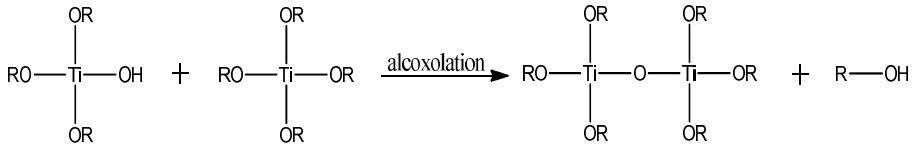

Scheme 1.2. Alcoxolation reaction

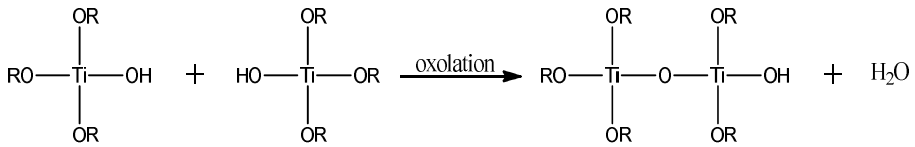

Scheme 1.3. Oxolation reaction

The thermodynamics of the hydrolysis and condensation reaction mainly depends: the electrophilicity of the metal, nucleophilicity of the entering molecule and stability of the leaving group. According to Livage *et al,* thermodynamically alcoxolation is more favourable than oxolation during a condensation reaction of hydroxy titanium ethoxide.[63] Based on these results Sanchez *et al* concluded that alcoxolation may be a favored condensation route than oxolation for all titanium alkoxides.[64]

The kinetics of condensation reaction depends:

- The extend of unsaturation of the metal
- Extend of molecular complexity of the metal alkoxide
- Usage of solvent
- Alkyl chain length of organic ligand
- The leaving ability of the proton to be transferred in the transition state.

Sols and gels are commonly treated as intermediates in the formation of powders, glasses, ceramics *etc.* Therefore, successive steps like aging, drying and calcination are important for the above conversion.

1.6.3. Aging:

This process occurs *via* three steps: continuing polymerisation, syneresis and coarsening. Polymerization of unreacted hydroxyl groups results an increment in the connectivity of the gel network. Syneresis is the irreversible and spontaneous shrinkage of the gel accompanied by the expulsion of pore liquid and finally coarsening or Ostwald ripening refers to an increase in the particle size, and change in crystalline structure and morphology.

1.6.4. Drying:

The simplest way for drying is to let the liquid evaporate at a very low rate and which avoid cracking of the gel during drying. This strategy is effective, but is not practicable because the process is time consuming.

Another method for drying is to keep the gel at 100 °C where large volumetric shrinkage occurs during the process. One of the main problems in the later method is possibility of cracking of the gel, due to the stresses caused by the capillary forces in between the gas-liquid interfaces. The direct solution to avoid all these to add drying control chemical additives (DCCAs) that reduce the capillary force at the gel interface, allowing rapid elimination of unwanted particles.[65] DCCAs are added into the starting mixture before gelation and after heat treatment, a crack-free xerogel results. Formamide is one of the most common DCCAs used for drying silica gels, which results increase in hardness and pore size of the dried gels.

1.6.5. Calcination:

This refers to heating of the dried gel at higher temperature (above 100 $^{\circ}$C) in the absence or limited presence of oxygen. Organic matter, moisture and volatile impurities already present in the sample are driven out on calcination and get pure oxide form of the metal. Calcination affects crystal size, densification, morphology and pore size and shape of the metal oxide.

1.7. Applications of titanium dioxide

In the early twentieth century, titanium dioxide has been widely used as a pigment[66] and in paints,[67] sunscreens,[68,69] toothpastes,[70] ointments and other instances in which white colouration is needed. The reason for this is the high refractive indices of anatase and rutile, which results high reflectivity from the surfaces.[71] In 1971, after the discovery of photocatalytic splitting of water on a TiO_2 electrode under UV light,[72]

enormous efforts have been devoted to the research of TiO_2 material, which has led to many promising applications (Figure 1.6).[12,73] TiO_2 photocatalysts are known to be applicable in a range of technologically important areas:

- **Environment**

Water treatment.[74,75,76,77,78]

Air purification.[79,80]

Used as sensors for humidity and various gases[81,82]

- **Energy**

Dye-sensitised solar cells (DSSCs)[83,84,85]

Electrolysis of water to generate hydrogen.[86,72 ,87,88,89]

- **Built Environment**

Non-spotting glass[90,91]

Self-cleaning coatings[76 ,77 ,79,92]

Explored as elctrochromic devices, such as elctrochromic displays and windows[93,94,95,96]

UV blocking applications[97,98]

- **Medicinal field**

Self-sterilising coatings.[99,100]

As biotracer[30]

Used to kill tumor cells in cancer treatment.[101,102,103,104,105]

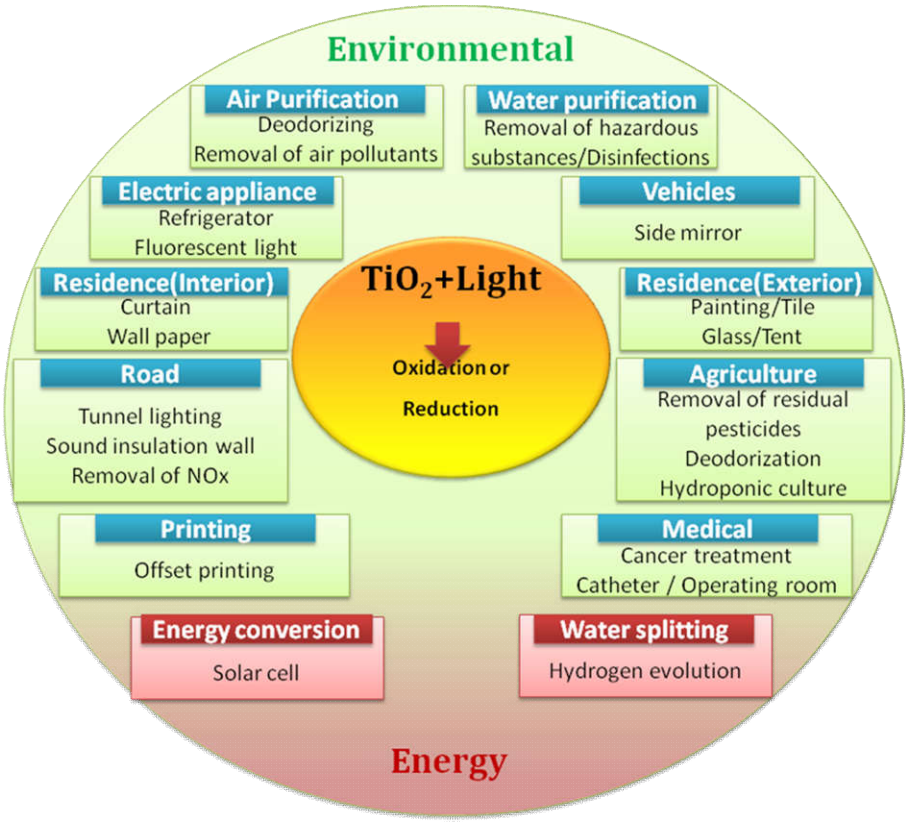

Figure 1.6: Applications of TiO_2 photocatalysis[106]

1.8. Advanced oxidation process

Environmental contamination by organic pollutant is an overwhelming problem all over the world. Over the last 10 years problems related to hazardous waste remediation have emerged as a high national and international priority.[107] The pollutants with high toxicity require some novel techniques to transform them into harmless and eco-friendly

compounds like carbon dioxide, water and other inorganic species. Several researches have been carried out to remove these pollutants rapidly and economically. The prime condition is that, the method should be inexpensive and green. That is a secondary pollution should not be produced upon this process.

Recently a new and promising approach, the advanced oxidation process (AOP) was developed for environmental purification and in which photocatalysis has become an integral part of AOPs, which referred to as a chemical treatment procedure designed to remove organic or inorganic material in water and waste water.[108] Key AOPs include homogeneous and heterogeneous photocatalysis based on UV or visible irradiation, ozonation, ultrasound, electrolysis, Fenton's reagent and wet air oxidation.[109] Generally, AOPs can be defined as an aqueous oxidation method which depends on the intermediacy of highly reactive species such as hydroxyl radicals, which leads to the destruction of the target pollutants.[109] The reactive hydroxyl radicals are the strongest oxidizing species that can virtually oxidize any organic/inorganic compound that may present as contaminants in the water bodies, often at diffusion controlled reaction speed.[110] Once formed hydroxyl radicals quickly and non-selectively fragmented the contaminants into small inorganic molecules. Usually, the $OH^{\cdot}$ radicals are generated with the help of primary oxidants such as ozone, hydrogen peroxide or oxygen etc, and/or energy sources like UV light or catalysts (eg, TiO_2). Precise, sequence, pre-programmed dosage and combinations of these reagents are applied to get a maximum yield of hydroxyl radicals. Summarizing, when applied in properly tuned

conditions, AOPs can reduce the total amount of contaminants from several hundred of ppm to less than 5 ppm and significantly bring down the TOC and COD value, which earned it the credit of water treatment processes of the 21st century.[110,111]

One of the most appropriate works done in this field is the semiconductor catalysed photo degradation of pollutants using solar irradiation as source of energy.[20] Metal oxides are recently used semiconductor photocatalyst and Chan *et al* categorised these oxides into three: (i) Titanium dioxide (TiO_2), (ii) Zinc oxide (ZnO) and (iii) other metal oxides (such as Vanadium oxide, Tungsten oxide, Molybdenum oxide, Indium oxide and Cerium oxide).[108] The photocatalytic properties of these metal oxides have been studied extensively, and the result shows that they have good photocatalytic efficiency in the degradation of dye in wastewater.[51,112,113,52] Of these photosensitive semiconductors, TiO_2 is considered as an ideal semiconductor for photocatalysis because of its chemical stability, low cost, availability and highly oxidizing nature.[114,115]

TiO_2 became one of the most attractive semiconductor materials in the research field. In 1972 when Fujishima and Honda reported the discovery of photoinduced water splitting ($2H_2O \rightarrow 2H_2 + O_2$) using a TiO_2 anode and platinum counter electrode prompted extensive research on TiO_2 and other semiconductor materials.[72] TiO_2 shows a promising remedy for the environmental pollutants was introduced, when Frank and Bard investigated the reduction of cyanide in water in 1977.[116,117] In 1983 Ollis reported the complete degradation of trichloroethylene in aqueous media. [118] Nano sized TiO_2 was employed

in an efficient solar cell, the dye sensitised solar cell (DSSC) as reported by Graetzel and O'Regan in 1991, led TiO_2 as one of the most internationally researched semiconductor materials.[85,119] UV illuminations on TiO_2 induce wettability termed as superhydrophilicity, which have a large range of applications in cleaning and anti-fogging surfaces.[73] In 1997 Wang *et al* reported TiO_2 surfaces with excellent anti-fogging and self-cleaning abilities which were attributed to the super hydrophilic nature of the TiO_2 surfaces.[120]In 1995 there were 700 TiO_2 publications, seven years later that number increased to over 2000 publications showing the importance of TiO_2 photocatalysis.

1.9. Photocatalysis

Photocatalysis is a redox reaction in which the electrons in the valence band get excited to the conduction band by creating positive holes in the valence band of semiconducting materials by the irradiation of light with suitable energy. [121,73] Among the photocatalysts, TiO_2 is the most available and known material as a photocatalyst. The high stability and higher quantum efficiency of TiO_2 are the key factors that make it an ideal catalyst. More significantly, it has been used as a white pigment from ancient times, and thus, its safety to humans and the environment is guaranteed by history.

Commercially, the possible application of TiO_2 material as a photocatalyst in water treatment is due to several factors:

1. Photocatalytic reactions take place at room temperature.

2. Usually, TiO_2 materials completely mineralized the organic pollutants into nontoxic substances such as CO_2, HCl and water without any production of intermediates. So photocatalytic reactions do not suffer the drawbacks of photolysis reactions in terms of toxic intermediates.[10,122 ,123,124]

3. Photogenrated holes are extremely oxidizing, can produce hydroxyl radicals from water molecule and photogenerated electrons reduce oxygen molecule to superoxide radicals.[73]

4. Comparatively the TiO_2 photocatalyst is inexpensive and can be used as a support on various substrates such as fibers, glass, sand, stainless steel, activated carbon, inorganic materials allowing continuous re-use.

1.10. Electronic process in pure TiO_2 photocatalysis

Titanium dioxide is an n-type semiconductor, which has a band gap of 3.2 eV for both anatase and brookite and 3 eV for rutile phase. In TiO_2, the titanium ions are in octahedral environment, generally have a Ti^{4+} ie $3d^{\circ}$ electronic configuration. The valence band of TiO_2 consists of 2p orbitals of oxygen, whereas the conduction band is made up from 3d orbitals of titanium.[125] Irradiation of UV light on TiO_2 surface excite electron from the filled valence band to the empty conduction band, creating electron-hole pairs as shown in Figure 1.7.[125] The photogenerated electron-hole pairs undergo recombination and dissipate the excess energy through nonradiatively or radiatively as light or heat (eq 1 and 2).

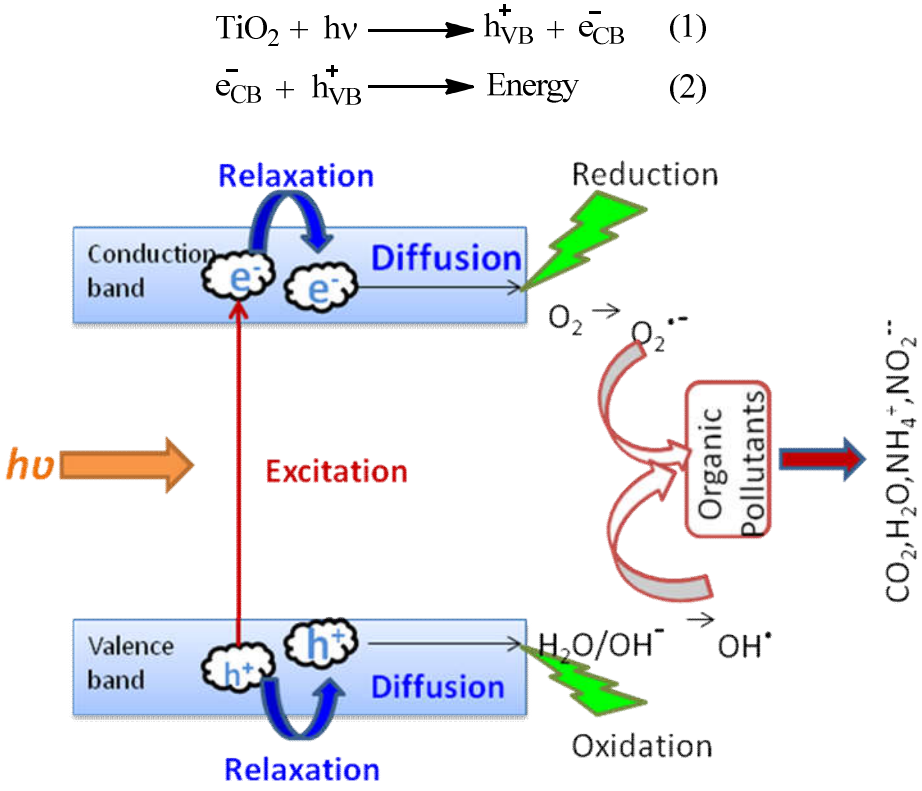

Figure 1.7: Band gap structure of UV active anatase TiO_2

This will scale down the overall efficiency of the light induced process. Various strategies have been adopted to reduce the rate of recombination and they are heterojunction coupling,[126,127] doping with ions[128] and nanosized crystalline particles.[129, 130] The excited electrons (e^-) in the conduction band are now in a pure 3d state and because of dissimilar parity, the transition probability of e^- to the valence band decreases, leading to a reduction in the probability of e^-/h^+ recombination.[131] These charge carriers, can easily migrate to the surface of the TiO_2 catalyst and trigger secondary reactions with the

molecules adsorbed on its surface or within the surroundings of the charged particles.

For example, the excited electrons in the conduction band can reduce the oxygen molecule to form superoxide ($\cdot O_2^-$) radicals, that may further react with H^+ ion to produce hydroperoxy radicals ($\cdot OOH$) and both of these reactive oxygen species (ROS) can take part in the oxidation of organic pollutants, whereas the positive holes in the valence band can oxidize the adsorbed water or hydroxyl molecule and produce hydroxyl radicals ($\cdot OH$), which in turn oxidizes the organic pollutants (Figure 1.7; equations 3 and 4).[132,133] The reactive oxygen species such as hydroxyl, superoxide or hydroperoxide radicals can subsequently oxidize organic pollutants producing mineral salts, CO_2 and H_2O (equation 5).[134]

$$h^+_{VB} + H_2O \longrightarrow \dot{O}H + H^+ \quad (3)$$

$$e^-_{CB} + O_2 \longrightarrow \dot{O}_2 \longrightarrow \dot{O}OH \quad (4)$$

$$\dot{O}H/O_2/OOH + \text{Pollutants} \longrightarrow \longrightarrow \longrightarrow H_2O + CO_2 \quad (5)$$

The primary condition for a semiconductor for organic compound degradation is that the oxidation potential for the conversion of OH^- /H_2O to hydroxyl radical lies above the position of TiO_2 valence band (3.2 eV). The band potential of a semiconductor is controlled by pH of the reaction medium. The reaction of OH^- to hydroxyl molecule is favored at basic condition and that from H_2O is favored at acidic range. At neutral pH also the oxidation potential of hydroxyl radical lies above the valence band position of TiO_2. Thus the formation of hydroxyl radical is thermodynamically favored at entire pH range. The

oxidation potential of several organic compound lies above the valence band of TiO_2 and direct oxidation of these pollutants by TiO_2 valence band holes are thermodynamically possible. But Cunningham and Srijaranai observed that presence of aqueous environment is important to achieve maximum rate for photocatalytic degradation of contaminants.[135]

Generally, the photocatalytic power of a semiconductor widely depends:

1. Light absorption characteristics
2. Rate of redox reaction by electron-hole pair on the surface of TiO_2
3. Rate of e^--h^+ recombination

Additionally, some factors related to the band structure of TiO_2 also have the greatest effect on photocatalysis and which follows:

1. Band gap energy
2. Position of highest point in the valence band
3. Position of lowest point in the conduction band

Anatase phase is commonly selected for photocatalytic applications due to its better photoactivity. The better photoactivity of anatase phase is due to its lower rate of electron-hole recombination, higher number of hydroxyl radicals present on the surface of TiO_2, lower cost and higher surface area.[136] The band gap of anatase TiO_2, 3.2eV

effectively utilize UV range of radiation for photocatalytic applications. In the photocatalytic reaction pathway, the band gap energy predominantly determines which the most effective light wavelength is, and the upward movement in the position of the valence band is the main element in the determination of the oxidative decomposition power of the photocatalyst. Solar radiation contain only 5% of UV, which limit the use of anatase titania for practical applications. Various chemical modifications have been proposed to modify TiO_2 for harvesting solar radiations in order to raise the photocatalytic efficiency of TiO_2.

1.11. Modifications of TiO_2

1.11.1. Doping

Doping is the process of adding impurities in very small concentration into the crystal structure of TiO_2 without giving rise to new crystallographic phases, forms or structures and aims to alter their properties. This can be accomplished through sol-gel process, microwave synthesis, hydrothermal method, magnetron sputtering etc. Historically, doping of TiO_2 has been taken as a common approach for bandgap engineering of the material, i.e., a decrease in the bandgap or introduction of intra-bandgap states, which results in the absorption of more visible light.[137] When employing dopants to diverse the optical response of a material it is desirable to maintain the integrity of the crystal structure of host material while changing its electronic structure.[138]

1.11.1.1. Self doping:

The property of semiconductor, TiO_2 is changed without the introduction of any metals or non metals. Justicia *et al* developed Self-doped titanium dioxide thin films for efficient visible light photocatalysis. Here doping induced oxygen vacancies which are known to be good electron trappers and these trapping states are located just below the conduction band of TiO_2. The surface promoted electrons after visible light absorption are employed in the photocatalytic oxidation of NO.[139,140] Hamdy *et al* reported the one step synthesis of Ti^{3+} rich blue coloured TiO_2, that is active under visible light irradiation, but the material was not much stable.[141] Whereas Etacheri *et al* developed a dopant free antatase TiO_2 photocatalyst stable upto 900 °C.[142]

1.11.1.2. Doping with metals:

Replacement of Ti^{4+} in TiO_2 with any cation is relatively appeared as an easy way than to substitute O^{2-} with any other anion because of the charge states and ionic radii.[138] Nano-materials exhibit higher tolerance to structural distortion than bulk materials due to their inherent lattice strain. As a result, modification on the surface of TiO_2 nanoparticles appears to be more beneficial than the modification of bulk TiO_2.[137] Modify the pure photocatalyst materials with metal ions, especially d-block metals such as Fe and Cr results in the insertion of impurity energy levels between the parent conduction and valence bands. In this case, electrons can be promoted from dopant d-band, (inserted energy level) to the conduction band or from the valence band to the dopant d-

band by lower energy photons than required by the pure photocatalysts.[110] The resulting energy level of the dopant and photo-catalytic activity strongly depends on various factors such as the chemical nature, and concentration of dopant and its structural, and chemical environment. With regard to dopant concentration, there is a general agreement that at lower amounts, the dopant may act as a trapping site by introducing localized states that can improve charge separation and hence increase the photocatalytic efficiency of TiO_2. Whereas at higher concentrations they can promote recombination of charge carriers.[143,144] Hence, an optimum amount of dopant often exist, which is typically in the order of one or less than one percentage. Nagaveni *et al* synthesized W, V, Ce, Zr, Fe and Cu ion doped anatase TiO_2 nanoparticles by a solution combustion method and found that the amount of dopant ion in the solid solution was limited to a narrow range of concentrations.[145]

In the last ten to five years extensive research has been performed on the enhancement of TiO_2 photocatalytic activities through doping of transition and rare earth metal ions, especially for air and water sanitization applications.[146,147] Choi *et al* reported 21 transition metal ion doped TiO_2 and found that Visible-light photo-responses were observed for TiO_2 photocatalyst as a result of most of these metal ion doping.[128] Li *et al* developed La^{3+}-doped TiO_2 by the sol-gel process and found that the lanthanum doping could inhibit the phase transformation of TiO_2, enhance the thermal stability of the TiO_2, reduce the crystallite size, and increase the Ti^{3+} content on the surface.[148] Xu *et al* compared photo-catalytic activities of various (La,

Ce, Er, Pr, Gd, Nd and Sm) rare earth metal ion doped TiO_2 and shows that TiO_2 loaded with optimum amount of dopant demonstrated superior band-gap narrowing and visible-light photo-catalytic activities. As a result of its ability to transfer both electrons and holes to the surface Gd-ions doped TiO_2 was found to be the most photoactive.[149]

1.11.1.3. Non-metal doping:

Unlike non-metal anions, metal cations frequently give well localized d-band deep in the band gap of TiO_2 and are likely to form recombination centers of charge carriers.[150,88] Therefore non-metal doping gives a promising way to absorb maximum sun radiation for photocatalytic applications of TiO_2. Numbers of studies are already done based on the non-metal doping on TiO_2 in the visible light responsive photocatalysis.

First report based on non-metal doped TiO_2 was in 1986 by Sato *et al* and the N-doped TiO_2 obtained shows higher photoactivity in the visible light region (434 nm) for the oxidation of CO and C_2H_6.[151] However, the result did not get any attraction at that time and get attention only after 2001 for non-metal doped TiO_2 after the report of Asahi *et al*, they account for the significant red shift in the wavelength of absorption.[150] According to the report of Asahi *et al*, N-doping shift the absorption edge of TiO_2 into visible region (λ<500nm) through the replacement of Oxygen in the anatase crystal lattice by N-atom and hence electrons from the 2p orbital of N can be excited to 3d orbital of Ti.[150,152,153] Deficiency in oxygen were also boost the visible light

absorption of TiO_2 and Ihara *et al* reported that nitrogen doped in the site of oxygen vacancy and block the tendency for reoxidation.[154,155]

Doping with sulphur also shows similar behaviour as that of nitrogen (Excitation of electrons from 3p orbital of S), but the incorporation of this ion into TiO_2 lattice is quite difficult due to its higher ionic radius, which is proved from the higher formation energy needed for the substitution of S than that of the nitrogen. [150,156] Mechanisms behind the sulphur doping are explained in various reports. Sulfur can enter into TiO_2 lattice either as anion or as cation. Umebayashi *et al*. have succeeded in doping with sulfur and it replaces the lattice oxygen atom by anionic sulphur (S^{2-}) in the TiO_2 crystal. [157] But Ohno *et al* described that sulphur replaces the Ti atom on the surface of TiO_2 and substituted as cation (S^{4+} or S^{6+}) and is confirmed by Yu et al.[158,156] Yu *et al* also proposed that doping with cationic sulfur is more favorable than anionic sulphur doping because Ti-S bonding from S^{2-}recquire more formation energy than that from S^{6+}.[156,159]Tachikawa *et al* suggested that visible light absorption through sulfur doping can be originated from the mixing of S 3p band with the valence band of TiO_2, leading to a decrease in band gap energy.[160]All these reports concluded that the lattice oxygen atoms were replaced by the non-metal atoms like N, S, C, F etc and produced an isolated narrow band in between the valence and conduction band of TiO_2 and results narrowed band gap.

Figure 1.8 shows that introduction of an extrinsic electronic level of 2p (N or C) or 3p (S) orbitals of dopant with a potential energy greater than that of O2p orbital cause an excitation of electron to the

conduction band using visible radiation in the case of N-doped or S-doped TiO_2.[161,162,163,164,165]

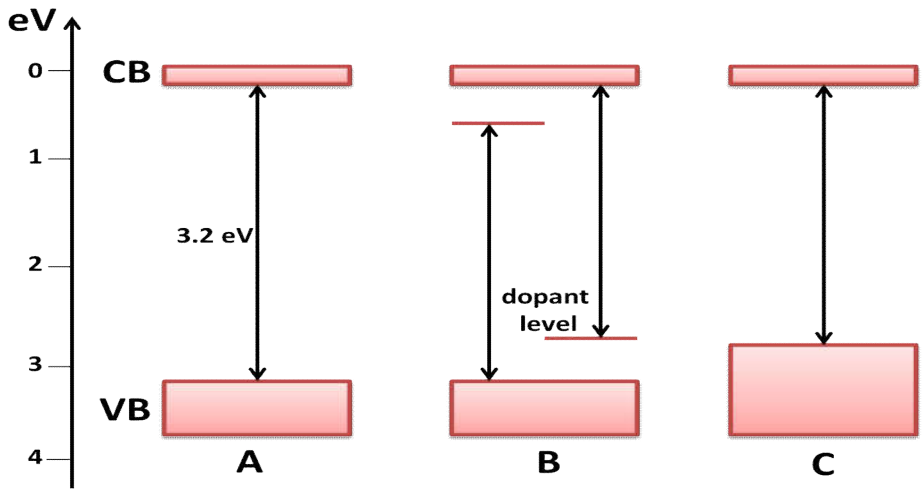

Figure 1.8. Various schemes illustrating the possible changes occur to the band gap of anatase TiO_2 on doping with various non-metals: A) band gap of pristine TiO_2, B) doped TiO_2 with localized dopant levels near the VB and the CB and C) band gap narrowing resulting from broadening of the VB.

1.11.1.4. Codoping:

Codoping of TiO_2 using different elements is not a new concept. However, the wavelength of absorption and photocatalytic activity of the codoped sample is differing to those doped individually.[166] Recently, non-metals have been codoped with metals and other non-metals to attain visible light photocatalysis more effectively. This recommend that more photons are being effectively utilizes by the codoped catalyst. Valentin *et al* have succeeded in synthesizing titanium dioxide codoped with nitrogen and fluorine show enhanced

visible light photocatalytic activity in comparison to N-doped or F-doped TiO_2.[167]

Codoping of TiO_2 can be used as successful way to improve the charge separation. Yang *et al* reported that TiO_2 codoped with Eu^{3+} and Fe^{3+} in optimal concentration significantly improved the photocatalytic activity compared with undoped TiO_2. Here Eu^{3+} serves as an electron trapping agent and Fe^{3+} as a hole trap, increasing the rates of oxidation and reduction processes *via* improved interfacial charge transfer.[168] Vasiliu *et al* suggested that Fe and Eu codoped TiO_2 system exhibit a red shift in the absorption spectrum and higher photoactivity for the catalytic oxidation phenol and degradation of styrene when exposed to visible light.[169]

There is several reports available based on metal-nonmetal codoped TiO_2 exhibiting efficient photocatalytic activity. Xu *et al* prepared Ce and C codoped TiO_2 using sol-gel method and the photocatalytic activity of the codoped system showed effective removal of Reactive Brilliant Red X-3B under visible light compared with that of Degussa P25, C-doped and undoped TiO_2 because cerium doping slow down the recombination of photogenerated electrons and holes in TiO_2.[170] Ce and N codoped TiO_2 showed an enhanced photocatalytic activity for the degradation of nitrobenzene under visible light. The nitrogen atom was incorporated into the TiO_2 crystal and narrows the band gap energy. The doped cerium atom existed in the forms of Ce_2O_3 and dispersed on the surface of TiO_2 and the improvement in the photocatalytic activity was ascribed due to the synergistic effects of the nitrogen and cerium co-doping.[171]

1.11.2. Surface chemical modifications[12]

When a photocurrent is produced with light energy less than that of the semiconductor band gap, the process is known as sensitization and the light-absorbing materials are referred to as sensitizers.[12,15] Any materials having narrowed band gap or absorption in the range of visible or infrared region can be used as sensitizer for TiO_2 materials. Examples of such materials include metals, organic dyes and inorganic semiconductors with narrow band gaps. Efficiency of the sensitized TiO_2 largely depends on how efficiently the sensitizer can interact with light and also the efficiency of the charge transfer from an excited state of the sensitizer to TiO_2. The match between the electronic structures of the sensitizer and TiO_2 plays a large role in this process, as does the structure of the interface, including the grain boundaries and bonding between the sensitizer and TiO_2.[12] Charge trapping and recombination is needed to avoid which may harm the performance of sensitized TiO_2, for that careful design should be necessary.[15,172,173]

1.11.2.1. **Dye sensitization**:[174,175,176]

Dye sensitization of wide band gap semiconductors is an expanding area which is the beginning principle in solar cell technology. The recent growth is basically due to the important advancement made by Gra¨tzel *et al* with TiO_2 having higher surface area sensitized by ruthenium bipyridyl complexes.[172, 177] Generally, dye sensitization occurs through excitation of the sensitizer adsorbed via physisorption or chemisorption on TiO_2 surface followed by charge transfer to the semiconductor. This sensitization shifts the wavelength of absorption

of TiO_2 to visible region, which is a very important criterion for a photocatalyst to operate under natural light.

1.11.2.2. Sensitization by Metal Nanoparticles.

Ohko *et al* found that Ag-TiO_2 film exhibiting multicolor photochromism and nonvolatalization when TiO_2 nanoparticle film was sensitized with silver nanoparticles under UV light. By regulating irradiation conditions as well as geometry and matrix materials of nanopores, we can control the multicolor photochromic behavior and the chromogenic properties. This type of photochromism is may be due to the oxidation of silver by oxygen under visible light and the reduction of Ag^+ under UV light.[178] The photochromism and rewritability of Ag–TiO_2 films were deactivated by modification with thiols to make it possible to retain color images displayed on the films while the deactivated properties were fully reactivated by UV-irradiation.[179] Nanoporous TiO_2 films loaded with gold and silver nanoparticles exhibit negative potential changes and anodic currents in response to visible light irradiation, so that the films would potentially be applicable to inexpensive photovoltaic cells, photocatalysts and simple plasmon sensors.[180]

1.11.2.3. Sensitization or coupling of TiO_2 by narrow bandgap semiconductors.

Narrow band gap semiconductors are widely used as sensitizers to enhance the optical absorption properties of TiO_2 nanomaterials in the visible region by various groups.[181,182,183] These type of sensitization of TiO_2 with other semiconductor provide a beneficial solution for the

recombination of photogenerated charge carriers. In coupled semiconductors, illumination of one semiconductor makes a response in the other semiconductor at the interface between them. Hoyer *et al* reported that comparing the absorption and photocurrent spectra of coupled TiO_2/PbS system, only PbS clusters of sizes smaller than ~25 A° contribute to the sensitization.[184] Fitzmaurice *et al* found that excitation of the AgI sensitized on TiO_2 nanoparticles results a stable electron-hole pairs with a lifetime beyond 100 μs and electron can easily migrated from AgI to TiO_2.[185] Vogel *et al* investigated sensitization of nanoporous TiO_2 by quantum sized CdS, PbS, Bi_2S_3, Ag_2S and Bi_2S_3 and found that the relative positions of the energetic levels at the interface between the quantum sized particles and TiO_2 could be optimized for efficient charge separation by using the size quantization effect and that the photostability of the electrodes could be significantly enhanced by surface modification of the TiO_2 nanoparticles with CdS nanoparticles.[186,12]

Bi_2S_3/TiO_2,[187,188] WO_3/TiO_2,[189,190] CdS/TiO_2,[183,191] SnO_2/TiO_2[192,193] etc are the other few of the examples for the photocatalytic system enhanced via heterojunction coupling.

1.11.2.4. Capping with other semiconductor or metal nanoparticles

The coating of one semiconductor or metal nanomaterial on the surface of another semiconductor or metal nanoparticle core is called capping. A semiconductor nanoparticle coated with another semiconductor having different band gap in core-shell geometry to passivate the

surface of initial nanoparticle and enhance its emissive properties. [137]However, the mechanism of charge separation in capped semiconductor system is similar to that of coupled semiconductor system, while the interfacial charge transfer and charge collection in both theses system are different. In coupled systems, the two semiconductors are in contact with each other and both electrons and holes are accessible for redox processes on different particle surfaces. Whereas, in capped semiconductor system only one of the charge carrier is accessible at the surface, while opposite charge transferred to the inner semiconductor system, thus improving the selectivity of the interfacial transfer and enhancing the oxidation or reduction reaction.[194, 137]The gold-capped TiO_2 nanoparticles improve the efficiency of interfacial charge-transfer process and enhance the efficiency of thiocyante oxidation.[195]

1.11.3. Combined effect of doping and coupling

From the above discussion, it is clear that doping introduces an additional state in TiO_2 bandgap and increase the visible light response. Also, coupling enhances the visible light activity through the formation of a heterojunction between TiO_2 and other small bandgap semiconductor. Numerous reports suggested that combination of doping and coupling further improve the photocatalytic performance of TiO_2. [196,197]

1.12. Factors affecting photocatalysis

The following factors, which affects the photocatalytic degradation of dyes in waste water:

1.12.1. Influence of pH on the reaction medium[198,199,200,201,202,203]

pH influences the surface charge, particle size and the band edge position of TiO_2. The isoelectric point for TiO_2 in water is approximately at a pH = 6.628, and thus a positive charged surface is expected at lower pH and a negatively charged surface above this pH, due to protonation or deprotonation of surface hydroxyl groups.[204] For an n-type semiconductor such as TiO_2, accumulation of negative charges at the surface causes an upward band bending and thus improved transfer of photogenerated holes. In general, there was found to be less than one order of magnitude difference in the rate of degradation between pH 2 and 12,[205,206] though this is highly dependent on substrate.

1.12.2. Crystal phase:

TiO_2 mainly exists in three crystalline phases: anatase, rutile and brookite. Of these, Anatase is generally considered as the photocatalytically active phase, though rutile phase has also been extensively studied. Because of the difficulty of Brookite phase to obtain in pure form, it is the least studied of the three.

Rutile was the first crystal phase of TiO_2 to be studied in detail and lot of theoretical and experimental work was done on photocatalytic activity using rutile TiO_2. Rutile (band gap = 3.0 eV (418 nm)), would seem to be a more ideal photocatalyst than anatase (3.2 eV, 387 nm), but it has been shown to be a less active photocatalyst than anatase.[87] It is reported that rutile is photocatlytically less active than anatase due to the tighter close packing in the rutile crystal structures, which has not

many defects to trap photoexcited electrons and holes, which reduce recombination of charge carriers. As a result of this, the majority of recent research on TiO_2 photocatalysts has been done on the crystalline anatase phase. The remarkable reason for the highest activity is due to the higher surface area, the difference in the structural energy between these two phase types, the slightly upward movement in the Fermi level, lesser capacity to adsorb oxygen and higher amount of hydroxylation in the anatase phase.[207]

In both rutile and anatase phases, the valence band position is deep, and the resulting positively charged holes display sufficient oxidative power. However, the conduction band of the anatase phase is close to the negative position than the rutile phase. Therefore, the reducing power of the anatase phase is stronger than that of rutile phase. Generally, the anatase crystal phase formed at lower temperature, shows higher surface area compared to the rutile phase. Larger surface area with a constant surface density of adsorbents provokes faster surface photocatalytic reaction rates. In this sense, the higher the specific surface area, the higher the photocatalytic activity that one can expect. Therefore, the anatase phase exhibits higher overall photocatalytic efficiency compared to the rutile phase.

However, Hermann *et al*[208] hypothesized that Mixture of rutile and anatase TiO_2 showed better photocatalytic activity than either phase alone. Because any kind of solid–solid interface is a key structural feature that facilitates the charge separation to hinder recombination. The interface also acts as an active site to initiate catalytic activity and enhance photocatalytic efficiency.[209] Commercially available catalyst,

Degussa P25 contains 80% anatase and 20% rutile with a BET surface area of 55±15 m^2g^{-1} and crystallite sizes of 30 nm in 0.1 μm diameter aggregates and is produced by high temperature sintering of $TiCl_4$ in the presence of hydrogen and oxygen.[210, 11] The enhanced photocatalytic activity of Degussa P25 is due to the ability of excited electrons generated in the anatase TiO_2 particles to be transferred to the rutile particles, thus minimizing charge recombination.[211] Recently, Degussa P25 TiO_2 has set the standard for photocatalysis in environmental applications.

1.12.3. Percentage of (001) facets of anatase phase

In recent years, several literatures attributes that different facets of anatase TiO_2 show different chemical activity, a property that is determined by the surface energy (ɣ) of the facet.[212] It is reported that surface energy of different facets of anatase TiO_2 follows the order $ɣ_{(001)}$ (0.90 J/m^2) > $ɣ_{(100)}$ (0.53 J/m^2) > $ɣ_{(101)}$ (0.44 J/m^2), that means the surface energy of (001) facet of anatase TiO_2 is almost double than that of the (101) facet.[213] Selloni *et al* found that the reactivity of (001) facets is greater than that of (101) facets in an anatase crystal,[214] which means that highly energetic and largely sized (001) facet exhibit higher photocatalytic activity. However, the lowest stability of (001) facet make its preparation difficulty. Although some researchers have reported that the exposed (001) facets in TiO_2 nanoparticles can be obtained by cautiously maintaining the growth process by adding suitable surfactants, the synthesis method is time-consuming with high cost, and midcult to scale-up.[212]

Generally, the anatase TiO_2 nanobelt grows along (101) direction, the facet with very low surface energy, and only small percentage of (001) facet is exposed on the top of the nanobelt, which explains the very low photocatalytic activity of TiO_2 nanobelts. By adjusting the synthesis procedure and the crystallization process, anatase TiO_2 nanobelts grown along the (101) direction with two dominant (001) facets can be obtained.[212] Yang *et al* synthesized uniform anatase crystal, which corresponds to 47% of (001) facets using hydrofluoric acid as a morphology controlling agent.[215]

From the above mentioned analysis, it can be concluded that exposing the most active facets of TiO_2 nanostructure is the main problem to be overcome for obtaining highly efficient TiO_2 photocatalysts. Figure 1.9 shows the increase in the percentage of (001) facets of TiO_2 anatase crystal by varying the reaction condition, modification using different dopant and amount of dopant.

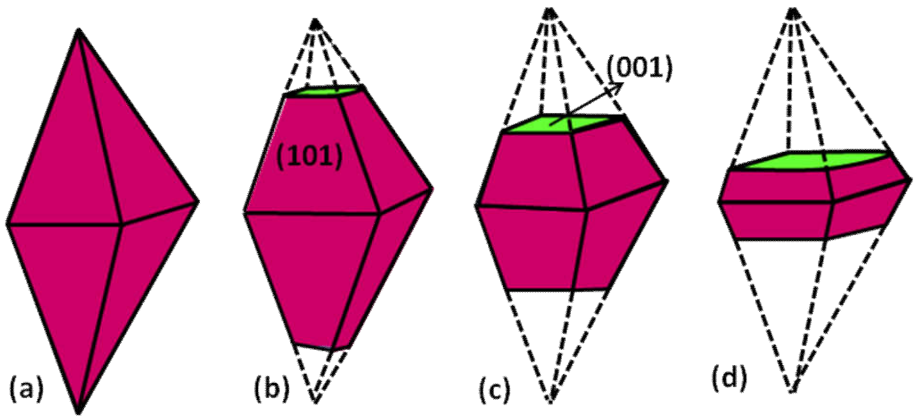

Figure 1.9: Different percentage of (001) facet formed on the anatase TiO_2 crystal (Percentage of (001) facet formation increases in the order d>c>b>a).[214]

1.12.4. Effect of concentration of oxygen

Since dioxygen serves as a trap for the photogenerated electrons, thus inhibiting the recombination of the electron/hole pair and the concentration of dissolved oxygen molecule also affects the reaction rate. The rate of degradation is proportional to the fraction of O_2, up to the point of saturation.[216]

1.12.5. Influence of catalyst loading[198,201]

Generally, the degradation rate is linearly related to the amount of TiO_2 present in the sample, eventually leveling off to a steady value,[217,218] although for some cases the rate can actually decrease when too much TiO_2 is present.[219,220] This behavior is expected with complete light absorption at the semiconductor surface. Rate of the reaction increases with the amount of TiO_2 because more active sites are available for the reaction, although when too much TiO_2 is present, aggregation of particles can occur, which reduces the availability of reaction sites. Rates may also decrease because of increased solution opacity and light scattering.

1.12.6. Effect of concentration of substrate

Most organic molecules obey the Langmuir-Hinshelwood kinetic model, although this is not always the case, particularly if the molecule in question absorbs UV light strongly. For representative molecules like 4-chlorophenol, the reaction rate increases as the initial rate increases.[221]

1.12.7. Crystal size/surface area of the catalyst[222]

Surface area and Particle size of TiO_2 has been extensively studied and shown to have a significant effect on photocatalytic activity. The surface area of the catalyst affects the number of molecules than can adsorb to the surface of the photocatalyst. Surface area also effects the rates of electron/hole recombination, as recombination is a surface process.[223,224] In general, nanometer size titanium dioxide has been shown to be the most effective (P25 has a particle size of 25-35 nm[210]), although some micrometer-sized catalysts are shown to be reasonably active. In addition to varying the size of TiO_2 nanoparticles, different particle shapes and coatings of titanium dioxide have been utilized for photochemical degradations.

1.12.8. Effect of reaction temperature

In general, photochemical reactions are not temperature-sensitive. Photodegradation is slightly temperature sensitive because important steps in the titanium dioxide degradations including adsorption and desorption, surface migration, and rearrangements. Activation energies of photodegradations are typically in the 5-15 kJ/mol range.[216]

1.12.9. Amount of dopant[225,226]

There should be an optimum amount of dopant on TiO_2 for the degradation of dyes in waste water and further increase in dopant content may result a negative effect on the activity of photocatalyst.[227] Excess amount of dopant on the surface of TiO_2 screen the UV light falls on the surface of TiO_2 and inhibit the interfacial electron- hole

transfer, which results a lesser photoactivity.[228] Xin *et al* observed that excess dopant produce excessive oxygen vacancies, which may become the recombination centers of photoinduced electrons and holes and excess Cu_2O cover the surface of TiO_2, leading to a decrease in the photodegradation efficiency of the catalyst.[229]

1.12.10. Calcination temperature of the catalyst[226]

Generally, photocatalytic activity was increased with increase in calcination temperature and reached the maximum, because of the complete crystallization of anatase phase at this temperature. Further increase in calcination temperature decreases the photocatalytic activity due to the transformation of anatase to rutile form, which has lesser photocatalytic activity.[226,230]

Therefore, it is very difficult to predict the photocatalytic activities from the physical and chemical properties of TiO_2nanomaterials. Optimal conditions are sought by taking into account all these considerations, which may vary from case to case.

1.13. Anatase to rutile transformation

Most probably anatase is the initial product in the low temperature synthesis of TiO_2 and is photocatalytically more active than rutile phase.[231,58] The metastable anatase phase begins to transform irreversibly to thermodynamically stable rutile phase at around 600 °C.[232] The fraction of rutile phase increases with increase in the calcination temperature. This conversion limits the applications of anatase TiO_2 at higher temperature such as porous gas separation

membranes and gas sensors, where the phase transformation alters the properties and performance of these devices.[233,234,235] The generally accepted theory for the phase transformation is that the thermal treatment facilitates the breaking of Ti-O bond in the anatase structure, allowing rearrangement of the Ti–O–Ti octahedra, which leads to a smaller volume, forming a dense rutile phase[236,237, 238] The removal of oxygen ions will generate oxygen vacancies, which accelerates the transformation rate. This transition follows first order kinetics and the activation energy for this conversion is approximately 418 kJ/mol. There are several factors which depends on the phase transformation of anatase to rutile such as addition of impurities, synthesis methods and thermal treatment.[239,240,241,242] K. Okada *et al* proposed that SiO_2 addition increased the anatase to rutile phase transition temperature from 680 °C to 1000 °C by forming a layer of SiO_2 on the surface of anatase to prevent the nucleation of particle.[58] S. Hishita *et al* observed that rare earth oxide doped TiO_2 suppress the nucleation of transformation.[242]

The anatase to rutile phase transformation is reconstructive, which means that the transformation involves the breaking and reformation of bonds.[243] This is different from displacive transformation, in which the original bonds are distorted but retained. The reconstructive mechanism of anatase to rutile transformation involves a contraction of the c-axis, which result the contraction in volume of 8%.[244, 245]

Non-selective Vs selective photocatalysis[246]

1.14. Achieving Selective photoctalysis in TiO_2

Nanocrystalline TiO_2 is receiving increasing attention because that degrades broad range of contaminants quickly and non-selectively. This non-selectivity/poor selectivity will limit its application to differentiate highly toxic contaminants and organic contaminants of low toxicity as well as selective formation of valuable organic products during the photocatalytic process. Mostly, less toxic substances are in high concentration and more toxic one will be the minor. Furthermore, lower toxic contaminants can be easily degraded by biological means and higher harmful one is non-biodegradable. Hence controlling the selectivity of the TiO_2 photocatalyst is an important goal in the frontiers of TiO_2 research.

TiO_2 based selective photocatalysis are categorized in to two: 1) Selective degradation: selectively degrade one of the contaminant without any concentration change in the other molecules from a mixture and 2) selective formation: desired product is formed through selective photocatalysis. Both selective degradation and selective

formation are worked under same principle, but in selective formation the desired product should be desorbed from the catalytic surface without undergo further degradation (Scheme 1.4).[246]

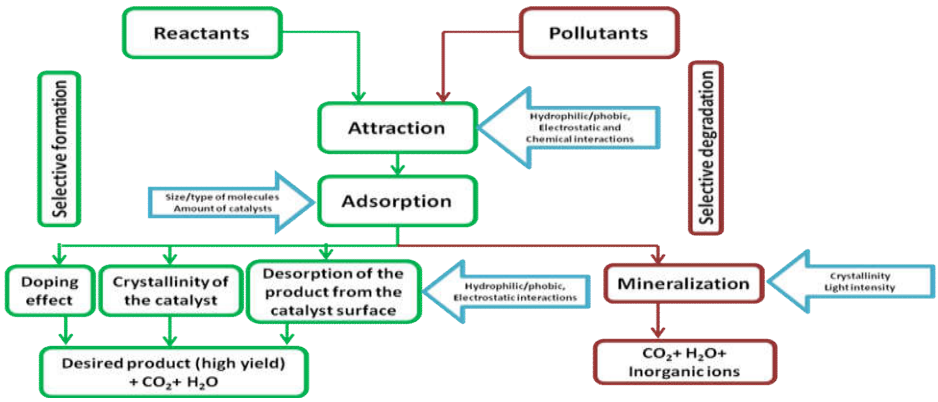

Scheme 1.4: Origin of selectivity in TiO_2 mediated photocatalytic organic transformations and in photocatalytic degradation reactions.[246]

1.15. Factors that affect selective photocatalysis

Recent reports shows that this non-selectivity can convert to selectivity by simply changing the physicochemical properties of the catalyst proceed *via* the following routes say,

1. Changing the pH of reaction medium[247,248]
2. Using substrates with different polarity[249]
3. With commercial TiO_2 at different calcination temperature[250]
4. Coating with a layer of polymer on TiO_2 surface[251,252]
5. Through anodization process to produce TiO_2 with appropriate pore size[253]

6. Fabrication of magnetic TiO_2 nanotubes for the destruction of cancer cells[254]

7. Changing the energy of the photons.[255]

Another method was inducing selectivity into nanocrystalline TiO_2 was doping with other metal oxide.[256] Molybdenum oxide (MoO) doped TiO_2 could selectively degrade cyclohexane into benzene, whereas undoped TiO_2 non-selectively degrade cyclohexane into carbon dioxide and water.[257] A similar principle was also observed by tungsten oxide (WO_3) coated TiO_2, iridium doped and iridium-palladium co-doped P25 catalyst for the selective photocatalytic oxidation of benzyl alcohol to benzaldehyde.[43,44] Similar studies like metal ions (Cu^{2+}, Co^{2+}, Ni^{2+}, Fe^{2+} and Mn^{2+}) doped titanate nanotubes for the conversion of benzylic and allylicc alcohols into their corresponding aldehyde have been reported.[258]Anatase TiO_2 modified with Na_2CO_3 and NH_4OH at low temperature exhibits selectivity in the degradation of dyes mainly due to the factors such as moderate crystallinity, lowest size and surface charge of the catalyst.[247,60,259]Negative effect on selective photocatalysis of TiO_2 through doping have also been reported. For example, gold deposited TiO_2 and zirconium oxide (ZrO_2) doped TiO_2 delayed the rate of selective formation of cyclohexanone from cyclohexane.[260,261,262] .

Non-selective photocatalysis using high temperature stable N-doped and F-doped anatase TiO_2 has been reported earlier for the degradation of methylene blue and acetone respectively.[263,264] N,F codoped TiO_2 for acetaldehyde decomposition was also reported and showed that the

photocatalytic activity of N,F-codoped powders seems to superior than the undoped TiO_2.[265] However no selective photocatalysis of N, F doped high temperature stable TiO_2 is not yet reported. Here we first report high temperature stable nanocrystalline TiO_2 for the selective photocatalytic degradation of one organic dye over the other from an aqueous mixture of methyl orange (MO) and methylene blue (MB) in UV light. N, F-codoped TiO_2 (TNF) was successfully prepared by simple sol-gel technique and characterised using various techniques such as XRD, DRS and TEM and surface potential measurements.

1.16. Objectives

The main objectives of this work are as follows:

a) Preparation of TiO_2 photocatalyst using sol-gel method.

b) Modify the TiO_2 using different organosulfur compound such as thiourea, thiosemicarbazide, sulfanilic acid and cysteine through chemical modification method.

c) Extent the preparation of TiO_2 using ammonium fluoride as a modifier to get photoactive and high temperature stable anatase TiO_2.

d) Optimize the concentration of ammonium fluoride to get high temperature anatase stability and higher photocatalytic activity.

e) Modify the ammonium fluoride doped TiO_2 system using manganese acetate as codopant.

f) Characterization of the catalyst using FTIR, FT Raman, XRD, DRS, BET measurements, zeta potential measurements, TEM and XPS.

g) Study the photocatlytic behavior of catalyst under UV and direct sunlight using methylene blue as a target organic molecule.

h) Study the selective photocatalytic behavior of N, F and N, F, Mn codoped TiO_2 system using methylene blue and methyl orange as target dyes.

1.17. Overview of the thesis

There is significant research have been carried out on TiO_2semiconductorsbecause of the wide range of applications associated with this material. The most investigated application of $TiO_2$is photocatalysis. Of the three common polymorphs of TiO_2, anatase is a widely accepted catalyst mostly towards photocatalytic applications. In order for TiO_2 to be utilized in wider areas, it is necessary that anatase can be stable at temperatures exceeding 1000 °C. Greater anatase to rutile transformation temperatures has been achieved through the addition of various dopants and contradictory results have been found.

The present research work focuses on two major aspects:

1) The effect of different non-metal dopant on TiO_2 for the retention of anatase phase at higher temperature for the applications in photocatalysis.

Nitrogen is well-accepted non-metal dopant as well as codopant due to shortening of the band gap of TiO_2 by the insertion of 2p orbital of nitrogen atom in between the valence and conduction band of TiO_2. Numbers of reports are already available regarding nitrogen codoped with other elements such as other non-metals and metals. However, only few reports are available based on codoping of nitrogen with sulphur using a single ion.[266,267,268] Of these Periyat *et al* developed N, S-codoped anatase TiO_2 stable at high temperature for visible light active photocatalysis using a single source ammonium sulphate $[(NH_4)_2SO_4]$.[266] Wei *et al* and Naik *et al* reported thiourea doped TiO_2 resulting N and S codoping for photocatalytic removal of pollutants under direct sunlight and they studied the photocatalytic activity of the modified sample only at low temperature.[267,268]In this present work, the aim is to synthesize high temperature stable N, S modified anatase TiO_2which exhibit photocatalytic efficiency at higher temperature.

Similarly, only limited reports are available based on N, F codoping from a single ion source as ammonium fluoride. Li *et al* prepared N, F-codoped $TiO_2$from a mixed aqueous solution containing $TiCl_4$ and NH_4F by spray pyrolysis for the photocatalytic decomposition of acetaldehyde.[265,269]Self-organized nitrogen and fluorine co-doped TiO_2 nanotube created by anodizing titanium foil in a fluoride and ammoniate-based electrolyte, followed by calcination under a nitrogen protective atmosphere and were found to have enhanced photodegradation efficiency on methylene blue under visible light over the TiO_2 nanotube.[270]However, Wu *et al* reported a simple one step and template free solvothermal method to synthesize mesoporous N, F

codoped TiO_2 microsphere using urea as nitrogen source and ammonium fluoride as fluorine source for enhancement of photodegradation activity of orange acid 7 under irradiation of visible light.[271] Simple sol-gel technique as reported by Yu *et al* derived only F-doped anatase TiO_2 from ammonium fluoride as the dopant source.[264,272,273,274] Huang *et al* developed F-doped TiO_2 sol with small percentage of nitrogen using tetrabutyltitanate and ammonium fluoride as the source of ions for boosting the photocatalytic properties of TiO_2 through sol-gel hydrothermal method, but the method was time consuming and tedious.[275]

Thus in the first part of the present thesis, we consider the modification of prepared TiO_2using non-metallic and low cost precursors such as thiourea, thiosemicarbazide, sulfanilic acid, cysteine and ammonium fluoride and which results in a high temperature stable codoped TiO_2 anatase system from a single source dopant precursor. All these modifiers were considered to improve the anatase phase stability and photocatalytic activity of TiO_2. Modifiers are selected in such a way that they contain non-metallic element as dopant nitrogen, sulfur and fluorine. Doping of these non-metallic atoms were reported to increase the photocatalytic activity of TiO_2.[150,162,276,156]

Lv *et al* have obtained F-doped titania via alcoholysis of $TiCl_4$ and shows very high thermal stability up to 1000 °C before being transformed into rutile phase.[274] Wang *et al* also developed N, F-codoped TiO_2 polycrystalline powder synthesized by calcination of the hydrolysis product of tetrabutyltitanate with ammonium fluoride and the obtained powder only contain anatase phases even at 1000 °C.[277]

High temperature treatment will result high crystallinity and higher surface area, which are the important factors that contribute to photocatalytic activity of anatase TiO_2. Therefore this thesis work aims the chemical modification process of TiO_2 using various non-metallic dopants to achieve dual aim *i.e.* high temperature anatase stability and higher photocatalytic activity.

2) Achieving Selective photoctalysis in TiO_2

Second major aim of this thesis work is to achieve selectivity in the photocatalytic activity of TiO_2. Generally photocatalytic degradation by TiO_2 follows free radical mechanism and which follows complete mineralization of pollutant non-selectively. This non-selectivity / poor selectivity limit its application to differentiate between highly toxic contaminants and the compounds to be recovered, in an effluent. Also, the non-selective nature of TiO_2photocatalysis hinders the advantage of selective formation of valuable organic products during the photocatalytic process, since the reaction proceeds to the complete mineralisation of all the intermediates. Hence, imparting selectivity in the TiO_2 photocatalysis is an important goal in the recent photocatalysis research. In this work we achieved the selectivity by F-doping and Mn, F-codoping for the degradation of dyes and mode of selectivity is based on the electrostatic interaction between the catalyst and pollutant and structural variation on the surface of TiO_2.

References

[1] Logothetidis, Nanoscience and Technology, Springer, Berlin, 2012.

[2] M. C. Roco, J. Nanopart. Res., 2011, **13**, 427.

[3] C. N. R. Rao and A. K. Cheetham, J. Mater. Chem., 2001, **11**, 2887.

[4] C. N. R. Rao, A. Müller and A. K. Cheetham, The Chemistry of Nanomaterials: Synthesis, Properties and Applications, 2006.

[5] S. Suresh, Adv. Nanosci. Nanotechnol., 2013, **3**, 62.

[6] T. Tervonen, I. Linkov, J. R. Figueira, J. Steevens, M. Chappell and M. Merad, J. Nanopart. Res., 2009, **11**, 757.

[7] M. L. Steigerwald and L. E. Brus, Acc. Chem. Res., 1990, **23**, 183.

[8] A. Henglein, Chem. Rev, 1989, **89**, 1861.

[9] M. G. Bawendi, M. L. Steigerwald and L. E. Brus, Annu. Rev. Phy. Chem, 1990, **41**, 477.

[10] U. G. Akpan and B. H. Hameed, J. Hazard. Mater., 2009, **170**, 520.

[11] M. R. Hoffmann, S. T. Martin, W. Choi and D. W. Bahenemann, Chem. Rev., 1995, **95**, 69.

[12] X. Chen and S. S. Mao, Chem. Rev., 2007, **107**, 2891.

[13] M. Gra¨tzel, J. Photochem. Photobiol., A, 2004, **164**, 3.

[14] M. Gra¨tzel, MRS Bull., 2005, **30**, 23.

[15] M. Gra¨tzel, Nature, 2001, **414**, 338.

[16] Y. Hu, H. L. Tsai and C. L. Huang, J. Eur. Ceram. Soc., 2003, **23**, 691.

[17] Y. Shao, D. Tang, J. Sun, Y. Lee and W. Xiong, China Particuol., 2004, **2**, 119.

[18] D. Dambournet, I. Belharouak and K. Amine, Chem. Mater., 2010, **22**, 1173.

[19] O. Carp, C. L. Huisman and A. Reller, Prog. Solid State Chem., 2004, **32**, 177.

[20] C. Chen, W. Ma and J. Zhao, Chem. Soc. Rev., 2010, **39**, 4206.

[21] J. Muscat, V. Swamy and N. M. Harrison, Phy. Rev. B, 2002, **65**, 1.

[22] A. Wisitsoraat, A. Tuantranont, E. Comini, G. Sberveglieri and W. Wlodarski, Thin Solid Films, 2009, **517**, 2775.

[23] L. Kavan, M. Gratzel, S. E. Gilbert, C. Klemenz and H. I. Scheel, J. Am. Chem. Soc., 1996, **118**, 6716.

[24] N. Hosaka, T. Sekiya, C. Aatoko and S. Kurita, J. Phys. Soc. Japan., 1997, **66**, 877.

[25] N. Hosaka, T. Sekiya, M. Fujisawa, C. Satokob and S. Kurita, J. Electron Spectrosc. Relat. Phenom., 1996, **78**, 75.

[26] A. Amtout and R. Leonelli, Phys. Rev. B, 1995, **51**, 6842.

[27] M. Koelsch, S. Cassaignon, C. T. Thanh Minh, J. F. Guillemoles and J. P. Jolivet, Thin Solid Films, 2004, **86**, 451.

[28] Y. Wang, Y. Huang, W. Ho, L. Zhang, Z. Zou and S. Lee, J. Hazard. Mater., 2009, **169**, 77.

[29] B. O'Regan and D. T. Schwartz, Chem. Mater., 1995, **7**, 1349.

[30] M. Gopal, W. J. M. Chan and L. C. De Jonghe, J. Mater. Sci., 1997, **32**, 6001.

[31] K. Ding, Z. Miao, Z. Liu, Z. Zhang, B. Han, G. An, S. Miao and Y. Xie, J. Am. Chem. Soc., 2007, **129**, 6362.

[32] X. J. Wang, W. Y. Yang, F. T. Li, Y. B. Xue, R. H. Liu and Y. J. Hao, Ind. Eng. Chem. Res., 2013, **52**, 17140.

[33] K. S. Yeung and Y. W. Lam, Thin Solid Films, 1983, **109**, l69.

[34] R. C. Smith, T. Ma, N. Hoilien, L. Y. Tsung, M. J. Bevan, L. Colombo, J. Roberts, S. A. Campbell and W. L. Gladfelter, Adv. Mater. Opt. Electron., 2000, **2000**, 105.

[35] J. M. Wu, H. C. Shih and W. T. Wu, Chem. Phys.Lett., 2005, **413**, 490.

[36] B. Xiang, Y. Zhang, Z. Wang, X. H. Luo, Y. W. Zhu, H. Z. Zhang and D. P. Yu, J. Phys. D: Appl. Phys., 2005, **38**, 1152.

[37] J. M. Wu, H. C. Shih, W. T. Wu, Y. K. Tseng and I. C. Chen, J. Cryst. Growth, 2005, **281**, 384.

[38] H. G. Yang, G. Liu, S. Z. Qiao, C. H. Sun, Y. G. Jin, S. C. Smith, J. Zou, H. M. Cheng and G. Q. Lu, J. Am. Chem. Soc., 2009, **131**, 4078.

[39] J. Liao, L. Shi, S. Yuan, Y. Zhao and J. Fang, J. Phys. Chem. C, 2009, **113**, 18778.

[40] D. Zhang, L. Qi, J. Ma and H. Cheng, J. Mater. Chem., 2002, **12**, 3677.

[41] L. L. Hench and J.K. West, Chem. Rev, 1990, **90**, 33.

[42] R. Roy, Science, 1987, **238**, 1664.

[43] D. Tsukamoto, M. Ikeda, Y. Shiraishi, T. Hara, N. Ichikuni, S. Tanaka and T. Hirai, Chem.-Eur. J., 2011, **17**, 9816.

[44] W. Feng, G. J. Wu, L. D. Li, and N. J. Guan, Green Chem., 2011, **13**, 3265.

[45] M. Iwasaki, M. Hara and S. Ito, J. Mater. Sci. Lett., 1998, **17**, 1769.

[46] P. Periyat, P. A. Saeed and S. G. Ullattil, Mater. Sci. Semicond. Process., 2015, **31**, 658.

[47] S. Sivakumar, C.P. Sibu, P. Mukundan, P. K Pillai and K.G.K. Warrier, Mater. Lett., 2004, **58**, 2664.

[48] S. S. Watson, D. Beydoun, J.A. Scott and R. Amal, Chem. Eng. J., 2003, **95**, 213.

[49] S. C. Pillai, P. Periyat, R. George, D. E. McCormack, M. K. Seery, H. Hayden, J. Colreavy, D. Corr and S. J. Hinder, J. Phys. Chem. ,C, 2007, **111**, 1605.

[50] K. Y. Jung and S. B. Park, Appl. Catal., B, 2000, **25**, 249.

[51] N. Wetchakun, S. Chaiwichain, B. Inceesungvorn, K. Pingmuang, S. Phanichphant, A. I. Minett and J. Chen, ACS Appl. Mater. Interfaces, 2012, **4**, 3718.

[52] J. Yu, L. Zhang, B. Cheng and Y. Su, J. Phys. Chem. C, 2007, **111**, 10582.

[53] N. T. Nolan, M. K. Seery and S. C. Pillai, J. Phys. Chem. C, 2009, **113**, 16151.

[54] A. E. Danks, S. R. Hall and Z. Schnepp, Mater. Horiz., 2016, **3**, 91.

[55] G. W. Schere, J. Am. Cerum. Soc., 1990, **73**, 3.

[56] F. J. M. Hódar, C. M. Castilla and J. R. Utrilla, Appl. Catal., A, 2000, **203**, 151.

[57] J. P. Jolivet, S. Cassaignon, C. Chane´ac, D. Chiche and E. Tronc, J. Sol-Gel Sci. Technol., 2008, **46**, 299.

[58] K. Okada,N. Yamamoto, Y. Kameshima and A. Yasumori, J. Am. Ceram. Soc., 2001, **84**, 1591.

[59] D. H. Napper and A. Netschey, J. Colloid Interface Sci., 1971, **37**, 528.

[60] S. Yurdakal, G. Palmisano, V. Loddo, V. Augugliaro and L. Palmisano, J. Am. Chem. Soc., 2008, **130**, 1568.

[61] S. B. Doeuff and C. Sanchez, Mat. Res. Bull., 1994, **29**, 1.

[62] J. Livage, C. Sanchez, M. Henry and S. Doeuff, Solid State lonics, 1989, **33**, 633.

[63] J. Livage, M. Henry and C. Sanchez, Prog. Solid St. Chem., 1988, **18**, 259.

[64] C. Sanchez, J. Livage, M. Henry and F. Babonneau, J. Non-Cryst. Solids, 1988, **100**, 65.

[65] L. L. Hench, G. Orcel and J. L. Nogues, MRS Online Proc. Libr., 1986, **73**, 35.

[66] G. Pfaff and P. Reynders, Chem. Rev., 1999, **99**, 1963.

[67] J. H. Braun, A. Baidins and R. E. Marganski, Prog. Org. Coat., 1992, **20**, 105.

[68] A. Salvador, M. C. Pascual-Marti, J. R. Adell, A. Requeni and J. G. March, J. Pharm. Biomed. Anal., 2000, **22**, 301.

[69] R. Zallen and M. P. Moret, Solid State Commun., 2006, **137**, 154.

[70] S. A. Yuan, W. H. Chen and S. S. Hu, Mater. Sci. Eng. C, 2005, **25**, 479.

[71] D. A. H. Hanaor and C. C. Sorrell, J. Mater. Sci., 2011, **46**, 855.

[72] A. Fujishima and K. Honda, Nature, 1972, **238**, 37.

[73] A. Fujishima, T. N. Rao and D. A. Tryk, J. Photochem. Photobiol. C, 2000, **1**, 1.

[74] Y. Bessekhouad, D. Robert and J. V. Weber, Int. J. Photoenergy, 2003, **5**, 153.

[75] R. L. Pozzo, M. A. Baltanas and A. E. Cassano, Catal. Today, 1997, **39**, 219.

[76] R. W. Matthews, J. Phys. Chem., 1987, **91**, 3328.

[77] K. Okamoto, Y. Yamamoto, H. Tanaka, M. Tanaka and I. Akira, Bull. Chem. Soc. Jpn., 1985, **58**, 2015.

[78] N. Baram, D. Starosvetsky, J. Starosvetsky, M. Epshtein, R. Armon and Y. Ein-Eli, Electrochem. Commun., 2007, **9**, 1684.

[79] D. S. Muggli and L. Ding, Appl. Catal., B, 2001, **32**, 181.

[80] A. Fujishima, X. Zhang and D. A. Tryk, Surf. Sci. Rep., 2008, **63**, 515.

[81] H. Miyazaki, T. Hyodo, Y. Shimizu and M. Egashira, Sens. Actuators, B, 2005, **108**, 467.

[82] A. M. Ruiz, A. Cornet and J. R. Morante, Sens. Actuators, B, 2005, **7**, 111.

[83] M. Gratzel, Inorg. Chem., 2005, **44**, 6841.

[84] S. Y. Huang, G. Schlichthorl, A. J. Nozik, M. Gratzel and A. J. Frank, J. Phys. Chem. B, 1997, **101**, 2576.

[85] B. O'Regan and M. Gratzel, Nature, 1991, **353**, 737.

[86] K. Fujihara, T. Ohno and M. Matsumura, J. Chem. Soc. Faraday Trans., 1998, **94**, 3705.

[87] A. Linsebigler, G. Lu and J. T. Yates, Chem Rev., 1995, **95**, 735.

[88] M. Ni, M. Leung, D. Leung and K. Sumathy, Renewable Sustainable Energy Rev., 2007, **11**, 401.

[89] A. Wold, Chem. Mater., 1993, **5**, 280.

[90] A. Mills, S. Hodgen and S. K. Lee, Res. Chem. Intermed., 2004, **31**, 295.

[91] A. Mills, A. Lepre, N. Elliott, S. Bhopal, I. P. Parkin and S. A. O'Neill, J. Photochem. Photobiol., A, 2003, **160**, 213.

[92] J. O. Carneiro, V. Teixeira, A. Portinha, A. Magalhaes, P. Countinho and C. J. Tavares, J. Mater. Sci. Eng. B, 2007, **138**, 144.

[93] A. E. Aliev and H. W. Shin, Solid State Ionics, 2002, **154-155**, 425.

[94] U. Bach, D. Corr, D. Lupo, F. Pichot and M. Ryan, Adv. Mater., 2002, **14**, 845

[95] P. Bonhote, E. Gogniat, F. Campus, L. Walder and M. Gra¨tzel, Displays, 1999, **20**, 137.

[96] F. Campus, P. Bonhote, M. Gra¨tzel, S. Heinen and L. Walder, Sol. Energy Mater. Sol. Cells, 1999, **56**, 281.

[97] K. K. Gupta, V. S. Tripathi, H. Ram and H. Raj, Colourage, 2002, **49**, 35.

[98] D. K. Hwang, J. H. Moon, Y. G. Shul, K. T. Jung, D. H. Kim and D. W. Lee, J. Sol-Gel Sci. Technol., 2003, **26**, 783.

[99] D. Mitoraj, A. Janczyk, M. Strus, H. Kisch, G. Stochel, P. B. Heczko and W. Macyk, Photochem. Photobiol. Sci., 2007, **6**, 642.

[100] H. Kisch, G. Burgeth and W. Macyk, Adv. Inorg. Chem., 2004, **56**, 241.

[101] D. M. Blake, P. C. Maness, Z. Huang, E. J. Wolfrum, J. Huang and W. A. Jacoby, Sep. Purif. Methods, 1999, **28**, 1.

[102] R. Cai, K. Hashimoto, Y. Kubota and A. Fujishima, Chem. Lett., 1992, **21**, 427.

[103] N. P. Huang, M. H. Xu, C. W. Yuan and R. R. Yu, J. Photochem. Photobiol., A, 1997, **108**, 229.

[104] S. Ivankovic, M. Gotic, M. Jurin and S. J. Music, Sol-Gel Sci. Technol., 2003, **27**, 225.

[105] H. Sakai, R. Baba, K. Hashimoto, Y. Kubota and A. Fujishima, Chem. Lett., 1995, **24**, 185.

[106] K. Nakata and A. Fujishima, J. Photochem. Photobiol., C, 2012, **13**, 169.

[107] R. Rife, T. W. Thomas, D. W. Norberg, R. L. Fournier, F. G. Rinker and M. S. Bonomo, Environ. Prog., 1989, **8**, 167.

[108] S. H. S. Chan, T. Y. Wu, J. C. Juan and C. Y. Teh, J. Chem. Technol. Biotechnol., 2011, **86**, 1130.

[109] C. Comninellis, A. Kapalka, S. Malato, S. A. Parsons, L. Poulios, and D. Mantzavinos, J. Chem. Technol. Biotechnol., 2008, **83**, 769.

[110] R. A. Elsalamony, Res. Rev.: J. Mater. Sci., 2016, **4**, 26.

[111] R. Munter, Proc. Estonian Acad. Sci. Chem., 2001, **50**, 59.

[112] Z. Zou, J. Ye, K. Sayama and H. Arakawa, Nature, 2001, **414**, 625.

[113] J. Mu, C. Shao, Z. Guo, Z. Zhang, M. Zhang, P. Zhang, B. Chen and Y. Liu, ACS Appl. Mater. Interfaces, 2011, **3**, 590.

[114] A. Alexiadis and I. Mazzarino, Chem. Eng. Process., 2005, **44**, 453.

[115] J. Saien, M. Asgari, A.R. Soleymani and N. Taghavinia, Chem. Eng. J., 2009, **151**, 295.

[116] S. N. Frank and A. J. Bard, J. Am. Chem. Soc., 1977, **99**, 303.

[117] S. N. Frank and A. J. Bard, J. Phys. Chem., 1977, **81**, 1484.

[118] A. L. Pruden and D. F. Ollis, J. Catal., 1983, **82**, 404.

[119] M. Grätzel, J. Photochem. Photobiol., C, 2003, **4**, 145.

[120] R. Wang, K. Hashimoto, A. Fujishima, M. Chikuni, E. Kojima, A. Kitamura, M. Shimohigoshi and T. Watanabe, Adv. Mater., 1998, **10**, 135.

[121] M. Fox and M. Dulay, Chem. Rev., 1995, **83**, 341.

[122] M. A. Aramendia, A. Marinas, J. M. Marinas, J. M. Moreno and F. J. Urbano, Catal. Today, 2005, **101**, 187.

[123] C. Guillard, H. Lachheb, A. Houas, M. Ksibi, E. Elaloui and J. M. Hermann, J. Photochem. Photobiol. A: chem., 2003, **158**, 27.

[124] S. Malato, J. Blanco, A. Compos, J. Caceres, C. Guillard, J. M. Herrmann and A. R. Fernandez-Alba, Appl. Catal. B: Environ., 2003, **42**, 349.

[125] R. Asahi, Y. Taga, W. Mannstadt and A. J. Freeman, J. Phys. Rev. B, 2000, **61**, 7459.

[126] H. Huang, D. Li, Q. Lin, W. Zhang, Y. Shao, Y. Chen, M. Sun and X. Fu, Environ. Sci. Technol., 2009, **43**, 4164.

[127] K. Li, B. Chai, T. Peng, J. Mao and L. Zan, ACS Catal., 2013, **3**, 170.

[128] W. Choi, A. Termin and M. R. Hoffmann, J. Phys. Chem., 1994, **98**, 13669.

[129] Z.L. Xu, J. Shang, C.M. Liu, C. Kang, H.C. Guo and Y.G. Du, J. Mater. Sci. Eng. B, 1999, **63**, 253.

[130] Y. Li, D.-S. Hwang, N.H. Lee and S.-J. Kim, Chem. Phys. Lett., 2005, **404**, 25.

[131] S. Banerjee, J. Gopal and P. Muraleedharan, Current Sci, 2006, **90**, 1378.

[132] S. Banerjee, S. C. Pillai, P. Falaras, K. E. O'Shea, J. A. Byrne and D. D. Dionysiou, J. Phys. Chem. Lett., 2014, **5**, 2543.

[133] M. Pelaez, N. T. Nolan, S. C. Pillai, M. K. Seery, P. Falaras, A. G. Kontos, P. S. M. Dunlop, J. W. J. Hamilton, J. A. Byrne, K. O'Shea, M. H. Entezari and D. D. Dionysiou, Appl. Catal., B, 2012, **125**, 331.

[134] A. Hoffman, E.R. Carraway and M. Hoffman, J. Environ. Sci. Technol., 1994, **28**, 776.

[135] J. Cunningham and S. Srijaranai, J. Photochem. Photobio. A: Chem., 1988, **43**, 329.

[136] A. Sclafani, L. Palmisano and E. Davi, J. Photochem. Phorobiol. A: Chem., 1991, **56**, 113.

[137] G. S. Mital and T. Manoj, Chin. Sci. Bull., 2011, **56**, 1639.

[138] G. K. Mor, O. K. Varghese, M. Paulose, K. Shankar and C. A. Grimes, Sol. Energy Mater. Sol. Cells, 2006, **90**, 2011.

[139] I. Justicia, G. Garcia, L. Vazquez, J. Santiso, P. Ordejon, G. Battiston, R. Gerbasi, and A. Figueras, Sens. Actuators, B, 2005, **109**, 52.

[140] E. Cho, Phys. Rev. B, 2006, **73**, 193.

[141] M. S. Hamdy, R. Amrollahi and G. Mul, ACS Catal., 2012, **2**, 2641.

[142] V. Etacheri, M. K. Seery, S. J. Hinder and S. C. Pillai, Adv. Funct. Mater., 2011, **21**, 3744.

[143] C. Burda, Y. Lou, X. Chen, A. C. S. Samia, J. Stout and J. L. Gole, Nano Lett., 2003, **3**, 1049.

[144] M. M. Joshi, Appl. Catal., A, 2009, **357**, 26.

[145] K. Nagaveni, M. S. Hegde and G. Madras, J. Phys. Chem. B, 2004, **108**, 20204.

[146] Y. Wang, H. Cheng, Y. Hao, J. Ma, W. Li, S. Cai, J. Mater. Sci., 1999, **34**, 3721.

[147] Y. Wang, H. Cheng, Y. Hao, J. Ma, W. Li and S. Cai, Thin Solid Films, 1999, **349**, 120.

[148] F. B. Li, X. Z. Li and M. F. Hou, Appl. Catal. B, 2004, **48**, 185.

[149] A. W. Xu, J. Catal., 2002, **207**, 151.

[150] R. Asahi, T. Morikawa, T. Ohwaki, K. Aoki and Y. Taga, Science, 2001, **293**, 269.

[151] S. Sato, Chem. Phys. Lett., 1986, **123**, 126.

[152] D. H. Lee, Y. S. Cho, W. I. Yi, T. S. Kim, J. K. Lee and H. J. Jung, Appl. Phys. Lett., 1995, **66**, 815.

[153] H. Irie, Y. Watanabe and K. Hashimoto, J. Phys. Chem. B, 2003, **107**, 5483.

[154] T. Ihara, M. Miyoshi, Y. Iriyama, O. Matsumoto and S. Sugihara, Appl. Catal., B, 2003, **42**, 403.

[155] I. N. Martyanov, S. Uma, S. Rodrigues and K. J. Klabunde, Chem. Commun. , 2004, **0**, 2476.

[156] J. C. Yu, W. Ho, J. Yu, H. Yip, P. K. Wong and J. Zhao, Environ. Sci. Technol., 2005, **39**, 1175.

[157] T. Umebayashi, T. Yamaki, H. Itoh and K. Asai, Appl. Phys. Lett., 2002, **81**, 454.

[158] T. Ohno, M. Akiyoshi, T. Umebayashi, K. Asai, T. Mitsui and M. Matsumura, Appl. Catal., A, 2004, **265**, 115.

[159] P. Periyat, S. C. Pillai, D. E. McCormack, J. Colreavy and S. J. Hinder, J. Phys. Chem. C, 2008, **112**, 7644.

[160] T. Tachikawa, S. Tojo, K. Kawai, M. Endo, M. Fujitsuka, T. Ohno, K. Nishijima, Z. Miyamoto and T. Majima, J. Phys. Chem. B, 2004, **108**, 19299.

[161] C Belver, R. Bellod, S.J. Stewart, F. G. Requejo and M. F. Garcı´a, Appl. Catal., B, 2006, **65**, 309.

[162] S. Sakthivel, M. Janczarek and H. Kisch, J. Phys. Chem. B, 2004, **108**, 19384.

[163] S. U. M. Khan, M. Al-Shahry and W. B. InglerJr, Science, 2002, **297**, 2243.

[164] Y. Wang, J. Li, P. Peng, T. Lu and L. Wang, Appl. Surf. Sci., 2008, **254**, 5276.

[165] X. Tang and D. Li, J. Phys. Chem. C, 2008, **112**, 5405.

[166] S. Bingham and W. A. Daoud, J. Mater. Chem., 2011, **21**, 2041.

[167] C. D. Valentin, E. Finazzi, G. Pacchioni, A. Selloni, S. Livraghi, A. M. Czoska, M. C. Paganini and E. Giamello, Chem. Mater., 2008, **20**, 3706.

[168] P. Yang, C. Lu and N. Hua, Mater. Lett, 2002, **57**, 794.

[169] F. Vasiliu, L. Diamandescu and D. Macovei, Top Catal., 2009, **52**, 544.

[170] J. Xu, Y. Ao and D. Fu, Appl. Surf. Sci., 2009, **256**, 884.

[171] X. Z. Shen, Z. C. Liu, S. M. Xie and J. Guo, J. Hazard. Mater., 2009, **162**, 1193.

[172] A. Hagfeldt and M. Gra¨tzel, Chem. ReV., 1995, **95**, 49.

[173] G. Meyer, J. Inorg. Chem., 2005, **44**, 6852.

[174] M. Zhang, C. Chen, W. Ma and J. Zhao, Angew. Chem., 2008, **120**, 9876.

[175] Y. Cho, W. Choi, C. H. Lee, T. Hyeon and H. I. Lee, J. Environ. Sci. Technol., 2001, **35**, 966.

[176] G. K. Mor, K. Shankar, M. Paulose, O. K. Varghese and C. A. Grimes, Nano lett., 2005, **6**, 215.

[177] S. Ferrere, A. Zaban and B. A. Gregg, J. Phys. Chem. B, 1997, **101**, 4490.

[178] K. Naoi, Y. Ohko and T. Tatsuma, J. Am. Chem. Soc., 2004, **126**, 3664.

[179] K. Naoi, Y. Ohko and T. Tatsuma, Chem. Commun., 2005, **0**, 1288.

[180] Y. Tian and T. Tatsuma, Chem. Commun., 2004, **0**, 1810.

[181] N. serpone, P. Maruthamuthu, P. Pichat, E. Pelizzetti and H. Hidaka, J. Photochem. Photobiol., A, 1995, **85**, 247.

[182] Z. Liu, D. D. Sun, P. Guo and J. O. Leckie, Nano Lett., 2006, **7**, 1081.

[183] S. Banerjee, S. K. Mohapatra, P. P. Das and M. Misra, Chem. Mater., 2008, **20**, 6784.

[184] P. Hoyer and R. Koenenkamp, R. Appl. Phys. Lett., 1995, **66**, 349.

[185] D. Fitzmaurice, H. Frei and J. Rabani, J. Phys. Chem., 1995, **99**, 9176.

[186] R. Vogel, P. Hoyer and H. Weller, J. Phys. Chem., 1994, **98**, 3183.

[187] H. Yu, J. Huang, H. Zhang, Q. Zhao and X. Zhong, Nanotechnology, 2014, **25**, 1.

[188] Y. Bessekhouad, D. Robert and J. V. Weber, J. Photochem. Photobiol., A, 2004, **163**, 569.

[189] H. Tada, A. Kokubu, M. Iwasaki and S. Ito, Langmuir, 2004, **20**, 4665.

[190] C. Shifu, C. Lei, G. Shen and C. Gengyu, Powder Technol., 2005, **160**, 198.

[191] Y. Bessekhouad, N. Chaoui, M. Trzpit, N. Ghazzal, D. Robert and J.V. Weber, J. Photochem. Photobiol., A, 2006, **183**, 218.

[192] K. Vinodgopal and P. V. Kamat, Environ. Sci. Technol., 1995, **29**, 841.

[193] C. Nasr, P. V. Kamat and S. Hotchandani, J. Phys. Chem. B, 1998, **102**, 10047.

[194] K. Rajeshwar, N. R. de Tacconi and C. R. Chenthamarakshan, Chem. Mater., 2001, **13**, 2765.

[195] A. Dawson and P. V. Kamat, J. Phys. Chem. B, 2001, **105**, 960.

[196] X. Zhang, L. Lei and J. Zhang, Sep. Purif. Technol., 2009, **66**, 417.

[197] A. Kumar and A. K. Jain, J. Mol. Catal. A: Chem., 2001, **165**, 265.

[198] I. K. Konstantinou and T. A. Albanis, Appl. Catal. B: Environ., 2004, **49**, 1.

[199] M. A. Fox and M. T. Dulay, Chem. Rev., 1993, **93**, 341.

[200] W. Z. Tang and H. An, Chemosphere, 1995, **31**, 4158.

[201] M. Saquiba, M. A. Tariqa, M. Faisala, M. Muneer, Desalination, 2008, **219**, 301.

[202] L. C. Chen, C. M. Huang and F. R. Tsai, J. Mol. Catal. A: Chem., 2007, **265**, 133.

[203] W. Baran, A. Makowski and W. Wardas, Dyes Pigm., 2008, **76**, 226.

[204] J. Augustinkski, Struct. Bonding, 1988, **69**, 1.

[205] R. Terzian, N. Serpone, C. Minero and E. Pelizzetti, J. Catal., 1991, **128**, 352.

[206] K. Okamoto, Y. Yamamoto, H. Tanaka, M. Tanaka and A. Itaya, Bull. Chem. Soc. Jpn., 1985, **58**, 2023.

[207] K. Tanaka, M. F. V. Capule and T. Hisanaga, Chem. Phys. Lett, 1991, **187**, 73.

[208] J. M. Herrmann, Topics in Catal., 2005, **34**, 49.

[209] A. J. Nozik and R. Memming, J. Phys. Chem., 1996, **100**, 13061.

[210] H. Tahiri, N. Serpone and R. L. V. Mao, J. Photochem. Photobiol., A, 1996, **93**, 199.

[211] D. C. Hurum and K. A. Gray, J. Phys. Chem. B, 2005, **109**, 977.

[212] J. Tian, Z. Zhao, R. I. Boughton and H. Liu, Chem. Soc. Rev, 2014, **43**, 6920.

[213] J. N. Nian and H. Teng, J. Phys. Chem. B, 2006, **110**, 4193.

[214] A. Selloni, Nat. Mater., 2008, **7**, 613.

[215] H. G. Yang, C. H. Sun and S. Z. Qiao, Nature, 2008, **453**, 638.

[216] A. Mills, R. H. Davies and D. Worsley, Chem. Soc. Rev., 1993, **22**, 417.

[217] N. Serpone and A. Salinaro, Pure Appl. Chem., 1999, **71**, 303.

[218] A. Salinaro, A. V. Emeline, J. Zhao, H. Hidaka, V. K. Ryabchuk and N. Serpone, Pure Appl. Chem., 1999, **71**, 321.

[219] A. Aguilar, K. E. O'Shea, T. Tobien and K. D. Asmus, J. Phys. Chem. A, 2001, **105**, 7834.

[220] N. San, A. Hatipoglu, G. Kocturk and Z. Cinar, J. Photochem. Photobiol., A, 2002, **146**, 189.

[221] X. Li, J. W. Cubbage and W. S. Jenks, J. Org Chem., 1999, **24**, 8525.

[222] M. A. Fox and M. T. Dulay, Chem. Rev., 1993, **93**, 341.

[223] N. Serpone, D. Lawless, R. Khairutdinov and E. Pelizzetti, J. Phys. Chem., 1995, **99**, 26655.

[224] P. Calza, E. Pelizzetti, K. Mogyorosi, R. Kun and I. Dekany, Appl. Cat. B., 2007, **72**, 314.

[225] P. Bouras, E. Stathatos and P. Lianos, Appl. Catal. B: Environ., 2007, **73**, 51.

[226] G. Liu, X. Zhang, Y. Xu, X. Niu, L. Zheng and X. Ding, Chemosphere, 2005, **59**, 1367.

[227] D. L. Liao, C. A. Badour and B. Q. Liao, J. Photochem. Photobiol., A, 2008, **194**, 11.

[228] Y. Li, S. Peng, F. Jiang, G. Lu and S. Li, J. Serb. Chem. Soc., 2007, **72**, 393.

[229] B. Xin, P. Wang, D. Ding, J. Liu, Z. Ren and H. Fu, Appl. Surf. Sci., 2008, **254**, 2569.

[230] J. Yu, H. Yu, B. Chenga and C. Trapalis, J. Mol. Catal. A: Chemical, 2006, **249**, 135.

[231] J. M. G. Amores, V. S. Escribano and G. Busca, J. Mater. Chem., 1995, **5**, 1245.

[232] J. F. Banfield, B. L. Bischoff and M. A. Anderson, Chem. Geol., 1993, **110**, 211.

[233] K. N. P. Kumar, K. Keizer and A. J. Burggraaf, J. Mater. Sci. Lett., 1994, **13**, 59.

[234] R. L. Penn and J. F. Banfield, Am. Mineral., 1999, **84**, 871.

[235] A. Rothschild, A. Levakov, Y. Shapira, N. Ashkenasy and Y. Komem, Surf. Sci., 2003, **532**, 456.

[236] D. A. H. Hanaor and C. C. Sorrell, J. Mater. Sci., 2011, **46**, 855.

[237] K. N. P. Kumar, K. Keizer and A. J. Burggraaf, Nature, 1992, **24**, 358.

[238] C. Su, B.-Y. Hong and C.M. Tseng, Catal. Today, 2004, **96**, 119.

[239] S. R. Yoganarasimhan and C. N. R. Rao, Trans. Faraday Soc., 1962, **58**, 1579.

[240] Y. Li, T.J. White and S.H. Lim, J. Solid State Chem., 2004, **177**, 1372.

[241] X. Z. Ding, X. H. Liu and Y. Z. He, J. Mater. Sci. Lett., 1996, **15**, 1789.

[242] S. Hishita, I. Mutoh, K. Koumoto and H. Yanagida, Ceram. Int., 1983, **9**, 61.

[243] M. Batzill, E. H. Morales and U. Diebold, Phys. Rev. Lett., 2006, **96**, 26103.

[244] D. A. H. Hanaor and C. C. Sorrell, J. Mater. Sci., 2011, **46**, 855.

[245] M. Razaee, S. M. M. Khoie and K. H. Liu, CrystEngComm, 2011, **13**, 5055.

[246] M. A. Lazar and W. A. Daoud, RSC adv., 2013, **3**, 4130.

[247] M. A. Lazar and W. A. Daoud, RSC Adv., 2012, **2**, 447.

[248] T. Karpova, S. Preis, J. Kallas and A. L. B. Torres, Environ. Chem. Lett., 2007, **5**, 219.

[249] Y. Shiraishi, Y. Sugano, D. Inoue and T. Hirai, J. Catal., 2009, **264**, 175.

[250] J. T. Carneiro, A. R. Almeida, J. A. Moulijn and G. Mul, Phys. Chem. Chem. Phys., 2010, **12**, 2744.

[251] X. T. Shen, L. H. Zhu, G. X. Liu, H. W. Yu and H. Q. Tang, Environ. Sci. Technol., 2008, **42**, 1687.

[252] X. T. Shen, L. H. Zhu, C. X. Huang, H. Q. Tang, Z. W. Yu and F. Deng, J. Mater. Chem., 2009, **19**, 4843.

[253] P. Roy, T. Dey, K. Lee, D. Kim, B. Fabry and P. Schmuki, J. Am. Chem. Soc., 2010, **132**, 7893.

[254] N. K. Shrestha, J. M. Macak, F. Schmidt-Stein, R. Hahn, C. T. Mierke, B. Fabry and P. Schmuki, Angew. Chem., Int. Ed., 2009, **48**, 969.

[255] P. Du, J. A. Moulijn and G. Mul, J. Catal., 2006, **238**, 342.

[256] Y. Ide, Y. Nakasato and M. Ogawa, J. Am. Chem. Soc., 2010, **132**, 3601.

[257] P. Ciambelli, D. Sannino, V. Palma, V. Vaiano and R. I. Bickley, Appl. Catal., A, 2008, **349**, 140.

[258] Z. R. Tang, Y. H. Zhang and Y. J. Xu, ACS Appl. Mater. Interfaces, 2012, **4**, 1512.

[259] G. Palmisano, S. Yurdakal, V. Augugliaro, V. Loddo and L. Palmisano, Adv. Synth. Catal., 2007, **349**, 964.

[260] J. T. Carneiro, C. C. Yang, J. A. Moma, J. A. Moulijn and G. Mul, Catal. Lett., 2009, **129**, 12.

[261] J. T. Carneiro, T. J. Savenije, J. A. Moulijn, and G. Mul. J. Photochem. Photobiol., A, 2011, **217**, 326.

[262] M. D. Hernandez-Alonso, A. R. Almeida, J. A. Moulijn and G. Mul, Catal. Today, 2009, **143**, 326.

[263] J. Geng, D. Yang, J. Zhu, D. Chen, and Z. Jiang, Mater. Res. Bull, 2008, **44**, 146.

[264] J.C.Yu, J. Yu, W.Ho, Z. Jiang and L, Zhang, Chem. Mater, 2002, **14**, 3808.

[265] D. Li, H. Haneda, S. Hishita and N. Ohashi, Chem. Mater, 2005, **17**, 2596.

[266] P.Periyat, D. E. McCormack, S. J. Hinder and S. C. Pillai, J. Phys. Chem. C, 2009, **113**, 3246.

[267] F. Wei, L. Ni and P. Cui, J. Hazard. Mater., 2008, **156**, 135.

[268] B. Naik, K. M. Parida and C. S. Gopinath, J. Phys. Chem. C, 2010, **114**, 19473.

[269] D. Li, N. Ohashi, S. Hishita, T. Kolodiazhnyi and H. Haneda, Journal of Solid State Chemistry, 2005, **178**, 3293.

[270] Q. Li and J. K. Shang, Environ. Sci. Technol., 2009, **43**, 8923.

[271] Y. Wu, M. Xing, B. Tian, J. Zhang and F. Chen, Chemical Engineering Journal, 2010, **162**, 710.

[272] M. V. Dozzi, B. Ohtani and E. Selli, Phys. Chem. Chem. Phys., 2011,**13**, 18217.

[273] J. Xu, Y. Ao, D. Fu and C. Yuan, Applied Surface Science, 2008, **254**, 3033.

[274] Y. Lv, L. Yu, H. Huang, H. Liu and Y. Feng, Applied surface science, 2009, **255**, 9548.

[275] D. Huang, S. Liao, S. Quan, L. Liu, Z. He, J. Wan and W. Zhou, J Mater Sci, 2007, **42**, 8193.

[276] W. Ho, J. C. Yu and S. Lee, J. Solid State Chem., 2006, **179**, 1171.

[277] W. Zheng-Peng, X. Jun, C. Wei-Min, Z. Bao-Xue, H. Zheng-Guang, C. Chun-Guang and H. Xiao-Ting, Journal of environmental sciences, 2005, **17**, 76.

CHAPTER 2
MATERIALS AND METHODS

CONTENTS

2.1. Experimental procedures

An account of the materials, experimental methods and different analytical techniques used for the characterisation of the samples are given in this chapter. The chemicals used for the sample preparation are tabulated in Table 2.1. The first part of the chapter explains the preparation procedures for the N, S and N, F codoped anatase titania for photocatalytic applications. Second part extends the preparation procedure of N, F codoped titania to obtain N, F, Mn tridoped titania for selective removal of pollutants. Brief description of the experimental procedures used for the synthesis of photocatalysts is given as third part. Different characterisation technique used to obtain the phase structure, crystallinity, crystallite size, surface area and surface charge are discussed in the final section of this chapter.

Table 2.1. List of chemicals used for the synthesis and application studies of TiO_2.

Sl No:	Name of chemical	Company	Purity
1	Titanium tetraisopropoxide, Ti $(OPr)_4$	Spectrochem	98%
2	Ammonium fluoride, NH_4F	HI Media Laboratories	98%
3	Isopropanol	Merck	99.5%
4	Manganese acetate tetra hydrate, $Mn(CH_3COO)_2.4H_2O$	Sisco Research Laboratories	97%
5	Thiourea, $(NH_2)_2CS$	Merck	99.5%
6	Thiosemicarbazide	Merck	99.5%
7	Sulfanilic acid	Merck	99.5%
8	Cysteine	Merck	99.5%
9	Methylene blue	Qualigens	
10	Methyl orange	Qualigens	

All the tabulated chemicals were used as received without further purification. Deionised water was used in all the experiments.

2.2. Synthesis of titanium dioxide

Titanium tetraisopropoxide, $Ti(OPr)_4$ (29.7 mL, 100 mmol) was added to isopropanol (100 mL) under stirring, to get a clear solution of $Ti(OPr)_4$. Water (50mL) was then added resulting a white precipitate, which was allowed to stir for 2 hrs before being filtered, washed with deionised water and then dried at 100 °C for 24 hrs. The dried TiO_2 powder was crushed into fine powder and was labelled as TC. The obtained powder was calcined at a heating rate of 5 °C/min at four different temperatures 300, 500, 700 and 800 $^{\circ}C$ (kept at a final temperature for 1 hr).

The prepared TiO_2 nanomaterials can be modified by N, S or N, F or N, F, Mn codoping for photocatalytic applications:

2.2.1. Synthesis of N, S codoped TiO_2

The dried powder before calcination was taken as the starting material for the synthesis of modified titania using four different nitrogen and sulphur containing modifiers. The four different modifiers used are:

- Thiourea
- Thiosemicarbazide
- Sulfanilic acid
- Cysteine

The procedure for the synthesis of TiO_2 using these four modifires are the same, i.e. using simple mechanical stirring method (Scheme 2.1). All the four modifiers were labelled as NS in the synthesis procedure and are described as follows:

The dried TiO_2, TC was mixed with NS in 1:1 ratio in a 100 mL beaker and make it as paste using 10mL of water. The obtained slurry was continuously stirred for one hour and dried at 100 ^oC for 24 hrs. Subsequently, the dried material was crushed into fine powder and then calcined in ceramic crucible. The calcination process was performed at 300, 500, 700 and 800 °C under air atmosphere with the heating rate of 5 °C min^{-1}, which was then followed by cooling at room temperature. The samples were labelled as given in Table 2.2.

Table 2.2. Designation and weight percentage of modified titania

Modifier	**Weight percentage**		**Designation**
	TC	**Modifier**	
Thiourea	1	0.25	TU1
		0.5	TU2
		1	TU3
		2	TU4
Thiosemicarbazide	1	0.25	TSC1
		0.5	TSC2
		1	TSC3
		2	TSC4
Sulfanilic acid	1	0.25	TSA1
		0.5	TSA2
		1	TSA3
		2	TSA4
Cysteine	1	0.25	TCS1
		0.5	TCS2
		1	TCS3
		2	TCS4

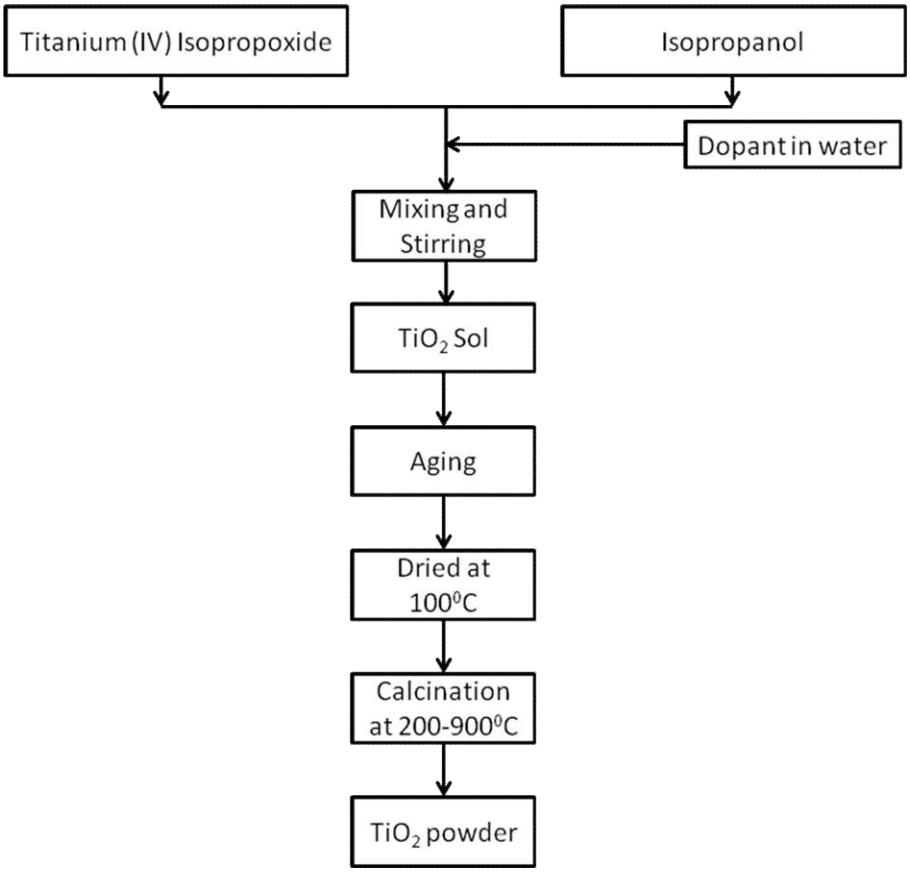

Scheme 2.1: Flow chart for the synthesis of N, S modified TiO_2

2.2.2. Synthesis of N, F codoped TiO_2

The reagents used in the study were titanium tetraisopropoxide (TTIP), ammonium fluoride (NH_4F) and isopropanol. To synthesis 1:1 TTIP/ NH_4F (TNF2) precursor solution, titanium isopropoxide (29.7 mL, 100 mmol) was mixed with 100 mL isopropanol followed by the dropwise addition of NH_4F solution (3.7 g in 50 mL water). The mixture was stirred for 2 hrs and then dried at 100 °C for 24 hrs. The dried TiO_2 powders were then calcined at a heating rate of 5 $^{\circ}$C / min at a

temperature range of 300-1000 °C for 1 hr. A similar route was followed to synthesize 1:0.5, 1:2 and 1:4 samples. Samples are named as TNF1, TNF3 and TNF4 respectively. Control TiO_2 sample was prepared by the same method without the addition of NH_4F and termed as TC.

2.2.3. Synthesis of N, F and Mn - tridoped TiO_2

The method described above was used to synthesize manganese modified TiO_2. The chosen TTIP: NH_4F ratio was 1:1 and varying amounts of manganese acetate were used and are listed in Table 2.3. The manganese was introduced to the mixture by dissolving $Mn(CH_3COO)_2$ in 50 mL of water before adding it to the titanium tetraisopropoxide-ammonium fluoride mixture. The stirring was continued for 2 hr and then dried at 100 °C for 24 hrs. The dried powder was then calcined at 500 °C for one hour at a ramp rate of 5 °C/min.

Table 2.3. Designation and weight percentage of TNFM samples

Sample	$Ti(OPr)_4$ (Wt. %)	NH_4F (Wt. %)	$Mn(CH_3COO)_2.4H_2O$ (Wt. %)
TNFM0.3	1.0	1.0	0.3
TNFM0.5			0.5
TNFM0.6			0.6
TNFM0.8			0.8

2.3. Photocatalytic studies

The photocatalytic measurements were carried out under both UV and sunlight and methylene blue was used as target system. UV measurements were done using a LZC-4X-Luzchem photoreactor with UV light intensity of 600 lux (or ≈5.82 mW/cm^2). For solar photocatalysis, the direct sunlight having 63.2-67.9mW/cm^2 intensity was used. The intensity of sunlight was measured using a Lutron, LX-107HA lux meter at the Calicut University Campus, Kerala, India (altitude: 11° 7′ 34″ North 75° 53′ 25″ East, time:12.00–1.30, temperature: 38 ± 1 °C) on 1st April 2016.

2.3.1. Methylene blue degradation

In a typical experiment, 0.1g of the sample was dispersed in 50 mL of methylene blue solution prepared in distilled water having a concentration of $3x10^{-4}$ M. This solution was stirred for 2 hr in the dark for the adsorption equilibrium to be established. The above suspension was then irradiated under UV/direct sun light with stirring. Constant stirring was continued throughout the reaction. The degradation of methylene blue dye was monitored by taking 5 ml aliquots at regular time interval. These aliquots were centrifuged at 5000 rpm for 15 minutes and absorption spectra of the samples were recorded using UV/Visible spectrometer. The same experimental procedure was adopted for all other samples discussed in different chapters of this thesis.

The rate of degradation of methylene blue was reported to obey (pseudo) first order kinetics and hence the rate constant for

degradation, k, was obtained from the first order plot of kinetic analysis according to equation 2.1.[1]

$$\ln\left(\frac{A_0}{A}\right) = kt \qquad (2.1)$$

Where, A_0 is the initial absorbance, A is the absorbance after a time (t) of the methylene blue dye degradation and k is the pseudo first order rate constant (min^{-1}).

2.3.2. Selective photocatalysis

For the experiment, 0.0159 g of methylene blue in 500 mL of deionized water ($5x10^{-4}$ M) and 0.0163 g of methyl orange in 500 mL of deionized water ($3x10^{-4}$ M) were separately prepared. 25 mL of each of the prepared solutions were mixed in a 100 mL beaker and 0.1 g of the photocatalyst was added to the dye mixture solution. Prior to photocatalytic study, adsorption study should be performed for 2 hr. under dark using all the prepared catalyst to remove the error due to initial adsorption effect.[2] The UV-Vis absorption spectra of MB (λ_{max}= 662 nm) and MO (λ_{max}= 466 nm) before and after 2 hrs were recorded. The above suspension was then irradiated under UV/direct sun light and stirring was continued throughout the reaction. Samples were collected at regular time interval and centrifuged. The clear solution was analysed by UV-Visible absorption to study the degradation behaviour of dye mixture.

2.4. Analysis of hydroxyl radical

The analysis of ·OH radical's formation on the sample surface under UV irradiation was performed by PL measurements by using terephthalic acid as a probe molecule. Terephthalic acid readily reacts with ·OH to produce highly fluorescent product, 2-hydroxyterephthalic acid (Figure 2.1).[3,4] This method relies on the PL signal at 415 nm of the hydroxylation of terephthalic acid with ·OH generated at the catalyst/water interface. The PL intensity of 2-hydroxyterephtalic acid is proportional to the amount of ·OH radicals produced by the photocatalyst.[3,4] The method is rapid, sensitive and specific, needs only a simple standard PL instrumentation.

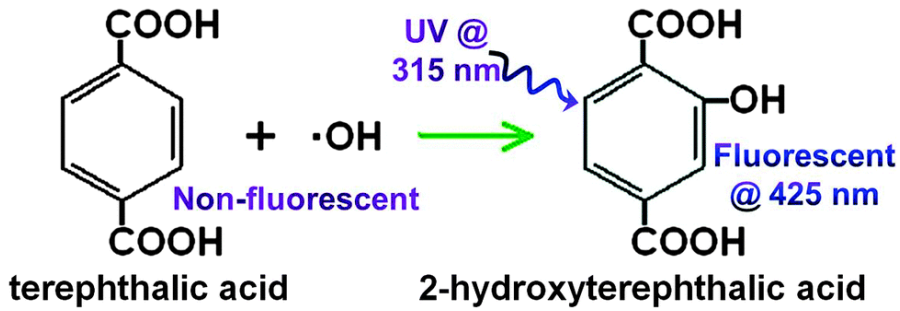

Figure 2.1. Formation of fluorescent 2-hydroxyterephthalic acid via the reaction of OH radicals with terephthalic acid.

The experimental procedures used are similar to the measurement of photocatalytic activity except that methylene blue aqueous solution is replaced by the 10^{-4} M terephthalic acid aqueous solution with a concentration of 10^{-3} M NaOH. The PL spectra of generated 2-hydroxyterephthalic acid were measured using fluorescence spectrophotometer. The experiment was conducted under

UV irradiation for 10 minutes and PL intensity was measured at 425 nm excited by 315 nm.

2.5. Characterisation Techniques

2.5.1. X-ray diffraction (XRD) technique

XRD patterns were obtained from Siemens D 500 X-ray diffractometer with the diffraction angle range of $10 \leq 2\theta \leq 80^0$ using Cu Kα radiation (λ=1.54 A^o). The X-ray diffraction technique is worked on the basis of Bragg's law, it can be defined as $n\lambda=2d\sin\theta$.Where 'λ' is the X-ray wavelength, θ is the incident angle, n is any integer and d is spacing between lattice planes.

The interaction of X-ray with the powder sample produces a constructive interference when satisfies the conditions of Bragg's law. These diffracted X-rays are detected and the intensity of these rays is plotted against 2θ values. Diffraction peaks are converted to d spacing and compared with standard reference pattern. Which helps in the identification of crystal since d spacing is a unique property of the crystal.

In the present work X-ray diffraction technique is used to

1. Identify the unknown crystalline material.
2. Measure crystallinity of the sample.
3. Calculate the crystallite size of the sample.
4. Obtain the phase purity of the crystal.

Qualitatively the anatase and rutile phase can be obtained from the X-ray diffraction diagram. Each diffraction peak in the XRD diagram can

be compared with the data of JCPDS card file and the obtained (h k l) value at a specified 2Θ value will be the unique identity of a particular crystal lattice system.

Scherrer equation (eqn 2) is used to estimate the crystallite size (T) of the sample.[5]

$$T = \frac{0.9\lambda}{\beta \cos\theta} \qquad (2.2)$$

Where λ is the wavelength of incident X-rays (1.54 Å), β is the peak width at half maxima and θ is the Bragg angle (Peak (101) located at 2θ=25.2° is of anatase and (110) peak at 27.4° is of rutile phase.

The phase composition of a sample can be measured from the integrated intensities of anatase, rutile and brookite peaks. If a sample contains only rutile and anatase, the percentage of rutile (%R) can be obtained from

$$\% R = [A_R / (0.884A_A + A_R)] \times 100 \qquad (2.3)$$

Where A_A and A_R represent the integrated intensity of anatase (101) and rutile (110) peaks respectively. If brookite is present in the sample then the above relation can be modified as:

$$\%A = [k_A A_A / (k_A A_A + A_R + k_B A_B)] \times 100 \qquad (2.4)$$

$$\%R = [A_R / (k_A A_A + A_R + k_B A_B)] \times 100 \qquad (2.5)$$

$$\%B = [k_B A_B / (k_A A_A + A_R + k_B A_B)] \times 100 \qquad (2.6)$$

Where %A and %B represents the percentage anatase and brookite phase, respectively. A_B is the integrated intensity of (121) peak of brookite phase and k_A and k_B are the two coefficients, where k_A = 0.886 and k_B= 2.721. [6,7]

2.5.2. FT-Raman Spectroscopy

FT-Raman spectra were recorded by using a BRUKER Multi RAM FT Raman spectrometer in the wave number range 3600-50 cm^{-1}.Raman spectroscopy is used to study the rotational and vibrational modes in a system. In this technique, laser beam in UV-Visible region interacts with phonons or other excitation in the sample and these will produce Raman scattering (inelastic scattering). A Raman spectrum consist of the plot of intensity of Raman scattered radiation Vs. Raman shift (frequency difference of Raman scattered radiation from the incident radiation).

In this work, Raman spectra were applied as an additional characterization tool to confirm the data such as crystallite size and high temperature stability of anatase phase as obtained from XRD.

According to factor group analysis, there are five Raman active modes {145($E_{g\ (1)}$), 197($E_{g(2)}$), 639 ($E_{g(3)}$), 399 (B_{1g}) and 513cm^{-1}(A_{1g}+ B_{1g})} for anatase TiO_2 and four for rutile phase {143(B_{1g}), 447(E_g), 612(A_{1g}) and 826 cm^{-1} (B_{2g})}[8,9]. Similarly, Raman spectra of brookite powder exhibit a characteristic intense band at 153 cm^{-1}, in addition to the weak sub band at 214, 247, 322, 366 and 454 cm^{-1}.

Peak broadening and a systematic frequency shift was observed when the particle size decreases.[10] $E_{g(1),}$ $E_{g(2)}$ and $B_{1g(1)}$ mode of anatase phase shows a blue shift and its shift in frequency was decreased from $E_{g(1)}$ to $B_{1g(1)}$ with decrease in crystallite size. But higher frequency mode like A_{1g}+ B_{1g} and $E_{g(3)}$shows red shift with decreasing crystallite size.[1]

2.5.3. UV-Visible Spectroscopy

The UV-Visible absorbance spectra were obtained using a Jasco-V-550-UV/VIS spectrophotometer. Mostly UV-Visible spectroscopy refers to absorption spectroscopy, in which liquid sample is used and for powder sample, we use diffuse reflectance spectroscopy to measure reflectance of light from the sample. The main advantage of using reflectance measurement is that the sample under investigation is not contaminated or consumed because this technique doesn't require the sample to disperse in liquid medium and sample can be reused for further analysis.

Absorption spectroscopy mainly used here for measuring the concentration of an absorbing species in dye solution (Methylene blue and methyl orange) used for photocatalytic degradation. The maximum wavelength of absorption (λ_{max}) was used to calculate degradation rate of the dye as a function of time. The absorption maximum for methylene blue is at a wavelength of 665 nm and that of methyl orange is 465 nm. The measurement of absorption follows Beer-Lambert law, which states that:

$$A = \log\frac{I_0}{I} = \varepsilon c l \qquad (2.7)$$

Where A is absorbance, I_0 and I are the intensity of incident light and transmitted light at a given wavelength respectively, ε is the molar extinction coefficient, c is the concentration of the sample solution and l is the path length through the sample.

Diffuse reflectance spectra of the powder sample can be used to determine the band gap energy of semiconducting nanoparticles with the help of tauc plot.[11] Tauc plot consist of $(\alpha h\upsilon)^{1/n}$ against $h\upsilon$. Where 'υ' is the frequency of radiation, 'h' is the plank's constant, 'α' is the absorption coefficient of the material and the value of 'n' depend upon the nature of transition, n may have values 1/2, 2, 3/2 and 3 corresponding to allowed direct, allowed indirect, forbidden direct and forbidden indirect transitions respectively.[12,13] Usually for anatase TiO_2, a linear nature in the plot were observed when n=2 and this indicate the indirect allowed transition for anatase TiO_2.[14,15] Extrapolating the slope of the graph to x-axis will get the band gap energy of TiO_2.

2.5.4. FTIR Spetcroscopy

FTIR spectroscopy (vibrational spectroscopy) helps to identify the characteristic bonds in TiO_2 framework. Change in dipole moment is the prime condition for a molecule to absorb IR radiation and drastic change in dipole moment results more intense absorption band. Interaction of IR radiation with chemical bond causes stretching, bending and other molecular vibrations and which helps in the

identification of unknown molecule. FTIR techniques were performed using a Jasco-FT/IR-4100 spectrophotometer and spectra were measured in the range of 400 to 4000 cm^{-1} at ambient temperature.

2.5.5. Surface area measurements

The BET (Brunauer, Emmett and Teller) surface area measurements and pore analysis were performed by nitrogen adsorption using a Micromeritics, Gemini model 2375 surface area analyzer. The measurements were carried out at liquid nitrogen temperature after degassing the powder samples for 2 h at 200 °C. BET equation is used to determine the specific surface area of the material. BET theory applies to multi-layer adsorption system, and usually utilizes probing gases (as adsorbent, usually nitrogen) that do not chemically react with the surfaces of material (as adsorbate) under study to quantify specific surface area.

In BET theory it is assumed that the adsorption of gas molecules on the sample surface can take place since the solid surface possesses uniform localized sites. The BET equation is:

$$\frac{P}{V(P_0 - P)} = \frac{1}{V_m C} + \frac{(C-1)P/P_0}{V_m C} \qquad (2.8)$$

Where, V = volume of gas adsorbed (in cm^3/g) at pressure P and P_0 is the saturation pressure of the gas. V_m = volume of the gas adsorbed on the surface of the solid when the entire surface is completely covered with a monolayer (in cm^3/g). C is the BET constant depending upon the nature of the gas. Since C and V_m are constants for a given gas-

solid system. A plot of $\frac{P}{V(P_0 - P)}$ *Vs* $\frac{P}{P_0}$ will give a straight line with slope of $(C-1)/V_mC$ and y-intercept $1/V_mC$. So V_m can be calculated.

Total surface area of the sample can be calculated using the equation,

Surface area, $S = V_mNA / M$

Where, N = Avagadro Number, 6.023×10^{23} mol^{-1}, A = Cross sectional area of a single molecule of the adsorbate (m^2) and M = Molecular weight of the adsorbate (g/mol).

2.5.6. Transmission Electron Microscopy (TEM)

Particle morphologies were studied using TEM by JEOL/JEM 2100 transmission electron microscope.The transmission electron microscope is a powerful tool for observing the property such as crystal structure, defects in semiconductors, etc and high resolution transmission electron microscope (HRTEM) can be used to study the quality, size and shape of nanoparticles. The basic principle of TEM and light microscope are same, but TEM uses electrons instead of light in light microscope. Wavelength of electron is much smaller than that of light so optimum resolution obtained for TEM image is much better than that of light microscope. This will make TEM as a distinctive tool for probing the internal structure details of nanoparticles.

SAED (Selected Area Electron Diffraction) pattern obtained from TEM analysis can be used:

i. To check the sample is amorphous (diffuse rings), crystalline (bright spots) or polynanocrystalline (small spots making up a

rings, each spot arising from Bragg reflection from an individual crystallite).

ii. To find out the crystalline phase of the sample (each phase has a characteristic SAED pattern)

2.5.7. Field emission scanning electron microscopy (FESEM)

Scanning electron microscopy of the samples were performed using a ZEISS Gemini SEM 300 which produces images at both normal and low operating voltages. The measurements were carried out with a low accelerating voltage range of 5-15 kV. Powdered samples were evenly distributed on a mounted carbon tape surface. Loose powdered sample was removed with canned air spray.

The field emission scanning electron microscope (FESEM) is a type of electron microscope that images the sample surface by scanning it with a high-energy beam of electrons in a raster scan pattern. The electrons interact with the atomic shells that make up the sample producing signals that contain information about the sample's surface topography, composition and other properties such as electrical conductivity. The beam-specimen interaction produces different signals including secondary electrons (SE), back scattered electrons (BSE), characteristic X-rays, light (cathodoluminescence), specimen current and transmitted electrons (STEM). SE imaging is the most common or standard detection mode. The spot size in a Field Emission SEM is smaller than in conventional SEM and can therefore produce very high-resolution images, revealing details in the range of 1 to 5 nm in size.

2.5.8. X-ray photoelectron spectroscopy (XPS)

X-ray photoelectron spectroscopy is a surface sensitive spectroscopic technique that provides quantitative as well as chemical state information from the surface of material under investigation.[2,16] The XPS analyses were performed on a Thermo VG Scientific (East Grinstead, UK) Sigma Probe spectrometer. The instrument employs a monochromated Al Kα X-ray source (hν = 1486.6 *eV*) which was operated at 140 W. The analysis area was approximately 500 μm in diameter. For survey spectra, pass energy of 100 *eV* and a 0.4 *eV* step size were employed. For N_{1s} and S_{2p} high resolution spectra, a pass energy of 50 *eV* and a step size of 0.2 *eV* were used. Charge compensation was achieved using a low energy electron flood gun. Quantitative surface chemical analyses were calculated from the high resolution core level spectra, following the removal of a non-linear Shirley background. The manufacturer's Avantage software was used to plot results which incorporates the appropriate sensitivity factors and corrects for the electron energy analyzer transmission function.

2.5.9. Photoluminescence Spectroscopy

Photoluminescence spectroscopy is a complimentary analytical tool to UV–Visible absorption spectrum. It is a simple, versatile, nondestructive and noncontact method for probing the electronic structure of the material by excitation with suitable radiation. Photo excitation and emission are the important processes in photoluminescence spectroscopy. Excitation is done with suitable wavelength of radiation. In photoluminescence spectrum, the intensity

of the emitted light is measured as a function of excitation or emission wavelength. The emission of light from excited electronic state occurs in two ways named as phosphorescence and fluorescence. Probability of fluorescence is high compared to phosphorescence it is a time delayed process. In fluorescence decaying of electrons takes place from singlet excited state while in phosphorescence it is from triplet excited state.

In the present study, the PL spectra of generated 2-hydroxyterephthalic acid were measured on an Agilent Technologies model Cary Eclipse Fluorescence Spectrophotometer.

2.5.10. Photoreactor

The photocatalytic measurements were carried out using a LZC-4X-Luzchem photoreactor equipped with 6 top lamps and 8 side lamps. Photoreactor provide UVA radiation with an emitting wavelength of 350 nm. Stirrer is installed under the aluminium floor slightly towards the front from the center of the irradiation chamber and is controlled by a switch and speed control in the front panel. The ventilation system in Luzchem photoreactor limits temperature increases in the chamber to 3-4 ^{o}C above room temperature, i.e. the heat generated by the lamps act as the thermal source and temperature is regulated by the cooling fan. A safe exhaust is also provided in the reactor system. The UV intensity in the photoreactor can be obtained using LZC - power meter and are found to be 5.82mW/cm^2.

References

[1] X. Chen and S. S. Mao, Chem. Rev., 2007**, 107**, 2891.

[2] S. G. Ullattil and P. Periyat, Nanoscale, 2015, **7**, 19184.

[3] Q. J. Xiang, J. G. Yu, B. Cheng and H. C. Ong, Chem. Asian. J., 2010, **5**, 1466.

[4] Q. Xiang, J. Yu and M. Jaroniec, Phys. Chem. Chem. Phys., 2011, **13**, 4853.

[5] A. L. Patterson, Phys. Rev., 1939, **56**, 978.

[6] H. Zhang and J. F. Banfield, J. Phys. Chem. B, 2000, **104**, 3481.

[7] J. G. Li and T. Ishigaki, Acta Mater., 2004, **52**, 5143.

[8] T. Ohsaka, F. Izumi and Y. Fujiki, J. Raman Spectrosc., 1978, **7**, 321.

[9] S. P. S. Porto, P. A. Fleury and T. C. Damen, Phys. Rev., 1967, **154**, 522.

[10] V. Swamy, A. Kuznetsov, L. S. Dubrovinsky, R. A. Caruso, D. G. Shchukin and B. C. Muddle, Phys. ReV. B, 2005, **71**, 184302.

[11] J. Tauc, Mat. Res. Bull., 1968, **3**, 37.

[12] R. Vijayalakshmi and V. Rajendran, Arch. Appl. Sci. Res., 2012, **4**, 1183.

[13] E. A. Davis and N. F. Mott, Philos. Mag., 1970, **22**, 903.

[14] Z. Wang, U. Helmersson and P. O. Kall, Thin Solid Films, 2002, **405**, 50.

[15] S. Sen, S. Mahanty, S. Roy, O. Heintz, S. Bourgeois and D. Chaumont, Thin Solid Films, 2005, **474**, 245.

[16] A. M. Czoska, S. Livraghi, M. Chiesa, E. Giamello, S. Agnoli, G. Granozzi, E. Finazzi, C. Di Valentin and G. Pacchioni, J. Phys. Chem. C, 2008, **112**, 8951.

CHAPTER 3

Synthesis, characterization and applications of solar active anatase $TiO_{2-x}(SN)_x$ photocatalyst modified with an organosulfur compound thiourea

CONTENTS

3.1. Introduction

In this chapter we aim to synthesize an efficient, photo stable and visible light active, TiO_2 based photocatalyst by mechanical mixing of thiourea as modifier with nanocrystalline anatase TiO_2. Nonmetal (mainly C, N, S, and F) donating modifiers are the best to reduce the band gap energy to visible region, one of the prime condition to be satisfied by TiO_2 for its boosted photocatalytic applications in day light.[1,2,3,4] The dopant ion depends, the ion donors to some extent.[5] Therefore, the ion donor selection is more predominant in the production of non-metal ion doped TiO_2 for photocatalytic applications.

Thiourea has been studied as a promising material for several decades due to its wide applications such as in metal complexation as ligand,[6] reducing agent,[7] catalysts inclusive of photocatalyst[8] and corrosion inhibitor.[9] In this section, we described the photocatalytic performance of TiO_2 modified by thiourea. Basca *et al* synthesized S-doped TiO_2 using thiourea, which results an enhancement in the photocatalytic peroxidation and mineralization (oxidation) of biomolecules.[13]But Sakthivel *et al* got a surprising result that thiourea doped sample do not contain sulfur but instead contain nitrogen as the doping component inducing visible light photocatalysis for the degaradation of 4-chlorophenol.[10] Wei *et al* was successfully prepared thiourea doped TiO_2 resulting N and S codoping for methyl orange degradation under UV as well as sunlight.[11] The above reports clearly show that thiourea often has been used as a sulfur donor,[12] as a nitrogen donor[10] or also as simultaneous donors of nitrogen and sulfur.[13] Only few reports are

available based on the simultaneous donation of N and S as donors from the same compound even though these two atoms are present in the dopant molecule.

This chapter demonstrates a systematic study on the effect of different percentage of thiourea on sol-gel derived titania and compare the efficiency of photocatalytic purification of water by taking methylene blue as a model dye. The photocatalytic activities of the prepared samples are evaluated with the help of photocatalytic experiments, XRD, Raman spectroscopy, TEM and XPS.

3.2. Results and discussion

3.2.1. X-ray diffraction technique

X-ray diffraction technique was employed to determine the phase composition and crystallite size of the prepared TiO_2 at different temperature. The XRD patterns of the TC and TU2 samples at different calcination temperature are shown in Figure 3.2 and 3.3 respectively and that of different TU samples at 700℃ are shown in Figure 3.1. The amount of rutile, anatase and brookite retained in the sample at various calcination temperature was measured from the XRD integrated intensities of (110) reflection of rutile, the (101) reflection of anatase and (121) reflection of brookite (Table 3. 1). It was found that all the doped TiO_2 with different thiourea concentration have observed 100% anatase phase upto 700 °C (Figure 3. 1). In comparison, from the Figure 3.1 to 3.3 and Table 3.1, the control sample showed rutile as the major phase at 700 °C, while in the case of modified TiO_2 the transformation of anatase to rutile occurred only

above 700 °C. It has been reported that the incorporation of non-metal such as nitrogen and sulphur retards anatase to rutile phase transformation and complete transformation to rutile occurred only at 900 °C.[14] Here also, 52% of anatase phase has been retained in the TU2 sample calcined at 800 °C (Figure 3. 3).

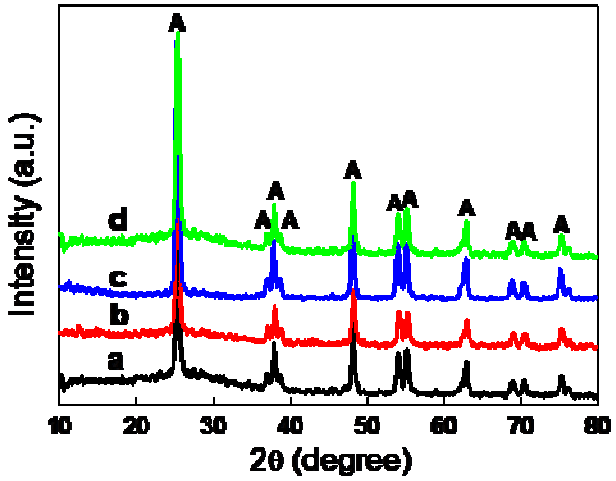

Figure 3. 1. X-ray diffraction pattern of a) TU1, b) TU2, c) TU3 and d) TU4 samples calcined at 700 °C.

Table 3. 1. Phase composition of the prepared TiO_2 at different calcination temperature (A: Anatase, R: Rutile and B: Brookite)

Sample	300			500			700			800		
	A	R	B	A	R	B	A	R	B	A	R	B
TC	67	0	32	62	0	38	17	83	0	0	100	0
TU1	100	0	0	100	0	0	100	0	0	48	52	0
TU2	100	0	0	100	0	0	100	0	0	54	46	0
TU3	100	0	0	100	0	0	100	0	0	51	49	0
TU4	100	0	0	100	0	0	100	0	0	49	51	0

The early formation of rutile phase in the control sample may be due to the appearance of brookite phase (2Θ=30.7 °) along with anatase phase (Figure 3. 2). It was found that the anatase to rutile transition seemed to start ahead of the anatase to brookite transition as in Figure 3. 2. Yu *et al* suggested that presence of brookite phase causes a slight shift in the anatase peak to higher angle due to the overlapping of brookite peak and this will enhance anatase to rutile transformation.[15] Absence of brookite phase in the doped sample delays anatase to rutile phase transition temperature.

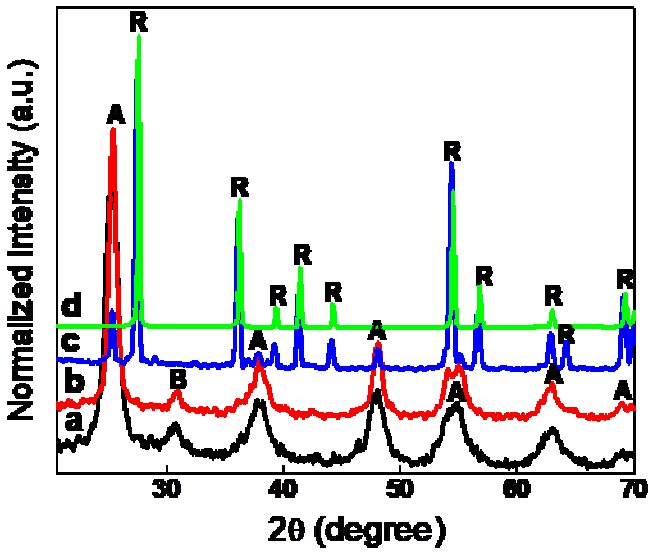

Figure 3. 2. X-ray diffraction pattern of TC sample at a) 300, b) 500, c) 700 and d) 800 °C.

To determine the optimum percentage of N and S modification 0.25, 0.5, 1 and 2 wt% of thiourea was mixed with TiO_2 and the obtained powder were calcined at temperatures of 300, 500 and 700 °C. The

crystallite size of the samples was calculated by applying scherrer equation and it was found that the crystal size was lessened upon thiourea doping (Table 3. 2). The optimized percentage of thiourea for better photocatalytic performance was found to be at 0.5% and the best calcination temperature is at 700 °C. Similarly, the X-ray diffraction pattern showed that the crystallinity of the doped sample is increased with temperature and the maximum intensity is observed for the (101) peak at 700 °C. Further increase in temperature decreased the intensity of (101) peak due to anatase to rutile transformation (Figure 3. 3).

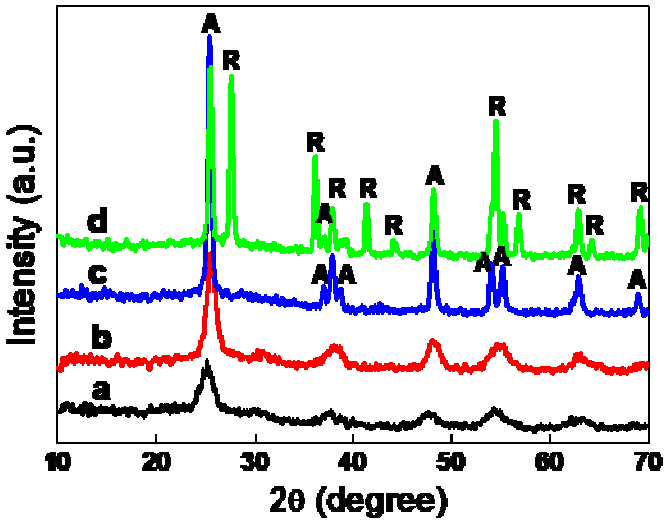

Figure 3. 3. X-ray diffraction pattern of TU2 sample at a) 300, b) 500, c) 700 and d) 800 °C.

Table 3. 2. Crystallite size of the sample calcined at 700 °C

Sample	Crystallite size (nm)
TC	32.1
TU1	16.82
TU2	15.45
TU3	18.91
TU4	16.81

3.2.2. FTIR study

Figure 3.4 shows the FT-IR spectra of the control and doped TiO_2 sample calcined at 300 °C, which can provide more information about functional groups on the surface of catalyst materials. The broad peak at around 600 cm^{-1} corresponds to the Ti–O–Ti bridging stretching modes.[16] The peaks around 3400 and 1630 cm^{-1} corresponds to the stretching and the bending vibrations of –OH or adsorbed water molecules, respectively.[17,18] The two absorption peaks in the 900-1300 cm^{-1} range were observed on the spectra of TU2 sample, but absent on the pure TiO_2 sample. The peaks at 1146 and 1054 cm^{-1} were the characteristic frequencies of a bidentate SO_4^{2-} co-ordinated to metals such as Ti^{4+} suggesting the successful doping of sulfur atom into TiO_2 in the doped sample (TU2).[11,13,19] Ammonium ions produced by the dissociation of thiourea were also found in the TU2 sample at 1400 cm^{-1} attributable to the deformation mode of ammonium ions.[20]

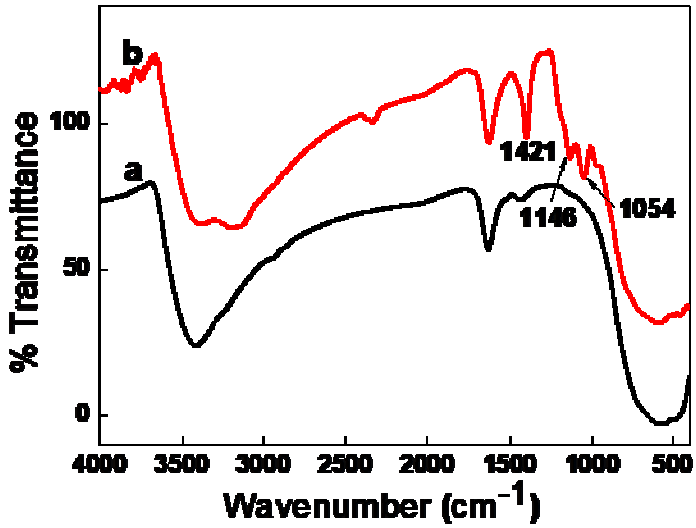

Figure 3.4. FT-IR spectra of a) TC and b) TU2 dried at 300 °C.

3.2.3. Raman spectra

Raman spectroscopy was applied as an additional characterization technique to confirm the phase transformation of control and doped sample from anatase to rutile form. According to factor group analysis, the anatase phase consist of six (144, 197, 399, 513, 519 and 639 cm^{-1}), rutile phase consist of four (143, 447, 612, and 826 cm^{-1}) and finally brookite phase consist of six (153, 214, 247, 322, 366 and 454cm^{-1}) Raman active modes.[21,22] Figure 3.5A shows the Raman spectra of doped sample with different thiourea concentration at 700 °C and have only 100% anatase phase. After baking at 800 °C, the crystalline structure of the doped sample transformed from anatase to rutile as in Figure 3.5(B-d). For comparison, Figure 3.6 shows the Raman spectrum of the control sample at different calcination temperature, in which a mixture of anatase and rutile can be observed even at 700 °C and complete transformation occurs at 800 °C.

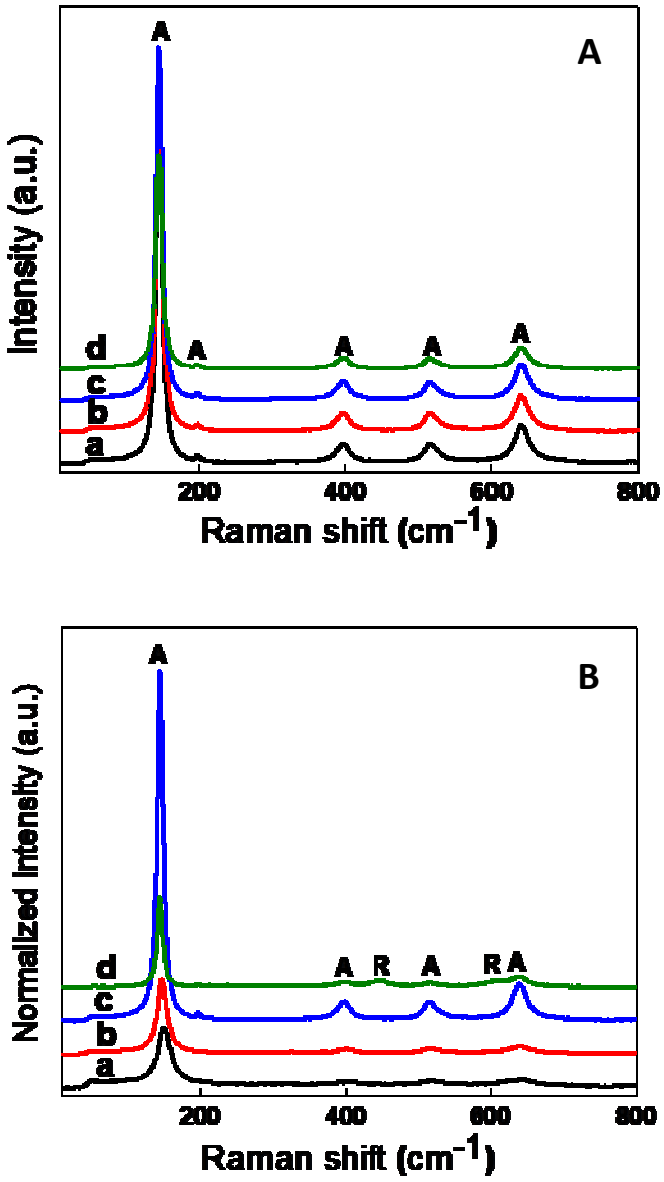

Figure 3.5. Raman spectra of A) -a)TU1, b) TU2, c) TU3 and d) TU4 at 700 °C and B) TU2 sample calcined at a) 300, b) 500, c) 700 and d) 800 °C.

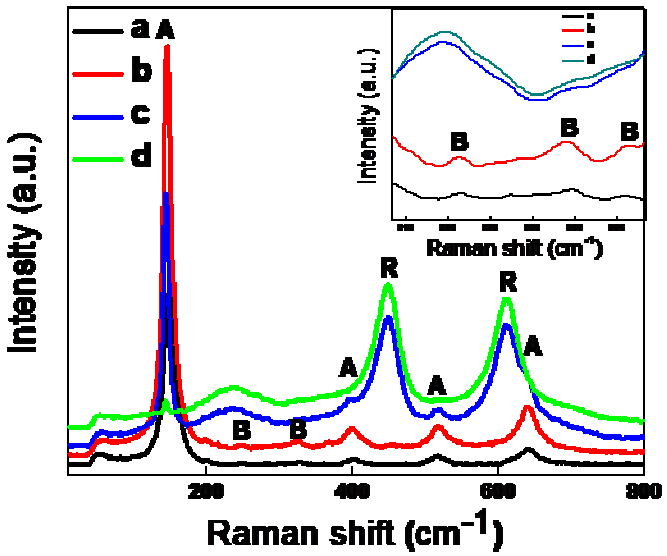

Figure 3.6. Raman spectra of the control sample TC calcined at a) 300, b) 500, c) 700 and d) 800 °C. (Inset shows the presence and absence of brookite phase at various calcination temperatures).

The existence of brookite phase in TC at 300 and 500 °C is evidenced from the Raman spectra at 153, 247, 323 and 368 cm^{-1} with relatively stronger intensity as in the inset of Figure 3.6. The strong band at 153 may merge with the high intense peak of anatase at 144 cm^{-1}.This is consistent with the observation that the XRD intensity of brookite phase is first increased from 300 to 500 °C and then decreased with further increase in temperature.

In Figure 3.6 (c and d), a strong band at about 238 cm^{-1} is exhibited. The appearance of this band with the opening of anatase to rutile transformation is distinctly shown in Figure 3.6. It cannot be assigned to the fundamental modes of anatase and rutile phase. A few

interpretations have been given for its origin: Porto *et al* proposed it to a combination band, Hara and Nicol attributed that the rutile lattice is disordered and this disorder can induce the band, and Balachandran *et al* recommended it might be due to the second-order scattering generated through a multiphonon process.[23,24,25] Ma *et al* also support this second order scattering.[26]

3.2.4. TEM

TEM was used to further examine the morphology, crystal size and crystallinity of TiO_2 samples. Figure 3.7 shows the tunneling electron micrographs of the undoped and doped TiO_2 modified at a calcination temperature of 700 °C. The TiO_2 powder before modification at a high temperature such as 700 °C, consist of large anatase particle having an average particle size in the range of 20-60 nm (Figure 3.7A). After the modification of TiO_2 using 0.5 wt% of thiourea calcined at the same temperature, the crystallite size of the anatase powder is decreased to the range 10-25 nm (Figure 3.7B).The distinct spots in the SAED (selected area electron diffraction) pattern of both TC and TU2 sample at 700 °C in Figure 3.7C and 3.7D support the higher crystalline nature as observed in the XRD pattern. It is seen that, for anatase TU2 sample, the crystal lattice plane (101) with d-spacing of 0.34 nm is obtained, whereas those of rutile give lattice plane with d-spacing of 0.32 nm of (110) plane.

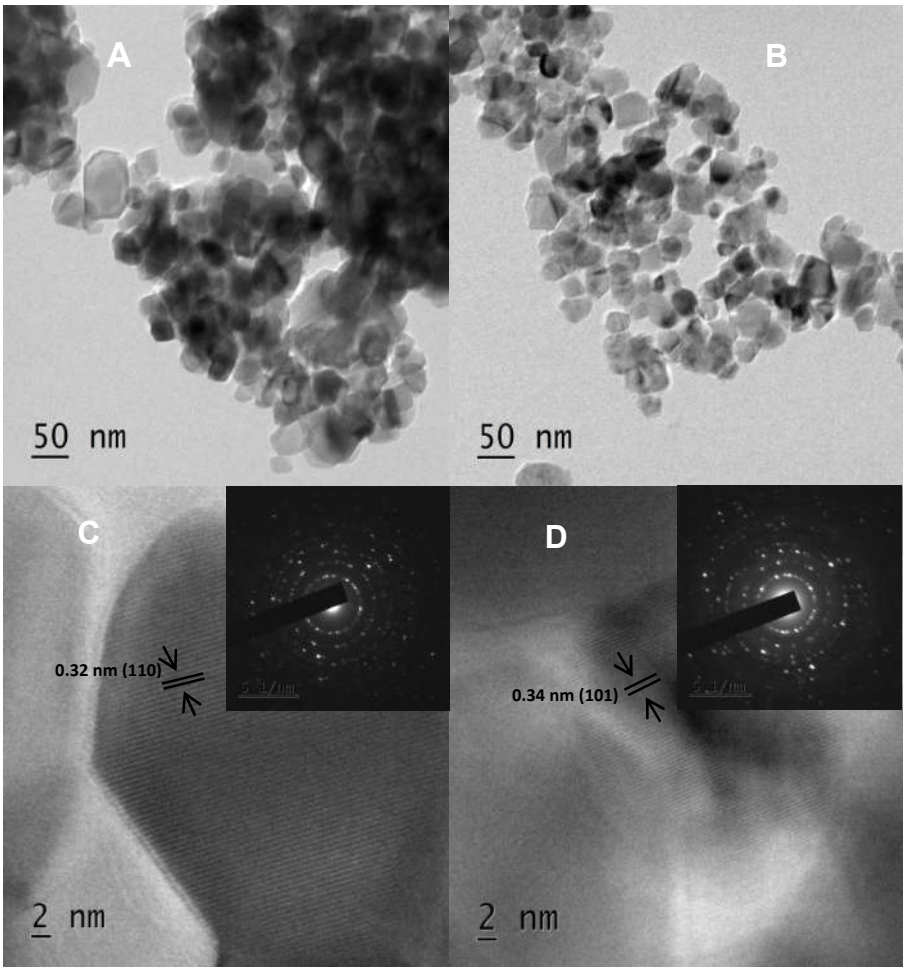

Figure 3.7. TEM and HRTEM images of A&C) TC, B&D) TU2 samples respectively. Inset shows the corresponding SAED pattern (all the samples are calcined at 700 °C).

3.2.5. XPS

XPS analysis was performed to investigate the incorporation of N and S in the TiO_2 sample and thereby their chemical state at 700 °C. The wide area XPS spectrum clearly shows the presence of nitrogen and sulfur in the doped TiO_2 in addition to titanium, oxygen and carbon in the control sample (Figure 3.8). The carbon peak in the control sample

is mainly due to the residual carbon from the precursor molecule and adventitious hydrocarbon from XPS instrument itself. In addition to the amount of carbon in the control sample, slightly higher intense peak of C1s was observed for the TU2 sample (Figure 3.8b).

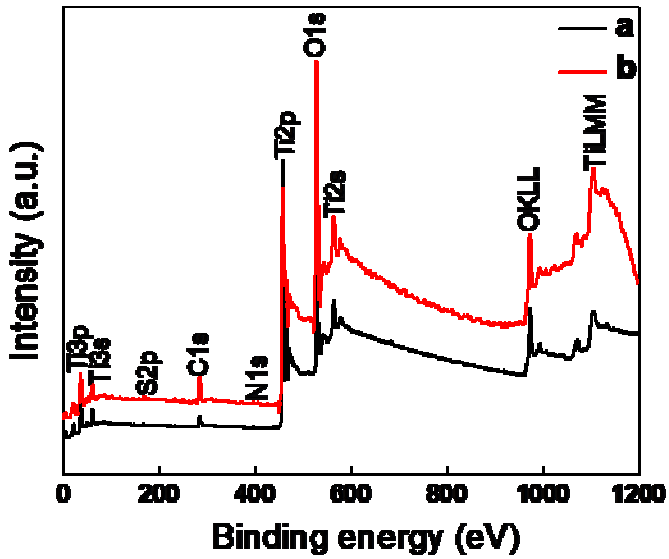

Figure 3.8. XPS survey spectra of a) TC and b) TU2 sample calcined at 700 °C

Previously it was found that, there is a possibility for the existence of three forms of carbon such as surface adsorbed (287.5 eV), solid solution (285 eV) and the carbide, Ti-C (281.5 eV).[27] Figure 3.9B shows the high resolution XPS spectra of C1s in TU2 sample at 700 °C and it can be seen that the majority of the carbon present in TiO_2 exist as solid solution (284.8 eV). This solid solution of carbon can locate within the octahedral and tetrahedral interstices existing within the anatase crystal.[28,27] Disappearance of peak at 281.5 eV confirms the absence of Ti-C phase. The survey spectrum of TU2 sample at 700 °C shows an intense peak of C1s at 284.8 eV than the control sample TC

at the same temperature, which indicates that the carbon atom from thiourea can be easily incorporated into TiO_2 lattice.

Previous reports shows that sulfur containing materials have a binding energy value of around 170 eV.[29] The S2p high resolution XPS spectra of TU2 sample calcined at 700 °C shows a peak at 168.4 eV, which confirm the presence of sulphur at 700 degree temperature (Figure 3.9A). It has been reported that the binding energy peak at 168.4 eV is due to the presence of S^{6+} cation and this will confirm that upon thiourea doping, sulphur can entered into TiO_2 lattice as cationic sulphur with a charge of +6.[30,12] Also, the replacement of Ti^{4+} by S^{6+} is chemically more favorable than the substitution of O^{2-} by S^{2-}. Because the bond strength of Ti-S bond (418 kJ/mol) is less than the existing Ti-O bond (672 kJ/mol) and the ionic radius of S^{2-} ion (1.7 A^o) is greater than that of O^{2-} ion (1.22 A^o).[14,30] Absence of binding energy peak at 160.7 eV in the TU2 sample clearly support the absence of Ti-S bond in the doped TiO_2 matrix.[4]

Figure 3.10 display the high resolution XPS of N1s of TU2 and TC sample at 700 °C, which shows that nitrogen also remains in the titania matrix as a codopant from thiourea. Nitrogen can be located in the anatase crystal lattice of TiO_2 either through substitutionally or interstitially. Fujishima *et al* summarized that, the N1s peak at ~396 eV is typically assigned to the substitutional nitrogen dopant as Ti-N bond while the peak at ~400 eV is ascribed to the interstitial nitrogen dopant.[31,32] The binding energy peak for N1s of TU2 sample at 700 °C observed a little broad peak at around 400 eV. Absence of this peak in the control sample TC at 700 °C shows the successful doping of nitrogen in the TU2 sample at the same temperature. It was previously observed that the molecular chemisorptions of nitrogen exhibit a peak

at around 400 eV.[33,34,28] Periyat *et al* suggested that the formation of chemisorbed nitrogen is due to the decomposition of NH_4^+ present in the sample when the temperature is elevated.[35] On the other hand, absence of peak at 396 eV indicates that Ti-N bond is not being present in the TU2 sample at high temperature.

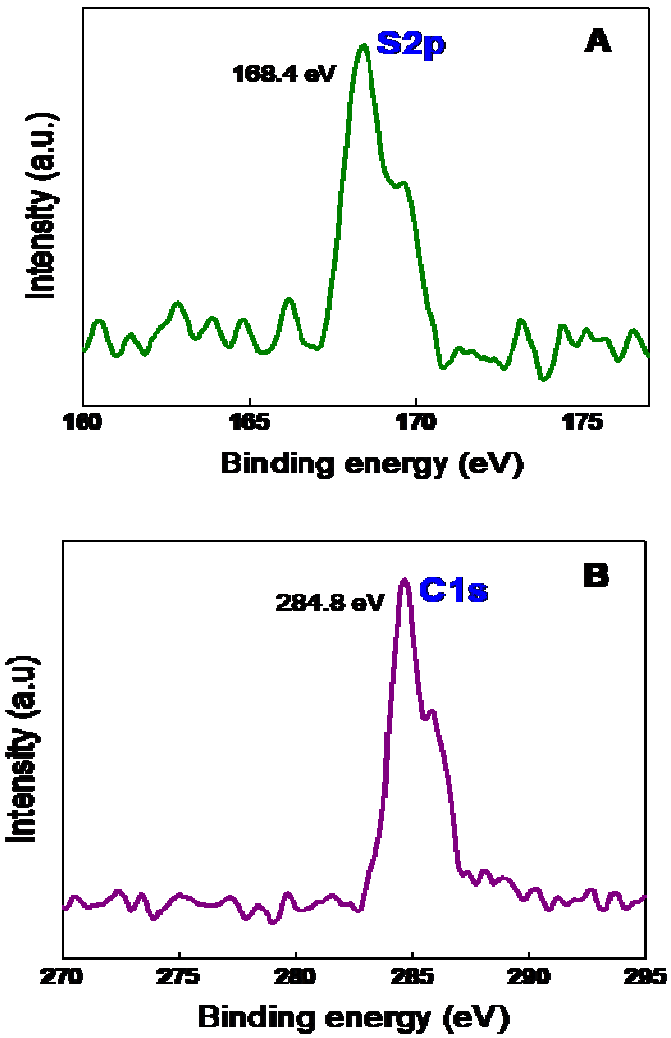

Figure 3.9. High resolution XPS spectra of A) S2p and B) C1s of TU2 sample calcined at 700 °C.

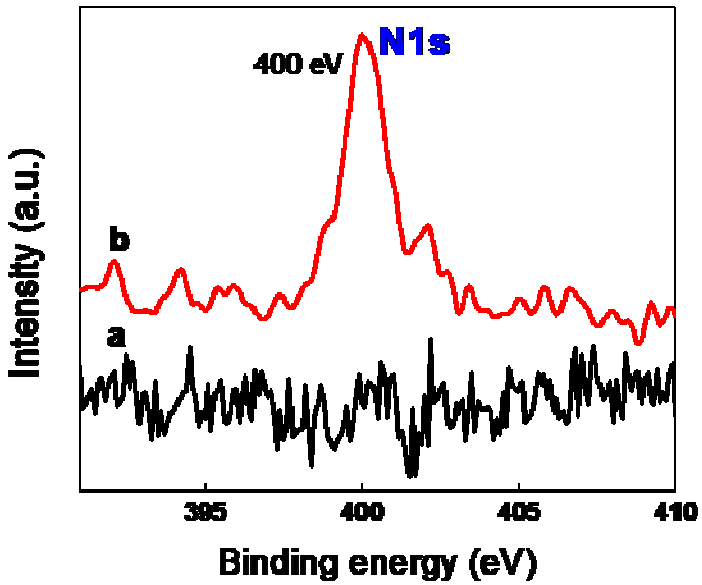

Figure 3.10. High resolution XPS of N1s of a) TC and b) TU2 sample at 700 °C

The obtained XPS spectrum of Ti2p core level from pure TiO_2 displayed a $Ti2p_{3/2}$ peak at 458.8 eV and O1s peak at 530.1 eV (Figure 3.11A and 3.11B). After modification using thiourea at 700 °C, the binding energy peaks of $Ti2p_{3/2}$ and O1s shifted to 458.4 eV and 529.6 eV respectively. The red shift in the peak position of Ti2p and O1s are primarily due to the introduction of oxygen vacancies into the TiO_2 lattice.

There are mainly two factors that support the oxygen vacancy site in the lattice of TiO_2.

(1) High temperature treatment of TU sample may leads to the formation of ammonium ion as evidenced from the FTIR

technique, this will further decomposed to ammonia and H_2 molecule. This reducing atmosphere can motive the partial reduction of TiO_2, which results a red shift in the peak position of both Ti2p and O1s.[32,36]

(2) It is well known that TiO_2 is very sensitive to oxygen and it can be easily reduced under an oxygen deficient environment.[36] If the dopants are non-isovalent when compared to titania, then the doped TiO_2 have to satisfy an additional charge neutrality condition. This charge neutrality condition can accelerate the formation of Ti or O vacancy, depending upon on the valency of dopant.[36] Here also the substitution of Ti^{4+} by S^{6+} leads to a charge imbalance in the TiO_2 matrix, which enhances the formation of oxygen vacancy environment.

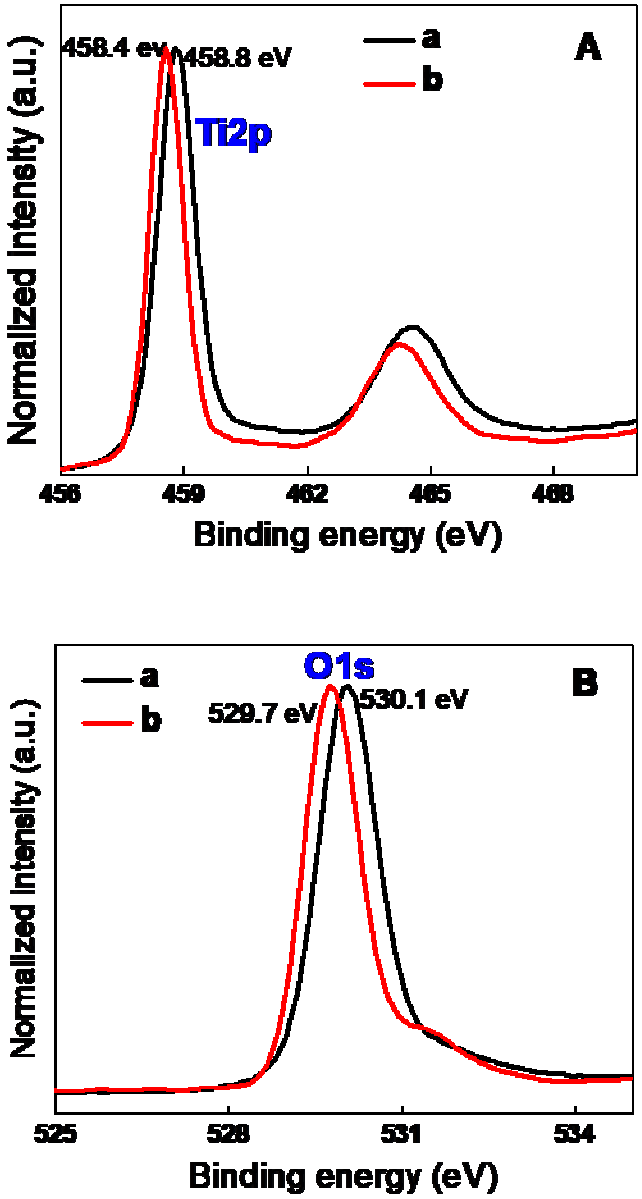

Figure 3.11. High resolution XPS spectra of A) Ti2p and B) O1s of a) TC and b) TU2 sample calcined at 700 °C.

3.2.6. UV-Visible diffuse reflectance spectra

The UV-Visible spectra (DRS) are used to determine the optical properties of the sample. Figure 3.12 records the UV-Visible spectra and corresponding tauc plot of the undoped and N, S- codoped TiO_2 calcined at 700 °C. The obtained result shows that thiourea has a significant effect on the light absorption characteristics of TiO_2. The control sample, TC shows an absorption edge at around 390 nm in the UV range as observed commonly for anatase TiO_2, while the absorption spectra of the doped sample exhibit a red shift in the absorption band. The decrease in band gap energy can be assign to the fact that high temperature calcination can induce N and S elements codoped into the TiO_2 lattice.[37] Further observation shows that, with the increase in dopant concentration, wavelength of absorption shifted to higher wavelength region and the band gap energies corresponding to this red shift are tabulated using tauc plot (Table 3.3). This may be attributed to the fact that the higher concentration of dopant induce more N and S atoms into the lattice of TiO_2, resulting in a large band gap narrowing.[38]

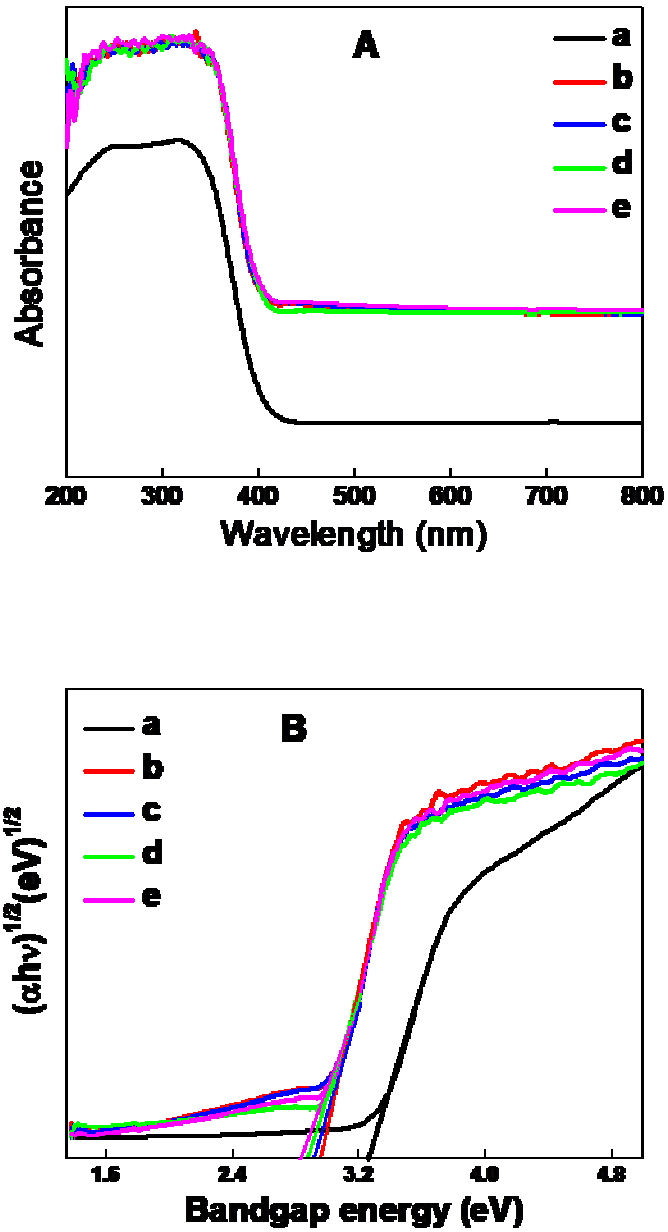

Figure 3.12. A) UV-Visible absorption spectra and B) corresponding tauc plot of a) TC, b) TU1, c) TU2, d) TU3 and e) TU4 calcined at 700 °C.

Table 3.3. Band gap energy calculated using tauc plot.

Sample	Band gap energy (eV)		
	300	**500**	**700**
TC	3.26	3.22	3.24
TU1	2.72	2.87	2.94
TU2	2.65	2.85	2.90
TU3	2.37	2.77	2.88
TU4	2.24	2.69	2.87

Compared to pure TiO_2, two prominent features clearly seen in the doped sample at a calcinations temperature of 300 °C: i) the appearance of a shoulder peak at around 390-500 nm and ii) the enhanced absorption band in the range of 500-800 nm. As the calcination temperature increases the intensity of these two bands is decreased due to the decreased amount of N and S content in the TiO_2 lattice (Figure 3.13). Generally, visible-light-absorption shoulder in the range of 390-500 nm results from the N-atom in the interstitial site of TiO_2 due to the introduction of some localized states near the valence band edge.[39] In the case of doped TU samples, the enlarged shoulder in the range of 390–500 nm is closely related to the doped N-atoms,[40] while the enhanced absorbance in the range of 500–800 nm is possibly due to the synergistic effect of nitrogen and sulfur co-doping on the electronic structure of TiO_2.[39] Unquestionably these results reveal that, doping incorporate nitrogen and sulfur into the TiO_2 lattice, which results an alteration in the crystal structure and electronic properties of TiO_2.

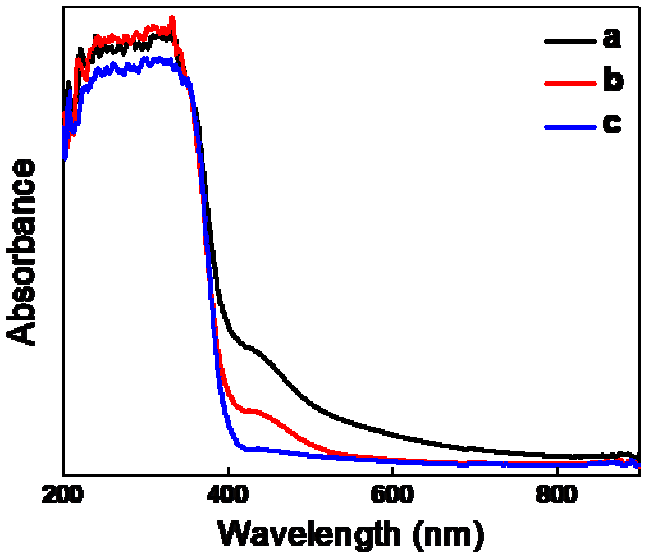

Figure 3.13. UV-Visible absorption spectra of TU2 sample calcined at a) 300, b) 500 and c) 700 °C.

Generally, the photocatalytic reaction rate is directly proportional to $(I\alpha\Phi)^n$ (n = 1 for low light intensity and n = 1/2 for high light intensity), where Iα is the photo numbers absorbed by photocatalyst per second and Φ is the efficiency of the band gap transition.[15] The enhancement of the photocatalytic activity with thiourea doping can be partly explained in terms of an increase in IαΦ resulting from an intense absorption in the visible region.

3.2.7. Analysis of hydroxyl radical

The higher activity of the prepared TU2 sample at 700 °C was further confirmed by the detection of hydroxyl radicals. Figure 3.14 shows the changes in PL intensity of terephthalic acid solution by various TC and TU samples calcined at 700 °C exposed for 10 minutes to UV light.

Changes in the PL intensity at about 425 nm is observed corresponds to hydroxyterephthalic acid by varying the concentration of thiourea on TiO_2 sample and the maximum intensity was observed for TU2 sample at 700 °C having 0.5 wt% of thiourea, which showed maximum photocatalytic activity. Similarly, PL intensity of TU2 sample increases with rise in calcination temperature and maximum obtained at 700 °C, which is shown in Figure 3.15. Further increase in calcination temperature to 800 °C for TU2 sample decreases the PL intensity. Hydroxyl radical formed on the surface of TiO_2 are the active species during a photocatalytic reaction and with increase in concentration of hydroxyl radical, photocatalytic activity increased. And also, the PL intensity of hydroxyterephthalic acid is directly proportional to the amount of hydroxyl radicals produced on the surface of TiO_2. Further observation shows that undoped TiO_2 sample, TC exhibit weak PL signal at 700 degree calcination because pure TiO_2 sample almost converted to rutile form in higher temperature calcination. Previous studies showed that lesser number of hydroxyl radicals are produced on the surface of rutile TiO_2 and which results lesser photocatalytic activity.[41]

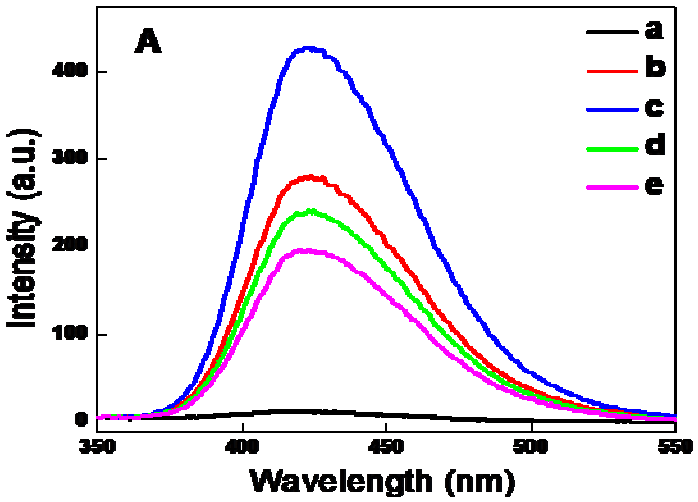

Figure 3.14. PL spectral changes upon UV irradiation of a) TC, b) TU1, c) TU2, d) TU3 and e) TU4 samples at 700 °C in a 10^{-4} M basic solution of terephthalic acid (All the samples were exposed to UV light for 10 minutes).

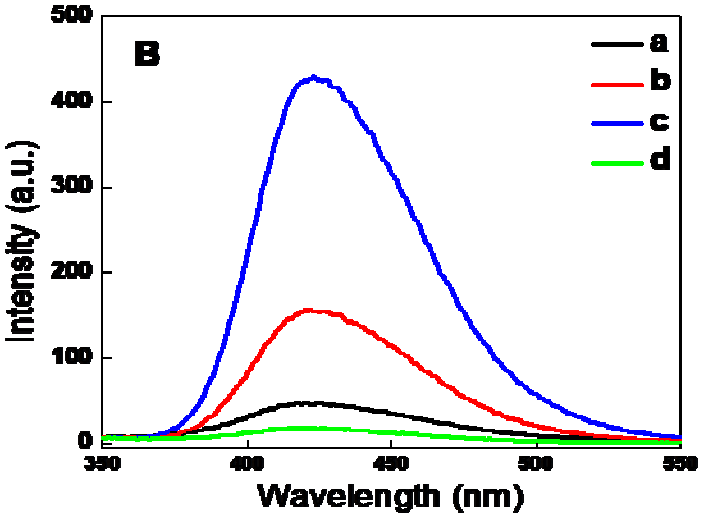

Figure 3.15. PL spectra of TU2 sample at a) 300, b) 500, c) 700 and d) 800 °C in 10^{-4} M basic solution of terephthalic acid (All the samples were exposed to UV light for 10 minutes).

3.2.8. Photocatalysis

To decide which of the prepared sample was the best photocatalyst, photocatalytic degradation study of methylene blue was conducted on each samples calcined at 300, 500 and 700 °C. The photocatalytic experiments were carried out under UV as well as direct solar light. Generally, the photocatalytic degradation reaction of methylene blue follows pseudo first order kinetics. Therefore the reaction rate constants for the degradation were obtained by plotting the natural logarithm of the absorbance against irradiation time for control and thiourea modified sample. In all samples the major peak of methylene blue having absorbance value at a wavelength of 656 nm was taken for the determination of concentration.[42]

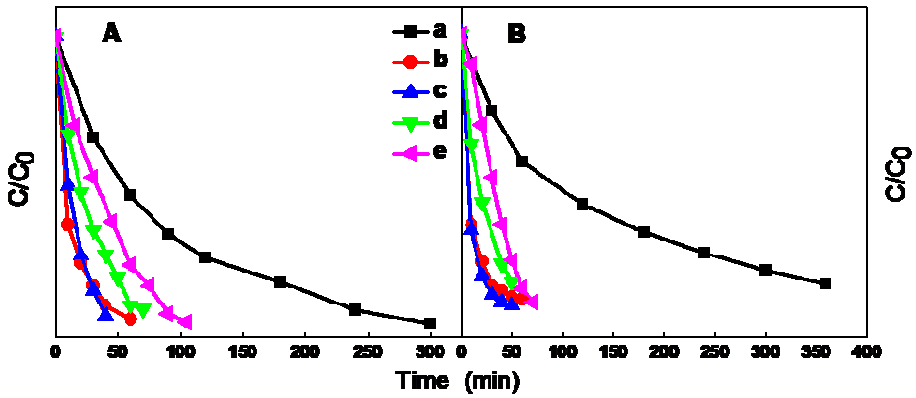

Figure 3.16. Degradation curve of a) TC, b) TU1, c) TU2, d) TU3 and e) TU4 sample calcined at 700 °C A) UV light B) Sunlight.

Figure 3.19 summarizes the reaction rate constant for all the samples calcined at different temperature. The photocatalytic activity of the

doped sample increases with calcination temperature and the optimized temperature for the photocatalytic degradation of methylene blue was found to be at 700 °C. Comparing UV and direct sunlight, rate of degradation under direct sunlight irradiation is more compared to UV light irradiation. This is because upon thiourea doping, TiO_2 extend its absorption range to longer wavelength region and decreases its band gap energy to lower value (Table 3.3).

The optimal level for photocatalytic modification was found in TU2 sample calcined at 700 °C. Figure 3.16 shows the degradation efficiency of methylene blue under both UV and sunlight irradiation using TC and 0.25, 0.5, 1 and 2% thiourea doped TiO_2 calcined at temperature of 700 °C. Figure 3.18 clearly shows that the most photoactive sample is TU2 calcined at 700 °C, degraded methylene blue with a rate constant of 0.0881 min^{-1} under direct sunlight, almost thirteen times greater than undoped sample at the same calcination temperature. However, the rate constant for the degradation of methylene blue of the same sample at 700 °C was 0.0643 min^{-1} under UV light (Figure 3.17), which is lower than rate constant under direct sunlight. For the control sample there is an initial increase in the photocatalytic activity with increase in calcination temperature and then decreases to lower value with further increase in temperature.

Number of factors depends upon photocatalytic degradation efficiency of the catalyst and they are crystallinity, crystallite size, rate of electron-hole recombination, assemblage of crystal phase, amount of hydroxyl radical and optical properties.[38] The synergistic effect of

these various properties determines the photodegradation efficiency of the prepared catalyst.

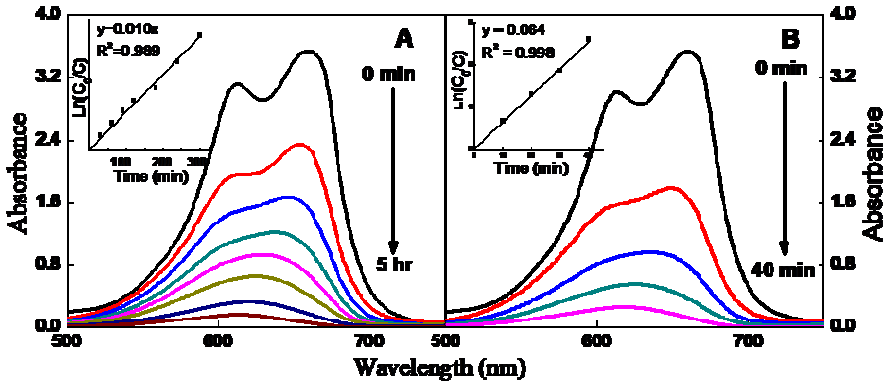

Figure 3.17. Photocatalytic degradation of methylene blue with A) TC and B) TU2 catalyst (700 °C) under UV light.

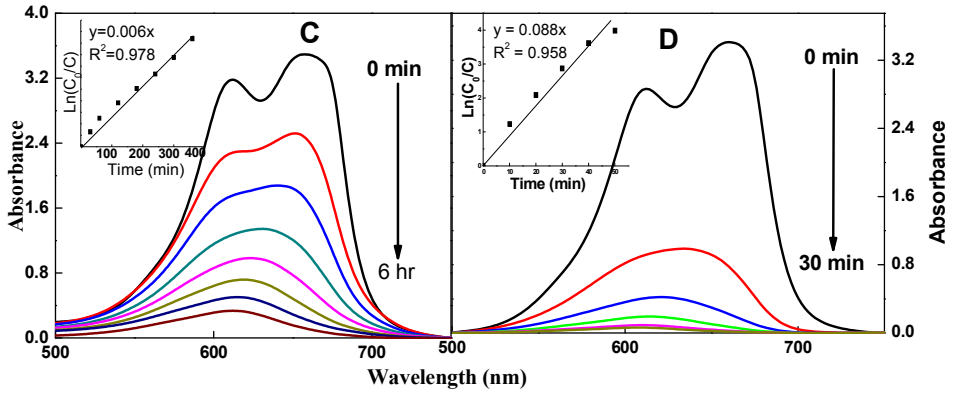

Figure 3.18. Photocatalytic degradation of methylene blue with C) TC and D) TU2 catalyst (700 °C) under direct sunlight.

N, S codoping significantly decreased the crystallite size of the high temperature stable anatase TiO_2 (as evidenced from XRD), especially TU2 sample at 700 °C (Table 3.2), which results higher surface area.

Higher the surface area, greater will be the adsorption rate and the adsorbed dye molecule near the active centers of TiO_2 enhance the photodegradation efficiency of TU2 sample. Secondly, In addition to the smallest crystallite size of TU2 sample, the crystallinity also affects the photocatalytic property of anatase TiO_2. Figure 3.3 clearly shows that as the calcination temperature increases, crystallinity of the sample also increases and highest crystallinity was obtained at 700 °C. Further increase in calcination temperature to 800 °C, rutile phase started to appear along with anatase phase with a phase ratio of 46/54% respectively (Table 3.1). Appearance of rutile phase at 800 °C in TU2 sample decreased the photocatalytic power of TiO_2. And also the decreased photocatalytic activity of the control sample at 700 °C, is due to the appearance of rutile phase as the major component and is evidenced from the XRD pattern of TC sample (Figure 3.2). It has been reported that presence of rutile phase decreased the photoactivity of anatase TiO_2.[41]

The XPS result obtained from Figure 3.11 (red shift in the binding energy peak of O1s and Ti2p upon doping) shows that doping processes can accelerate the formation of oxygen ion vacancies.[4] The oxygen molecule absorbed by the oxygen vacancy sites was active for the formation of superoxide ($O_2^{\bullet-}$) radicals. Similarly the doped nitrogen amount in TU2 sample is very small (Figure 3.10), although N doping expected to introduce more oxygen vacancies at the surface than commonly observed for the anatase surface and which also support the higher degradation efficiency of doped sample.[43,44] The photoactivity of modified TiO_2 was decreased when the concentration

of thiourea increases. Because the content of nitrogen atom doping in TiO_2 increases, which cause an increase in the oxygen vacancies and some oxygen vacancy sites become the recombination center of photo-produced holes and electrons when thiourea concentration increases continuously.[44]

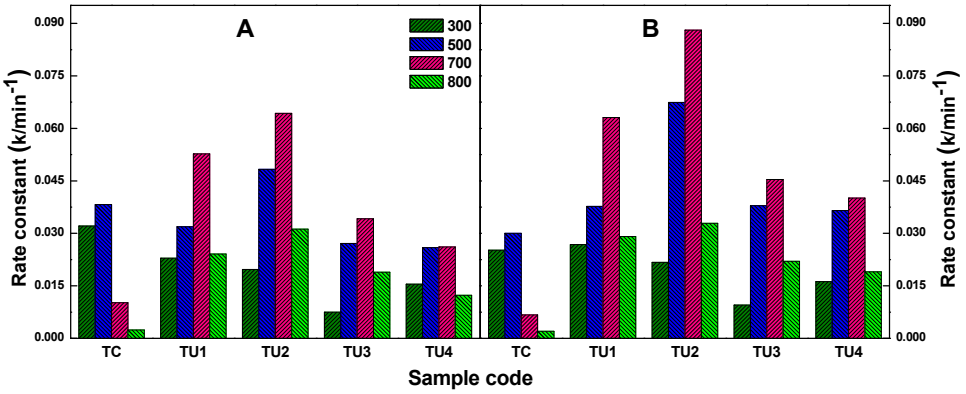

Figure 3.19. Reaction rate constants (k/min-1) for the degradation of methylene blue by various catalyst at different calcination temperature in presence of A) UV and B) direct sunlight.

3.3. Conclusions

N, S codoped TiO_2 were simply prepared by mechanical mixing of the prepared TiO_2 and thiourea. Their structures, optical and photocatalytic properties were characterized by using various characterization techniques such as X-ray diffraction studies, UV–VIS absorption spectroscopy, transmission electron microscopy (TEM) and X-ray photoelectron spectroscopy (XPS). The anatase phase stability was improved through doping and the phase transition occurs only after 700 °C. Whereas, 84% rutile phase was formed in the sample even at 700 °C. The N, S-codoped TiO_2 powder exhibit higher photocatalytic activity under both UV and Visible irradiation as compared to undoped

TiO_2 at a calcinations temperature of 700 °C and the maximum activity was obtained for 0.5 weight percentage of thiourea. The higher activity was ascribed to the synergetic effect of special characteristics such as lowest size, higher crystallinity, lower band gap energy, and oxygen vacancy. The simulation of the results points out that our TU powder is a promising photocatalyst and has a good application for the purification of both air and water.

References

[1] S. U. M. Khan, M. A. Shahry and W. B. InglerJr, Science, 2002, **297**, 2243.

[2] R. Asahi, T. Morikawa, T. Ohwaki, K. Aoki and Y. Taga, Science, 2001, **293**, 269.

[3] Y. Wang, J. Li, P. Peng, T. Lu and L. Wang, Appl. Surf. Sci., 2008, **254**, 5276.

[4] G. Yang, Z. Jiang, H. Shi, M. O. Jones, T. Xiao, P. P. Edwards and Z. Yan, Appl. Catal., B, 2010, **96**, 458.

[5] H. Sun, Y. Bai, Y. Cheng, W. Jin and N. Xu, Ind. Eng. Chem. Res., 2006, **45**, 4971.

[6] Y. E. Filinchuk, V. V. Oliinik, T. Glovyak and M. G. Mys'kiv, Russ. J. Coord. Chem., 2001, **27**, 139.

[7] H. Uggerud and W. Lund, J. Anal. At. Spectrom., 1995, **10**, 405.

[8] S. J. Connon, Chem. Commun., 2008, **0**, 2499.

[9] A. M. ShamsElDin, A. A. ElHosary, R. M. Saleh and J. M. A. Kader, Mater. Corros., 1977, **28**, 26.

[10] S. Sakthivel, M. Janczarek and H. Kisch, J. Phys. Chem. B, 2004, **108**, 19384.

[11] F. Wei, L. Ni and P. Cui, J. Hazard. Mater., 2008, **156**, 135.

[12] T. Ohno, M. Akiyoshi, T. Umebayashi, K. Asai, T. Mitsui and M. Matsumura, Appl. Catal., A, 2004, **265**, 115.

[13] R. Bacsa, J. Kiwi, T. Ohno, P. Albers and V. Nadtochenko, J. Phys. Chem. B, 2005, **109**, 5994.

[14] P. Periyat, S. C. Pillai, D. E. McCormack, J. Colreavy and S. J. Hinder, J. Phys. Chem. C, 2008, **112**, 7644.

[15] J. C. Yu, J. Yu, W. Ho, Z. Jiang and L. Zhang, Chem. Mater. 2002, **14**, 3808.

[16] D. Huang, S. Liao, S. Quan, L. Liu, Z. He, J. Wan and W. Zhou, J. Mater. Res., 2007, **22**, 2389.

[17] P. Cheng, J. Qiu, M. Gu, W. Shangguan, Mater. Lett., 2004, **58**, 3751.

[18] Y. Huo, Y. Jin, J. Zhu, H. Li, Appl. Catal. B, 2009, **89**, 543.

[19] X. Wang, J. C. Yu, P. Liua, X. Wanga, W. Sua and X. Fu, J. Photochem. Photobiol., A, 2006, **179**, 339.

[20] L. Ren, X. Huang, F. Sun and X. He, Mater.Lett., 2007, **61**, 427.

[21] G. A. Tompsett, G. A. Bowmaker, R. P. Cooney, J. B. Metson, K. A. Rodgers and J. M. Seakins, J. Raman Spectro., 1995, **26**, 57.

[22] Y. Hu, H. L. Tsai and C.L. Huang, J. Eur. Ceram. Soc., 2003, **23**, 691.

[23] S. P. S. Porto, P. A. Fluery and T. C. Damen, Phys. Rev., 1967, **154**, 522.

[24] Y. Hara and M. Nicol , Phys. Status. Solidi B, 1979, **94**, 317.

[25] U. Balachandran and N. G. Eror, J Solid State Chem., 1982, **42**, 276.

[26] W. Ma, Z. Lu and M. Zhang, Appl. Phys. A, 1998, **66**, 621.

[27] Z. M. Shi, X. Y. Ye, K. M. Liang, S. R. Gu and F. Pan, J. Mater. Sci. Lett., 2003, **22**, 1255.

[28] S. C. Pillai, P. Periyat, R. George, D. E. McCormack, M. K. Seery, H. Hayden, J. Colreavy, D. Corr and S. J. Hinder, J. Phys. Chem. C, 2007, **111**, 1605.

[29] G. Colon, M. C. Hidalgo, G. Munuera, I. Ferino, M. G. Cutrufello and J. A. Navio, Appl. Catal. B: Environ., 2006, **63**, 45.

[30] J. C. Yu, W. Ho, J. Yu, H. Yip, P. K. Wongn and Zhao, J. Environ. Sci. Technol., 2005, **39**, 1175.

[31] A. Fujishima, X. Zhang and D. A. Tryk, Surf. Sci. Rep., 2008, **63**, 515.

[32] J. Wang, D. N. Tafen, J. P. Lewis, Z. Hong, A. Manivannan, M. Zhi, M. Li and N. Wu, J. Am. Chem. Soc., 2009, **131**, 12290.

[33] H. Irie, Y. Watanabe and K. Hashimoto, J. Phys. Chem. B, 2003, **107**, 5483.

[34] X. Chen, Y. Lou, A. C. S. Samia, C. Burda and J. L. Gole, Adv. Funt. Mater., 2005, **15**, 41.

[35] P. Periyat, D. E. McCormack, S. J. Hinder and S. C. Pillai, J. Phys. Chem. C, 2009, **113**, 3246.

[36] A. K. Rumaiz, B. Ali , A. Ceylan, M. Boggs, T. Beebe and S. I. Shah, Solid State Commun., 2007, **144**, 334.

[37] J. Yu, M. Zhou, B. Cheng and X. Zhao, J. Mol. Catal. A: Chem., 2006, **246**, 176.

[38] F. Dong, W. Zhao and Z. Wu, Nanotechnology, 2008, **19**, 365607.

[39] Q. Xiang, J. Yu and M. Jaroniec, Phys. Chem. Chem. Phys., 2011, **13**, 4853.

[40] D. Li, H. Haneda, S. Hishita and N. Ohashi, Chem. Mater., 2005, **17**, 2596.

[41] A. Sclafani and J. M. Herrmann, J. Phys. Chem., 1996, **100**, 13655.

[42] K. V. Baiju, P. Periyat, W. Wunderlich, P. K. Pillai, P. Mukundan and K. G. K. Warrier, J Sol-Gel Sci Technol, 2007, **43**, 283.

[43] Y. Li, C. Xie, S. Peng, G. Lu and S. Li, J. Mol. Catal. A: Chem., 2008, **282**, 117.

[44] J. Geng, D. Yang, J. Zhu, D. Chen and Z. Jiang, Mater. Res. Bull., 2009, **44**, 146.

CHAPTER 4
Synthesis of solar active TiO_2 photocatalyst modified using thiosemicarbazide

CONTENTS

4.1. Introduction

In continuation to chapter 3, which describe the photocatalytic activity of N, S-codoped TiO_2 using thiourea, chapter 4 modified the TiO_2 sample using a different N and S containing modifier such as thiosemicarbazide. To the best of my knowledge, there is no study available in the literature by using thiosemicarbazide as the modifier to improve the photocatalytic efficiency of TiO_2. The existing literature shows that N and S containing modifiers are the best to enhance the photocatalytic efficiency of TiO_2.

In the present chapter, TiO_2 was modified by mixing the synthesized TiO_2 and thiosemicarbazide in different molar ratio by keeping the concentration of TiO_2 as constant.

The samples were labelled as TSC1, TSC2, TSC3 and TSC4 respectively for 0.25, 0.5, 1 and 2 weight percentage of thiosemicarbazide. The starting TiO_2 used for the modification was taken as the control sample and were named as TC.

The chapter investigate the photocatalytic activity of TiO_2 modified by sintering with thiosemicarbazide under excitation with UV (5.82 mW/cm^2) and direct sunlight (63.2-67.9 mW/cm^2). We chose the oxidation of methylene blue dye to carbon dioxide and water as model reaction.

4.2. Results and Discussion

4.2.1. X-ray diffraction analysis

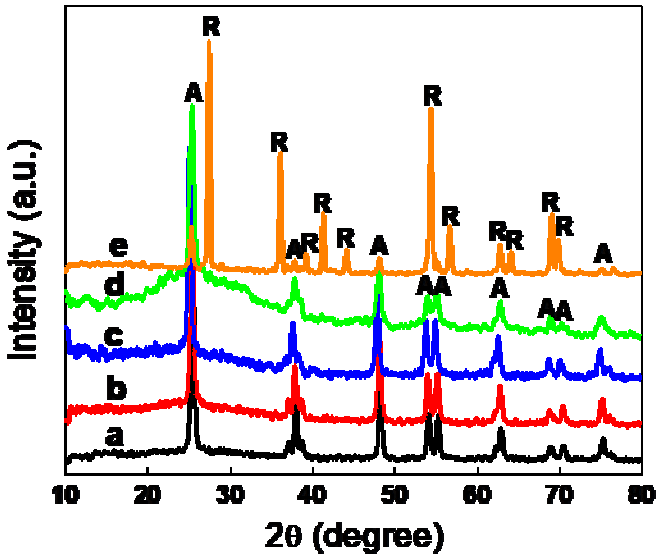

Figure 4.1. XRD pattern of a) TSC1, b) TSC2, c) TSC3, d) TSC4 and e) TC at 700 °C.

Figure 4.1 shows the x-ray diffraction pattern of the modified and control sample at 700 degree calcination temperature. Figure 4.2 presents the diffractogram of the TSC3 sample calcined at different temperature in air. It can be observed that the most photoactive crystalline anatase phase has been retained in 100% for all modified samples even at a calcination temperature of 700 °C. Whereas the control sample TC were almost converted to rutile phase at the same temperature. Furthermore, as the temperature of calcination increases, the main Bragg peak at (101) plane of anatase is observed to become

intense and sharper, indicative larger average crystalline size and higher crystalline nature for the entire codoped sample up to 700 °C. Further increase in calcination temperature of TSC3 sample started to transform the anatase to rutile form and 51.5% anatase structure was retained at a calcination temperature of 800 °C. Prior reports substantiate that doping of TiO_2 using N and S will not induce the phase transformation at lower temperatures. Similarly the X-ray diffraction pattern of any N, S codoped powder does not show any sign of brookite phase, whereas, the control sample TC exhibit brookite phase along with anatase at a temperature of 300 and 500 °C (Figure 4.3).

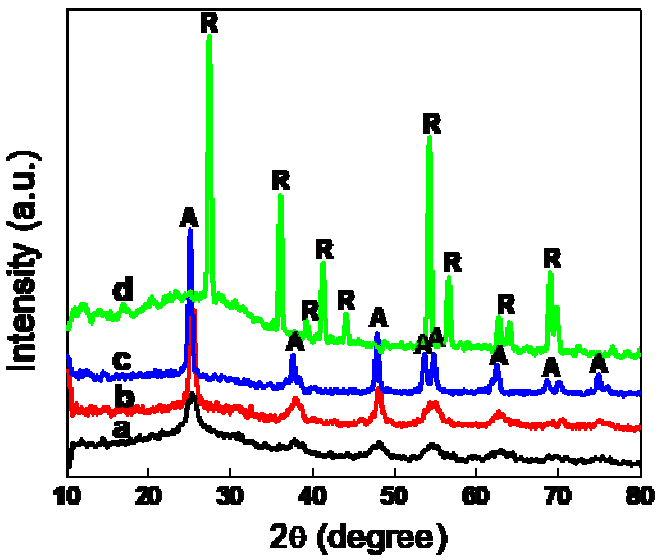

Figure 4.2. XRD of TSC3 sample at a) 300, b) 500, c) 700 and d) 800 °C.

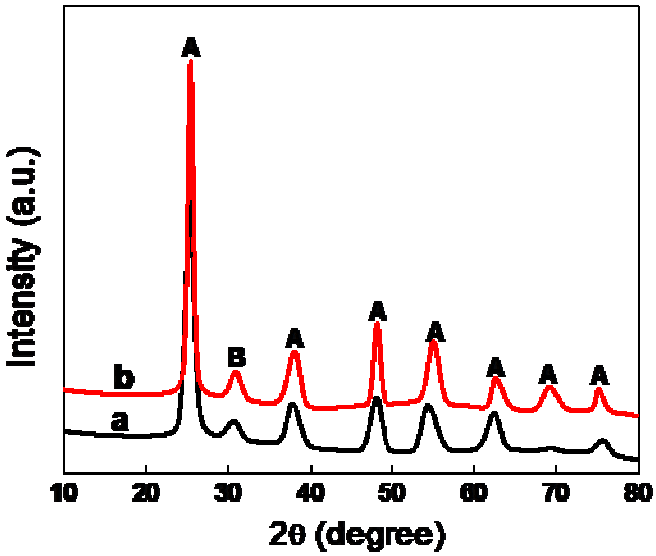

Figure 4.3. X-ray diffraction pattern of TC at a) 300 and b) 500 °C.

From Table 4.1, it can be obtained that the particle size decreased with increase in concentration of thiosemicarbazide and increased with increase in calcination temperature. However, as the concentration of dopant increases, the crystallinity of anatase peak also increases and reached maximum crystallinity at 1 wt % thiosemicarbazide. Further increase in concentarion of dopant decrease the crystalline nature of TSC sample as observed in Figure 4.1.

Table 4.1. Crystallite size calculated from the (101) peak of anatase at different calcination temperature.

Sample	Crystallite size (nm)		
	300	**500**	**700**
TC	7.25	13.6	32.1
TSC1	6.52	12.47	22.28
TSC2	6.29	12.44	22.22
TSC3	6.08	9.05	20.25
TSC4	4.92	8.52	19.9

4.2.2. FTIR spectra

The structure of thiosemicarbazide on the surface of TiO_2 was also examined by Fourier transform technique. FTIR spectra of the doped and undoped sample ranging from 400 to 4000 cm^{-1} are shown in Figure 4.4. The FTIR peak below 1000 cm^{-1} corresponds to TiO_2 crystal lattice vibration.[1] The broad peak centered at 3400 cm^{-1} and a sharp peak at 1630 cm^{-1} corresponds to the stretching and bending vibrations of –OH or adsorbed water molecule respectively. [2,3] Two absorption peaks within a region of 1000-1300 cm^{-1} were present in the spectra of doped sample, but absent in the control sample TC. These two peaks positioned at 1051 and 1136 cm^{-1} were found to be the characteristic frequencies of bidentate SO_4^{2-} group coordinated to Ti^{4+} ion.[4,5] Ammonium ions produced by the dissociation of thiosemicarbazide were also found in the TU2 matrix positioned at 1411 cm^{-1}, which indicate the deformation mode of ammonium ions.[6]

The result obtained from FT-IR technique is in good agreement with the observed XPS data.

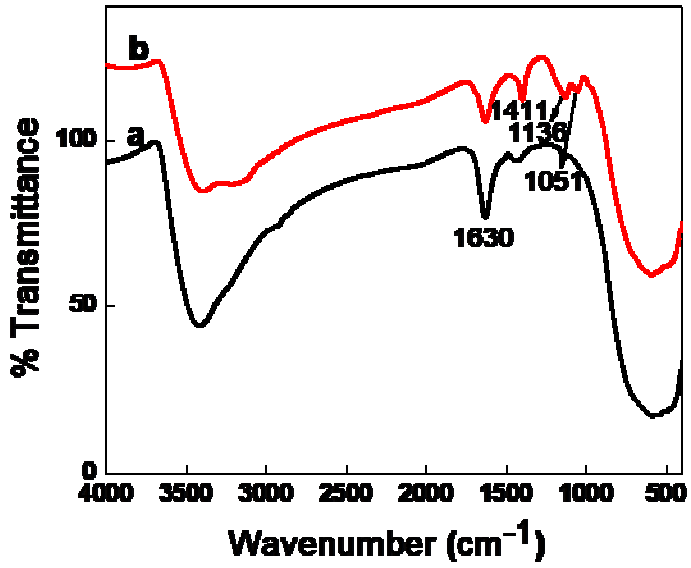

Figure 4.4. FTIR spectra of a) TC and b) TSC3 sample calcined at 300 °C.

4.2.3. Raman spectra

In Raman spectroscopy, anatase to rutile phase transition can be observed since the two phases have well distinguishable finger prints in the Raman spectra. Figure 4.5 shows the changes in the Raman spectra of the TiO_2 powder before and after doping at various calcination temperatures. Two intense peaks of E_g observed at 144 and 639 cm^{-1}, and two weaker peaks of $B1_g$ at about 399 cm^{-1} and (A_{1g}+B_{1g}) at about 513 cm^{-1} are seen as the characteristic Raman active modes of anatase

crystal.[7] Generally, Raman active modes of rutile phase were observed at 143, 447, 612 and 826 cm^{-1}.

It can be seen from figure 4.5A that the strongest Eg mode of anatase at 144 cm^{-1} of the control sample TC is attenuated when the rutile modes at 447 and 612 cm^{-1} intensify at a calcination temperature of 700 $^{\circ}C$, which clearly shows the transformation of anatase to rutile phase. However, in the case of doped sample, rutile phase started to appear only at 800 °C (Figure 4.5B). The data obtained from Raman spectroscopy clearly support the anatase/rutile phase composition as observed from x-ray diffraction technique in different calcination temperature. Raman spectra of the control sample in different calcination temperature can be seen in Figure 4.6.

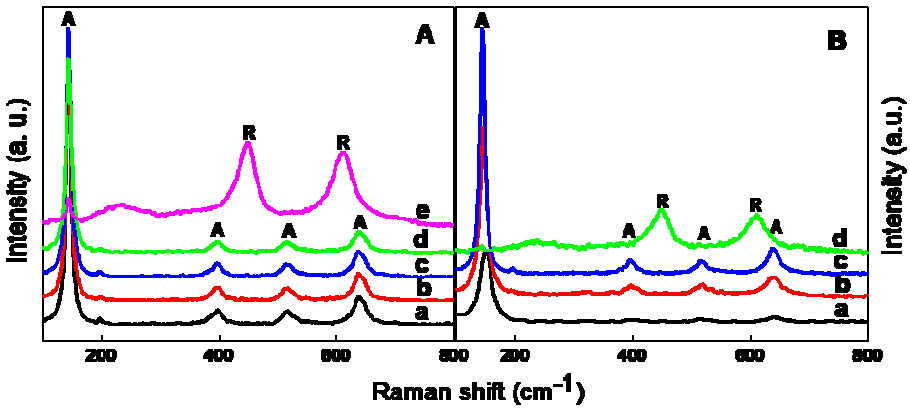

Figure 4.5. Raman spectra of – A): a) TSC1, b) TSC2, c) TSC3, d) TSC4 & e) TC calcined at 700 °C and B): TSC3 calcined at a) 300, b) 500, c) 700 and d) 800 °C.

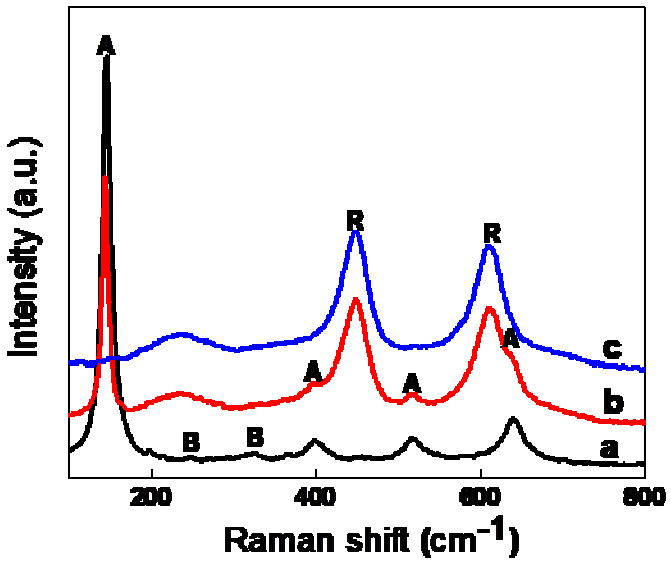

Figure 4.6. Raman spectra of TC sample at a) 500, b) 700 and c) 800 °C

4.2.4. TEM

Particle size, crystallinity and morphology of samples obtained from XRD were corroborated by TEM, HRTEM and SAED investigations in Figure 4.7. The crystallite size obtained from the TEM images of undoped sample (20-60 nm) reveal that the samples are in rutile form at 700 degree calcination temperature. However, modification using thiosemicarbazide sustain TiO_2 in anatase structure at 700 $^{\circ}$C and the supporting information can be obtained from the crystal size (20-25 nm) in the TEM images of TSC3 sample. Similarly, the fringe width obtained from the HRTEM images of doped and undoped sample also support the anatase and rutile structure respectively (Figure 4.7 C and D). SAED pattern of both TC and TSC3 sample support the crystalline nature as observed from the x-ray diffraction technique. Additionally, well defined diffraction spots exist in the SAED pattern of TSC3 at

700 °C compared to TC at the same temperature further support the higher crystalline nature of the sample.

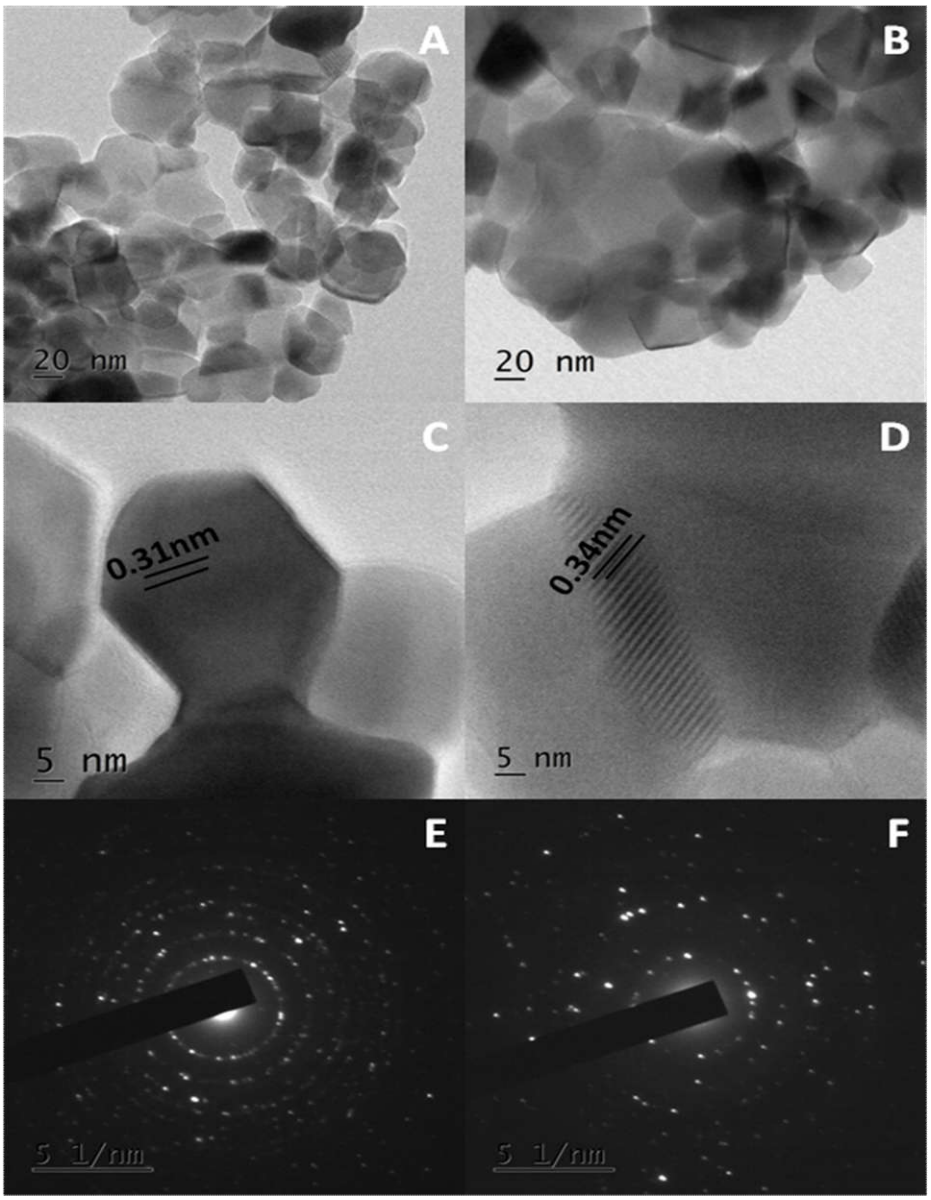

Figure 4.7. TEM image of A) TC, B) TSC3, HRTEM images of C) TC, D) TSC3 and SAED pattern of E) TC and TSC3 (both the samples were calcined at 700 °C).

4.2.5. XPS analysis

Figure 4.8 shows the XPS survey spectra of the N, S codoped and undoped samples calcined at 700 °C. It can be seen that the undoped sample contain only Ti, O and C elements, with a sharp photoelectron peaks obtained at binding energies of 458.8 (Ti2p), 530.08 (O1s) and 284 eV (C1s). The carbon peak in the TC sample is mainly due to the residual carbon from the precursor molecule and adventitious hydrocarbon from XPS instrument itself. In addition to the amount of carbon in TC, increased intensity peak of C1s is observed for TSC sample due to the incorporation of carbon from the modifier itself as solid solution. [8,9] On the contrary, the codoped sample TSC not only contains C, O and Ti, but also a small amount of S and N atoms (binding energy peak at 400.2 and 168.4 eV, respectively), which probably comes from the precursor CS (NH_2) ($NHNH_2$) during the calcination.

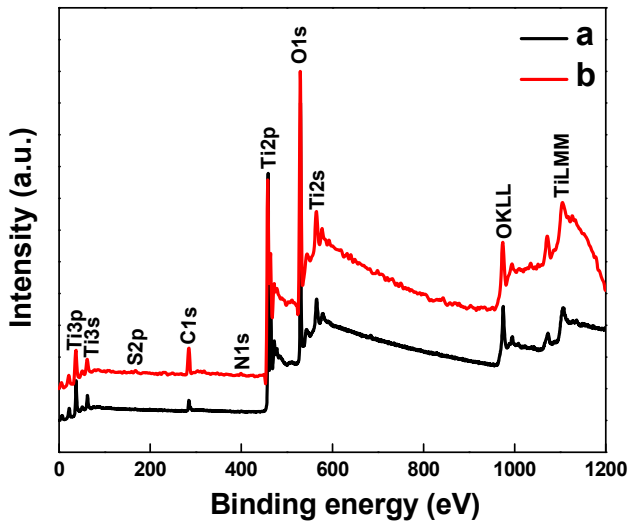

Figure 4.8. XPS survey spectra of a) TC and b) TSC3 calcined at 700 °C.

The high resolution XPS spectra of N1s region of TSC3 sample are shown in Figure 4.9 at a binding energy peak of 400.2 eV and which can be assign to some NH_3 molecule adsorbed on the surface of TiO_2.[10] The state of nitrogen in the TiO_2 crystal lattice and the mechanism behind the band gap reduction has still been in arguing. Satish et al have observed N1s core level at 398.2 eV from the XPS spectra of N-doped TiO_2 and suggested that there is no indication for the formation of Ti-N bond due to nitrogen doping.[11] Some studies observed that the N1s peak at 400 and 402 eV on nitrogen doped TiO_2 is due to chemisorbed nitrogen and adsorbed organic impurities. [12,13] However, Diwald *et al* suggested that the observed binding energy peak of N1s at 399.6 eV is in effective for reducing the photon energy for solar applications.[14] In all the above observations, the adopted preparation procedure was different and which result different observation in XPS.

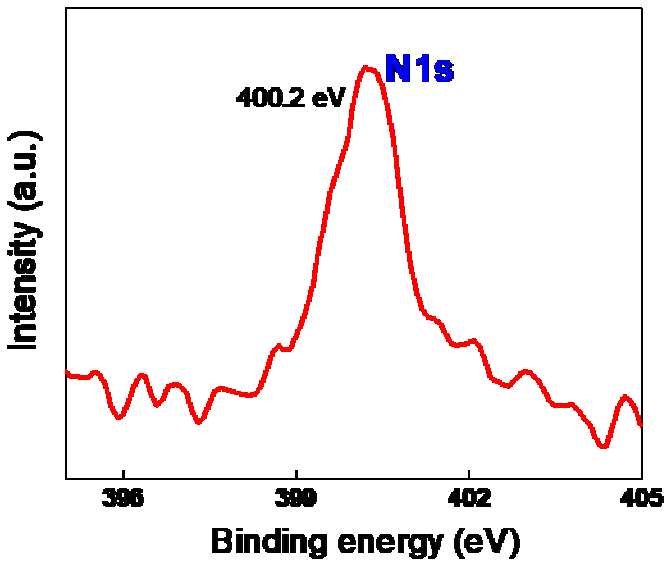

Figure 4.9. High resolution XPS spectra of N1s of TSC3 sample calcined at 700 °C.

Figure 4.10 shows the high-resolution XPS spectrum of S2p region of TSC3 sample at 700 °C. It could be noticed that the S2p peak of doped TiO_2 contain an isolated peak at binding energies of 168.4 eV, which uphold the existence of sulphur in +6 oxidation state. The S^{6+} may be attributed to adsorbed SO_4^{2-} ion on the surface of TSC sample. Similarly different observation has been made by Xiang *et al* that cationic sulphur may replace titanium atom from the lattice of TiO_2.[15] Absence of peak at 162 eV indicates the absence of Ti-S bond formation.

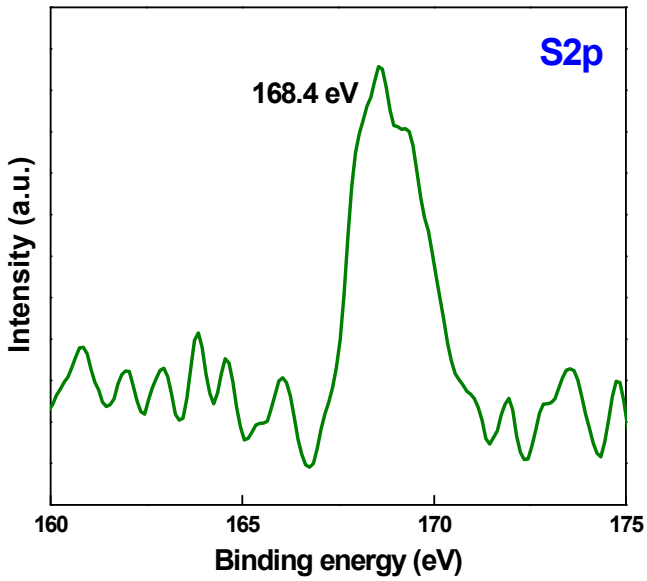

Figure 4.10. High resolution XPS spectra of S2p of TSC3 sample calcined at 700 °C.

The binding energy peak of Ti2p in the TSC3 sample at 700 °C negatively shifted to 458.4 eV from the BE peak of TC (458.8 eV) at same temperature calcination (Figure 4.11A). Correspondingly, the binding energy value of O1s of TC (430.08 eV) deviated negatively to

429.7 eV through doping (Figure 4.11B). The red shift in the above two BE peaks are considered to be due to the oxygen vacancy produced because of the specific interactions between TiO_2 and N or S at high temperature calcination. Charge imbalance produced by the replacement of Ti^{4+} by S^{6+} also induces an oxygen vacancy site in the TiO_2 matrix.

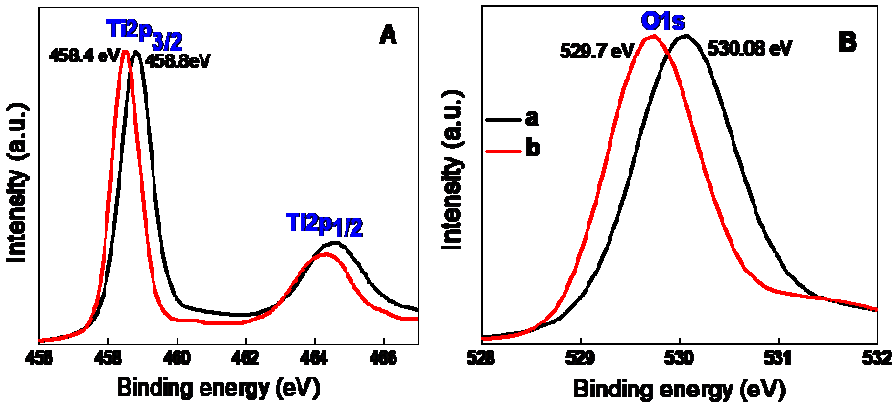

Figure 4.11. High resolution XPS spectra of A) Ti2p and B) O1s of a) TC and b) TSC3 sample at 700 °C

4.2.6. Optical characterization

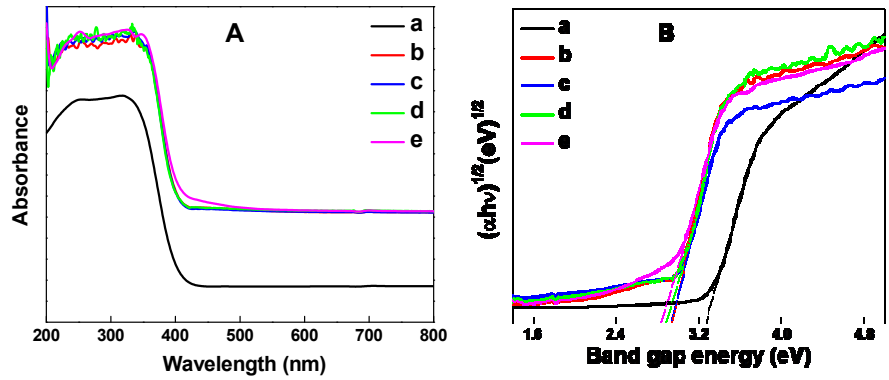

Figure 4.12. A) UV-Vis absorption spectra and B) corresponding Tauc plot of a) TC, b) TSC1, c) TSC2, d) TSC3 and e) TSC4 (all the samples were calcined at 700 °C).

UV-visible absorption spectra of TSC and TC samples calcined at a temperature of 700 °C are shown in Figure 4.12. Generally, doping with non metals induce a shift in the light absorption characteristics of TiO_2.[1] The optical absorption edge in the spectra clearly indicates a red-shift and hence a band gap narrowing for TSC samples compared to pure TiO_2. The reason behind this red shift in the absorption is due to two prominent features: (1) one being the presence of N atom, which tends to absorb the radiation within a wavelength ranging from 390 to 500 nm by the TiO_2 molecule,[16] (2) Synergistic effect of both N and S induce an extended absorption for the TiO_2 system in the range of 500-800 nm.[15] These two peaks clearly be seen in the doped TiO_2 matrix at low temperature calcination (Figure 4.13) due to increased amount of both N and S and this is the reason for why doped sample exhibit lower band gap energy at 300 °C than at 500 than 700 °C (Table 4.2).[17] Similarly, increased amount of N and S with increase in concentration of dopant raise the energy of absorption. Absence of both N and S in the pure TiO_2 sample results higher bandgap energy corresponding to UV region.

Table 4.2. Bandgap energy of TSC and TC samples at various calcination temperatures.

Sample	Band gap energy (eV)		
	300	**500**	**700**
TC	3.26	3.22	3.24
TSC1	2.76	2.83	2.92
TSC2	2.73	2.82	2.92
TSC3	2.51	2.63	2.89
TSC4	1.47	2.57	2.85

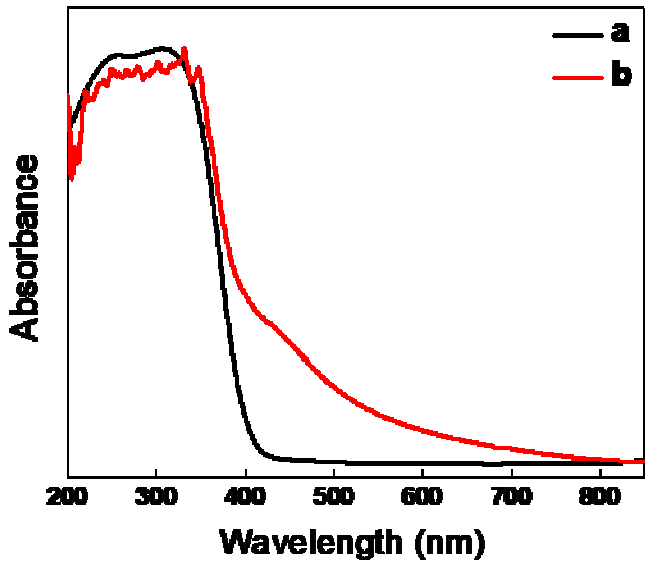

Figure 4.13. UV-Vis absorption spectra of a) TC and b) TSC sample at 300 °C.

4.2.7. Measurement of hydroxyl radical

The higher activity of the prepared TSC3 sample at 700 °C was further confirmed by the detection of hydroxyl radicals. Figure 4.14A shows the changes in PL intensity of terephthalic acid solution by various TC and TSC samples calcined at 700 °C exposed for 10 minutes to UV light. Changes in the PL intensity at about 425 nm is observed corresponding to hydroxyterephthalic acid by varying the concentration of thiosemicarbazide on TiO_2 sample and the maximum intensity was observed for TSC3 sample at 700 °C having 1 wt% of thiosemicarbazide, which showed maximum photocatalytic activity. Similarly, PL intensity of TSC3 sample increases with rise in calcination temperature and maximum obtained at 700 °C, which is shown in Figure 4.14B. Further increase in calcination temperature to

800 °C for TSC3 sample decreases the PL intensity. Hydroxyl radical formed on the surface of TiO_2 are the active species during a photocatalytic reaction and with increase in concentration of hydroxyl radical, photocatalytic activity increased.[18,19] And also, the PL intensity of hydroxyterephthalic acid is directly proportional to the amount of hydroxyl radicals produced on the surface of TiO_2. Similarly, the number of hydroxyl radical produced on the surface of TiO_2 was increased with time and are represented in Figure 4.15. Further observation shows that undoped TiO_2 sample, TC exhibit weak PL signal at 700 degree calcination because pure TiO_2 sample almost converted to rutile form in higher temperature calcination. Previous studies showed that lesser number of hydroxyl radicals is produced on the surface of rutile TiO_2 and which results lesser photocatalytic activity.[20]

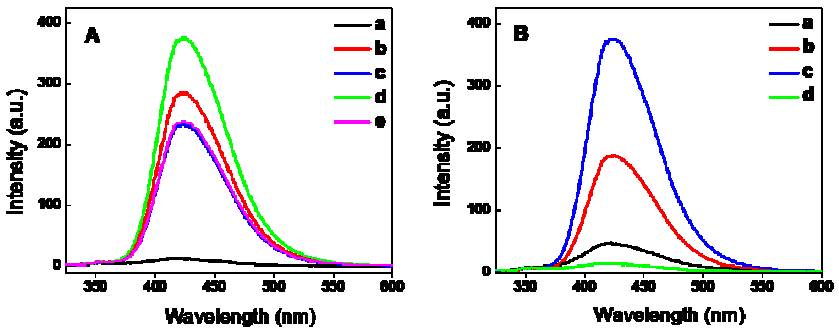

Figure 4.14. (A) PL spectral changes upon UV irradiation of a) TC, b) TSC1, c) TSC2, d) TSC3 and e) TSC4 samples at 700 °C in a 10^{-4} M basic solution of terephthalic acid and (B) PL spectra of TSC3 sample at a) 300, b) 500, c) 700 and d) 800 degree calcination temperature in 10^{-4} M basic solution of terephthalic acid (All the samples were exposed to UV light for 10 minutes).

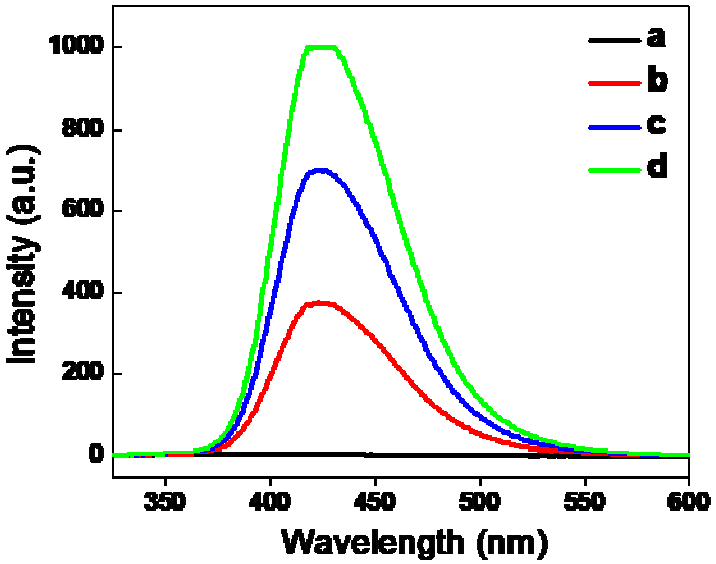

Figure 4.15. PL spectral changes observed during illumination time of a) 0 min, b) 10 min, c) 20 min and d) 30 min of TSC3 sample calcined at 700 °C in a basic solution of terephthalic acid.

4.2.8. Photocatalysis

The photocatalytic studies were conducted by measuring the degradation rate of methylene blue at regular time interval. The concentration of methylene blue does not change under dark using various synthesized TiO_2 samples. Similarly, Illumination of MB in the absence of TiO_2 powder does not result a photocatalytic reaction. Therefore, both light and catalytic powder is necessary for efficient photocatalytic degradation. Figure 4.16 shows the photocatalytic degradation pattern of MB using various catalytic systems calcined at 700 °C under both UV and direct sunlight. The observed degradation pattern follows pseudo first order kinetics and the corresponding reaction rate constant values of the prepared catalyst at various calcination temperatures are graphically represented in Figure 4.18. It

is observed that the TSC3 sample at 700 °C possessed highest photocatalytic activity with a rate constant value of 0.064 min^{-1} under direct sunlight and 0.0487 min^{-1} under UV irradiance (Figure 4.17 B and D). For TC at 700 °C, the rate constant value under UV irradiation (0.0102 min^{-1}) is higher than that under sunlight (0.0067 min^{-1}) to some extent (Figure 4.17 A and C). Moreover, TC displays poor photodegradation ability than the doped one under both UV and sunlight. Figure 4.17 shows the absorption spectra and corresponding kinetic analysis of MB degradation using TSC3 and TC sample at 700 °C.

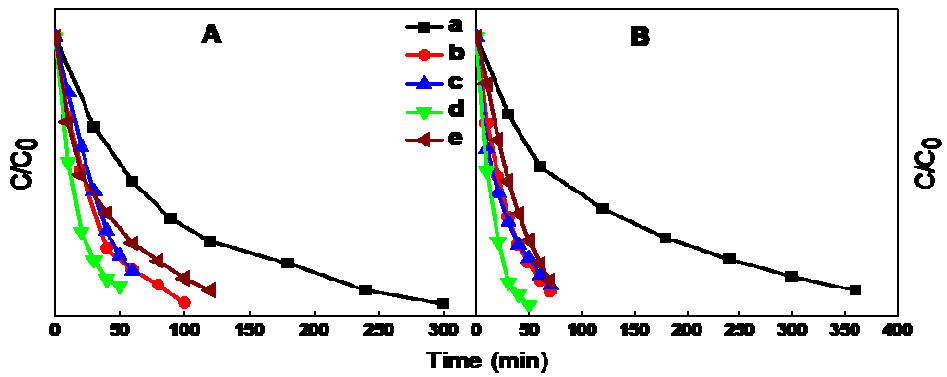

Figure 4.16. Photodegradation pattern of methylene blue using a) TC, b) TSC1, c) TSC2, d) TSC3 and e) TSC4 at 700°C under A) UV and B) direct sunlight.

Result obtained from XPS, XRD and FTIR technique revealed that N and S were perfectly codoped into the lattice of TiO_2 as in the form of SO_4^{2-} and chemisorbed nitrogen. The adsorbed SO_4^{2-} improves the surface acidity and generates Bronsted and Lewis acidic sites on the surface of TiO_2. These acidic sites could provide more chemisorption centers on the surface to adsorb more reactants and oxygen molecules,

also trap excited electrons, which would enhance the separation of photo-generated charge carriers and improve the photocatalytic effieciency.[1,4] The diffuse reflectance spectra in Figure 4.12 clearly shows that N and S codoping narrow the band gap of TiO_2 because of an obvious shift observed in the absorption edge of TSC sample and did improve the wavelength of absorption in the visible region. And which results an enhanced photodegradation in sunlight than UV light. In addition to these, N-doping results the creation of surface oxygen vacancies and these oxygen deficient sites boost the photocatalytic power of TSC samples.

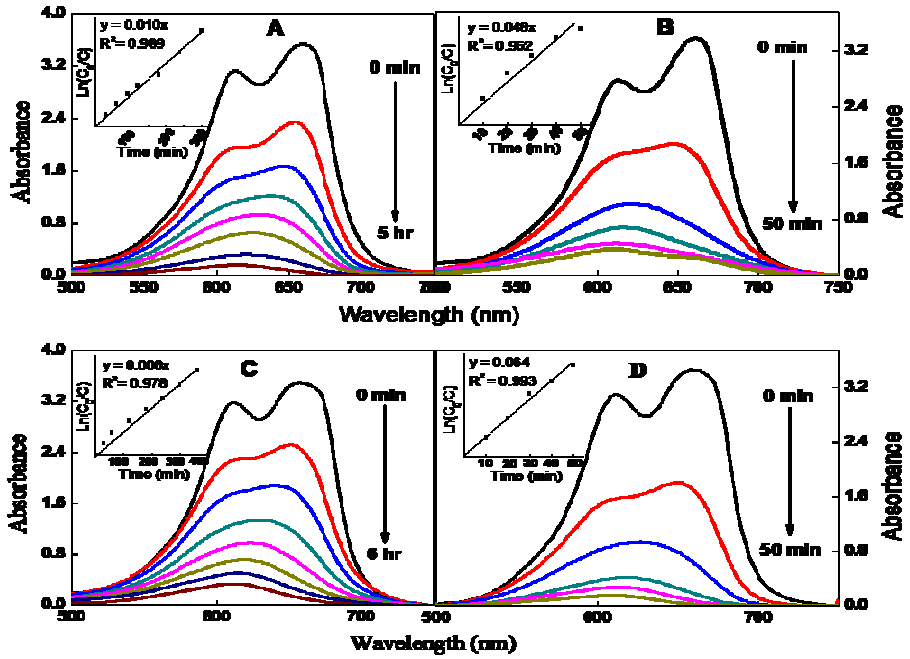

Figure 4.17. Absorption spectra of MB degradation using (A & C) TC and (B & D) TSC3 sample at 700 °C (A, B carried out under UV and C, D under direct sunlight)- Inset shows the corresponding kinetic study of the sample, where C_0 is the initial absorbance and C represents the absorbance after a time for MB degradation.

Many studies have shown that calcination is an effective treatment method to enhance the photoactivity of nanosized TiO_2 photocatalysts.[21] Figure 4.18 shows the dependence of the apparent rate constants (k/min^{-1}) on calcination temperature. The reaction rate constant value of the doped sample increases with raise in temperature and at a calcination temperature of 700 °C, the k value of TSC sample reaches the highest value under UV as well as direct sunlight. Calcination temperature of doped sample above 700 °C is not desirable and samples calcined at 800 °C exhibit poor photocatalytic activity. Such a high temperature treatment, would transform anatase TiO_2 into rutile structure and in the case of control sample, this transformation occur already at 700 °C. So the least photocatalytic activity has been exhibited by the control sample at 700 °C (Figure 4.17 A and C). Previous reports suggested that appearance of rutile structure decreased the photoactivity of TiO_2.

As observed from Figure 4.18, the best photocatalyst is found to be TSC3 sample at 700 degree calcination temperature and the highest activity is attributed to the above mentioned sample is due to the synergistic effect of its characteristic features such as higher crystallinity, smallest crystallite size, 100% anatase structure, higher concentration of hydroxyl molecule on the surface of TiO_2 and lower electron-hole recombination rate.

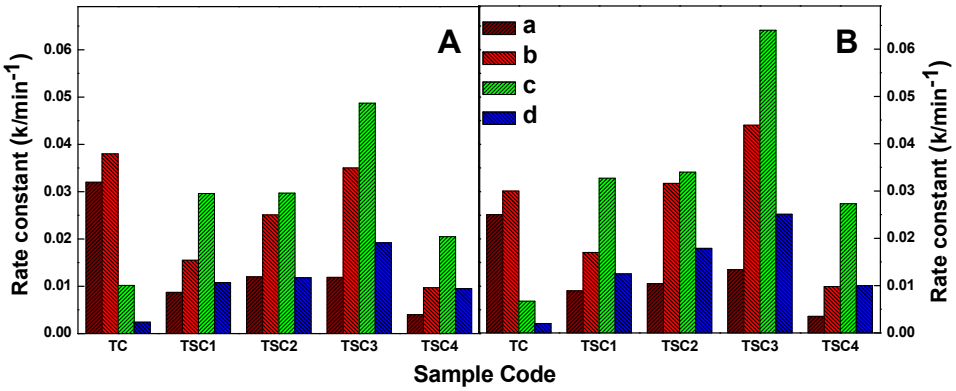

Figure 4.18. Bar diagram that shows the reaction rate constant for the degradation of MB using various synthesized photocatalyst at a) 300, b) 500, c) 700 and d) 800 °C in presence of A) UV and B) direct sunlight.

4.3. Conclusion

N, S-modified TiO_2 powders have been successfully synthesized by stirring the sol-gel derived anatase TiO_2 with the modifier, thiosemicarbazide. The obtained slurry were dried at 100 °C and then calcined at different temperature. The phase composition, size and morphology of the synthesized powder were investigated using various techniques such as XRD, XPS, FTIR, UV-Vis spectroscopy etc. The absorption spectra of the prepared powder shifted from UV to visible region in accordance to the introduction of dopant. Diffractogram of the modified sample revealed that, thiosemicarbazide extend anatase to rutile phase transition temperature, decrease crystal size and improve the crystallinity of anatase TiO_2. Photocatalytic studies showed that, at 700 °C, N, S codoped TiO_2 powders were most effective for the degradation of methylene blue than the control sample.

References

[1] F. Wei, L. Ni and P. Cui, J. Hazard. Mater., 2008, **156**, 135.

[2] D. C. M. Dutoit, M. Scmeider and A. Baiker, J. Catal., 1995, **153**, 165.

[3] J. Rubio, J. L. Oteo and M. Villegas, J. Mater. Sci., 1997, **32**, 643.

[4] X. C. Wang, J. C. Yu, P. Liu, X. Wang, W. Su and X. Fu, J. Photochem. Photobiol., A, 2006, **179**, 339.

[5] R. Bacsa, J. Kiwi, T. Ohno, P. Albers and V. Nadtochenko, J. Phys. Chem. B, 2005, **109**, 5994.

[6] L. Ren, X. T. Huang, F. L. Sun and X. He, Mater. Lett., 2007, **61**, 427.

[7] Z. Wang and S.K. Saxena, Solid State Commu., 2001, **118**, 75.

[8] S. C. Pillai, P. Periyat, R. George, D. E. McCormack, M. K. Seery, H. Hayden, J. Colreavy, D. Corr and S. J. Hinder, J. Phys. Chem. C, 2007, **111**, 1605.

[9] Z. M. Shi, X. Y. Ye, K. M. Liang, S. R. Gu and F. Pan, J. Mater. Sci. Lett., 2003, **22**, 1255.

[10] J. G. Yu, M. H. Zhou, B. Cheng, X. J. Zhao, J. Mol. Catal. A, 2006, **246**, 176.

[11] M. Sathish, B. Viswanathan, R. P. Viswanath and C. S. Gopinath, Chem Mater, 2005, **17**, 6349.

[12] X. Li, R. Xiong and G. Wei, Catal Lett, 2008, **125**, 104.

[13] T. Sano, N. Negishi, K. Koike, K. Takeuchi and S. Matsuzawa, J. Mater. Chem., 2004, **14**, 380.

[14] O. Diwald, T. L. Thompson, T. Zubkov, E. G. Goralski, S. D. Walck, J. T. Yates, J. Phys. Chem. B, 2004, **108**, 6004.

[15] Q. Xiang, J. Yu and M. Jaroniec, Phys. Chem. Chem. Phys., 2011, **13**, 4853.

[16] D. Li, H. Haneda, S. Hishita and N. Ohashi, Chem. Mater., 2005, **17**, 2596.

[17] F. Dong, W. Zhao and Z. Wu, Nanotechnology, 2008, **19**, 365607.

[18] R. Asahi, T. Morikawa, T. Ohwaki, K. Aoki and Y. Taga, Science, 2001, **293**, 269.

[19] T. Ohno, M. Akiyoshi, T. Umebayashi, K. Asai, T. Mitsui and M. Matsumura, Appl. Catal., A, 2004, **265**, 115.

[20] A. Sclafani and J. M. Herrmann, J. Phys. Chem., 1996, **100**, 13655.

[21] J. C. Yu, J. Yu, W. Ho, Z. Jiang and L. Zhang, Chem. Mater. 2002, **14**, 3808.

CHAPTER 5

Sulfanilic acid modified anatase TiO_2 nanoparticles with improved photocatalytic degradation on methylene blue under visible light

CONTENTS

5.1. Introduction

In this chapter chemical modification of the precursor, anatase TiO_2 using sulfanilic acid to synthesize high temperature stable and visible light active anatase TiO_2 is explained. To the best of my knowledge, only one report is available based on N, S-modified TiO_2 using sulfanilic acid (SA).[1] In their work, only low temperature (160 °C) modified P25 TiO_2 nanoparticles with sulfanilic acid ligand was discussed. However, in the present chapter, we describe the photocatalytic activity of SA modified TiO_2, stable at a temperature of 500 °C in 100% anatase form. At 700 °C, rutile formation will take place and percentage of rutile phase increases with rise in concentration of sulfanilic acid.

Recently, much attention have been concentrated in the direction of TiO_2 modified with organic chelating ligands because it results a dramatic changes in the optical and electrical properties as well as other desirable properties of the catalyst. Cozzoli *et al* demonstrated organic capped TiO_2 nanorods using oleic acid as surfactant molecule for many technological applications.[2] Whereas Tahir *et al* synthesized dopamine functionalized monocrystalline rutile TiO_2 nanorods, which offer amine group functionality on the surface for preparing future TiO_2 nanobiocomposites and biotracers.[3] TiO_2 nanoparticles modified by poly (3-hexylthiophene) were prepared by Wang *et al* by blending TiO_2 nanoparticles and the modifier in chloroform solution for getting better visible light response.[4] Niederberger *et al* provide a simple non-aqueous route to in situ surface functionalization via dopamine to titania nanoparticles to have a high impact on solar applications.[5]

Beside these reports there also reports available based on ligand functionalized TiO_2 nanoparticles for better applications.[6,7,8]

Sulfanilic acid is a commercially available and light sensitive material, often used as molecular catalyst in the asymmetric synthesis of organic compounds.[9] In the present study, based on the above mentioned viewpoints, a simple method to prepare sulfanilic acid modified anatase TiO_2 nanoparticles was developed. The photocatalytic degradation property of methylene blue using SA modified TiO_2 photocatalysts under UV and sunlight irradiation was also examined.

5.2. Results and Discussion

5.2.1. X-ray diffraction studies

The crystallographic structure of both undoped and doped TiO_2 at various calcination temperatures are examined by x-ray diffraction technique. The x-ray diffraction pattern of undoped and non metal codoped TiO_2 (TSA2) at 500 °C is shown in Figure 5.1. The codoped TSA2 powder obtained after the calcination at 300 and 500 °C shows 100% anatase phase. Whereas the corresponding control sample, TC exhibit a mixture of anatase and brookite phases. The small peak centered at $2\Theta = 30.7$ ° in TC sample indicates brookite phase of TiO_2. The diffraction peaks of TSA2 sample at 500 °C were slightly sharper and well-defined than those of bare TiO_2, which indicates higher crystalline nature for the former one. And also at 700 °C, the relative crystallinity of anatase phase of TSA sample significantly decreased due to the formation of a large amount of rutile as shown in Table 5.1. Similarly, the observed phase composition of the catalyst at 300 and

500 °C are also displayed in Table 5.1. It can be seen from Table 5.1 that, at 700 °C, anatase and rutile were coexisted for both doped and undoped samples but there is a greater transformation percentage for control TiO_2 (0 to 83% rutile) than codoped sample (0 to 9.45%-TSA2). It can also be observed that increase in dopant concentration can promote the transformation of TiO_2 from anatase to rutile at 700 degree calcination. Figure 5.2 shows the effect of dopant concentration on phase structures of TiO_2 powder calcined at a temperature of 700 °C.

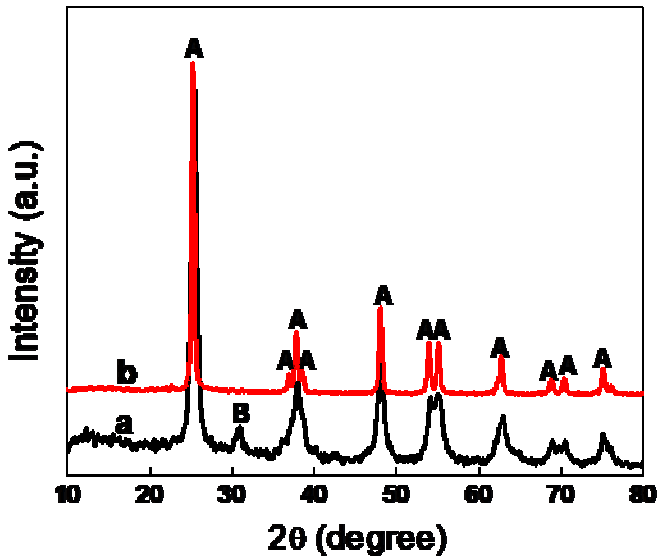

Figure 5.1. X-ray diffraction pattern of a) TC and b) TSA2 sample at 500 °C.

Table 5.1. Phase composition of the prepared TiO_2 sample at different temperature (A: Anatase, R: Rutile and B: Brookite)

Sample	300			500			700		
	A	**R**	**B**	**A**	**R**	**B**	**A**	**R**	**B**
TC	67	0	32	62	0	38	17	83	0
TSA1	100	0	0	100	0	0	90.82	9.18	0
TSA2	100	0	0	100	0	0	90.55	9.45	0
TSA3	100	0	0	100	0	0	80.39	19.61	0
TSA4	100	0	0	100	0	0	62.88	37.12	0

Table 5.2 shows the average crystalline size TiO_2 samples at different calcination temperature. Doping decrease the average grain size of TSA samples compared to undoped TiO_2 and grains of various phases dramatically increases with rise in temperature. This is due to the fact that the phase transitions accelerate the process of grain growth by providing the heat of phase transformation. [10,11]

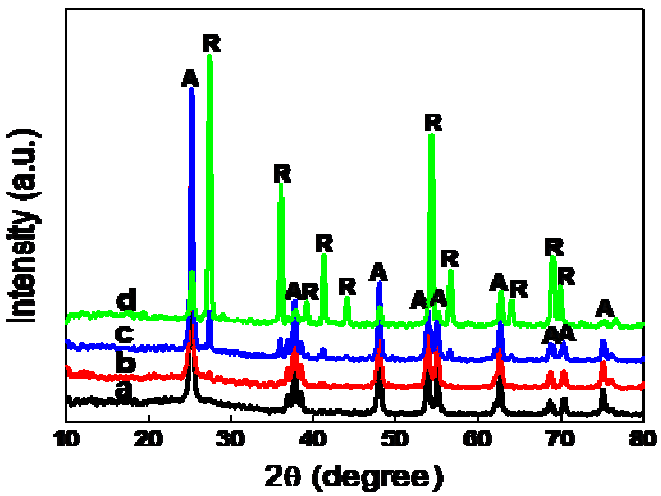

Figure 5.2. XRD of a) TSA1, b) TSA2, c) TSA3 and d) TC at 700 °C.

Table 5.2. Average crystalline size of the TiO_2 sample calculated using Scherrer equation

Sample	Crystallite size (nm)		
	300	**500**	**700**
TC	7.25	13.6	32.1
TSA1	7.19	12.11	23.06
TSA2	6.98	11.08	23.34
TSA3	6.27	10.78	24.98
TSA4	5.38	10.02	26.00

5.2.2. FTIR spectroscopy

The IR spectra of modified (TSA2) and pure TiO_2 sample dried at 100 °C are shown in Figure 5.3. IR spectrum of both the sample contain common band at 1630, 3390 and wide absorption at 500 $cm^{-1,}$ which are the characteristic peaks of the asymmetric and symmetric stretching vibrations of O-H bond and vibrations of Ti-O-Ti framework bonds respectively.[12] Characteristic peaks of benzene ring came from sulfanilic acid present in the TSA2 sample at 1504, 1425 and 1319 cm^{-1}.[1] Meanwhile, the peaks at 1005 and 1035 cm^{-1} in the modified TCS2 sample can be assigned to the S=O asymmetric and symmetric stretching vibrations respectively.[1] Notably, the band at 708 cm^{-1} can be assigned to the stretching vibration of the S-O bond in the TSA2 spectra. This indicates that SA modified the surface of TiO_2 nanoparticles through Ti-O-S bond, which was further confirmed from the XPS results.

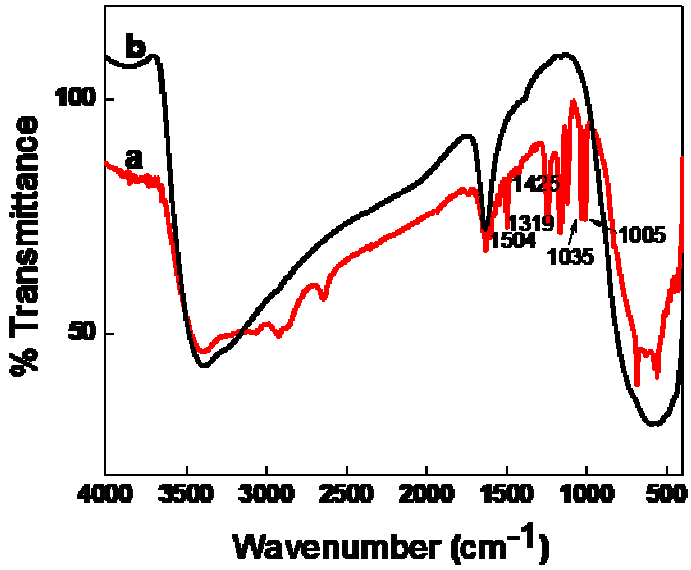

Figure 5.3. FTIR spectra of a) TSA2 and b) TC sample dried at 100 °C.

5.2.3. Raman Spectroscopy

Raman spectrum of anatase crystal was measured by Ohaska *et al* and six Raman active fundamental modes were identified in the vibrational spectrum of anatase phase: three Eg modes centered at around 144, 197 and 639 cm^{-1}, two B1g modes at 399 and 519 $cm^{-1}$and an A1g mode at 513 cm^{-1}.[13, 14, 15] The separate symmetry assignment of the 513 and 519 cm^{-1} modes has been found to be difficult because of the overlap of two modes in experimental Raman spectrum.[16] Similarly, Raman spectra of rutile phase was investigated by Porto *et al* and four raman active phonons were detected at 143 cm^{-1} (B_{1g}), 447 cm^{-1} (E_g), 613 cm^{-1} (A_{1g}) and 826 cm^{-1} (B_{2g}).[17,18] In the mixed phase TiO_2 (rutile and anatase), separate identification of raman peak at 144 and 143 cm^{-1} is difficult due to high intense peak of anatase at 144 cm^{-1}.

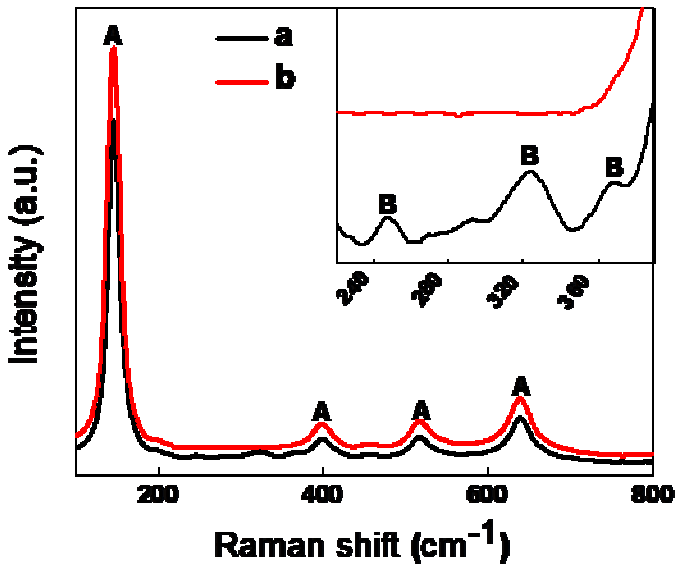

Figure 5.4. Raman spectra of a) TC and b) TSA2 calcined at 500 °C.

Raman spectra of TSA2 and TC sample at 500 °C are shown in Figure 5.4. TSA2 sample at 500 °C exhibit clear Raman features at around 144, 396, 513 and 639 cm^{-1}, which is associated with the vibrational modes of anatase phase, whereas those of TC sample display brookite peak at 247, 324 and 367 cm^{-1}(inset of Figure 5.4) along with anatase form. Figure 5.5 shows the Raman spectra of both doped and undoped sample after a heat treatment at 700 °C. One significant observation of these spectra is that rutile phase started to appear at 447 cm^{-1} with increase in concentration of dopant in TSA sample and which support the corresponding x-ray diffraction pattern as observed from Figure 5.2.

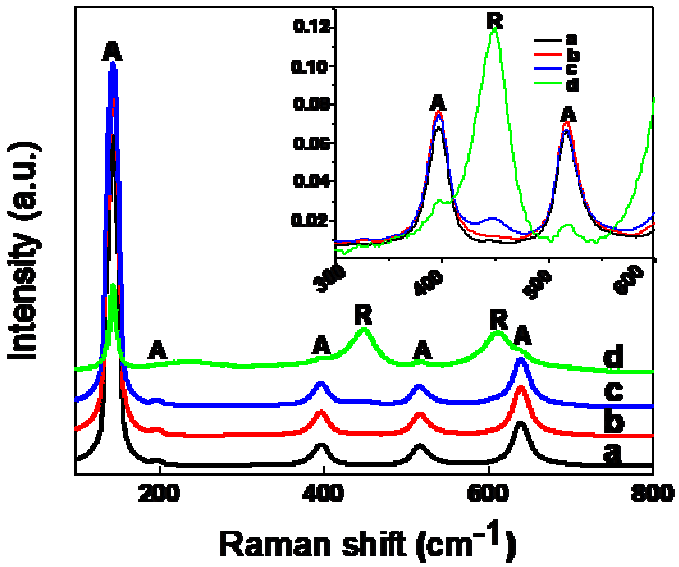

Figure 5.5. Raman spectra of a) TSA1, b) TSA2, c) TSA3 and d) TC at 700 °C.

5.2.4. TEM

The particle size of both TC and TSA sample calcined at 500 °C are in the nanometer range and are obtained from the TEM studies (Figure 5.6 A and D). TEM studies also reveal that both TC and TSA samples have relatively uniform spherical morphology with average particle size of around 10-15 nm which are in good agreement with the size calculated from x-ray diffraction studies. The displayed HRTEM images (Figure 5.6 B and E) reveal that the fringe widths of both these samples are in good agreement with the standard (101) plane of anatase TiO_2. The sharp SAED pattern of TSA nanoparticle calcined at 500 °C indicate the higher crystalline nature of the sample when compared with the TC particles at the same temperature calcination.

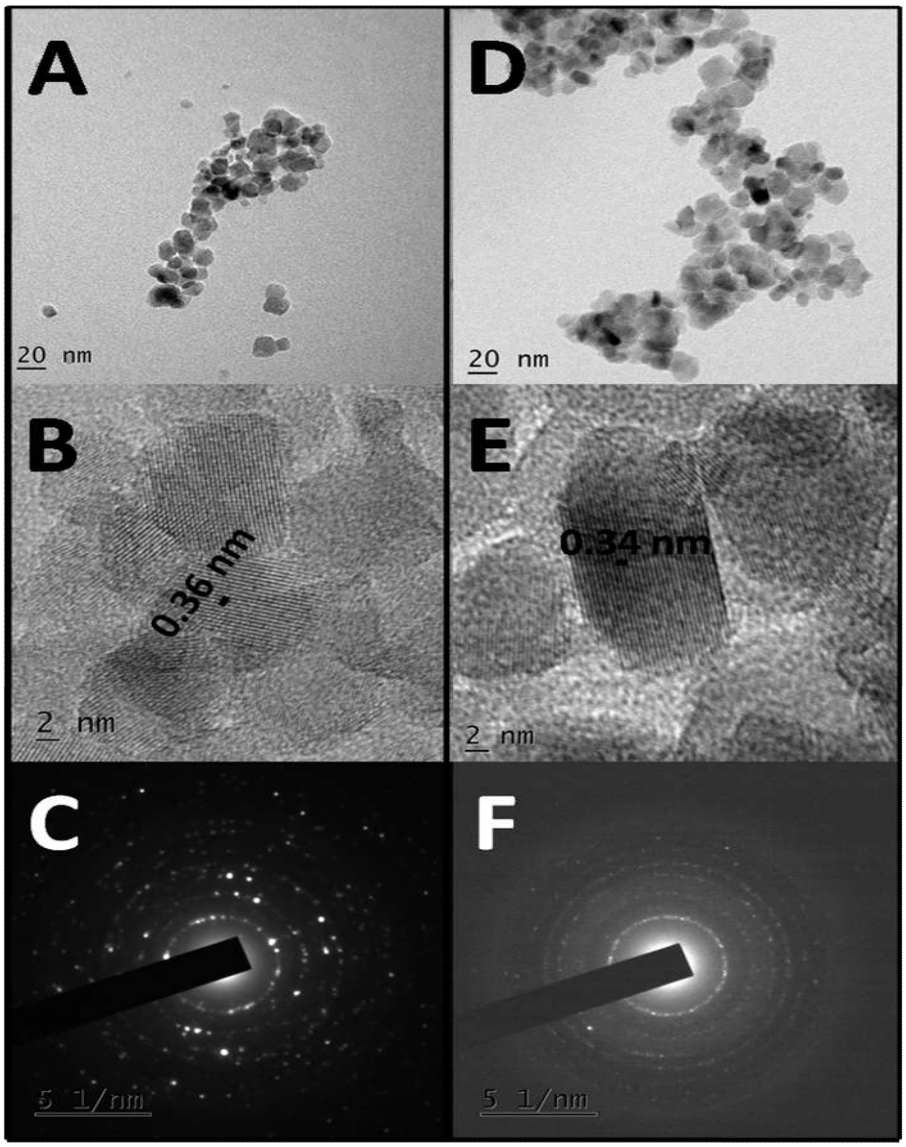

Figure 5.6. A) TEM, B) HRTEM and C) SAED pattern of TSA2; D) TEM, E) HRTEM images and F) SAED pattern of TC (Both the samples were calcined at 700 °C).

5.2.5. XPS

XPS analysis confirms the presence of S and N in the doped TSA samples at 500 °C in addition to the C, Ti and O as in TC sample at 500 °C indicating successful doping of S and N in TiO_2(Figure 5.7). The high resolution XPS spectra of Ti2p of TSA2 sample at 500 °C exhibit a binding energy peak at 458.5 and 464.2 eV corresponding to $Ti2p_{3/2}$ and $Ti2p_{1/2}$ respectively (Figure 5.8B). These values are elevated to 458.8 eV and 464. 6 eV respectively for TC at 500 °C. The negative shift in the binding energy peak of Ti2p upon doping indicates the oxygen vacancy richness of TSA2 sample.[19] Similarly, splitting between $Ti2p_{3/2}$ and $Ti2p_{1/2}$ are 5.7 and 5.8 eV respectively for TSA2 and TC sample at 500 °C, indicating the state of Ti in +4 oxidation states in the anatase TiO_2 of both doped and undoped sample.[20] In the high resolution XPS spectrum of O1s, the binding energy peak corresponding to Ti-O-Ti mode at 530.1 eV for TC at 500 °C is negatively shifted to 529.7 eV for TSA2 at 500 °C (Figure 5.8A), which indicates a change in the oxygen environment in TiO_2 nanoparticles.[21,22] In addition to the highest binding energy peak at 529.7 eV, a small peak at 531.7 eV is also observed for TSA2 sample and which can be assigned to the hydroxyl groups present on the surface of TiO_2.[1, 23]

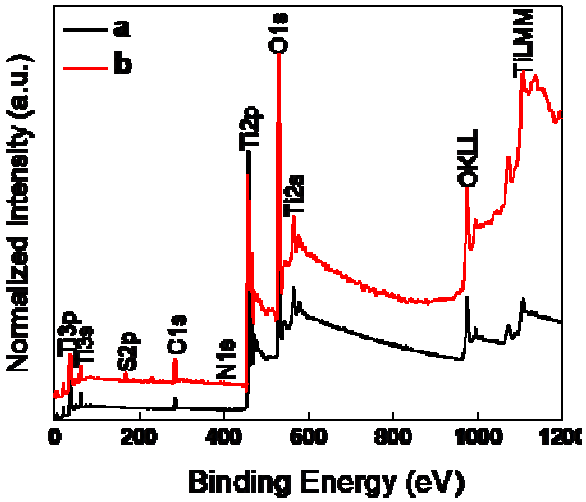

Figure 5.7. XPS survey spectra of a) TC and b) TSA2 sample calcined at 700 °C.

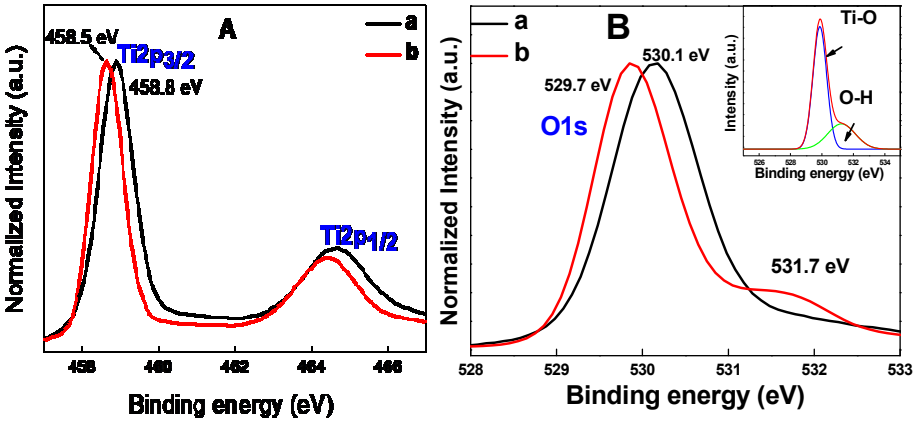

Figure 5.8. High resolution XPS spectra of A) O1s and B) Ti2p of a) TC and b) TSA2 sample at 700 °C (Inset of B shows the corresponding deconvoluted XPS spectra of O1s of TSA sample).

Figure 5.10 shows the high resolution XPS spectra in the S2p binding energy region of TSA2 sample calcined at 700 °C. It could be observed that TSA2 sample exhibit a single binding energy peak at 168.4 eV and which can be attributed that sulphur atom existed in a +6 oxidation state.[24,25] S^{6+} may exist as SO_4^{2-} ion adsorbed on the surface of TSA2 catalyst at 700 °C.

The high resolution N1s XPS of TSA2 sample at 700 °C shows that N exhibit a characteristic main binding energy peak at 401.4 eV along with a sub peak at 400 eV (Figure 5.9). The peak detected at 401.4 eV was assigned to the substitutional O-Ti-N sites in the TiO_2 lattice, while the other peak at 400 eV was attributed to the molecularly chemisorbed N_2.[26] These two results confirmed that N and S are present in a chemically bonded state in the TSA2 system.

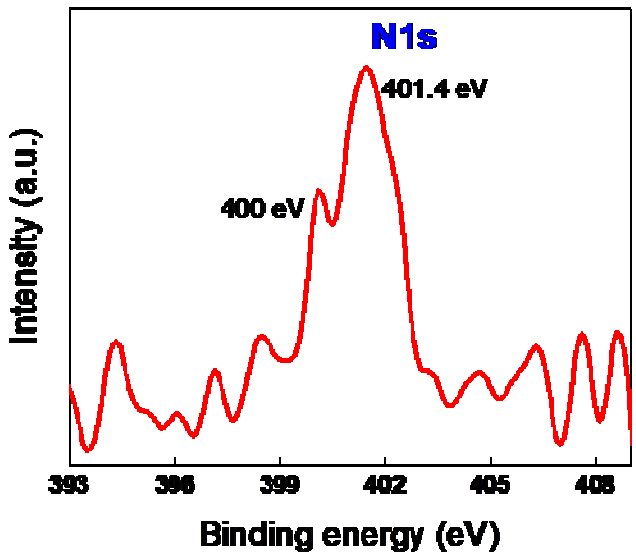

Figure 5.9. High resolution XPS spectra of N1s of TSA2 sample calcined at 500 °C.

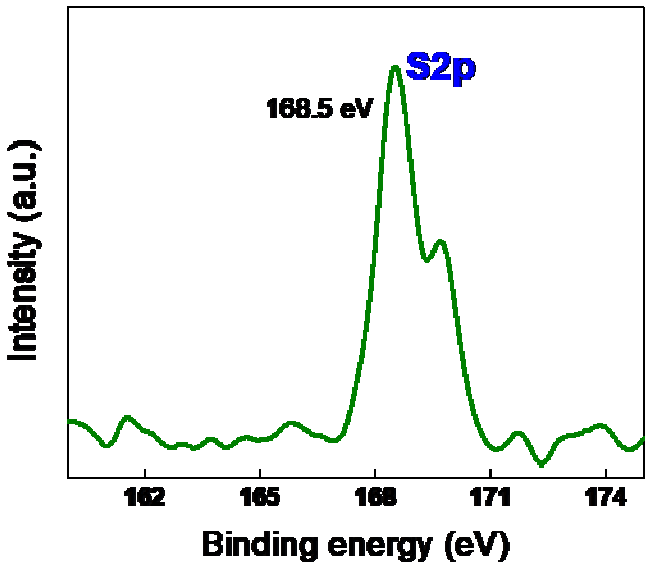

Figure 5.10. High resolution XPS spectra of S2p of TSA2 sample calcined at 500 °C.

5.2.6. UV-Visible DRS

The UV-Visible diffuse reflectance spectra (DRS) of TSA catalysts calcined at 500 °C are shown in Figure 5.11. It is seen from Figure 5.11A that the undoped TiO_2 nanocatalyst showed strong absorption band at around 380 nm in the ultraviolet region. But TSA sample is showing absorbance at 400-510 nm with red shift (approximately 100 nm) towards visible region. This shift in the absorption edge decreases the direct bandgap of TSA catalyst compared to undoped TiO_2 and this may be due to the insertion of nitrogen and sulphur in to the TiO_2 lattice.[27] Furthermore, the red shift in the DRS band increases with increase in doped elements content in the TiO_2 lattice. Bandgap energy (Eg value) of all the catalysts is estimated from the tauc plot of

absorbance versus photon energy (hυ). The obtained tauc plot is extrapolated to get the bandgap energy for the TSA catalysts with good approximation as observed in Figure 5.11B. The estimated bandgap energies of TC, TSA1, TSA2, TSA3 and TSA4 are found to be 3.22, 2.81, 2.76 and 2.66 eV respectively. From the DRS results it is clear that N and S doping can shift the absorption edge of TiO_2 to the visible region and hence reduce the band gap, which is beneficial for improving the photoabsorption and ultimately photocatalytic performance of TiO_2.

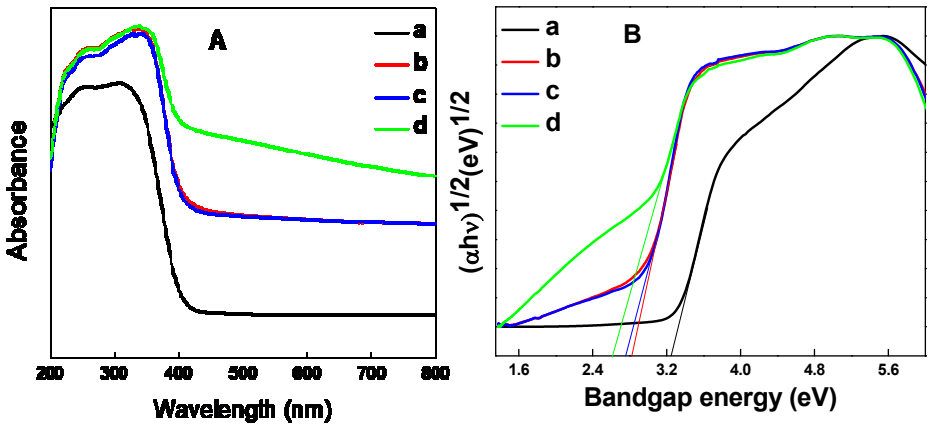

Figure 5.11. A) DRS spectra and B) corresponding tauc plot of a) TC, b) TSA1, c) TSA2 and d) TSA3 catalysts calcined at 500 °C.

5.2.7. Detection of hydroxyl radical

Hydroxyl radicals produced on the surface of TiO_2 can be easily detected by using terephthalic acid as a probe molecule. Here terephthalic acid easily reacts with hydroxyl radical and form a highly fluorescent hydroxyterephthalic acid. The fluorescent intensity of hydroxyterephthalic acid is in directly propotional to the amount of hydroxyl radicals produced on the surface of TiO_2. Hydroxyl radical

formed on the surface of TiO_2 make responsible for the higher photocatalytic degradation of MB molecules adsorbed on the surface of TiO_2. Figure 5.12 show the fluorescent intensity of hydroxyterephthalic acid formed on the reaction between terephthalic acid and various catalysts prepared at a calcination temperature of 500 °C (The reaction is carried out in 10 minute irradiation of UV light). It can be seen from Figure 5.12 that the TSA2 catalyst calcined at 500 °C emits higher intensity radiation and which represents the higher amount of hydroxyl radicals produced on the surface of TiO_2. Similarly TSA2 catalyst, shows maximum photocatalytic activity at a calcination temperature of 500 °C and above or below this temperature photocatalytic activity was decreased (Figure 5.13).

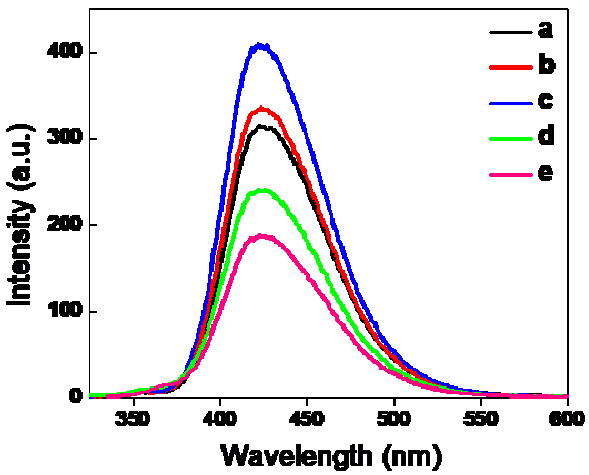

Figure 5.12. PL intensity of hydroxyterephthalic acid formed after a 10 minute irradiation of UV light on a 50 mL solution of terephthalic acid containing 0.1 g of a) TC, b) TSA1, c) TSA2, d) TSA3 and e) TSA4 samples calcined at 500 °C.

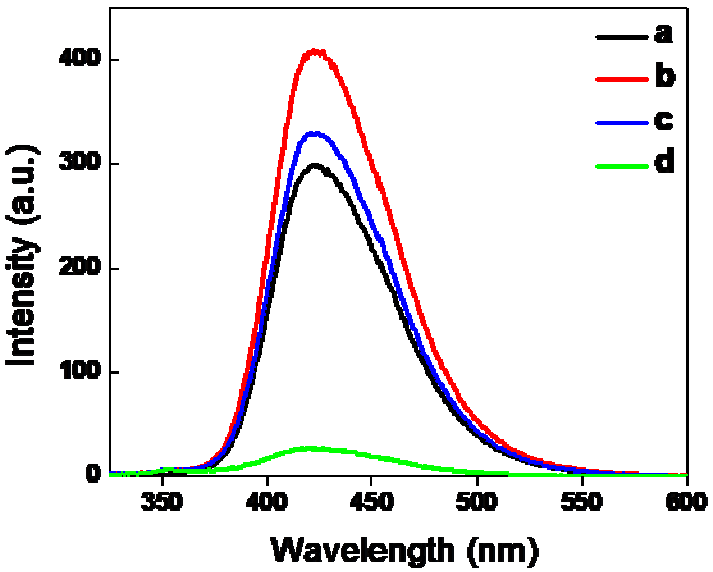

Figure 5.13. PL intensity of hydroxyterephthalic acid formed after a 10 minute irradiation of UV light on a 50 mL solution of terephthalic acid containing 0.1 g of TSA2 catalyst calcined at a) 300, b) 500, c) 700 and d) 800 °C.

5.2.8. Photocatalysis

Photocatalytic studies were carried out to measure the decomposition rate of the dye. Figure 5.14 shows the degradation pattern of both doped and undoped sample at 500 degree calcination under the irradiance of UV and direct solar radiation. The rate of reaction follows pseudo first order kinetics and the reaction rate constant (k) is obtained from the plot of Ln (C_0/C) *vs* time (t) giving a straight line having a slope of k. The reaction rate constant value of all the samples calcined at various temperatures is graphically represented in Figure 5.17. The rate constant of all the samples increases with increase in calcination temperature, maximum is obtained for the sample calcined at 500 °C and above this temperature the rate constant value decreases. Similarly

doped titania exhibit higher degradation rate of methylene blue than undoped titania. Among all the catalyst prepared, best photocatalytically active catalyst is the TSA2 catalyst calcined at 500 °C under UV as well as solar irradiation. The calculated k value for the TSA2 sample at 500 °C was 0.103 min^{-1}, over three and half times faster than the control sample TC at same calcination temperature under the action of sunlight (Figure 5.16). Generally, the reaction rate constant value of the control TiO_2 under UV radiation is little higher than that under solar radiation. However, reverse happened in the case of doped titania sample using sulfanilic acid for the rate constant value.

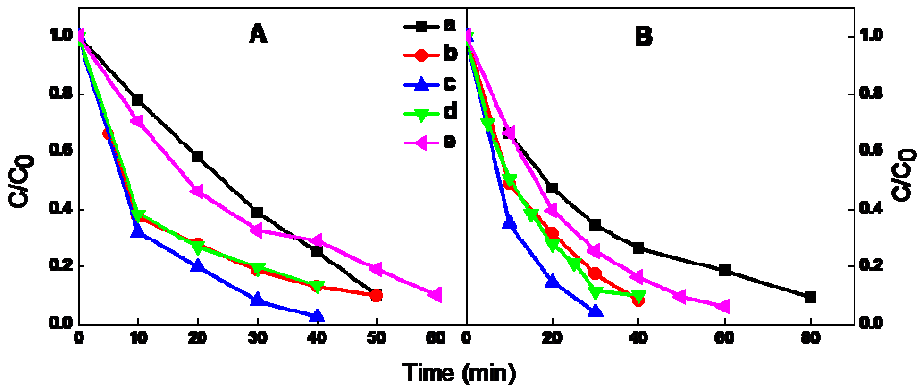

Figure 5.14. Photocatalytic degradation pattern of a) TC, b) TSA1, c) TSA2, d) TSA3 and e) TSA4 at 500 °C under A) UV and B) direct sunlight.

The reason behind the photocatalytic activity of different TSA samples having different rate constant value can be attributed to the following factors. It is known that doping of N and S elements in titania matrix brings the photocatalytic activity of titania in to visible region. It can be seen from the diffuse reflectance spectra that the N and S doping shift the absorption edge of titania from UV to visible region and this

red shift in the absorption is responsible for the higher activity of doped sample than undoped under UV as well as direct sunlight, especially in direct solar irradiation. The ban-gap narrowing of TSA samples lead to enhanced photocatalytic degradation under solar light. Because the synthesized doped TiO_2 sample can be activated by visible light by giving more and more electrons and holes and participate in the redox reaction occurred during photocatalysis.[28] We can also see from Figure 5.11 that higher loading of sulfanilic acid into TiO_2 will induce more red shift in the absorption edge. However, the observed photocatalytic activity of the samples gradually increased with increasing amount of dopant concentration, reaches the optimum at 0.5 wt% loading (TSA2) and then decreased gradually with further increase in concentration. It might be due to the fact that, the excess amount of dopant can acts as recombination centers which promotes the electron-hole recombination and thus lowering the activity. So, the photocatalytic activity is depressed to certain extent.

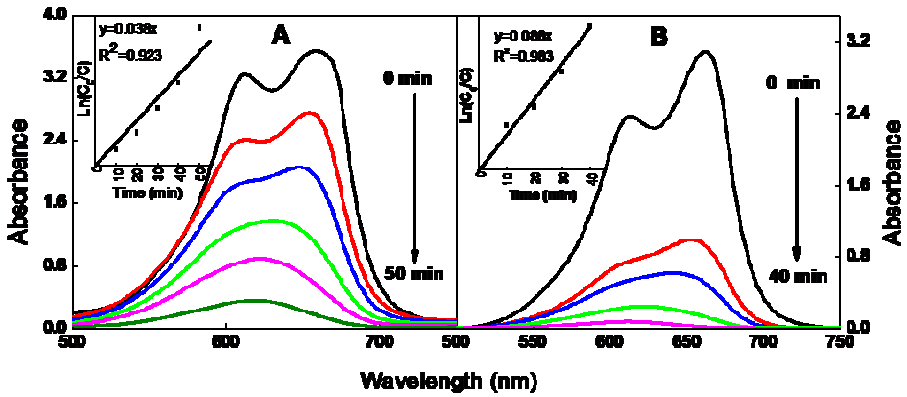

Figure 5.15. Photocatalytic degradation pattern of MB by A) TC and B) TSA2 catalyst at 500 °C under UV light (Inset shows the corresponding kinetic data).

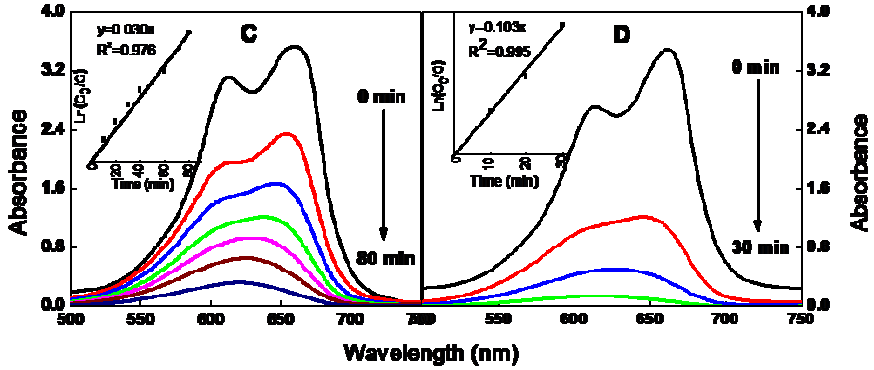

Figure 5.16. Photocatalytic degradation pattern of MB by C) TC and D) TSA2 catalyst at 500 °C under direct sunlight (Inset shows the corresponding kinetic data).

Table 5.1 shows the effect of calcination temperature on the phase structure of doped and undoped sample. From Figure 5.1, it can be seen that at a calcination temperature of 500 °C, TSA2 catalyst exhibit 100% anatase phase. Whereas, the corresponding undoped sample exist in a mixture of anatase and brookite phases. The higher photoactivity of TSA2 at 500 °C can be ascribed to an obvious improvement in the crystallinity of anatase.[10] Crystal size also has a little effect on the photoactivity of TiO_2 and generally lowest crystal size support the higher photocatalytic activity. Here also, doping decrease the crystallite size of TSA samples and lowest crystallite size can be attained at a temperature of 300 °C. However, crystallinity of the anatase phase is little lower in low temperature calcination. The maximum crystallinity of anatase phase is attained at calcination temperature of 500 °C (Figure 5.1) and further increase in temperature (700 °C) decrease the peak intensity of anatase phases due to the appearance of rutile phase. So the calcination of TSA samples above 500 °C are not desirable and the corresponding photocatytic activity

was slowly decreased from 500 to 700 and then to 800 °C. Similarly as seen from Figure 5.12 and 5.13 that doping of sulfanilic acid in TiO_2 can increase the number of surface hydroxyl groups and subsequently increase the number of free hydroxyl radicals, which is proved to be beneficial for photocatalytic reactions.[23] Higher amount of hydroxyl radical can be formed on the surface of TSA2 catalyst calcined at 500 °C and which is clear from Figure 5.12 and 5.13.As the number of hydroxyl radical formed on the surface of TiO_2 increases, the photocatalytic activity also increases.

To conclude, the higher efficiency of TSA2 catalyst for photocatalytic degradation at 500 °C can be attributed to the combined effect of lowest crystallite size, stronger absorption in visible region, higher crystalline nature, higher concentration of hydroxyl radical on the surface of TiO_2 and lower rate of electron-hole recombination.

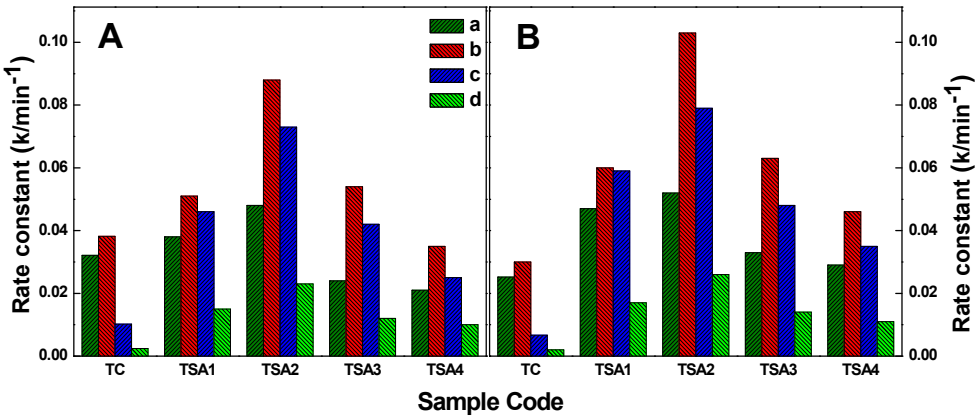

Figure 5.17: Rate constant value of TC and TSA catalysts calcined at a) 300, b) 500, c) 700 and d) 800 °C in presence of A) UV and B) direct sunlight.

5.3. Conclusions

Through the discussion above, the MB oxidation by TSA photocatalysis was driven mainly by the participation of $O_2^{\bullet-}$, holes, and $^{\bullet}OH$ radicals. The obtained photocatalyst were analyzed in detail by the characterizations techniques such as X-ray diffraction studies, UV–VIS absorption spectroscopy, transmission electron microscopy (TEM) and X-ray photoelectron spectroscopy (XPS). Surface hydroxyl groups were the important sources of hydroxyl radicals. In addition to the surface hydroxyl radicals, improvement in UV-Visible absorption, creation of surface oxygen vacancies and good crystallisation are mainly responsible for the higher photocatalytic activity of TSA catalyst calcined at 500 °C.

References

[1] H. X. Guo, K. L. Lin, Z. S. Zheng, F. B. Xiao and S. X. Li, Dyes pigm., 2012, **92**, 1278.

[2] P. D. Cozzoli, A. Kornowski and H. Weller, J. Am. Chem. Soc., 2003, **125**, 14539.

[3] M. N. Tahir, P. Theato, P. Oberle, G. Melnyk, S. Faiss, U. Kolb, A. Janshoff, M. Stepputat and W. Tremel, Langmuir, 2006, **22**, 5209.

[4] D.Wang, J. Zhang, Q. Luo, X. Li, Y. Duan and J. An, J. Hazard. Mater., 2009, **169**, 546.

[5] M. Niederberger, G. Garnweitner, F. Krumeich, R. Nesper, H. Co¨lfen and M. Antonietti, Chem. Mater., 2004, **16**, 1202.

[6] T. Rajh, L. X. Chen, K. Lukas, T. Liu, M. C. Thurnauer and D. M. Tiede, J. Phys. Chem. B, 2002, **106**, 10543.

[7] N. M. Dimitrijevic, Z. V. Saponjic, D. M. Bartels, M. C. Thurnauer, D. M. Tiede and T. Rajh, J. Phys. Chem. B. 2003, **107**, 7368.

[8] J. Moser, S. Punchihewa, P. P. Infelta and M. Gra¨tzel, Langmuir, 1991, **7**, 3012.

[9] I. V. Gulyaiko and O. I. Kolodyazhnyi, Russ. J. General. Chem., 2005, **11**, 1848.

[10] J. C. Yu, J. Yu, W. Ho, Z. Jiang and L. Zhang, Chem. Mater., 2002, **14**, 3808.

[11] X. Ye, J. Sha, Z. Jiao and L. Zhang, Nanostruct. Mater., 1997, **8**, 919.

[12] T. Ohno, T. Tsubota, Y. Nakamura and K. Sayama, Appl. Catal. A: Gen., 2005, **288**, 74.

[13] V. Swamy, A. Kuznetsov, L. S. Dubrovinsky, R. A. Caruso, D. G. Shchukin and B. C. Muddle, Phys. Rev. B, 2005, **71**, 184302.

[14] T. Ohaka, J. Phys. Soc. Jpn., 1980, **48**, 1661.

[15] T. Ohsaka, F. Izumi, and Y. Fujiki, J. Raman Spectrosc., 1978, **7**, 321.

[16] M. Mikami, S. Nakamura, O. Kitao, and H. Arakawa, Phys. Rev. B, 2002, **66**, 155213.

[17] S.P.S. Porto, P.A. Fluery and T.C. Damen: Phys. Rev., 1967, **154**, 522.

[18] W. Ma, Z. Lu and M. Zhang, Appl. Phys. A, 1998, **66**, 621.

[19] S. G. Ullattil and P. Periyat, Nanoscale, 2015, **7**, 19184.

[20] T. Harifi and M. Montazer, Appl. Catal., A, 2014, **473**, 104.

[21] V. Etacheri, M. K. Seery, S. J. Hinder and S. C. Pillai, Adv. Funct. Mater., 2011, **21**, 3744.

[22] R. Ren, Z. Wen, S. Cui, Y. Hou, X. Guo and J. Chen, Sci. Rep., 2015, **5**, 10714.

[23] X. Lin, F. Rong, D. Fu and C. Yuan, Powder Technol., 2012, **219**, 173.

[24] Y. Okamoto, M. O. Hara, A. Maezawa, T. Imanaka, S. Teranishi, J. Phys. Chem., 1986, **90**, 2396.

[25] X. Wang, J. C. Yu, P. Liu, X. Wang, W. Su and X. Fu, J. Photochem. Photobiol., A, 2006, **179**, 339.

[26] F. Wei, L. Ni and P. Cui, J. Hazard. Mater., 2008, **156**, 135.

[27] B. Naik, K. M. Parida and C. S. Gopinath, J. Phys. Chem. C, 2010, **114**, 19473.

[28] Y. Ao, J. Xu, D. Fu, and C. Yuan, Microporous and Mesoporous Mater., 2008, **122**, 1.

CHAPTER 6

Cysteine modified anatase TiO_2 nanomaterials with improved visible light driven photocatalytic activity

CONTENTS

6.1. Introduction

In the area of the controlled synthesis of inorganic nanomaterials, living organisms were proved to be very effective even in aqueous solution and at ambient temperatures.[1] Shells and sea urchins can synthesize a mineral defense made of calcium carbonate with a well defined structure and a morphological control from the nanometer to the centimeter scale.[1] Nanometric magnetic iron oxide particles were also found in magnetotactic bacteria.[2] In all the cases, proteins and biological membranes are actively involved in the biomineralization process. The charge, shape and chemical functionalities on the surface of those proteins are of particular importance in the synthesis of inorganic nanomaterials.

Durupthy *et al* have been used amino acids for the first time as controlling agent in the sol–gel formation of titanium oxide below 100 °C. The amino acid side chain functions have been shown to be of particular importance in regard to the modification of the TiO_2 structure and morphology. Makarova *et al* modified the TiO_2 surface with arginine resulted in enhanced nitrobenzene adsorption and photodecomposition when compared to unmodified TiO_2.[3] In 2012, Lv *et al* modified anatase TiO_2 hollow microsphere at 300 °C using cysteine with enhanced visible light driven photocatalytic activity.[4]

Cysteine is a semi-essential proteinogenic amino acid and has good antioxidant properties. Beyond the iron-sulfur proteins, many other metal cofactors in enzymes are bound to the thiolate group of cysteinyl residues and thiol group also has high affinity for heavy metals. So that proteins containing cysteine will bind metals such as mercury, lead and cadmium tightly. To the best of my knowledge, only one report is

available based on N, S modified TiO_2 using cysteine as modifier for photocatalytic applications.[4] In the present chapter we prepared cysteine modified anatase TiO_2 stable at 700 °C in 100% anatase form and exhibit high photocatalytic performance. The consequences of the effect of cysteine on the structure of TiO_2 were characterized by a variety of techniques including X-ray diffraction, Raman spectra, TEM, UV-Visible spectra and XPS analysis.

6.2. Results and Discussion

6.2.1. X-ray diffraction studies

To study the phase structure of doped and undoped samples, XRD was employed and the observed results are shown in Figure 6.1 and 6.2. It can be seen that TCS catalysts display only the characteristic peaks of anatase phase up to a calcination temperature of 700 °C. Similarly, the diffraction peaks of TCS2 catalyst became sharp and well-defined with the enhancement in the degree of crystallinity when the temperature of calcination was increased to 700 °C (Figure 6.1). However, formation of rutile phase started at the calcination temperature of 800 °C for all the TCS samples, which usually happens in control sample, TC at 600-700 °C (Figure 6.2). The high temperature anatase phase stability of TCS samples may be due to the doping effect. Generally, anatase to rutile phase transition involves a rearrangement in the TiO_6^{2-} octahedron. The presence of doped species, especially the sulfate ions, seemed to delay the octahedral rearrangement, which stabilize the anatase structure at high temperature. Further increase in calcination temperature above 800 °C, expelled all the doped elements gradually from the lattice of TiO_2, which results the complete transition of anatase to rutile form.

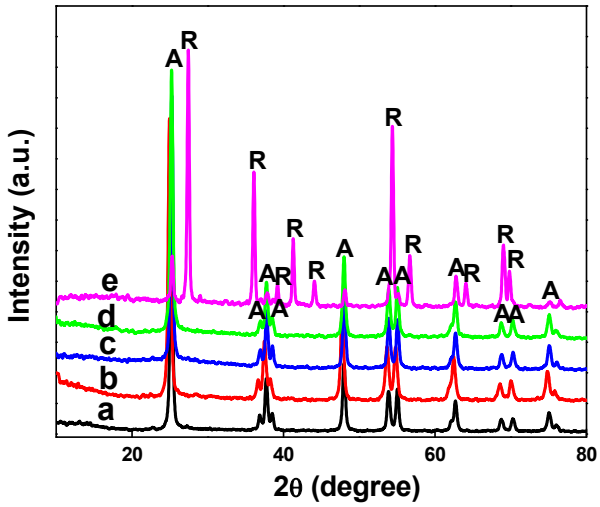

Figure 6.1: X-ray diffraction pattern of a) TCS1, b) TCS2, c) TCS3, d) TCS4 and e) TC at a calcination temperature of 700 °C.

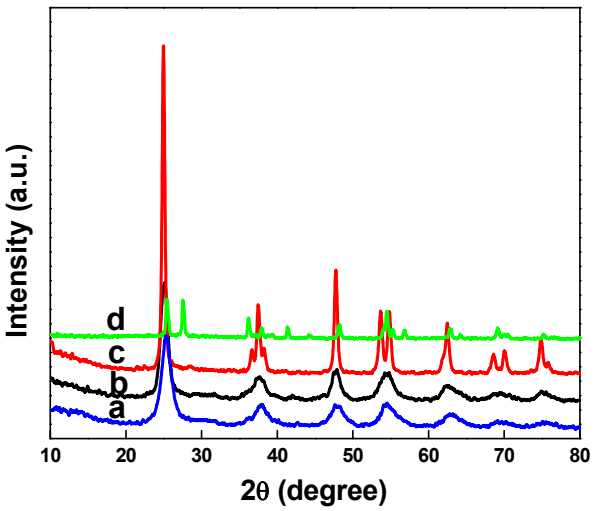

Figure 6.2: XRD pattern of TCS2 catalyst calcined at a) 300, b) 500, c) 700 and d) 800 °C.

The observed results also shows that, doped TSC sample exhibit characteristic peaks of TiO_2 crystal without any appearance of dopant related peaks, which indicates perfect doping of cysteine in TiO_2 system. Here, dopant atoms may either moved to substitutional sites or interstitial positions of the TiO_2 crystal structure.[5,6] Debye-Scherrer equation is applied to calculate the average crystallite size using full width at half maximum value of (101) diffraction peak for anatase TiO_2 and is found to be about 25.39, 21.6, 24.52, 27.26 nm for TCS1, TCS2, TCS3 and TCS4 samples at 700 °C respectively. Whereas, those of control sample TC at the same temperature calcination exhibits slightly higher crystallite size (32 nm) due to rutile formation. Doping decrease the crystal size of TCS catalyst due to the fact that doped non-metals can hinder the phase transition from anatase to rutile and restricts the crystal growth.[7]

6.2.2. FTIR spectroscopy

FTIR measurements were shown to be helpful in investigating the structure of nitrogen and sulfur complexes on the surface of TiO_2. Figure 6.3 represents the FTIR spectra of the as-prepared doped (TCS2) and undoped (TC) samples ranging from 400 to 4000 cm^{-1}. The broad peak below 1000 cm^{-1} corresponds to the Ti-O-Ti crystal lattice vibrations.[8] The broad peak at 3400 cm^{-1} corresponds to the O-H stretching mode, whereas the peak at 1630 cm^{-1} results from the O-H bending mode of adsorbed water molecules.[9] The deformation mode of C-N-H bond was found to be at 1566 cm^{-1} for TCS2 sample.[10] Ammonium ions produced by the dissociation of cysteine were also found in the TCS2 sample at 1413 cm^{-1} attributable to the deformation mode of ammonium ions.[9] The peaks at 1197, 1135, 1043, and 961 cm^{-1} were the characteristic frequencies of a bidentate

SO_4^{2-} co-ordinated to metals such as Ti^{4+} ion.[11, 12, 13] The results of FTIR are in good agreement with the XPS spectra.

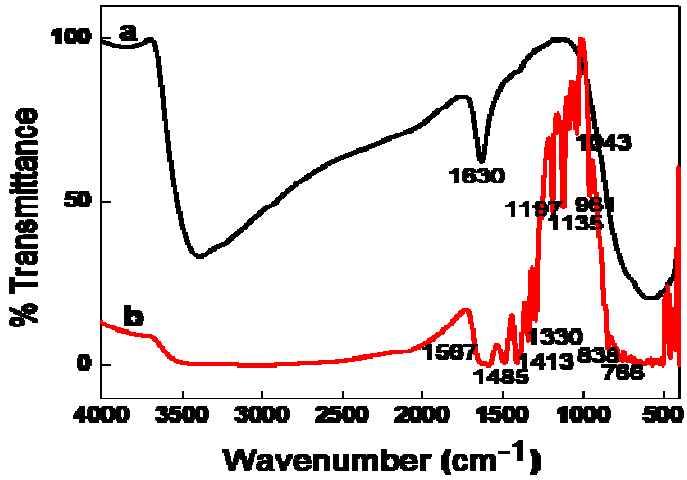

Figure 6.3: FTIR spectra of a) TC and b) TCS2 sample dried at 100 °C.

6.2.3. Raman spectra

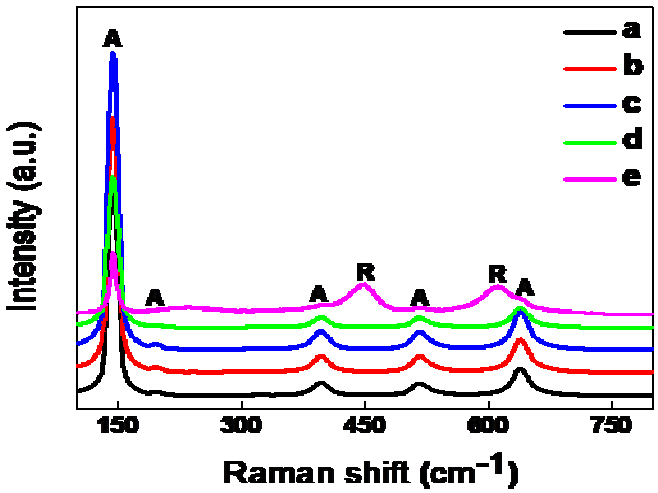

Figure 6.4: Raman spectra of a) TCS1, b) TCS2, c) TCS3, d) TCS4 and e) TC at 700 °C.

Raman spectra are used to identify different phases of TiO_2 (rutile, anatase and brookite) in TCS and TC samples (Figure 6.4 and 6.5). According to Ohaska *et al*, the prepared TCS powder in different composition showed only the Raman bands of anatase phase at 700 degree calcination temperature, indicating that rutile formation does not occur at 700 °C for doped samples (Figure 6.4).[14] The characteristic Raman bands of anatase TiO_2 was seemed to be at 147 (E_g), 198 (E_g), 398 (B_{1g}), 515 (A_{1g}+ B_{1g}) and 639 cm^{-1} (E_g). The Raman peak corresponding to rutile phase was investigated by Porto et al and was found to be at 144 (B_{1g}), 448 (E_g) and 612 cm^{-1} (A_{1g}).[15] It can be seen from Figure 6.4 that TC form rutile phase at a calcination temperature of 700 °C and all these results from Raman spectra clearly support the data obtained from X-ray diffraction studies.

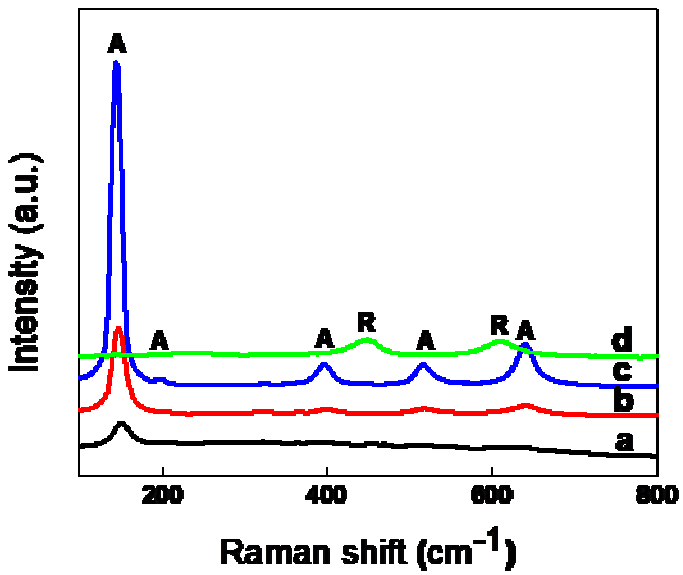

Figure 6.5: Raman spectra of TCS2 catalyst calcined at a) 300, b) 500, c) 700 and d) 800 °C.

6.2.4. Transmission electron microscopy

TEM analysis were carried out for TCS and TC catalyst prepared at a calcination temperature of 700 °C in order to provide a structural insight in to the catalytic properties of the system. The TEM images of both TC and TCS sample at 700 °C was given in Figure 6.6. Typically, slightly higher agglomeration in structure was observed for TC at 700 °C when compared to TCS at the same temperature calcination and the particle size distribution seems to be comparatively uniform. Agglomeration may reduce the surface area of the sample, which delay the photoactivity of the catalyst. The particle size noticed from the TEM images of the crystalline particles of TCS2 catalyst at 700 °C is found to be in the range of 20-25 nm, which is lesser than that of TC at same temperature (30-40 nm).

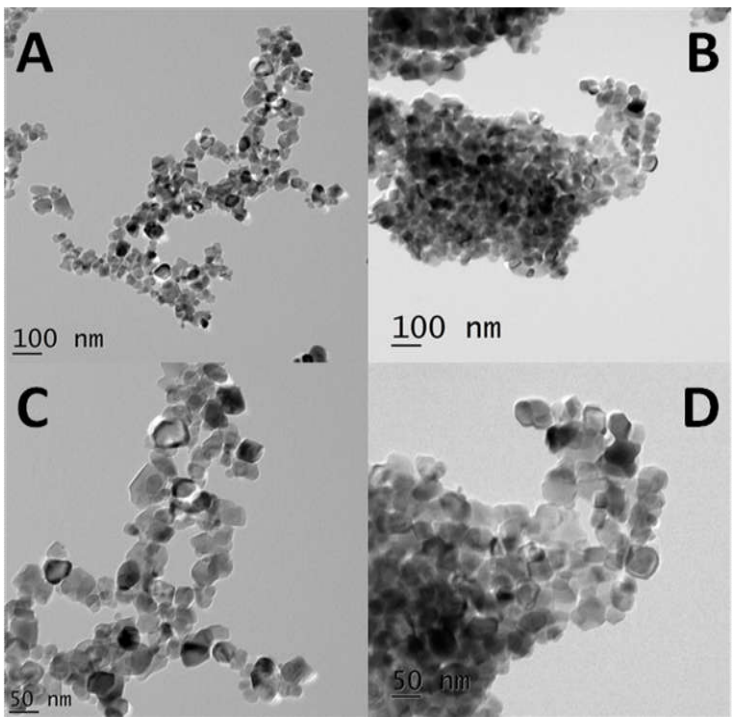

Figure 6.6: TEM images of TCS (A&C) and TC (B&D) at 700 °C.

Similarly, HR-TEM and SAED pattern of both TC and TCS sample at 700 °C are shown in Figure 6.7. From the HR-TEM images of TCS sample, it is observed that the fringe width obtained at 0.34 nm support the anatase crystal lattice system and that of TC (0.32 nm) support the rutile system. The more bright spotty images of TCS at 700 °C in the SAED pattern support the higher crystallinity of the sample than that in TC at 700 °C. All the information obtained from the transmission electron microscopy for TC and TCS2 sample at a calcinations temperature of 700 °C are in good agreement with the x-ray diffraction data.

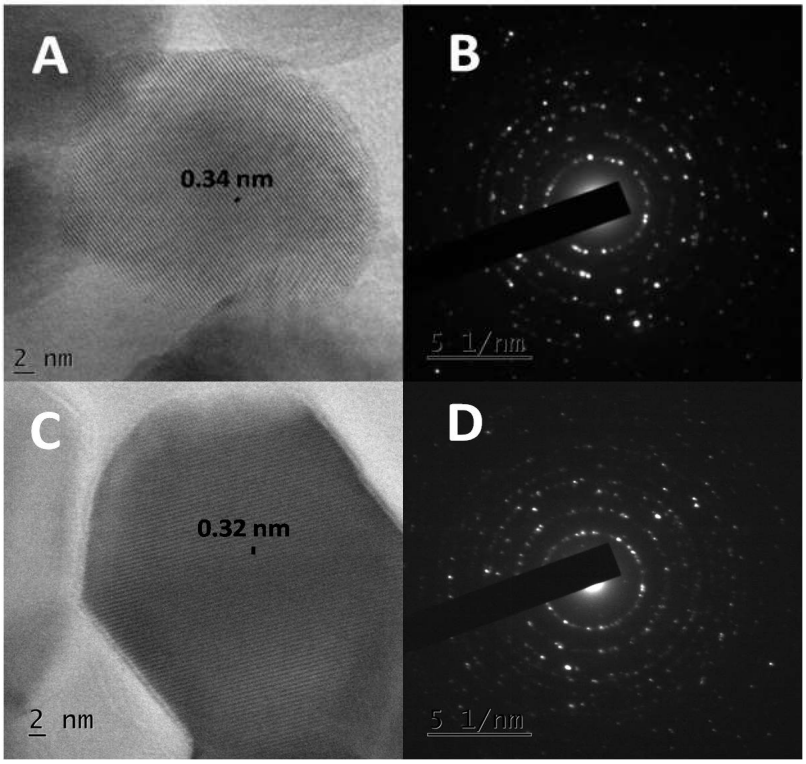

Figure 6.7: HRTEM image and corresponding SAED pattern of A, B) TCS and C, D) TC samples respectively at a calcination temperature of 700 °C.

6.2.5. XPS analysis

XPS (X-ray photoelectron spectroscopy) measurements were carried out to further elucidate the interrelation between cysteine and anatase TiO_2 particles. Figure 6.8 shows the wide area XPS spectra of TCS2 and TC samples calcined at 700 °C. It can be seen that TCS2 sample not only contains Ti, O and C elements with a sharp photoelectron peaks appeared at binding energies of 458 (Ti2p), 529 (O1s) and 286 eV (C1s), but also contain small percentage of N and S elements with photoelectron peak at 168 (S2p) and 400 eV (N1s) respectively. The carbon peak in TC sample is attributed to the adventitious hydrocarbon form XPS instrument and also from the starting materials. [4]

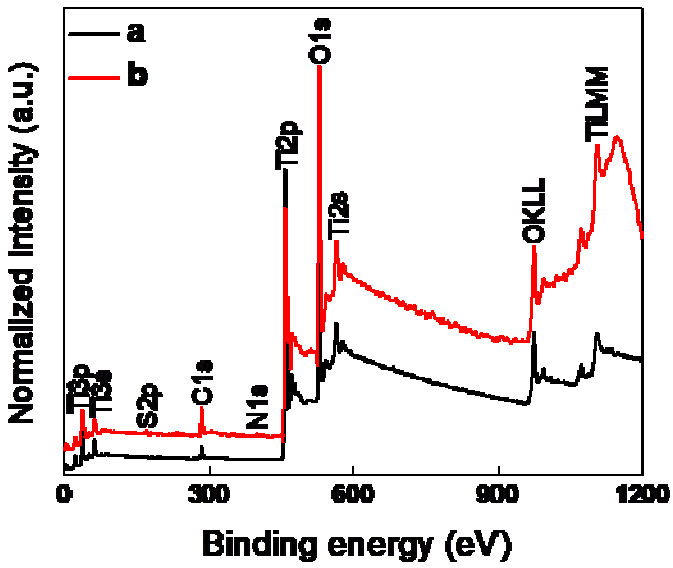

Figure 6.8: Wide area XPS spectrum of a) TC and b) TCS2 catalyst calcined at 700 °C.

The high resolution N1s XPS spectra of TCS2 catalyst calcined at 700 °C shows that N1s region can mainly be fitted into three peaks in the spectrum at around 395, 400.5 and 401.5 eV (Figure 6.9 A). The small peak detected at 395 eV is attributed to the Ti-N bond, while the one peak at 400.5 eV with stronger intensity was detected, which is assigned to the molecularly chemisorbed N_2 and at a position of 401.5 eV, low intensity peak was also detected, which was attributed to the substitutional O-Ti-N sites in the TiO_2 lattice. [16, 17, 9] Therefore all these results confirmed that N1s is not only implanted in the structure but also exist in a chemically bonded state which indicates that N is an active doping species in TCS2 catalyst calcined at 700 °C.

Figure 6.9 B clearly shows that there was no sulfur signal present in the TC sample at 700 °C when compared to TCS2 sample at same temperature calcination. The high resolution S2p XPS spectrum of TCS2 catalyst at 700 °C shows a sharp binding energy peak at 168.4 ev, which suggested that sulfur exist in a six oxidation state (S^{6+}) in the TCS2 sample. The characteristic peaks in the FTIR spectra of TCS2 sample in the range of 900-1300 cm^{-1} confirm the presence of SO_4^{2-} ion bind on the surface of TiO_2 and which was further confirmed from the XPS measurement.

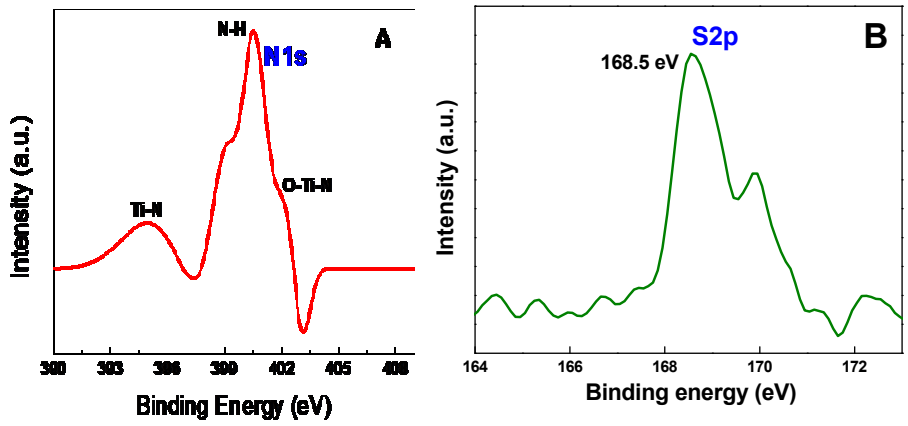

Figure 6.9: High resolution XPS spectra of A) N1s and B) S2p region of TCS2 sample calcined at 700 °C.

The high resolution O1s XPS spectra of TC and TCS2 catalyst calcined at 700 °C are shown in Figure 6.10A. Only a single peak at 530.1 eV was observed in the O1s spectra of TC sample, whereas TCS2 sample exhibit two isolated peak at 529.2 and 531.1 eV. The two peaks observed at 530.1 and 529.2 eV respectively present in O1s spectra of TC and TCS2 catalysts at 700 °C corresponds to O-Ti-O linkage present in the TiO_2 lattice. The negative shift observed in the binding energy peak of the O1s spectra of TCS2 sample may due to the oxygen vacancy sites produced in the lattice of TiO_2. The second peak at 531.1 eV in TCS2 sample is related to the surface hydroxyl groups, which mainly results from the chemisorbed water molecule. The increased concentration of surface hydroxyl molecule is advantageous for trapping photogenerated holes and thus preventing the recombination of electrons.[7]

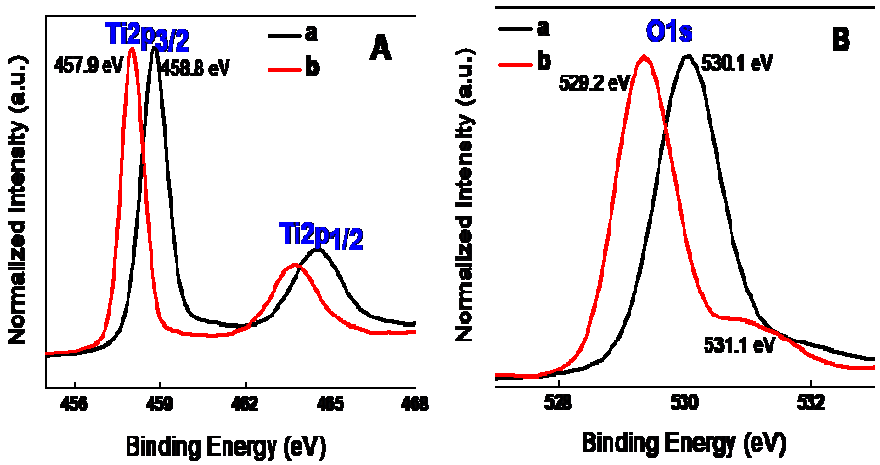

Figure 6.10: High resolution XPS spectra of A) O1s and B) Ti2p region of a) TC and b) TCS2 sample calcined at 700 °C.

Similarly, the high resolution spectra of Ti2p of TCS2 and TC sample at 700 degree calcination are given in the Figure 6.10B. The binding energy observed for the $Ti2p_{1/2}$ and $Ti2p_{3/2}$ core level peaks for TC sample at 458.8 and 463.7 eV respectively, which are attributed to O-Ti-O linkages in TiO_2.[7] Whereas $Ti2p_{3/2}$ and $Ti2p_{1/2}$ core level peaks for TCS2 sample at 700 degree temperature are observed at 457.9 and 464.1 eV with a decrease in the binding energy value compared to TC indicating that lattice of TiO_2 is considerably modified due to N and S doping.[6] Doping of non-isovalent ion like S^{6+} induce a charge imbalance in TiO_2 matrix, which enhance the formation of oxygen vacancy environment and which results a negative shift in the binding energy peak of Ti2p as well as O1s.[18]

6.2.6. UV-Visible analysis

To investigate the optical absorption properties of the prepared catalysts, the UV-Visible diffuse reflectance spectra pure TiO_2 (TC)

and N, S codoped TiO_2 (TSC) calcined at 700 °C were measured using the absorption data in the range of 200–900 nm and the obtained results were shown in Figure 6.11A. It can be observed that the pure TiO_2 sample has no absorption in the wavelength range greater than 400 nm (visible region), while the incorporation of N and S ions into TiO_2 leads to a reduction in the band gap energy with respect to the red shift in the optical response (Figure 6.11B). The given experimental results indicate that the pure TiO_2 powder shows stronger absorption only at wavelengths less than 400 nm, while TCS nanoparticles shows photoabsorption in the visible region and the absorption edge of TiO_2 shifts to longer wavelength region (Table 6.1). The red shift in absorption spectra of TCS sample is attributed to the transfer of electrons from the filled N2p level formed in between the bandgap to the conduction band of TiO_2, which increased with increase in concentration of non-metal content.

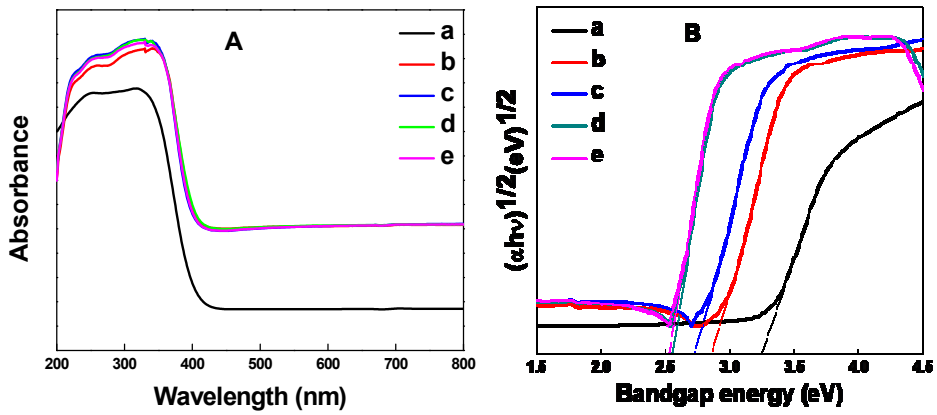

Figure 6.11: A) UV-Visible spectra and B) corresponding Tauc plot of a) TC, b) TCS1, c) TCS2, d) TCS3 and e) TCS4 samples calcined at 700 °C.

According to previous studies, the band gap of TiO_2 nanoparticles can be reduced by non-metal doping and the bandgap narrowing was mostly attributed to the substitution of non-metal ions which introduce a new electronic states into the bandgap of TiO_2 to form a new lowest unoccupied molecular orbital (LUMO), called conduction band (CB).[19,20] The difference in energy between the highest occupied molecular orbital (HOMO), called valence band (VB) and the lowest unoccupied molecular orbital (LUMO), called conduction band (CB) is regarded as band gap energy.[21] Li et al considered that the formation of defects in the TiO_2 crystal lattice by the addition of non-metal ions is the most probable explanation.[22] Similar report regarding the reduction in the bandgap of TiO_2 nanoparticles doped with non-metal ions is also available in the literature.[23] The absorption edge of pure TiO_2 sample was determined at below 400 nm (~3.2 eV). The as prepared samples of TiO_2 are not ideal materials. There are lots of defects found in the crystal structure, mainly oxygen vacancies that influence the absorption edge of TiO_2. Therefore further investigations are needed for the better understanding of the reason behind the band gap narrowing of N, S codoped TiO_2.

Table 6.1: Bandgap energies of the prepared TiO_2 samples calcined at 700 °C

Sample	Bandgap energy (eV)
TC	3.24
TCS1	2.83
TCS2	2.70
TCS3	2.55
TCS4	2.53

6.2.7. Analysis of hydroxyl radical

The emission spectrum of terephthalic acid solution excited at 315 nm was measured after 10 minute illumination of UV radiation on terephthalic acid solution containing 0.1g of the prepared photocatalyst and the results were shown in Figure 6.12 and 6.13. Based on the reports in sonochemistry and radiation chemistry, it was assume that photogenerated O_2^-, $HO_2^{\cdot}$ and H_2O_2 did not interfere in the reaction between $OH^{\cdot}$ and terephthalic acid.[24,25,26] The obtained fluorescence spectrum had the identical shape having an emission intensity at 425 nm. All these results suggested that the fluorescent product, 2-hydroxylterephthalic acid formed during TiO_2 photocatalysis due to the specific reaction between terephthalic acid and hydroxyl radicals. The formed hydroxyl radicals are in directly proportional to the fluorescent intensity of terephthalic acid solution.

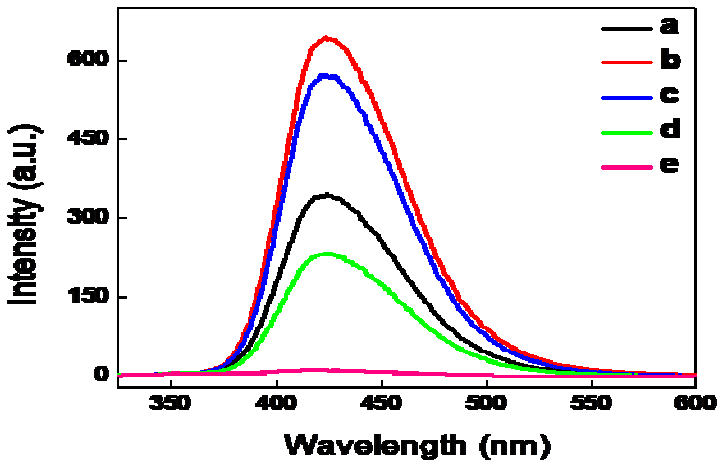

Figure 6.12: Fluorescence spectral changes observed during the UV illumination of a) TCS1, b) TCS2, c) TCS3 ,d) TCS4 and e) TC samples calcined at 700 °C in 4×10^{-4} M NaOH solution of terephthalic acid (Each fluorescence spectrum was recorded at 10 min illumination of UV radiation).

As shown in the Figure 6.12, gradual increase in the intensity of fluorescence at about 425 nm was observed with increase in concentration of dopant in TiO_2 and maximum was obtained at 0.5 weight percentage of dopant (TCS2). Further increase in concentration of dopant decrease the fluorescent intensity of hydroxyterephthalic acid. Therefore, according to Figure 6.12, the formation rate of hydroxyl radicals formed on the surface of cysteine doped TiO_2 was in the order of TCS2>TCS3>TCS1>TCS4>TC, which suggested that doping enhances the formation rate radicals and optimum doping content of cysteine was found to be in TCS2 catalyst. Similarly, calcination temperature also influences the formation rate of hydroxyl radical upon illumination with UV radiation. Figure 6.13 shows that fluorescent intensity increases with calcination temperature and maximum was obtained at a temperature of 700 °C. Further increase in calcination temperature to 800 °C decrease the fluorescent intensity to very lower value due to the decreased amount of hydroxyl radicals formed on the surface of TiO_2 at such a high temperature.

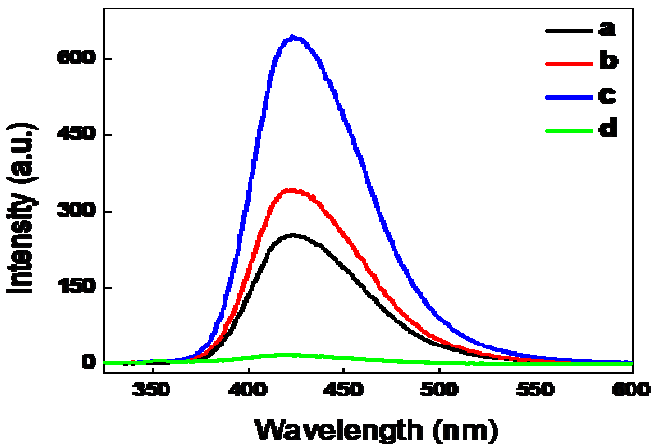

Figure 6.13: Fluorescence spectral changes observed during the UV illumination of TCS2 catalyst calcined at a) 300, b) 500, c) 700 and d) 800 °C in 4×10^{-4} M NaOH solution of terephthalic acid (Each fluorescence spectrum was recorded at 10 min illumination of UV).

6.2.8. Photocatalysis

Methylene blue can be considered as a ubiquitous pollutant and therefore we selected it as a target contaminant chemical for photocatalysis. Generally, the photocatalytic degradation reaction of MB can be described by the pseudo first order reaction. By calculating the apparent reaction rate constant, k_a we can studied the photocatalytic activities of the prepared photocatalyst. The photocatalytic degradation efficiencies of various samples calcined at a temperature of 700 °C are displayed in Figure 6.14. In addition, the apparent reaction rate constant of the as-prepared photocatalysts at various calcination temperature are also displayed in Figure 6.16. For comparison, as-prepared pure TiO_2 catalyst, TC was chosen as reference sample as shown in Figure 6.14 and 6.16. TC shows low efficiency in the photocatalytic degradation of MB under UV as well as direct sunlight irradiation and TCS2 catalyst displayed highest activity. There are also difference in the photodegradation efficiency among TCS1, TCS2, TCS3 and TCS4 catalysts and which reveal the effect of different percentage of the modifier, cysteine. Similarly, TCS2 exhibit higher photodegradation efficiency at a calcination temperature of 700 °C. As shown previously, photocatalytic activity strongly depends the calcination temperature and this temperature affects the crystalline particle size, crystalline phase and optical properties of TiO_2 particles. All these properties vary in accordance with calcination temperature and strongly depends the photodegradation efficiency of the catalyst under solar irradiation.

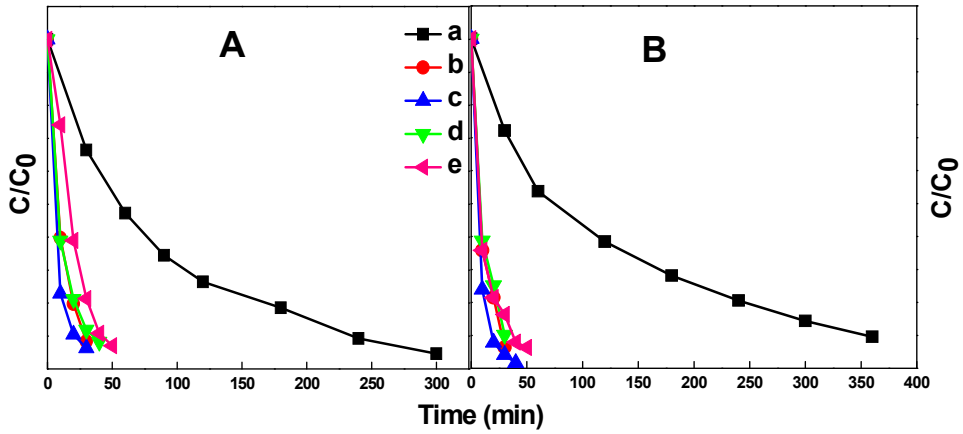

Figure 6.14: Phtodegradtion of MB dye using a) TC, b) TCS1, c) TCS2, d) TCS3 and e) TCS4 calcined at 700 °C under A) UV and B) direct solar irradiation.

For example, high temperature calcination will results an increase in particle size, which might lower the photodegradation efficiency. Yet, higher temperature calcination will also increase crystallinity of anatase phase, which might be enhancing the photodegradation efficiency. Moreover, calcination decreases the capability of the catalyst to absorb in the visible region, which may weaken the photocatalysis under solar irradiation. Therefore cysteine doped TiO_2 calcined at 700 °C exhibited highest photocatalytic efficiency, possibly which was due to synergistic effect of various properties of TCS catalyst like crystallite size, amount of crystalline anatase phase content and red shift in the absorption of radiation. Beside these properties, amount of hydroxyl radical formed on the surface of TiO2 also affect the photodegradation efficiency of the catalyst. Figure 6.12 and 6.13 clearly indicates that, higher amount of hydroxyl radical

formed on the surface of TCS2 catalyst at 700 degree calcination and which support the higher degradation efficiency of the catalyst.

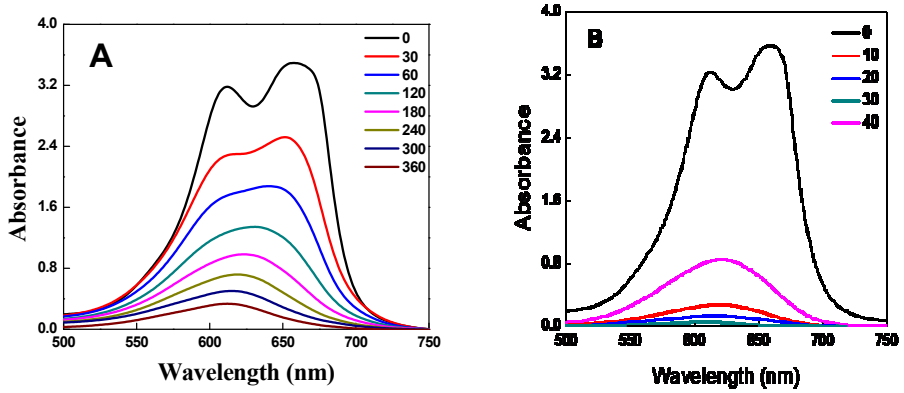

Figure 6.15: Absorption spectra of MB degradation by A) TC and B) TCS2 catalyst calcined at 700 °C under direct sun light.

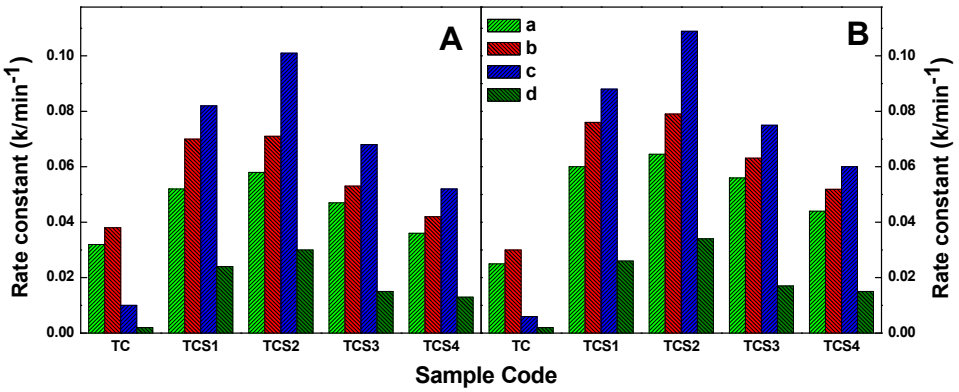

Figure 6.16: Photocatalytic degradation pattern of MB by various catalysts at a calcination temperature of a) 300, b) 500, c) 700 and d) 800 °C in presence of A) UV and B) direct sunlight.

6.3. Conclusions

Visible-light-activated N-S-codoped TiO_2 photocatalyst was synthesized by direct mixing the anatase TiO_2 and cysteine. UV-Vis diffuse reflectance spectroscopy showed that the catalyst exhibited stronger absorption in the visible light region with a red shift in the band gap transition. The phase composition, size and morphology of the synthesized powder were investigated using various techniques such as XRD, XPS, TEM, FTIR, UV-Vis spectroscopy etc. N, S-codoped TiO_2 (TCS) catalyst with 0.5 weight percentage cysteine (700 °C) having entire anatase phase and 21 nm mean diameter shows significantly higher photocatalytic activity under UV and direct solar light irradiation.

References

[1] O. Durupthy, J. Bill and F. Aldinger, Crystal. Growth Des., 2007, **7**, 2696.

[2] D. A. Bazylinski, R. B. Frankel, B. R. Heywood, S. Mann, J. W. King, P. L. Donaghay and A. K. Hanson, Appl. EnViron. Microbiol., 1995, **61**, 3232.

[3] O. V. Makarova, T. Rajh and M. C. Thurnauer, Environ. Sci. Technol., 2000, **34**, 4797.

[4] K. Lv, J. Hu, X. Li and M. Li, J. Mol. Catal. A: Chem., 2012, **356**, 78.

[5] J. Sun, L. Qiao, S. Sun, and G. Wang, J. Hazard. Mater., 2007, **155**, 312.

[6] F. Peng, L. Cai, H. Yu, H. Wang and J. Yang, J. Solid State Chem., 2007, **181**, 130.

[7] P. A. K. Reddy, P. V. L. Reddy, V. M. Sharma, B. Srinivas, V. D. Kumari and M. Subrahmanyam, J. Water Resour. Prot., 2010, **2**, 235.

[8] Y. Zhu, T. Liu and C. Ding, J. Mater. Res., 1999, **14**, 444.

[9] F. Wei, L. Ni and P. Cui, J. Hazard. Mater., 2008, **156**, 135.

[10] L. Ren, X. Huang, F. Sun and X. He, Mater. Lett., 2007, **61**, 427.

[11] X. wang, J. C. Yu, P. Liu, X. Wang, W. Su and X. Fu, J. Photochem. Photobiol., A, 2006, **179**, 339.

[12] J. R. Sohn, H. J. Jang, M. Y. Park, E. H. Park and S. E. J. Park, Mol. Catal., 1994, **93**, 149.

[13] T. Yamaguchi, Appl. Catal., 1990, **61**, 1.

[14] T. Ohsaka, S. Yamaoka and O. Shimomura, Solid state commun., 1979, **30**, 345.

[15] S. P. S. Porto, P. A. Fleury and T. C. Damen, Phys. Rev., 1967, **154**, 522.

[16] M. C. Yang, T. S. Yang and M. S. Wong, Thin Solid Films, 2004, **162**, 469.

[17] Y. Suda, H. Kawasaki, T. Ueda and T. Ohshima, Thin solid films, 2004, **162**, 453.

[18] A. K. Rumaiz, B. Ali , A. Ceylan, M. Boggs, T. Beebe and S. I. Shah, Solid State Commun., 2007, **144**, 334.

[19] J. Yu, M. Zhou, B. Cheng and X. Zhao, J. Mol. Catal. A: Chem., 2006, **246**, 176.

[20] Q. Xiang, J. Yu and M. Jaroniec, Phys. Chem. Chem. Phys., 2011, **13**, 4853.

[21] D. Zhang and F. Zeng, Russ. J. Phys. Chem. A, 2011, **85**, 1825.

[22] D. Li, H. Haneda, S. Hishita and N. Ohashi, Chem. Mater., 2005, **17**, 2596.

[23] F. Dong, W. Zhao and Z. Wu, Nanotechnology, 2008, **19**, 365607.

[24] Q. Xiao, Z. Si, J. Zhang, C. Xiao and X. Tan, J. Hazard. Mater., 2008, **150**, 62.

[25] H. M. Khan, M. Anwar and G. Ahmad, J. Radioanal. Nucl. Chem., 1995, **200**, 521.

[26] X. Fang, G. mark and C. V. Sonntag, Ultrason. Sonochem., 1996, **3**, 57.

CHAPTER 7
Effect of N, F-codoping on the photocatalytic activity of high temperature stable anatase TiO_2

CONTENTS

7.1. Introduction

In the previous chapters we describe the photocatalytic activity of TiO_2 modified by four different organosulfur compounds. All the above modified samples display free radical mediated non-selective photocatalysis. In this chapter, we also elucidate the photocatalytic activity of N, F-doped TiO_2 containing different percentage of ammonium fluoride by taking methylene blue as a target pollutant.

The existing reports shows that fluorine doped TiO_2 is a good challenger in the field of photocatalysis for the mineralisation of various organic pollutant under UV as well as direct sunlight.[1, 2] Yu *et al* reported that the enhanced photoactivity of F^- doped TiO_2 is due the incorporation of fluorine into TiO_2 lattice, which reduce Ti^{4+} into Ti^{3+} and thereby lower the electron-hole recombination rate.[3] Minero *et al* and Park *et al* proposed that F^- ion replaced the surface hydroxyl molecule and hence surface fluorination of TiO_2 enhanced the photocatalytic oxidation of phenol.[4,5] These two reports strongly suggest that both surface and bulk F^- dopant enhanced the photocatalytic performance of TiO_2. However, Yamaki *et al* argued that electronic structure has been modified upon F^- doping around the CB edge of TiO_2 and leads to a good optical response in the visible light region.[6]

In the present chapter, fluorine doped nano dimensional titanium dioxide were successfully prepared through the modification of TiO_2 with various molar ratios of ammonium fluoride (1:0, 1:0.5, 1:1, 1:2 and 1:4 TTIP: NH_4F) by sol-gel method is reported. The modified

samples were labelled as TC, TNF1, TNF2, TNF3 and TNF4 respectively and characterized by various techniques such as XRD, Raman spectra, FTIR, Diffuse reflectance spectroscopy, TEM, FESEM, BET and X-ray photoelectron spectroscopy. A considerable furtherance in the photodegradation efficiency was found for all the fluorine doped TiO_2 with an optimal composition of 1:1 in comparison to the control sample prepared under the same condition.

This chapter further researched the extent to which fluorine modification can enhance the anatase phase stability at higher temperature. Anatase phase is commonly selected for photocatalytic applications due to its better photoactivity. The better photoactivity of anatase phase is due to its lower rate of electron-hole recombination, higher number of hydroxyl radicals present on the surface of TiO_2, lower cost and higher surface area.[7] 100% anatase phase is confirmed from XRD and Raman analysis even at 1000 °C via ammonium fluoride doping. Whereas the control sample contain 86% of rutile as major phase along with anatase at 700 °C. Considerable degradation efficiency is found for the TNF2 catalyst calcined at 900 and 1000 °C.

Unexpectedly F doped sample dried at 100 °C exhibit selective photocatalysis under UV radiation in the degradation of methylene blue over methyl orange. Generally, Nano crystalline TiO_2 follows free radical mechanism for the photocatalytic removal of hazardous compounds seldom resulting in non-selective degradation of compounds.[8] This non-selectivity/poor selectivity limits its application to total selective mineralization of organic pollutants into environmentally benign CO_2, H_2O *etc.* Hence, imparting selectivity in

the TiO_2 photocatalysis is an important goal in the recent photocatalysis research. The selectivity exhibited by TNF catalyst at 100 °C may be due to the moderate crystalline nature and negative charge on the surface of TiO_2, the charge is confirmed from zeta potential measurements.

High temperature stable nanocrystalline anatase TiO_2 is well known for its aqueous mediated non-selective photocatalysis. Non-selective photocatalysis using high temperature stable N-doped and F-doped anatase TiO_2 has been reported for the degradation of methylene blue and acetone respectively.[9,3] N, F co-doped TiO_2 for acetaldehyde decomposition was also reported and results showed that N, F co-doped TiO_2 samples have superior photocatalytic activity compared to the undoped TiO_2.[10] However, selective photocatalysis and/or selective organic pollutant (*e.g.* dyes) degradation of high temperature stable TiO_2 is not yet reported. Here we report high temperature stable nanocrystalline TiO_2 for the selective photocatalytic degradation of ionic dyes from an aqueous mixture of methyl orange (MO) and methylene blue (MB) under UV light.

TiO_2 samples calcined at 500 and 700 $^{\circ}$C (TNF2 at 500 & 700 °C) selectively degraded cationic methylene blue (MB) over anionic dye, methyl orange (MO) from an aqueous mixture of MB and MO dye. The selective photocatalysis was well accounted by zeta potential measurements.

7.2. Results and Discussion

7.2.1. X-ray diffraction technique

X-ray diffraction pattern was used to determine the crystallite size and phase compositions of the control and N, F-codoped TiO_2 at different calcination temperatures. Anatase titania has a main peak at $2\theta = 25.2°$ (characteristic diffraction of 101 plane), that of rutile phase is at 27.4 ° (characteristic diffraction of 110 plane) and brookite at 30.8 ° (characteristic diffraction of 121 plane). The X-ray diffraction patterns of the control sample TC, 0.5, 1 and 2 weight% of NH_4F doped TiO_2 powders calcined at 500 °C are given in Figure 7.1 and which shows that all the TNF samples calcined at 500 °C are completely in anatase form which is evident from the absence of characteristic diffraction peaks of rutile and brookite. Whereas the control sample TC at 500 °C comprise a mixture of anatase and brookite phases, dominated by the former one (Figure 7.1-a).

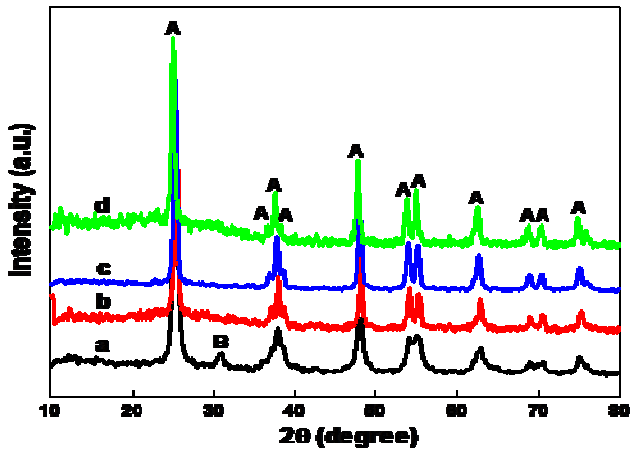

Figure 7.1: X-ray diffractogram of a) TC, b) TNF1, c) TNF2 and d) TNF3 calcined at 500 °C.

The XRD pattern of TNF powder indicates that presence of fluoride ion has a greater effect on the phase transition temperature of anatase to rutile TiO_2. Phase transformation temperature of anatase to rutile is increased in the case of ammonium fluoride doped sample and about 100% anatase phase is present at both 500 and 700 °C. Further increase in temperature of TNF sample to 1000 °C sustains the titania sample in 100% anatase form (Figure 7.3). However, in the control sample TC, anatase to rutile conversion started at calcination temperature above 500 °C and at 700 °C, rutile appeared as the major phase with a phase composition of 84/16 for rutile/ anatase respectively, and the brookite phase was disappeared (Figure 7.2). The major reason behind the early transformation of anatase to rutile in the control sample, TC at 500 °C is due to the presence of brookite phase along with anatase. Hu *et al* reported that presence of brookite form enhance the anatase to rutile phase transformation.[11] The absence of brookite peak in TNF sample may be due to the presence of F^- ion, which suppress the crystallisation of brookite by adsorbing on to the surfaces of TiO_2 particles and thereby enhanced the anatase to rutile phase transition temperature.[10]

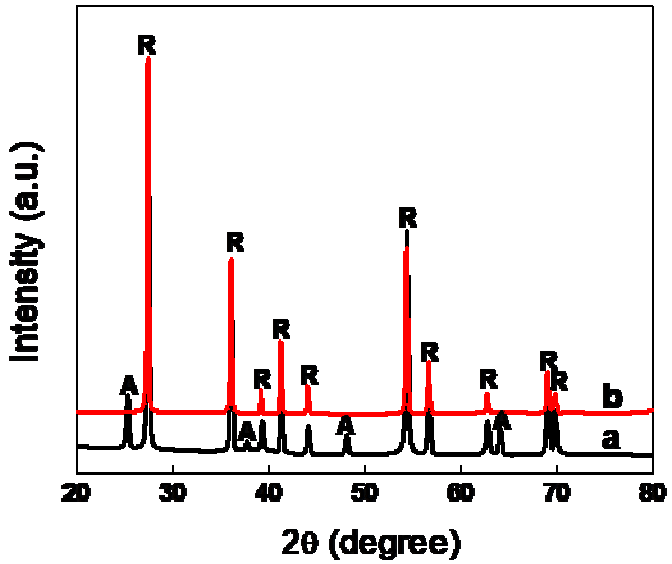

Figure 7.2: Diffractogram of TC at a) 700 and b) 800 °C.

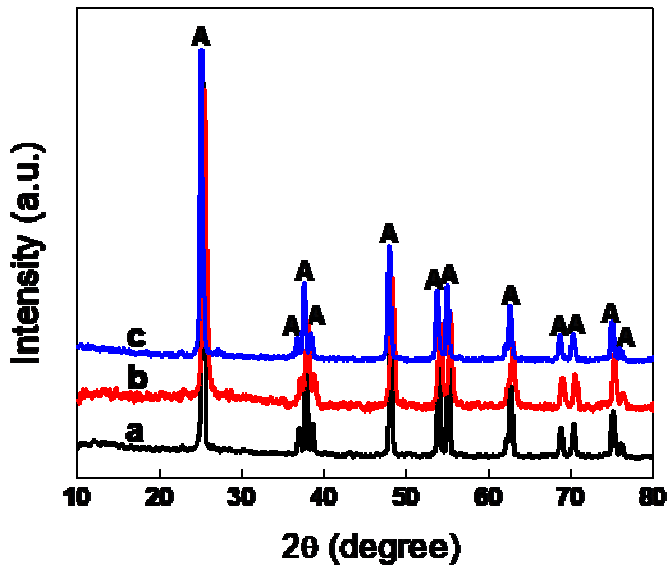

Figure 7.3: X-ray diffractogram of TNF catalyst at a) 700, b) 800 and c) 1000 °C.

Explanation has been given for the improved anatase to rutile phase transition temperature of F-doped TiO_2 based on HSAB principle by Izumi *et al.* According to HSAB principle, hard acid like Ti^{4+} have a strong affinity with hard base like fluoride ion and this will inhibit the anatase to rutile phase transition.[12] The easiness of the incorporation of fluoride ion into TiO_2 matrix due to the similarities in electronegativity and ionic radius between fluoride and oxide ion also support the above fact.[13]

Table 7.1 shows the crystallite size of the prepared samples calcined at 500 and 700 °C by using Scherrer formula (equation 2.1). The crystallite size of the nanoparticle at a calcination temperature of 700 °C is noted to be higher than that at 500 °C. The sudden increase in the crystallite size of the undoped sample at 700 °C may be due to the conversion of anatase to rutile phase at above 500 °C.[14, 15]

Table 7.1: Crystallite size of the sample at 500 and 700 °C

Sample	Crystallite size (nm)	
	500 °C	700 °C
TC	12.02	28.4
TNF1	16.45	20.07
TNF2	15.05	19.38
TNF3	16.85	21.52

7.2.2. FTIR spectroscopy

Figure 7.4 shows the FTIR spectra of TNF2 and TC measured in the range of 400 to 4000 cm^{-1} at room temperature. The broad peak at 2800–3500 and 1600 cm^{-1} in all spectra indicate stretching and bending vibrations of the hydroxyl group respectively, present on the surface of TiO_2 catalyst.[16] The broad peak centered at 540 cm^{-1} is attributed to the Ti-O-Ti stretching vibrations.[17] FTIR peak at 1448 cm^{-1} corresponding to the N-H bending vibration has been reported for gas phase NH_4F. Here as synthesised TNF samples have recorded a sharp peak at 1405 cm^{-1} which could attributed to N-H bending vibrations.[18,19] The peak shift could be attributed to the weakening of N-H bond as a result of the interaction of newly formed Ti-F bond at 927 cm^{-1}.[20] The newly formed Ti-F bond indicates the incorporation of F^- ion into TiO_2 crystal lattice in TNF samples. Due to the decreased amount of fluorine in the calcined sample (TNF2 at 500 and 700 °C), the peak at 927 cm^{-1} corresponding to Ti-F bond has been slightly vanished (Figure 7.4).

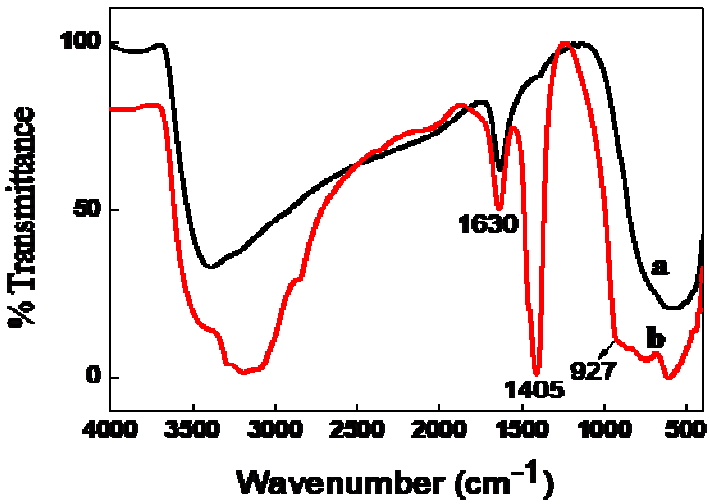

Figure 7.4: FTIR spectra of the TiO_2 samples (a) TC and (b) TNF dried at 100 ºC.

7.2.3. Raman spectra

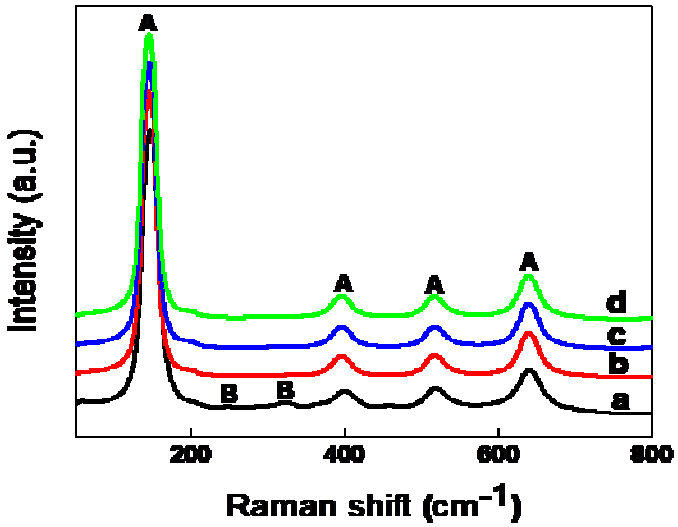

Figure 7.5: Raman spectra a) TC, b) TNF1, c) TNF2, d) TNF3 calcined at 500 °C.

The formation anatase phase via ammonium fluoride doping is further confirmed by Raman analysis. According to factor group analysis, there are five Raman active modes { 145 (E_g), 197 (E_g), 639 (E_g), 399 (B_{1g}) and 513cm^{-1} (A_{1g}+ B_{1g}) } for anatase TiO_2 and four for rutile phase { 143 (B_{1g}), 447(E_g), 612(A_{1g}) and 826 cm^{-1} (B_{2g}) }.[21,22] Two intense peaks at 145 and 639 cm^{-1}, and two less intense peaks at 399 and 513 cm^{-1} clearly shows the presence of anatase phase for the doped and control sample calcined at 500 °C as shown in Figure 7.5. Presence of brookite phase in the sample, TC at 500 °C is confirmed from the observed Raman peak at 251 and 321 cm^{-1}, which are the characteristic Raman peaks of brookite phase (Figure 7.5-a). The peaks at 447 and 612 cm^{-1} appears along with other characteristic peak of anatase phase in TC at 700 °C indicating the conversion of anatase to rutile in the control sample and which is consistent with the XRD results (Figure

7.6). Figure 7.6-b confirms the complete rutile formation occurred in the control sample, TC at 800 °C. Absence of rutile phase in the Raman spectra of doped samples even at 1000 °C (Figure 7.7) confirms high temperature anatase phase purity of TNF2 catalyst.

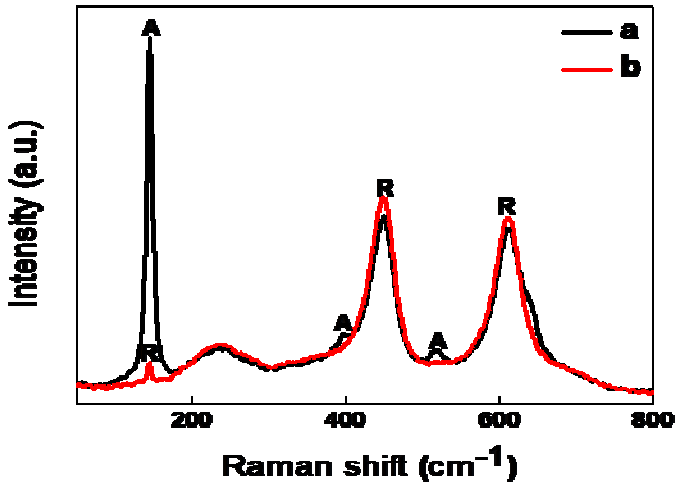

Figure 7.6: Raman spectra of the control sample TC at a) 700 and b) 800 °C.

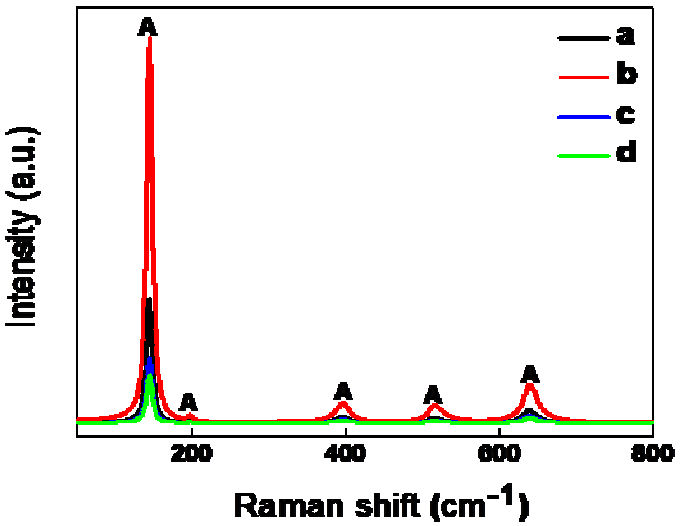

Figure 7.7. Raman analysis of TNF2 catalyst calcined at a) 700, b) 800, c) 900 and d) 1000 °C.

7.2.4. Diffuse Reflectance Spectroscopy

The diffuse reflectance spectral analysis was carried out to study the optical absorption properties of TNF and TC samples at various calcination temperatures. Figure 7.8 clearly shows the absorption characteristics of N, F – codoping on TiO_2. As in the previous report, control sample TC shows an absorption edge at 390 nm in the UV range. The absorption spectra of the doped sample exhibit a red shift in the absorption band when we compare with that of pure TiO_2 sample, TC (Figure 7.8A). It is also observed that when doping concentration increased from 0.5 to 4 %, the absorption edge shifted to higher wavelength in the visible region (Table 7.2). Li *et al* observed that F-doping did not cause any significant shift in the fundamental absorption edge of pure TiO_2.[23,6] However, Burda *et al* reported N-doping shift the band gap absorption onset from 380 to 600 nm.[24] Due to the combined effect of both nitrogen and fluorine on TiO_2, a new absorption band at 390-540 nm in the visible range was observed for the TNF2 sample calcined at 500 °C (Figure 7.9).[10]

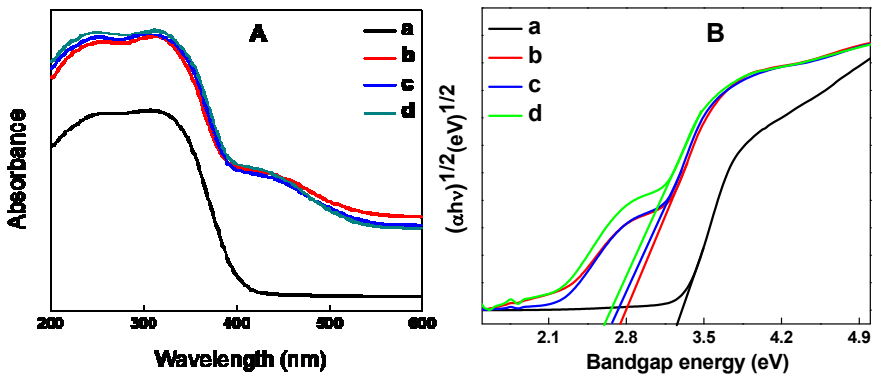

Figure 7.8: A) Diffuse reflectance spectral analysis and B) corresponding Tauc plot of a) TC, b) TNF1, c) TNF2 and d) TNF3 calcined at 500 °C.

Similarly, Figure 7.9 shows that as the calcination temperature increases from 300 to 500 °C, the absorption band at 390-540 nm is retained as such. However, further increase in the calcination temperature to 700 °C almost lost the absorption band intensity, which may be due to the escaping tendency of N and F as the calcination temperature increases. XPS spectra confirm the presence of N and F in TNF2 catalyst at 500 °C as shown in Figure 7.14.

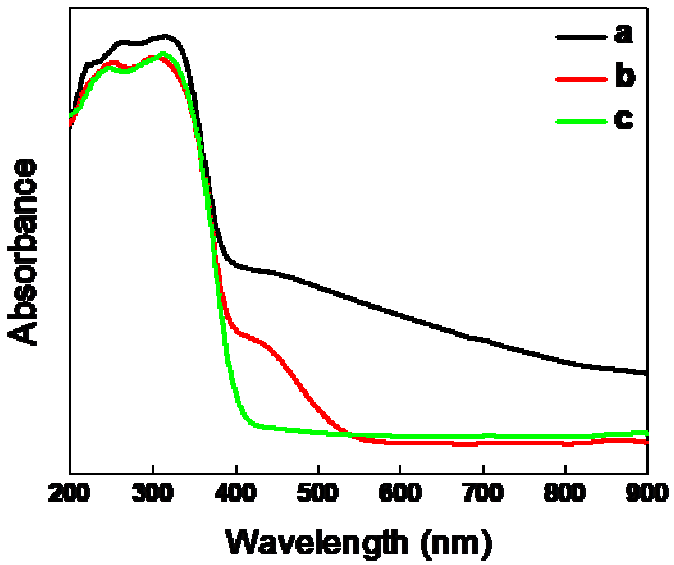

Figure 7.9: Diffuse reflectance spectra of TNF2 catalyst at a) 300, b) 500 and c) 700 °C.

Usually, the photocatalytic reaction rate is directly proportional to $(I_\alpha \phi)^n$ (n=1/2 for high light intensity and n=1 for low light intensity), where I_α is the photon number absorbed by the photocatalyst/second and ϕ is the band gap transition efficiency.[25] The enhancement in the photocatalytic activity through NH_4F doping can be partially explained

on the basis of an increase in the value of $I_{\alpha}\phi$ which results from the intense absorption of radiation from the visible region of solar light.[3,25] The observed red shift in the absorption spectra of TNF sample from UV to visible region increased the number of photogenerated electrons and holes in photocatalytic reactions, which results an enhancement in the photocatalytic activity.

The band gap energy can be determined from the tauc plot of $(\alpha h\upsilon)^{1/2}$ against photon energy ($h\upsilon$) as shown in figure 7.8B (where α is the tauc function) and which can be calculated by extrapolating the interception of the tangent of the plot. The calculated band gap energies of the doped and undoped sample calcined at different temperature were shown in Table 7.2.

Table 7.2. DRS data of TC and TNF2 samples.

Calcination temperature (°C)	Band gap energy (eV)				
	TC	**TNF1**	**TNF2**	**TNF3**	**TNF4**
100	3.16	3.14	3.12	3.02	3.0
300	3.23	2.65	2.47	2.45	2.43
500	3.22	2.72	2.64	2.6	2.57
700	3.24	2.96	2.77	2.76	2.74

7.2.5. TEM

Figure 7.10 shows the TEM and HRTEM images of TC and TNF2 powders calcined at 500 °C. From TEM, the average crystallite size calculated for TC and TNF2 sample is 11 and 22 nm respecively. These results reveal that TNF sample has larger anatase crystal size

compared to the control TC. This is ascribed to the fact that greater the amount of F^- ions incorporated into the TiO_2 xerogel network, stronger is the promoting action of anatase TiO_2 crystallization.[10] This would favour the formation of larger TiO_2 crystallites in TNF2 compared to undoped TiO_2 at 500 °C. The selected area diffraction (SAED) pattern of F^- doped (TNF2 at 500 °C) sample (inset of Figure 7.10D) showed sharp polymorphic ring connected via distinct spots point out the sharp diffraction pattern and crystallinity of anatase TiO_2 and it is in accordance with the data obtained from the XRD results.

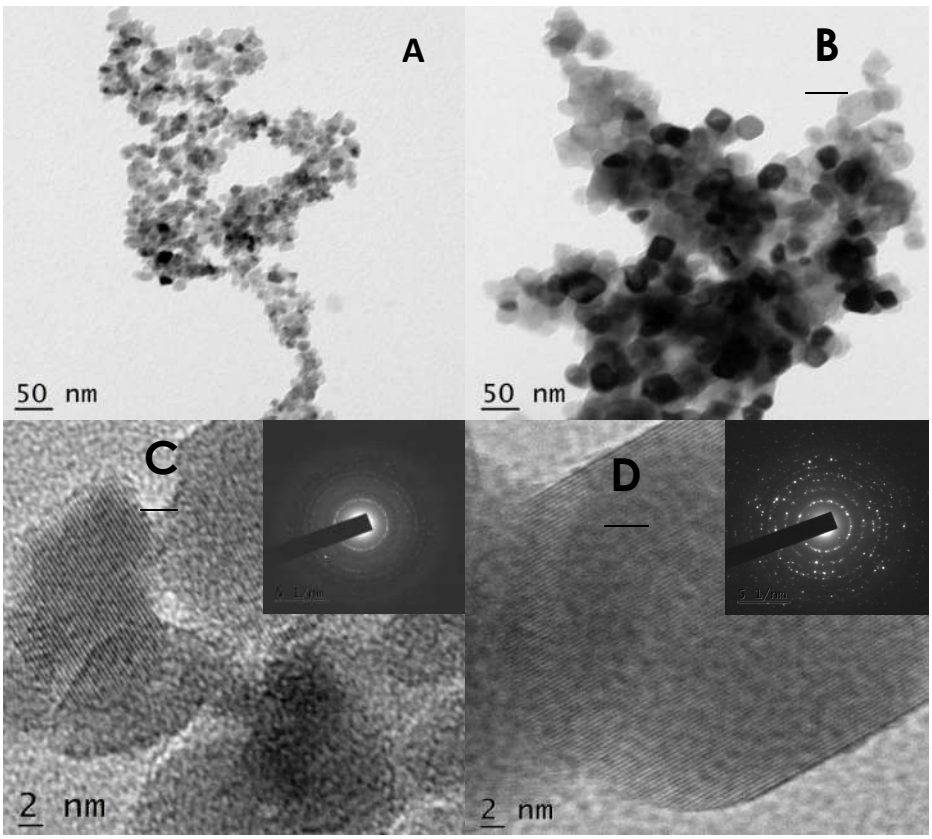

Figure 7.10: TEM images of (A) TC, B) TNF2 sample and HRTEM images of C) TC and D) TNF2 (all the samples were calcined at 500 °C) inset shows the corresponding SAED pattern.

7.2.6. FESEM images

FESEM technique was used in order to determine the shape and morphology of the calcined materials. Figure 7.11 shows the FESEM images of TC and the modified TNF2 nanoparticles calcined at 500 °C. From the image shown in Figure 7.11B, it is evident that the undoped TiO_2 particles at 500 °C are highly agglomerated and no definite shape or morphology can be seen. However, doped TNF2 sample at same temperature calcination (Figure 7.11A) clearly show the presence of individual particles grouping up to form large agglomerated, rugged structures. Clearly, the modified TNF2 particles were 15- 25 nm in size with uniform distribution and that of TC is in between 10-20 nm at a calcination temperature of 500 °C.

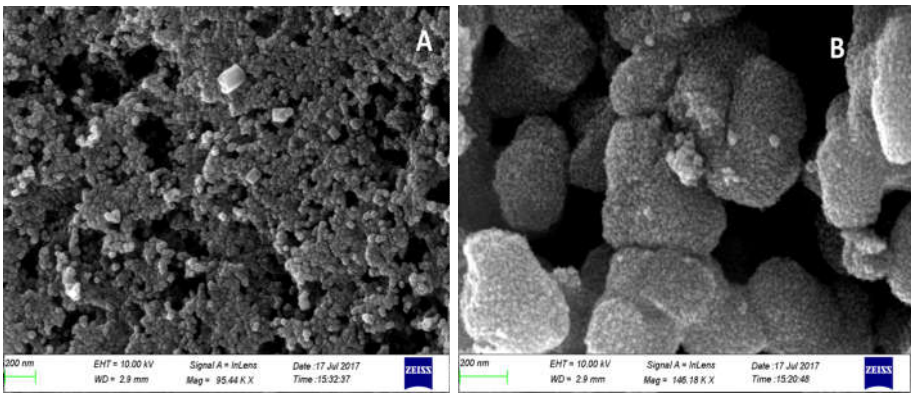

Figure 7.11: FESEM images A) TNF2 and B) TC calcined at 500 °C.

7.2.7. Surface area analysis

The surface area, pore volume and desorption pore size of the synthesized TiO_2 sample were measured using the BET surface area analyzer. Figure 7.12 shows the nitrogen adsorption-desorption

isotherms of doped and undoped TiO_2 at 500 °C. The adsorption and desorption isotherm of all the titania samples exhibit Type IV behaviour with a typical hysteresis loop and which represents the mesoporous nature of the material.[26] The mesoporous nature of the samples is also evident from the adsorption and desorption pore size measurement (Table 7.3). TNF2 sample display slightly higher surface area than TC and which showed a dependence of ammonium fluoride on the surface area of TiO_2. FESEM images clearly shows the existence of highly agglomerated structure for TC than TNF2 at 500 °C and this aggregation of particle will reduce the surface area of undoped TiO_2.

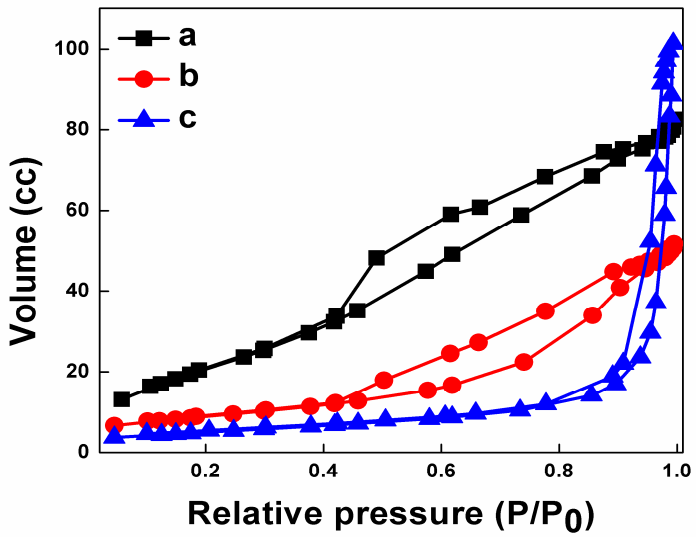

Figure 7.12: Nitrogen adsorption-desorption isotherm of a) TNF2 and b) TC at 500 and c) TNF2 at 700 °C.

Table 7.3. Surface area (BET) and pore parameters of TC and TNF2 samples.

Sample	BET surface area (m^2/g)	Pore volume (cm^3/g)	BJH desorption pore size (nm)
TC100	79.19	0.219	8.76
TC500	34.54	0.092	12.96
TNF100	139.27	0.102	3.42
TNF500	82.35	0.130	9.32
TNF700	18.46	0.1001	31.97

7.2.8. X-ray photoelectron spectroscopy

X-ray photoelectron spectroscopy (XPS) was carried out to explore the incorporation of nitrogen and fluoride ion in the doped sample (TNF2) at 500 and 700 °C. Figure 7.13 A and B shows the XPS survey spectrum of TC and TNF2 sample calcined at 500 and 700 °C and peaks appeared at 684.9 (F1s) and 400.8 eV (N1s) for TNF2 sample indicating the successful doping of fluorine and nitrogen atom on TiO_2.

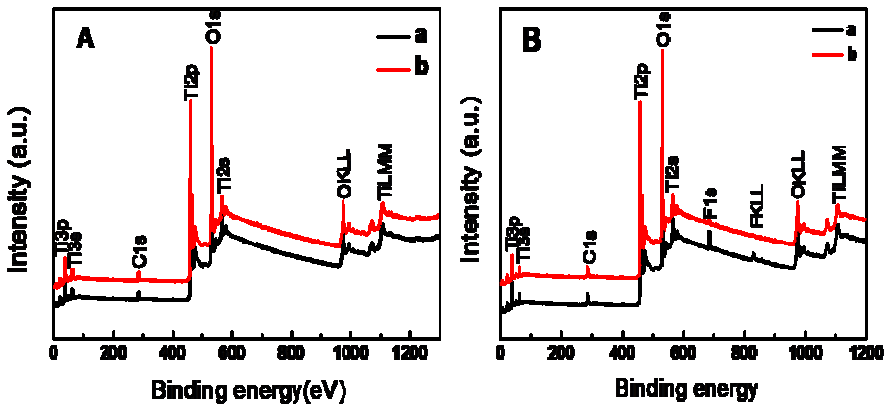

Figure 7.13: XPS survey spectra of A) TC and B) TNF2 sample calcined at a) 500 and b) 700 °C.

The high resolution XPS spectra of F1s and N1s region of TNF2 sample at 500 and 700 degree calcination are portrayed in Figure 7.14B. Yu *et al* observed the presence of higher binding energy peak at 688.4 eV for substitutional lattice fluorine ion and peak centered at 684.6 eV is to be associated with surface fluorination. The photoelectron peak observed at a binding energy of 684.9 eV for TNF2 sample at 500 °C confirm the surface fluorination *via* the formation of terminal Ti-F bond.[3,27] However after 700 degree calcination the intensity of XPS peak of F1s is diminished due to the slow evaporation of elemental F, suggesting that the F^- ion is not stable in TiO_2 surface at such a high temperature (Figure 7.14B).

In the case of surface fluorination, F^- ion replaces an isoelectronic OH^- group to form terminal Ti-F bond without generating reduced centres as well as no alteration in the charge. However,

the free hydroxyl molecules may occupy on the surface of TNF2 samples, which enhanced the photoactivity of titania.

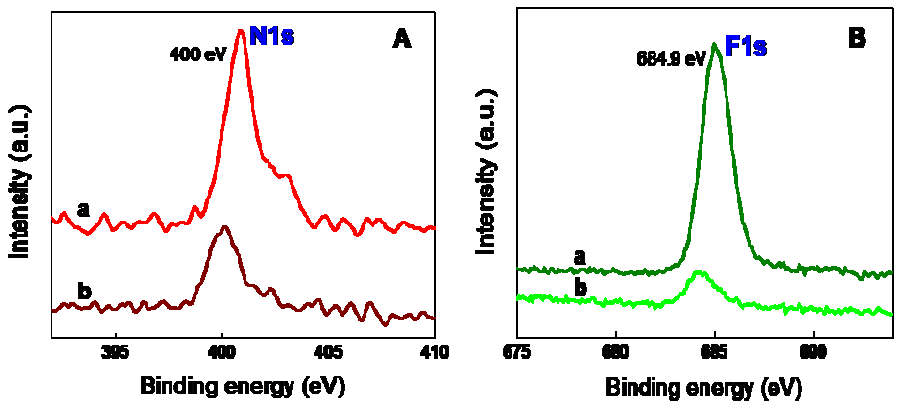

Figure 7.14: High resolution XPS spectra of A) N1s and B) F1s of TNF2 sample at a) 500 and b) 700 °C.

It was previously reported that two peaks, peak 1 at the range of 400-402 eV and peak 2 at 396 eV, were observed for N-doped sample. Generally peak 2 can be considered as the sign for the presence of Ti-N bond through the replacement of oxygen atom by nitrogen in the TiO_2 crystal lattice.[28,29] The signal observed at 400.8 eV for TNF2 at 500 °C shows the absence of Ti-N bond formation, which suggests the presence of nitrogen as a result of chemisorbed N_2 molecule in the doped sample.[30,31]

Blue shift in the binding energy peak of Ti2p and O1s is observed for TNF2 from TC at 500 °C, which represents a change in the oxygen environment (Figure 7.15 C and D).[32,33] TiO_2 having oxygen rich compositions usually exhibit a light yellow colour

(inset of Figure 7.15D). The light yellow colour of TNF sample well support the oxygen rich nature as evidenced from the XPS and the control sample doesn't exhibits such oxygen richness as evidenced from its pure white colour. High temperature Calcination again shifted back the binding energy peak of TNF2 to the peak position of TC at 500 °C indicating the absence of oxygen rich environment in TNF2 at 700 °C.

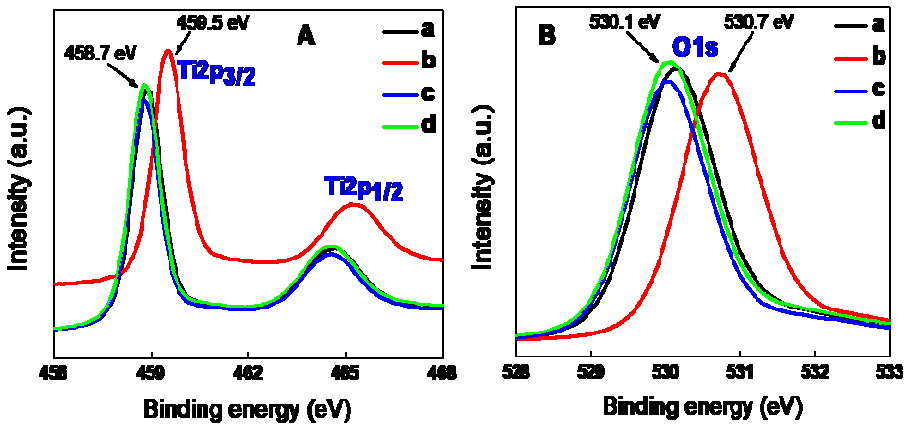

Figure 7.15: High resolution XPS spectra of A) Ti2p and B) O1s of a) TC at 500 °C, b) TNF2 at 500 °C, c) TC at 700 °C and d) TNF2 at 700 °C.

The valence band XPS (Figure 7.16) shows that the valence band edge is located at 2.71 eV and 2.14 eV for TC500 and TNF500 below the Fermi energy confirming the substantial binding energy shift of 0.57 eV by introducing oxygen richness.[32] Since the optical band gap of TC at 500 °C is 3.22 eV, the conduction band minimum would occur at -0.51 eV as depicted in the DOS diagram (Figure 7.17). From Figure 7.17, TNF2 at 500 ° displays a conduction band minimum at -0.5 eV.[31]

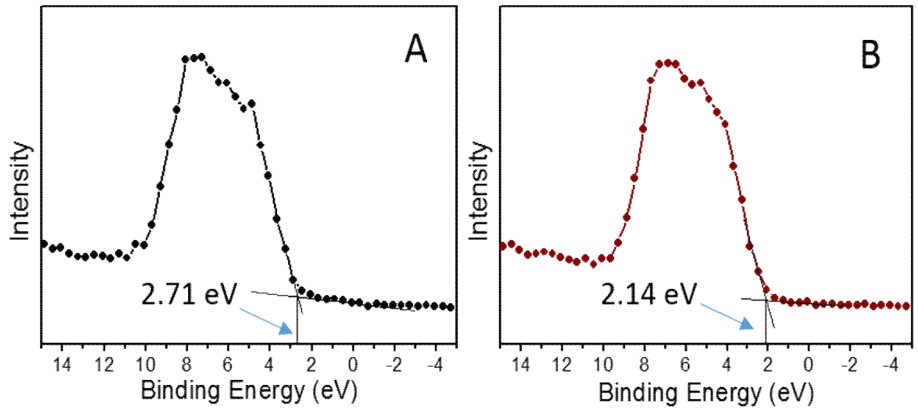

Figure 7.16. Valence band XPS spectra of A) TC500 and B) TNF500.

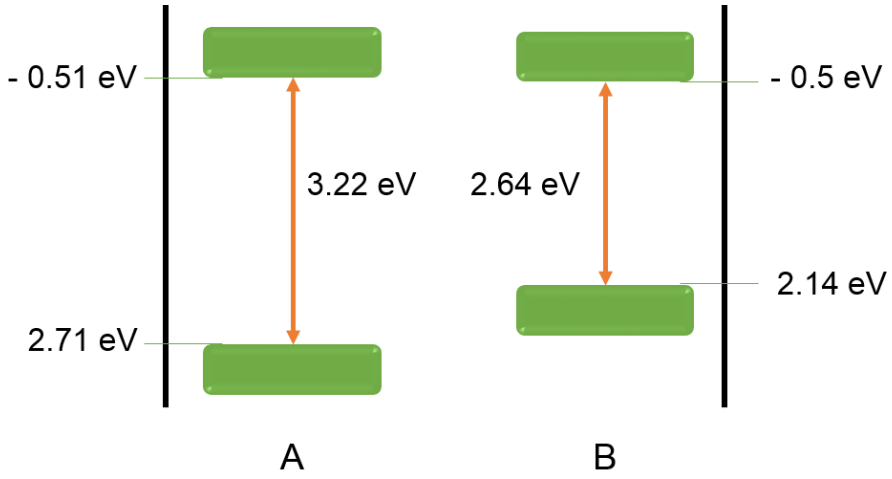

Figure 7.17: Density of States (DOS) of A) TC500 and B) TNF500.

7.2.9. Zeta (ζ) potential measurements

The Zeta (ξ) potential is the electrostatic potential that exists at the shear plane of a particle, which is related to both surface charge and the local environment of the particle.[34] In order to have a better understanding on the charge on the TiO_2 surface

which may favour the selectivity of dye mixture during the photocatalysis reaction, ζ–potentials of TiO_2 nanoparticles dispersed in distilled water were measured and the result is pictorially represented in Figure 7.18. TNF2 at 100 (-23.3 mV) and 500 °C (-12.4 mV) showed negative surface charge whereas the control sample TC at 100 (0.183 mV) and 500 °C (1.08 mV) showed positive surface charge. The surface charge of TNF2 at 500 °C was decreased by 10.9 mV from TNF2 at 100 °C because of the increased mobility of ions by getting thermal energy through calcination. Calcination at 700 °C further decreased the zeta potential value to -4.97 mV from -12.4 mV due to the same reason as that of TNF2 at 500 °C.

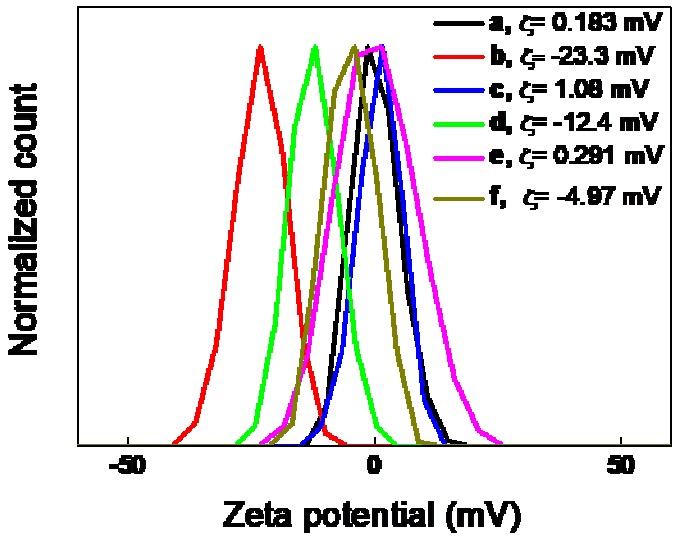

Figure 7.18: Zeta potential measurements of a) TC100, b) TNF100, c) TC500, d) TNF500, e) TC700 and f) TNF700.

7.2.10. Measurement of hydroxyl radical concentration

The photocatalytic activity was further confirmed by the detection of hydroxyl radical formed on the surface of TNF and TC samples. Figure 7.19 and 7.20 shows the changes in the intensity of fluorescence spectra of terephthalic acid solution containing prepared TiO_2 catalyst at various calcination temperatures exposed for 10 minute irradiation of UV light. The PL intensity is shown maximum at about 425 nm for the N, F codoped TiO_2 sample, TNF2 calcined at 500 °C. However, no fluorescent emission is observed in the absence of UV light irradiation or the N, F –TiO_2 sample. This result indicates that fluorescence arises from the chemical reactions between terephthalic acid and OH radical formed on the illuminated TiO_2 sample.[35] Consequently, it can be suggested that the amount of OH radicals generated on the surface of TiO_2 is proportional to the PL intensity. This result also inferred that the holes generated by the UV light excitation acquire su□cient oxidation power and can be transferred to the surface adsorbed hydroxyl groups and /or water molecules. In addition to these, it should be noted that along with effective route that holes attack hydroxyl groups or water molecules, another well-known route of producing $OH^{\cdot}$ radicals is that the photogenerated electrons on the conduction band participate in redox reactions on the TiO_2 surface.[35] All these results obtained in Figure 7.19 and 7.20 imply that the samples showing higher PL intensity has the highest photocatalytic activity.

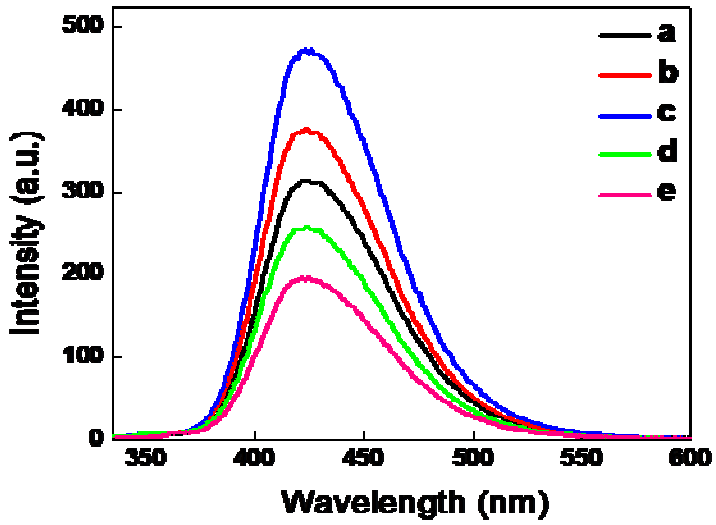

Figure 7.19: PL changes observed during illumination of a) TC, b) TNF1, c). TNF2, d) TNF3 and e) TNF4 samples calcined at 500 °C for 10 minute in 10^{-4} M NaOH solution of terephthalic acid under UV illumination (excitation at 315nm).

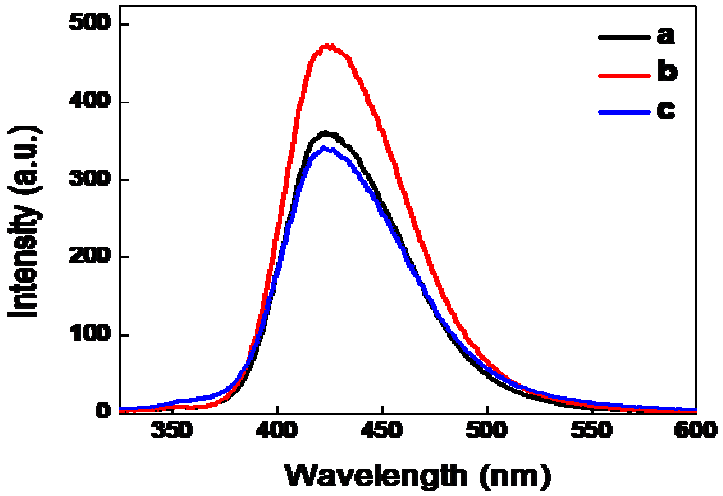

Figure 7.20: PL changes observed during illumination of TNF2 samples calcined at a) 300, b) 500 and c) 700 degree temperature for 10 minute in10^{-4} M NaOH solution of terephthalic acid under UV illumination (excitation at 315nm).

7.2.11. Photocatalysis

The photocatalytic degradation efficiency depends upon several parameters such as crystallinity, number of hydroxyl radical formed on the surface of TiO_2, assemblage of crystal phase and optical properties. The synergistic effect of these various properties plays a major role in the photodegradation efficiency of the prepared catalyst.

The photocatalytic property was studied using both TC and TNF samples synthesized at a calcination temperature of 300,500 and 700 °C under UV and sunlight and the corresponding reaction rate constant obtained from the degradation kinetics were summarised in Figure 7.21. Generally, the photodegradation reaction of methylene blue follows pseudo first order kinetics. Comparing the photocatalysis in the presence of UV and sunlight, reaction rate for the degradation of methylene blue under direct sunlight irradiation is more compared to UV light irradiation. Usually, the photocatalytic reaction rate is directly proportional to $(I_\alpha \phi)^n$ (n=1/2 for high light intensity and n=1 for low light intensity), where I_α is the photon number absorbed by the photocatalyst/second and ϕ is band gap transition efficiency.[25] Upon N, F codoping, TiO_2 increases its wave length of absorption from UV to visible region and decreases its band gap energy to lower value. The enhancement in the photocatalytic activity in sunlight through doping can be partially explained on the basis of an increase in the value of $I_\alpha \phi$ which results from the intense absorption of radiation from the visible region of solar light.[3, 10]

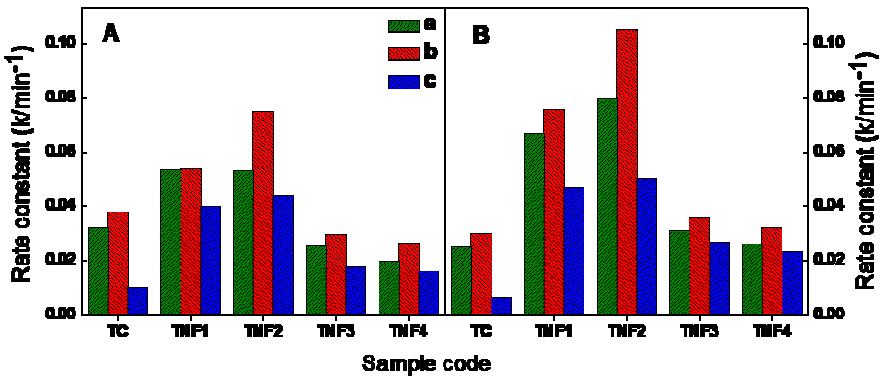

Figure 7.21: Reaction rate constant for the degradation of methylene blue by different wt% ammonium fluoride doped TiO_2 at 300, 500 and 700 °C under A) UV and B) direct sunlight.

The calcination temperature seems to influence the photoactivity of both doped and undoped samples and same trend was followed by both with increase in calcination temperature. That is, both the doped and undoped sample initially rise the photocatalytic activity with calcination temperature and maximum is obtained at 500 °C. Above 500 °C, the photoactivity seem to decrease and which clearly shown in Figure 7.21.

From the rate constant calculated through the degradation kinetics, highest activity was obtained for 1 wt% ammonium fluoride doped TiO_2 (TNF2) at 500 °C with a value of 0.1074 min^{-1} under sunlight while its control sample has only a value of 0.03 min^{-1}. Figure 7.22 shows a decrease in the concentration of methylene blue content in the presence of TNF catalyst in different dopant concentration at 500 °C with respect to undoped sample at the same temperature. All the N, F codoped catalyst calcined at 500 °C has 100% anatase phase and there is no contribution from the phase structure of titania to differentiate the

photo activity. It is well known that crystallite size strongly depends the photocatalytic activity of nanocrystalline titania and so the crystallite size of TNF catalyst determines the highest activity. To get better photocatalytic activity for nano TiO_2, the reported critical size limit is approximately 15 nm and above or below this value, the photoactivity of titania decreases.[36,37] Maximum number of hydroxyl radicals formed on the surface of TiO_2 at critical crystallite size limit and factor support the better photocatalytic performance of TNF2 catalyst at 500 °C. From Table 7.1, it is understood that crystal size of TNF2 at 500 °C is 15.05 nm and which strongly support the highest activity. Figure 7.19 and 7.20 clearly shows that maximum number of hydroxyl radical formed on TNF2 catalyst calcined at 500 °C.

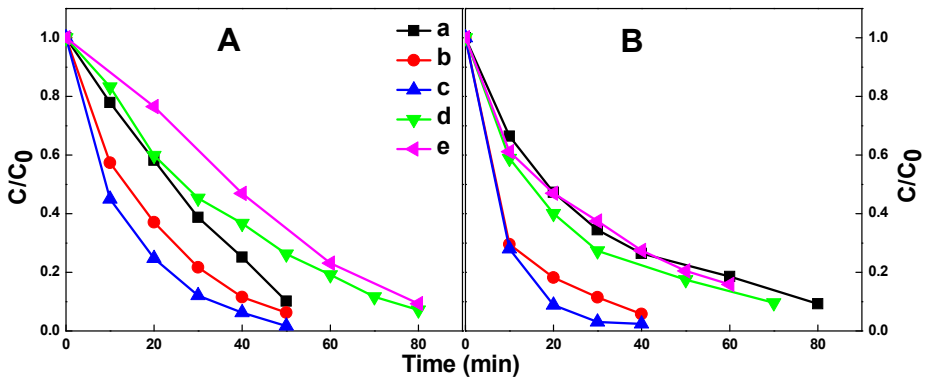

Figure 7.22: PhotodegradationVs time plot of methylene blue using a)TC, b)TNF1, c)TNF2, d)TNF3 and TNF4 calcined at 500^0C A) UV light B) Sunlight.

The high resolution XPS of Ti2p of TNF2 at 500 °C (Figure 7.14B) confirm the oxygen richness of the sample and which support the higher photodegradation efficiency of the sample. XPS spectra of F1s

of TNF2 catalyst strongly suggest the replacement of hydroxyl molecule on the surface of TiO_2 by fluoride ion. The replaced hydroxyl molecules easily converted to hydroxyl radical and boost the photodegradation efficiency of TNF2 catalyst at 500 °C. Higher temperature calcination (700 °C) again decreased the photodegradation efficiency by half and which is due to the decreased fluorine content in the sample (confirmed from XPS- Figure 7.14B). The difference in the photocatalytic activity of TNF2 at 500 and 700 °C indicate the significance of fluorine in the photocatalysis of TiO_2.

7.2.12. Amplified photoactivity of titania at high temperature calcination

The photocatalytic study of TNF2 sample is further extended to high temperature calcination due to the anatase phase stability observed for the sample at high temperature calcination. There are several factors which depends on the phase transformation of anatase to rutile such as grain size, surface area of the anatase phase, presence of impurity, surface structure and concentration of anion vacancy.[38,39,40,41] This transition follows first order kinetics and the activation energy for this conversion is approximately 418 kJ/mol. Thermal treatment facilitates the breaking of Ti-O bond in the anatase phase and simultaneous rearrangement of atoms will boost the anatase to rutile transformation.[42] Several researchers have discussed the anatase to rutile phase transition and how different type of additives affects these phase transformation. Of these Periyat *et al* developed 20% anatase phase at 900 °C for sulphur doped TiO_2,[37] Fagan *et al* recently reported the stability of 100% anatase phase even at 1000 °C for N, P,

F codoped TiO_2,[43] etc. However, we prepared 100% anatase TiO_2 stable at 1000 °C through simple F-doping by sol gel technique.

Table 7.4: Anatase and rutile phase composition present in the control and modified samples at different temperatures.

Temperature (°C)	Sample			
	TNF2		TC	
	Anatase	Rutile	Anatase	Rutile
700	100	0	14	86
800	100	0	0	100
900	100	0	0	100
1000	100	0	0	100

The anatase phase stability of nanocrystalline TiO_2 powders upon codoping with N and F has a significant influence in improving the photocatalytic efficiency of TiO_2 samples calcined at higher temperature. Table 7.4 shows the anatase to rutile phase composition obtained from the X-ray diffraction technique of TC and TNF2 sample at different temperature. X-ray diffraction study revealed that TNF2 sample calcined at 1000 °C exist in 100% anatase form, whereas those of the control sample completely converted to rutile form at 800 °C (Figure 7.2 and 7.3). Raman spectra also confirm this high temperature anatase phase stability of TNF2 sample as shown in Figure 7.6 and 7.7.

Table 7.5: Reaction rate constants of the TNF2 and TC at different temperatures.

Temperature (°C)	Reaction rate constant of the samples (min^{-1})			
	UV light		Direct solar light	
	TNF2	TC	TNF2	TC
800	0.0323	0.0045	0.0372	0.0041
900	0.0264	0.0018	0.0296	0.0013
1000	0.0136	0.0008	0.0154	0.0009

The photocatalytic activity of this high temperature stable anatase TiO_2 is characterized by methylene blue degradation in aqueous solution. Rate constant for the reaction was obtained by plotting the natural logarithm of the absorbance against irradiation time for the TNF2 and control samples calcined at higher temperature are tabulated (Table 7.5). All the TNF2 samples at different temperature shows significantly higher photocatalytic efficiency compared to the control titania prepared under identical conditions. Figure 7.23 shows the absorption spectra of methylene blue and corresponding kinetic data in the presence of TNF2 and TC sample calcined at 1000 °C. The photocatalytic activity of TNF2 sample calcined at 1000 °C exhibit a degradation rate of 0.015 min^{-1}, whereas the control sample shows a negligible amount of photocatalytic activity at this temperature (rate constant 0.0009 min^{-1}). The higher photocatalytic activity obtained for TNF2 sample may be attributed due to the existence of photoactive higher crystalline anatase phase at higher temperature calcination. The existing literature showed that, rutile phase exhibit negligible

photocatalytic activity and 100% rutile phase is confirmed for TC sample above 700 °C. This may be a reason for the decreased photoactivity of TC sample at higher temperature calcination. It is also observed from Table 7.5 that the photoactivity of TNF2 sample seems to decrease as the calcination temperature increases to 1000 °C. The decreasing tendency of photoactivity of TNF2 sample with temperature is due to the increasing particle size (Table 7.6).

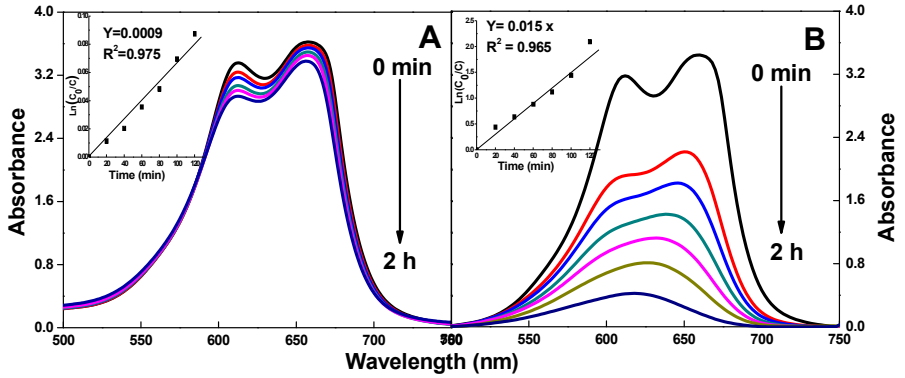

Figure 7.23: absorption spectra of methylene blue degradation as a function of time using A) TC and B) TNF2 at 1000 °C. Inset shows the corresponding kinetic data of both TC and TNF2 sample respectively.

Table 7.6: Crystallite size of (101) peak of anatase phase at different temperatures.

Temperature (°C)	Crystallite size of (101) peak of anatase (nm)	
	TC	TNF2
700	28.4	19.38
800	Absent	22.41
900	Absent	25.62
1000	Absent	32.1

7.2.13. Selective photocatalysis

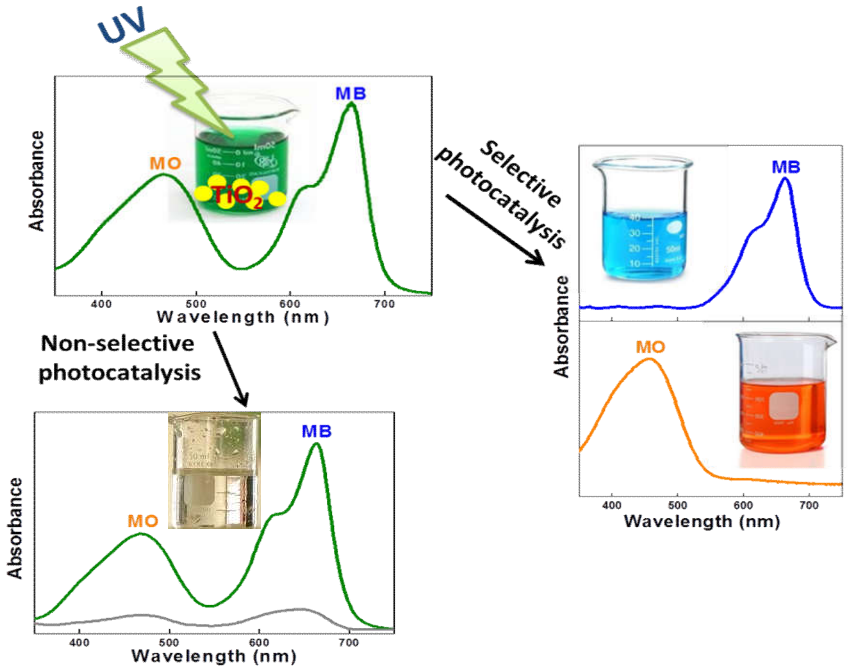

Scheme 7.1. Schematic representation of selective and non-selective photocatalysis

High temperature stable nanocrystalline anatase TiO_2 is well known for its aqueous mediated non-selective photocatalysis and we report the photocatalytic activity of N, F-codoped anatase TiO_2 for the degradation of methylene blue in the previous section, section 7.2.10. Among the prepared TNF catalyst in different composition, the best photocatalyst was found to be the TNF2 catalyst having 1:1 composition of ammonium fluoride and $Ti(OPr)_4$. In addition to the photocatalytic degradation of methylene blue by TNF2 catalyst, it

exhibit selective photocatalysis at lower as well as higher temperature calcination. So the selective photocatalytic study was carried out on best active TNF2 catalyst in comparison to the control sample, TC in different calcination temperature using an equiv molar mixture of MO and MB.

7.2.13.1. Adsorption study: Prior to photocatalytic study, adsorption study should be performed for 2 hr under dark using TNF2 and TC samples prepared at different calcination temperature to remove the error due to initial adsorption effect.[32] There is no appreciable change in the wavelength of absorption in the case of calcined samples before and after 2 hr indicating the absence of adsorption (Figure 7.24). However, TC100 (control sample died at 100 °C) shows a slight decrease in the absorption value of both methylene blue and methyl orange and this may be due to the slight amorphous nature of the sample. Whereas, TNF2 sample dried at 100 °C (TNF100) slightly adsorb methylene blue only due to the negative charge of catalyst in addition to the amorphous characteristics. The amorphous nature of the sample (TNF100 and TC100) is confirmed from XRD (Figure 7.25) and charge of TNF100 is from zeta potential measurements (Figure 7.18).

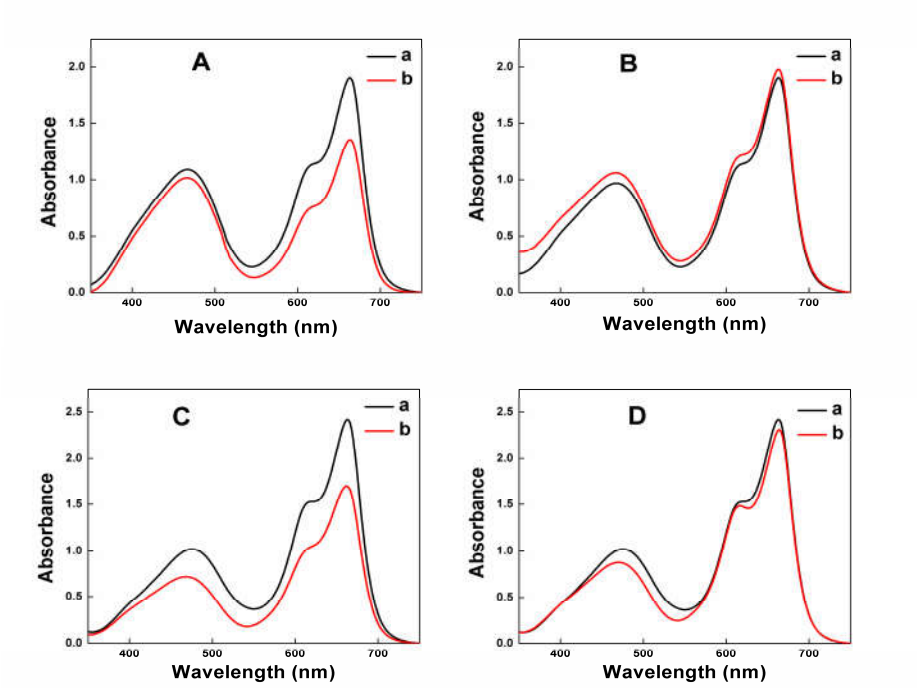

Figure 7.24. Adsorption characteristics of A) TNF100, B) TNF500, C) TC100 and D) TC500 samples under dark (a - absorbance of MB and MO before adsorption and b - corresponding adsorption after 2 hrs)

7.2.13.2. Photocatalytic selectivity: Nano crystalline TiO_2 exhibits non-selective photocatalysis in the presence of UV light, however, doping with non-metals induces selectivity to TiO_2.[2] TNF100 can selectively degrade positively charged pollutants from the dye mixture due to the negative charge present on the surface of TiO_2. Negative charge on the surface of TiO_2 attracts positively charged pollutants towards it and simultaneously degraded. Moderate crystalline nature decrease the photocatalytic selectivity of TNF100 in comparison with the high temperature calcined sample TNF500. Negative charge (-23.3 mV) of TNF100 can be confirmed form zeta potential measurements and

moderate crystallinity from X-ray diffraction technique. Figure 7.25 shows the XRD patterns of TNF and TC samples dried at 100 °C. The broadness of 110 peak of anatase phase indicates the moderate crystalline nature of pure and doped samples. Raman spectra of also support the slight amorphous characteristics of both TNF2 and TC sample at 100 °C as obtained from x-ray diffraction studies.

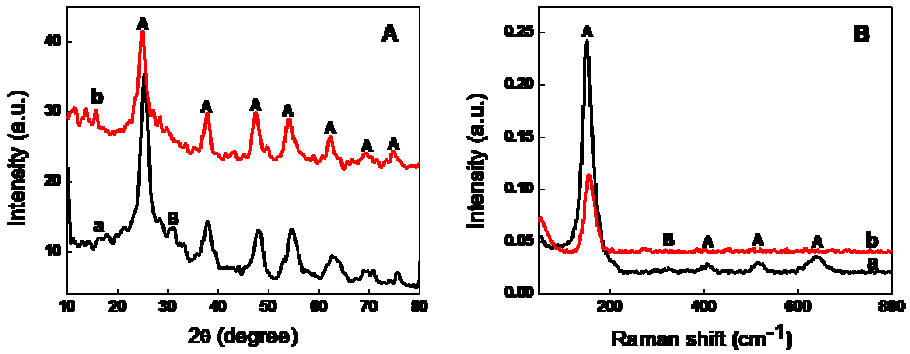

Figure 7.25: A) X-ray diffractogram and corresponding Raman spectra of a) TC and b) TNF2 sample dried at 100 °C.

Previous reports showed that TiO_2 exhibit photocatalytic selectivity in the presence of UV light depending upon the crystallite size, surface charge, crystalline nature and surface area.[2] Combined effect of both surface charge and crystalline nature of nano TiO_2 sample results the preferential degradation of one of the pollutant from the mixture.

So far no literature report is available on the selectivity of high temperature stable anatase TiO_2 nanomaterials towards the degradation of organic dyes. Hence the most exciting observation in this study is the selective photocatalysis exhibited by the high

temperature stable TNF500 and TNF700 in UV light. Figure 7.27 shows the absorption spectra and corresponding concentration versus time plot of TC500 and TNF500. TC500 sample degraded both MO and MB dye in almost equal rate whereas the TNF500 selectively degraded the MB dye only leaving MO dye as such. This can be easily explained from the zeta potential measurement of the TC and TNF2 samples. TC100 and TC500 samples show the zeta potential value 0.18 mV and 1.0 mV respectively, whereas TNF100 and TNF500 samples showed a high negative value of 23.3 mV and 12.4 mV. This negative surface charge on TNF2 sample definitely will enhance adsorption of more amount of positive charged MB dye on the surface and gets degraded at a faster rate. Moreover, the selective degradation of MB by TNF sample calcined at higher temperature will also be facilitated due to the replacement of OH^- ion on the surface of TiO_2 by F^- ion and form surface fluorinated TiO_2 as evidenced from XPS. The free OH^- ion present on the surface of F^- terminated TiO_2 can easily attract oppositely charged dye towards itself and promote the degradation of MB dyes.

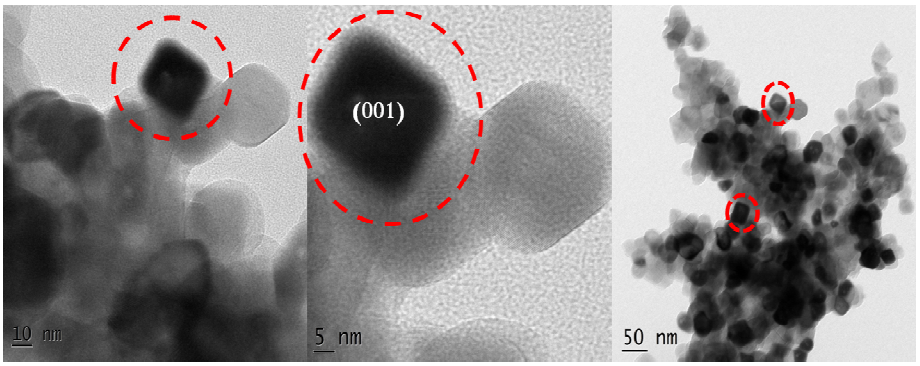

Figure 7.26: TEM images of TNF2 sample at 500 °C

The photocatalytic selectivity of TNF2 sample at 500 °C can also be explained on the basis of (001) facet formation (Figure 7.26). Zhang et al reported that formation of (001) facets of anatase Tio2 exhibit excellent photocatalytic selectivity and theses (001) facet can preferentially adsorb and degrade methylene blue dye than methyl orange.

The Ti-O-Ti bond angles on exposed (001) facets are very large and 2p states on the surface oxygen atoms are destabilized and reactive. Adsorption on (001) facets mainly react with the oxygen atoms, and when the surface Ti-O-Ti bond is broken, the reactive $Ti\text{-}O^-$ preferentially bonds with ionization atoms S^+ in MB or N^+ in MB than O^- in MO. Furthermore, many reports shows that under irradiation photoproduced electrons move to the (101) facets while photoproduced holes move to the (001) facets of anatase TiO2. The lower ionization energy of MB (5.3 eV) makes MB as a better electron donor and this make MB to easily adsorb on and interact with electron deficient (001) facets of anatase TiO2, which leads to higher selective photodegradation of MB.

However, the decrease in the selectivity of TNF700 may be due to the decrease in surface charge and higher crystallinity. Higher crystalline nature of the sample degrades all the substituent which is adsorbed on its surface whether it is charged or not. Crystallinity of TNF700 is quite high when we compare with that of TNF500 (Figure 7.1 and 7.2).

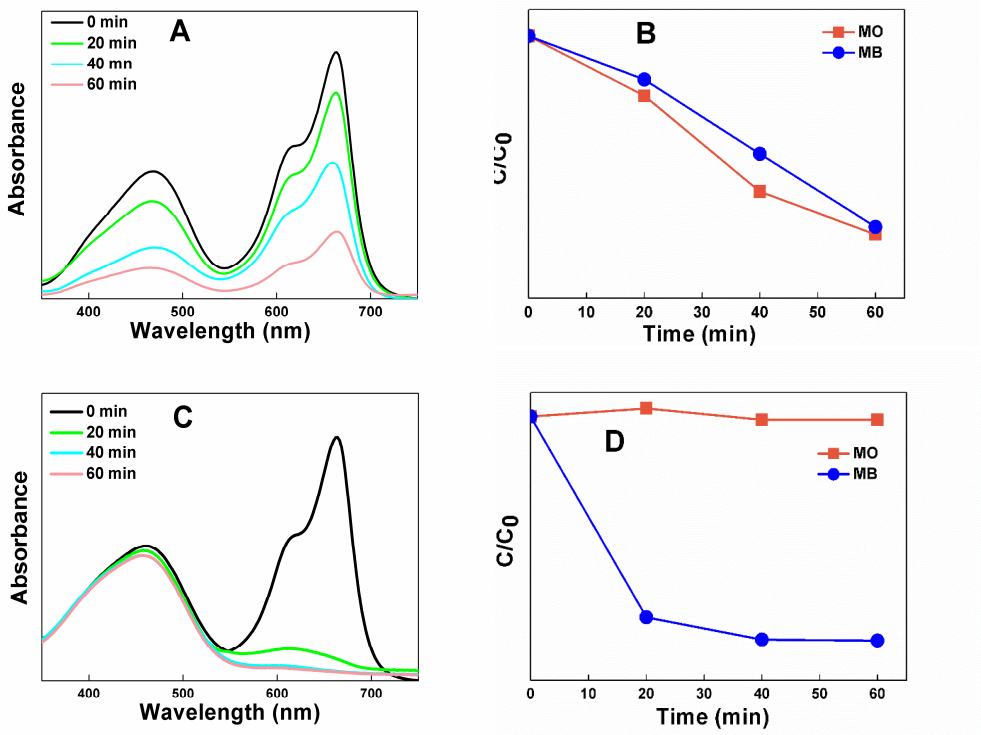

Figure 7.27: UV-Visible absorption spectra and corresponding concentration versus time plot of (A and B) TC500 and (C and D) TNF500.

The selectivity of the prepared photocatalyst can also be expressed in terms of ratio (r) of the rate constant for the degradation of MO and MB.[39] The corresponding 'r' values for the photodegradation of MB and MO for TC and TNF sample calcined at different temperatures were depicted in Figure 7.28. The value of 'r' equal to 1 indicates non-selectivity and r value greater than 1 shows the increase in selectivity of the dyes by the photocatalyst. Hence higher 'r' value (35.17) is observed for TNF500 and it decreases to 29.7 for TNF700. From XRD it is clear that TNF700 has higher crystalline nature, which may be a

reason for the decrease in selectivity and increase in photocatalytic activity. Thus presence of hydroxyl ions on the surface of TiO_2, surface charge and higher surface area of TNF500 may be the reason for the higher selective photocatalytic degradation of methylene blue than methyl orange by TNF500. However, decreased amount of selectivity in TNF sample at 700 °C may be attributed to the higher crystalline nature, decreased surface charge due to decreased amount of fluorine on TiO_2 surface and decreased surface area.

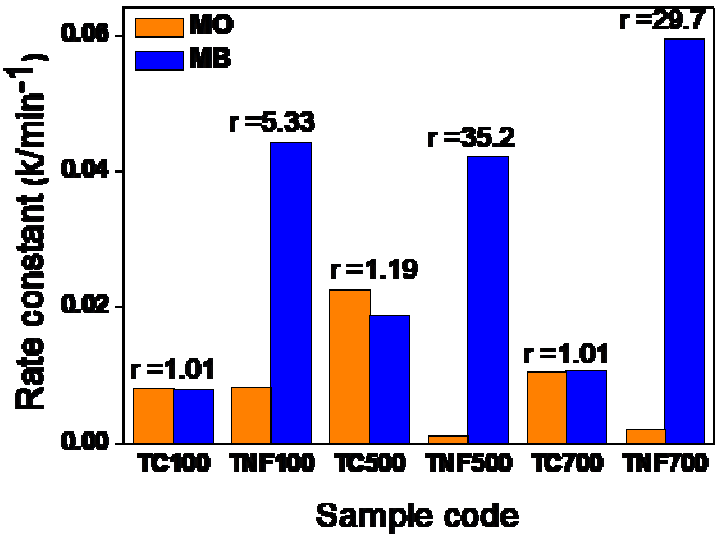

Figure 7.28. Reaction rate constant for the degradation of dye mixture by various catalysts carried out under UV light.

7.3. Conclusions

High temperature stable nanocrystalline anatase TiO_2 photocatalyst were synthesized by simple sol-gel method using

ammonium fluoride modifier. As synthesised TiO_2 sample showed fully selective degradation of cationic organic dye methylene blue (MB) from a mixture of cationic (methylene blue) and anionic (methyl orange) dyes. The control TiO_2 sample without any modification showed non-selective degradation of both cationic (methylene blue) and anionic (methyl orange) dyes. This observed selectivity could have wide implications in the recovery/destruction of precious dyes or toxic compounds from a mixture of pollutants.

References

[1] G. Wu, J. Wang, D. F. Thomas and A. Chen, Langmuir, 2008, **24**, 3503.

[2] W. Ho, J. C. Yu and S. Lee, Chem. Commun., 2006, **10**, 1115.

[3] J. C. Yu, J. Yu, W. Ho, Z. Jiang and L. Zhang, Chem. Mater., 2002, **14**, 3808.

[4] C. Minero, G. Mariella, V. Maurino and E. Pelizzetti, Langmuir, 2000, **16**, 2632.

[5] H. Park and W. Choi, J. Phys. Chem. B, 2004, **108**, 4086.

[6] T. Yamaki, T. Umebayashi, T. Sumita, S. Yamamoto, M. Maekawa, A. Kawasuso and H. Itoh, Nucl. Instrum. Methods Phys. Res., Sect. B, 2003, **206**, 254.

[7] A. Sclafani, L. Palmisano and E. Davi, J. Photochem. Phorobiol. A: Chem., 1991, **56**, 113.

[8] A. Mills, R. H. Davies and D. Worsley, Chem. Soc. Rev., 1993, **22**, 417.

[9] J. Geng, D. Yang, J. Zhu, D. Chen, and Z. Jiang, Mater. Res. Bull, 2009, **44**, 146.

[10] D. Li, H. Haneda, S. Hishita and N. Ohashi, Chem. Mater, 2005, **17**, 2596.

[11] Y. Hu, H. L. Tsai and C. L. Huang, J. Eur. Ceram. Soc., 2003, **23**, 691.

[12] F. Izumi, Bull. Chem. Soc. Jpn., 1978, **51**, 1771.

[13] C. F. Lin, C. H. Wu and Z. N. Onn, J. Hazard. Mater., 2008, **154**, 1033.

[14] H. Zhang and J. F. Banfield, J. Phys. Chem. B, 2000, **104**, 3481.

[15] A. A. Gribb and J. F. Banfield, Am. Mineral., 1997, **82**, 717.

[16] Y. Li, C. Xie, S. Peng, G. Lub, and S. Li, J. Mol. Catal. A: Chem, 2007, **282**, 117.

[17] P. Cheng, J. Qui, M. Gu and W. Shangguan, Mater. Lett., 2004, **58**, 3751.

[18] L. F. H. Bovey and G. B. B. M. Sutherland, J. Chem. Phys., 1949, **17**, 843.

[19] L. F. H. Bovey, J. Chem. Phys. 1950, **18**, 1684.

[20] G. Yang, Z. Jiang, H. Shi, M. O. Jones, T. Xiao, P. P. Edwards and Z. Yan, Appl. Catal., B, 2010, **96**, 458.

[21] T. Ohsaka, F. Izumi and Y. Fujiki, J. Raman Spectrosc., 1978, **7**, 321.

[22] S. P. S. Porto, P. A. Fleuryand T. C. Damen, Phys. Rev., 1967, **154**, 522.

[23] D. Li, H. Haneda, S. Hishita, N. Ohashi, N. K. Labhsetwar, J. Fluorine Chem., 2005, **126**, 69.

[24] C. Burda, Y. Lou, X. Chen, A. C. S. Samia, J. Stout and J. L. Gole, Nano Lett., 2003, **8**, 1049.

[25] A. Hattori and H. Tada, J. Sol-Gel Sci. Technol., 2001, **22**, 47.

[26] S. J. Gregg and K. S. W. Sing, Adsorption, Surface Area and Porosity, Academic Press, London, 1967.

[27] A. M. Czoska, S. Livraghi, M. Chiesa, E. Giamello, S. Agnoli, G. Granozzi, E. Finazzi, C. D. Valentin and G. Pacchioni, J. Phys. Chem. C, 2008, **112**, 8951.

[28] Di Li, Naoki Ohashi, Shunichi Hishita, TarasKolodiazhnyi, Hajime Haneda, J. Solid State Chem., 2005, **178**, 3293.

[29] H. Irie, Y. Watanabe and K. Hashimoto, J. Phys. Chem. B, 2003, **107**, 5483.

[30] N. C. Saha and H. G. Tompkins, J. Appl. Phys., 1992, **72**, 3072.

[31] S. C. Pillai, P. Periyat, R. George, D. E. McCoormack, M. K. Seery, H. Hayden, D. Corr and S. J. Hinder, J. Phys. Chem. C, 2007, **111**, 1605.

[32] S. G. Ullattil and P. Periyat, Nanoscale, 2015, **7**, 19184.

[33] V. Etacheri, M. K. Seery, S. J. Hinder and S. C. Pillai, Adv. Funct. Mater.,2011, **21**, 3744.

[34] Y. Zhang, M. Yang, N. G. Portney, D. Cui, G. Budak, E. Ozbay, M. Ozkan and C. S. Ozkan, Biomed. Microdevices, 2008, **10**, 321.

[35] Q. Xiang, J. Yu and M. Jaroniec, Phys. Chem. Chem. Phys., 2011, **13**, 4853.

[36] K. V. Baiju, S. Shukla, K. S. Sandhya, J. James and K. G. K. Warrier, J. Phys. Chem. C, 2007, **111**, 7612.

[37] P. Periyat, S. C. Pillai, D. E. McCormack, J. Colreavy and S. J. Hinder, J. Phys. Chem. C, 2008, **112**, 7644.

[38] S. R. Yoganarasimhan and C. N. R. Rao, Trans. Faraday Soc., 1962, **58**, 1579.

[39] Y. Li, T.J. White and S.H. Lim, J. Solid State Chem., 2004, **177**, 1372.

[40] X. Z. Ding, X. H. Liu and Y. Z. He, J. Mater. Sci. Lett., 1996, **15**, 1789.

[41] S. Hishita, I. Mutoh, K. Koumoto and H. Yanagida, Ceram. Int., 1983, **9**, 61.

[42] C. Su, B. Y. Hong and C. M. Tseng, Catal. Today, 2004, **96**, 119.

[43] R. Fagan, D. E. McCormack, S. J. Hinder and S. C. Pillai, Mater. Des., 2016, **96**, 44.

CHAPTER 8
Tuning of selective solar photocatalysis by Mn^{2+} decorated nanocrystalline mesoporous TiO_2

CONTENTS

8.1. Introduction

Water contamination by organic pollutant is one of the major issues for the worldwide concern. A significant amount of water pollution covers dye effluents from textile industry. Most of the dyes cause serious environmental and health issues and it is essential to eliminate them from waste water before mixing into the fresh water bodies. Diverse range of techniques have been developed to remove these dyes from waste water, among them photocatalytic dye degradation is considered as an environmental friendly approach.[1,2] Photocatalytic degradation/oxidation follows free radical mechanism. Performance of indiscriminate oxidizing agents like highly oxidizing holes and hydroxyl radicals will result complete mineralization of contaminants to CO_2, H_2O and harmless inorganic anions.[3,4] This non-selective nature of TiO_2 has some constraints in the selective degradation of certain organic moiety from their counterparts. In order to overcome this, researchers focus on the synthesis of TiO_2 nanomaterials for selective degradation.[5]

Attraction of the targets towards the photocatalyst is one of the effective ways to achieve selective degradation by TiO_2. For example, P25 photocatalyst selectively degrade 4-hydroxybenzoic acid over benzamide at pH<6.4 and reverse process takes place at pH>6.4 under simulated sunlight.[6] Negatively charged surface generated upon the incorporation of Faujasite type zeolite on P25 and can selectively adsorb and degrade positively charged dyes such as rhodamine B, anilinium ion and tetramethyl ammonium ion.[7] These two reports strongly suggest the selective degradation exhibited due to the

introduction of polar nature on the surface of TiO_2. Fluorinated hollow TiO_2 anatase microspheres (HTS) have been reported for the selective degradation of anionic dye methyl orange (MO) in comparison to cationic dye methylene blue (MB).[8,9] Surface modified HTS by either surface rehydroxylation through NaOH washing or calcination at 600 °C preferentially degrade MB over MO. This selective degradation of MB exhibited by modified HTS is related to its structural features like exposure of (001) facets along with (101) phase.[8,9]

Recently, improvement in the photocatalytic efficiency of TiO_2 by extending its optical response into the visible and IR range has been studied extensively.[10,11] The present chapter is a modified form of the previous chapter, chapter 7, in which we describe the photocatalytic degradation of N, F codoped TiO_2 catalyst and corresponding selective photocatalysis exhibited by the same catalyst at lower and higher temperature calcination. Here we report a novel design for visible light activated mesoporous titania (TiO_2) for selective photocatalysis. Here selectivity is achieved by introducing the polar nature on the surface of TiO_2 through electrostatic interaction between oppositely charged dopants. Surface charge on TiO_2 helps it to attract oppositely charged ions from solution; thereby TiO_2 can selectively degrade both anionic and cationic pollutants. This hypothesis was tested with commonly used dyes in textile industry, *viz*, methyl orange and methylene blue. The photocatalytic selective decomposition of positively and negatively charge dye can be controlled by varying the concentration of dopant. An extra advantage of this method is that selective photocatalysis can be achieved under natural sunlight as well.

8.2. Results and Discussion

8.2.1. X-ray diffraction technique

The PXRD patterns of the TNFM samples at 100 and 500 °C are shown in Figure 8.1 and it confirm the anatase phase formation (JCPDS 75-1537) for all the prepared samples. The crystallite size of (101) plane of the anatase phase was calculated using Scherrer equation and the results are tabulated in Table 8.1. The PXRD patterns of all the samples dried at 100 °C shows the reflection corresponds (101) plane with appreciable intensity, which confirms the crystalline nature of the samples. As the concentration of Mn^{2+} changed from 0.3 to 0.8 weight percentages, the crystal size of all the samples dried at 100 °C vary in between 4 to 8 nm (Table 8.1). According to Zhang and Bandfield, anatase phase is thermodynamically stable below 11 nm and this supports the anatase phase stability in the crystalline state of TNFM, TC and TNF samples dried at 100 °C.[12] The TNFM calcined at 500 °C shows more crystallinity and crystallite size than the samples dried at 100 °C. However at 500 °C, the intensity of characteristic peaks of anatase phase of TNFM0.3 decreases with increase in concentration of Mn^{2+} which promotes the conversion of anatase to rutile phase (Figure 8.1B). Devi *et al* found that localized charge perturbation produced by Mn^{2+} and its higher ionic size (0.80 Å) would persuade oxygen vacancies on the anatase grains surface promoting bond rupture and favored rutile phase formation, which is consistent with the observed results.[13,14]

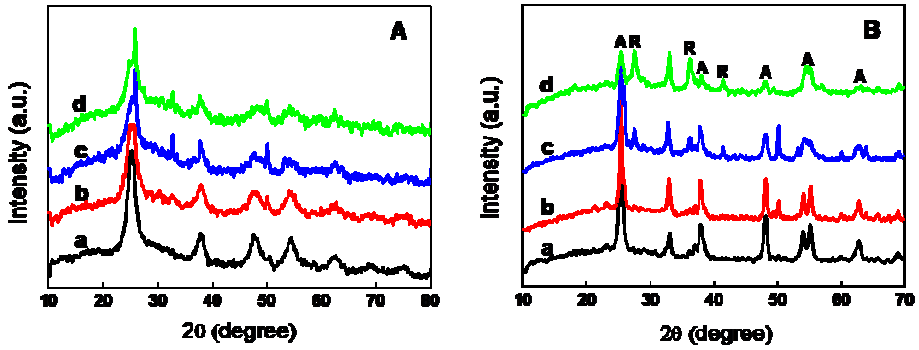

Figure 8.1. PXRD patterns of a) TNFM0.3, b) TNFM0.5, c) TNFM0.6 and d) TNFM0.8 at A) 100 and B) 500 °C.

Table 8.1. Crystallite size of TNFM samples

Sample	Crystallite size (nm)	
	100 ^{O}C	500 ^{O}C
TNFM0.3	5.40	16.4
TNFM0.5	4.78	15.3
TNFM0.6	4.34	9.9
TNFM0.8	7.4	12.5

Figure 8.2 shows the x-ray diffraction pattern of TC, TNF and TM at 100 °C and the calculated crystallite size of these samples were found to be 5.25, 4.67 and 4.32 respectively.

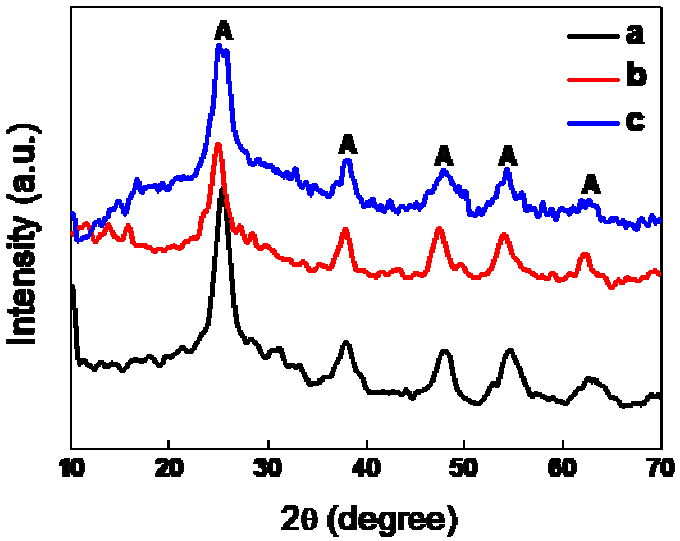

Figure 8.2: X-ray diffraction pattern of a) TC, b) TNF and c) TM dried at 100 °C.

8.2.2 FT-IR spectra

FT-IR is a powerful tool to analyze the structural features of the chemical compounds. The FT-IR spectra of TNFM (0.3, 0.5, 0.6 and 0.8) samples have been recorded and displayed in Figure 8.3. The observed broad peak at 3400 cm^{-1} in the entire sample and a single peak at 1651 cm^{-1} for TNFM samples and 1637 cm^{-1} for TC and TNF sample correspond to the surface adsorbed water and hydroxyl groups respectively.[15,16] The characteristic absorption band of Ti-O-Ti bridging stretching mode lies at around 500 cm^{-1} (Figure 8.3).[17] The spectrum shows bands at 3186 cm^{-1} and 1406 cm^{-1}, which can be attributed to the N-H stretching and bending vibration of NH_4^+ respectively.[18,19] The peak observed at 1588 cm^{-1} is due to the CO_2 molecule liberated from the decomposition of acetic acid.[20,21] The two

peaks located at around 658 and 614 cm^{-1} corresponds to Mn-O stretching and bending vibrations respectively.[22] These peaks confirms the integration of Mn^{2+} ion with titanium ion. The Ti-F vibrational mode is seen in the FTIR spectra of TNF sample at 927 cm^{-1} (Figure 8.3b), which indicates the successful doping of fluorine into TiO_2 matrix.[8,3] The gradual decrease in the intensity of Ti-F bond was also observed with increase in Mn concentration. An observable peak at 1024 cm^{-1} can be attributed to δ^{-}(Ti–OH) deformation and the peak intensity increased with the concentration of Mn^{2+} ion, showing the highly deformed crystal lattice of TNFM0.8.[8]

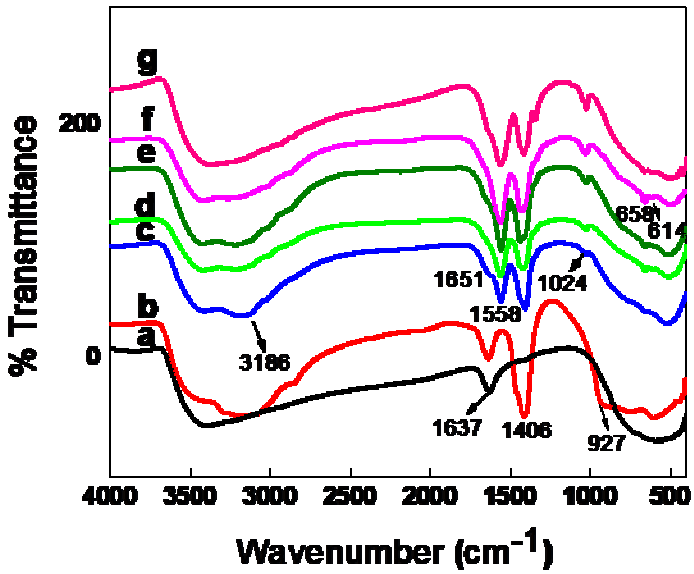

Figure 8.3: FT-IR spectra of a) TC, b) TNF, c) TNFM0.3, d) TNFM0.5, e) TNFM0.6, f) TNFM0.8 and g) TM dried at 100 °C.

8.2.3. SEM/EDS

Composition and morphology of the as prepared TiO_2 nanoparticles were analyzed through SEM (Scanning Electron Microscopy) analysis and EDS. Figure 8.4 represents the SEM image and Energy Dispersive Spectra (EDS) of TNFM0.3, TNFM0.6 and TNFM0.8 samples at 100 °C. The wt% of manganese and fluorine obtained from EDS analysis is shown in Table 8.2. The evaluation of TNFM powders by the SEM technique confirms the presence of Mn^{2+} and F^{-} in the TiO_2 matrix. In the light of EDS spectroscopy, the increase in concentration of Mn^{2+} ion in TNFM samples from TNFM0.3 to TNFM0.8 are clearly observed, whereas the amount of fluoride ions remains constant in all the samples (Table 8.2). The presence of carbon in all the samples is due to the use of carbon grid as sample holder for the analysis technique.

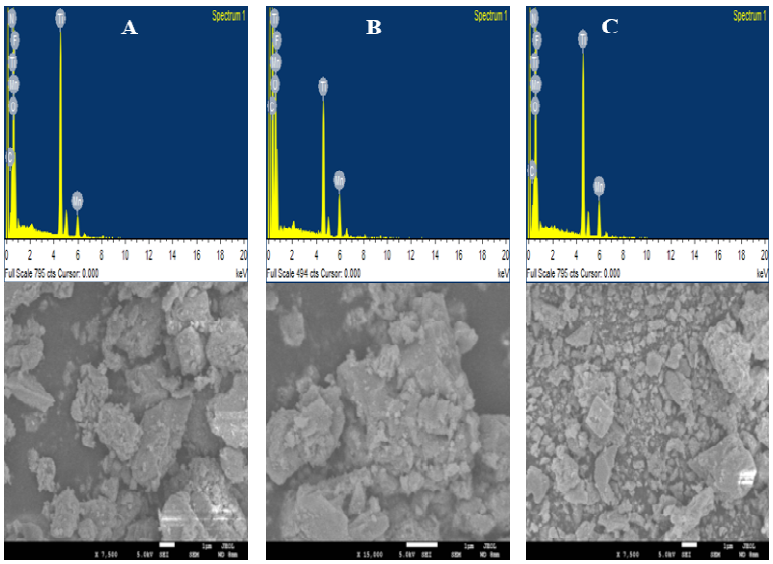

Figure 8.4. SEM/EDS spectra of A) TNFM0.3 B) TNFM0.6 and C) TNFM0.8

Table 8.2. Atomic percentage of Mn and F ion in the TNFM samples.

Sample	Atomic Percentage of	
	Mn	**F**
TNFM0.3	2.40	17.93
TNFM0.6	3.42	17.72
TNFM0.8	4.33	18.02

8.2.4. TEM analysis

Further TEM and HRTEM analysis were employed for examining the morphological and crystalline features. Figure 8.5 represents the TEM and HRTEM images, which confirm the crystalline nature of the samples as evidenced from Powder X-ray diffraction technique. The average crystallite size obtained from HRTEM analysis were 5.39, 4.3 and 6.99 nm respectively for TNFM0.3, TNFM0.6 and TNFM0.8 samples which supports the size calculated using Scherrer equation. HRTEM images of all samples exhibit a fringe width of around 0.35 nm correlating to (101) plane of anatase TiO_2 and the results are in agreement with the interplanar distance values (d) obtained from the PXRD results.

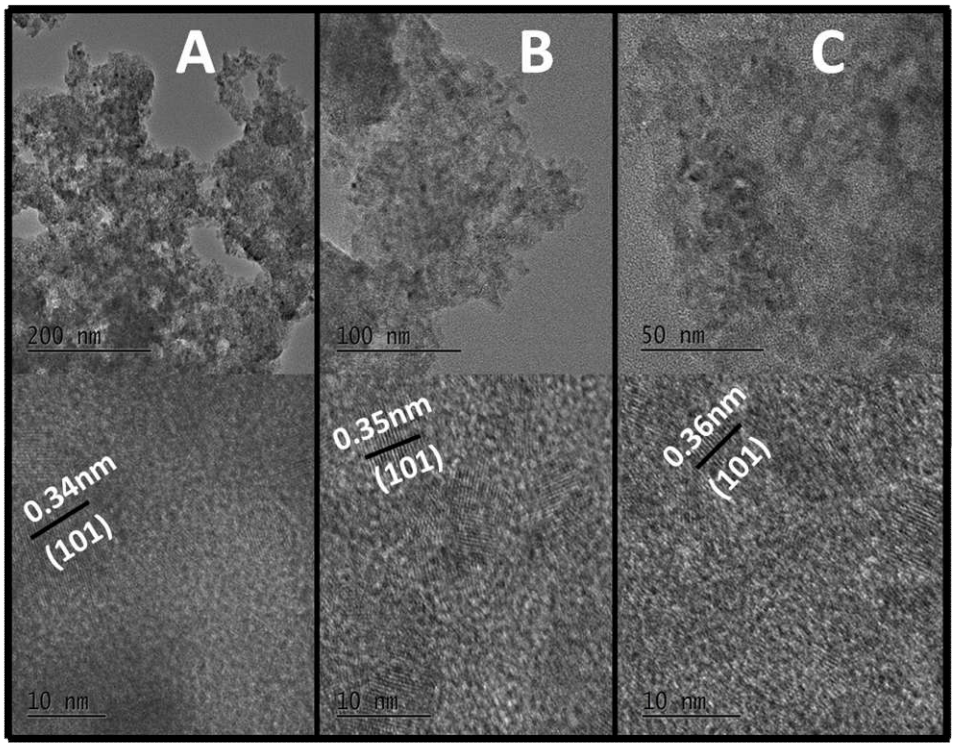

Figure 8.5. TEM and HRTEM images as prepared A) TNFM0.3, B) TNFM0.6 and C) TNFM0.8 samples.

8.2.5. UV-Visible spectra

The UV–Visible light absorption experiments were carried out to examine the absorption characteristics of the synthesized samples. The UV–Visible absorption spectra of TNFM samples dried at 100 °C exhibit characteristic absorption in the visible range and are displayed in Figure 8.6. Tauc plots were constructed by plotting $(\alpha E)^{1/2}$ Vs E with α being the absorption coefficient, the band gap energies were calculated (Figure 8.6B). The optical absorption of TNFM samples has a red shift with increase in concentration of Mn^{2+} ion and is shown in Figure 8.6. The obtained band gap energy of TNFM samples at 100

and 500 °C are tabulated in Table 8.3 and which shows that, calcination extends the visible light absorption of TNFM samples from visible to IR region. It has been reported that fluorine doping does not lead to a significant red shift.[23] Here the introduction of Mn^{2+} ion into F^- doped TiO_2 leads to a considerable red shift in the absorption spectrum corresponding to lower band gap energy which may further help to increase selective degradation of dyes under sunlight.

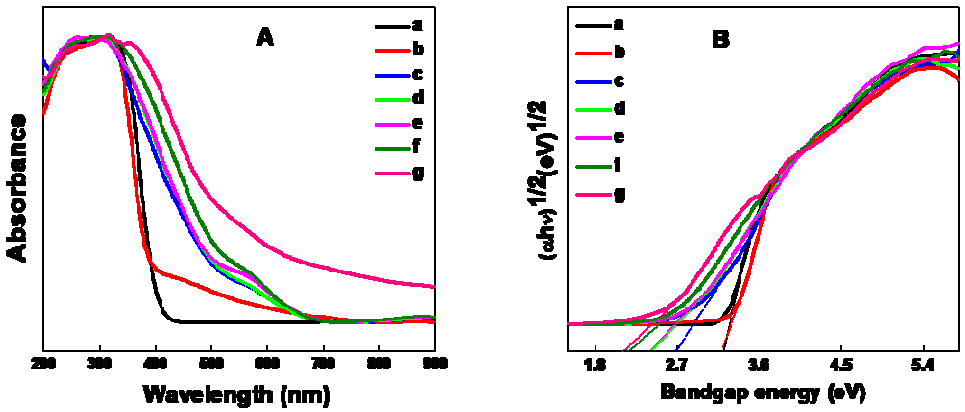

Figure 8.6. UV-Visible absorption spectra and corresponding band gap energy of a) TC, b) TNF, c) TNFM0.3 d) TNFM0.5 e) TNFM0.6 f) TNFM0.8 and g) TM dried at 100 °C.

Table 8.3: Bandgap energy of TNFM samples

Sample	Bandgap energy (eV)	
	100 °C	**500 °C**
TNFM0.3	2.68	1.66
TNFM0.5	2.38	1.61
TNFM0.6	2.32	1.57
TNFM0.8	2.16	1.16
TNF	3.12	2.64
TC	3.16	3.22
TM	2.08	1.09

8.2.6. BET measurements

BET analysis provides specific surface area of materials by nitrogen multilayer adsorption as a function of relative pressure. The nitrogen adsorption and desorption isotherms are shown in Figure 8.7 and the surface area obtained from BET analysis is tabulated in Table 8.4. The adsorption and desorption isotherms of all the samples show type IV behavior with the typical hysteresis loop and this is the characteristic feature of mesoporous materials.[24,11] Table 8.4 shows that TNFM0.3 and TNFM0.8 have higher surface area when compared with other two samples and it may be due to the excess concentration of F^- and Mn^{2+} ions respectively present on the surface of TiO_2. The decrease in surface area of TNFM0.5 and TNFM0.6 is due to the agglomeration of

F^- and Mn^{2+} particles due to the electrostatic attraction in almost equal proportions. The surface area of TNFM0.3 is lower than that of the TNFM0.8 due to the larger size of F^- ion (133 pm) than that of Mn^{2+} ion (81 pm).[25] BJH analysis was employed to determine pore size and specific pore volume by using adsorption and desorption techniques. The mesoporous nature of the samples is evident from the adsorption and desorption pore size measurement using BJH method (Table 8.4) and the type IV isotherm behavior with the typical hysteresis loop as shown in Figure 8.7. As evidenced from Table 8.3, the pore size of all samples ranges from 4 to 7 nm.

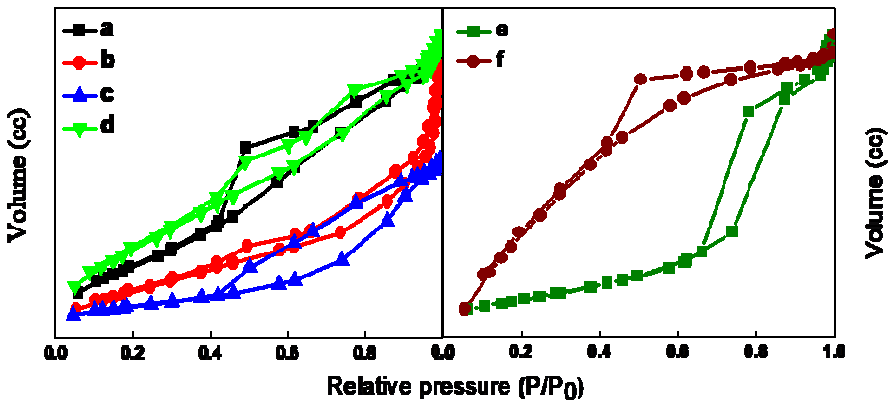

Figure 8.7. Type IV isotherm of (a) TNFM0.3, (b) TNFM0.5, (c) TNFM0.6,(d) TNFM0.8 and B) a) TC and b) TNF.

Table 8.4: Physical properties from N_2 adsorption and desorption studies of TNFM samples.

Sample	BET surface area (m^2/g)	Pore volume (cm^3/g)	BJH desorption pore size (nm)
TNFM0.3	83.68	0.121	4.79
TNFM0.5	54.25	0.093	7.64
TNFM0.6	32.39	0.075	6.11
TNFM0.8	104.46	0.124	4.89
TC	79.19	0.219	8.76
TNF	139.27	0.102	3.42

8.2.7. XPS

To confirm the presence of dopants (F and Mn) and to analyze their chemical states in TiO_2, XPS analyses were carried out. The wide area XPS spectrum of TNFM0.3 and TNFM0.8 shows significant amount of manganese and fluorine with a trace amount of nitrogen in addition to titanium and oxygen in TiO_2 matrix (Figure 8.8). The following binding energies are used in XPS measurements: Ti2p at 458 eV, O1s at 530 eV, F1s at 684 eV, Mn2p at 642 eV, N1s at 400 eVand C1s at 284 eV. The existence of these peaks in the XPS spectra of TNFM samples shows the presence of fluorine and manganese ions in TiO_2. The amounts of manganese (atomic wt%) in TNFM0.3 and TNFM0.8 are 2.38 and 4.34 respectively and are in accordance with the wt% obtained from EDX data (Table 8.2). The atomic wt% of fluorine in the above two samples are 17.26 and 17.92 respectively, which also support the EDX data as in Table 8.2.

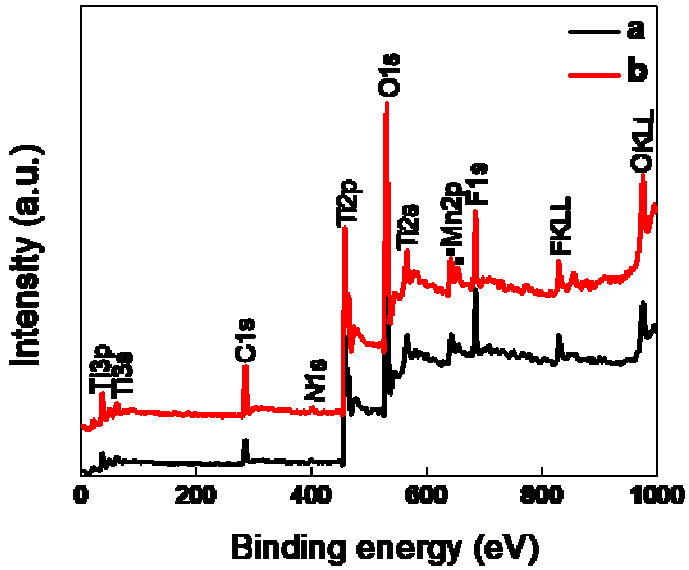

Figure 8.8: XPS survey spectra of a) TNFM0.3 and b) TNFM0.8 at 100 °C.

The binding energy peak at 641.9 eV corresponding to $Mn2p_{3/2}$ and at 653.3 eV to $Mn2p_{1/2}$ was observed in the high resolution XPS spectra of Mn2p, which indicates that the oxidation state of Mn ion in TNFM sample is +2 (Figure 8.9A).[26] The satellite feature at around 647 eV is confirmed from Figure 8.9A, which is not shared by other oxidation state of manganese ions and is the characteristic peak of Mn ion in +2 oxidation state.[26] Figure 8.9B shows the high resolution XPS of F1s region at 684.4 eV indicating successful doping of fluorine as a dopant in TiO_2. Yu *et al* observed the presence of higher binding energy peak at 688.4 eV for substitutional lattice fluoride ion and peak centered at 684.6 eV is to be associated with surface fluorination.[23] The peak obtained at 684.9 eV for TNFM sample confirms the surface fluorination via the formation of terminal Ti-F bond through the

replacement of surface hydroxyl group.[23] Figure 8.9C represents the XPS of Ti 2p which shows the signals correspond to $Ti2p_{3/2}$ and $Ti2p_{1/2}$ at 458.5 and 464.4 eV respectively.[27] In the TNFM samples, the XPS of O1s displays a center peak with another peak at 531.4 eV, which indicates the presence of lattice oxygen (Ti-O-Ti) and surface bound Ti–OH groups, respectively (Figure 8.9D). A slight negative shift in the peak position if Ti2p and O1s are observed for TNFM0.8 sample at100 °C, which indicates the oxygen vacancy site produced in TNFM0.8 sample.

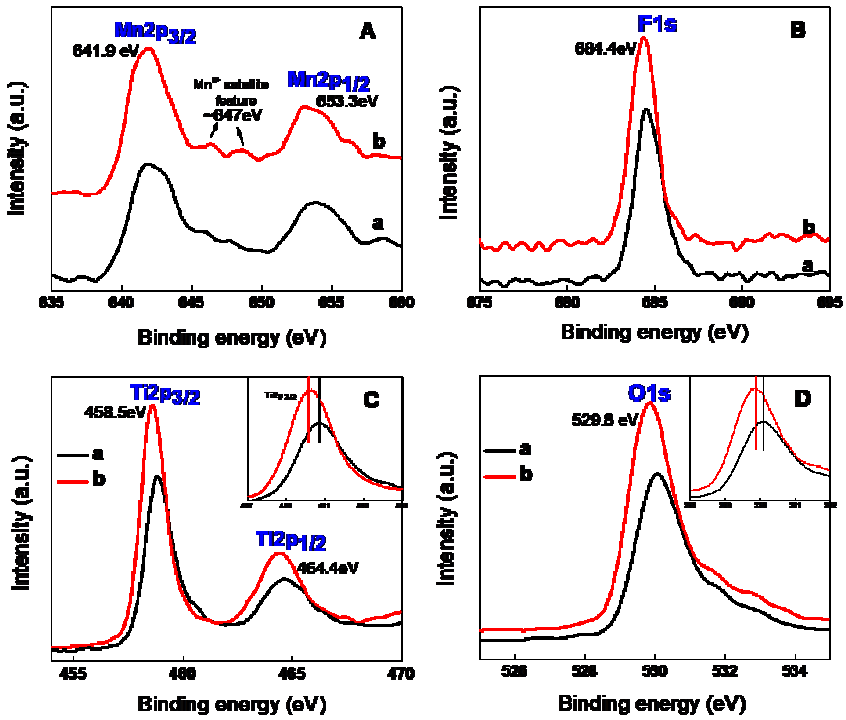

Figure 8.9: High resolution XPS spectra of A) Mn2p, B) F1s, C) Ti2p and D) O1s of a) TNFM0.3 and b) TNFM0.8 samples (Inset of C and D represents the enlarged images of the respective spectra at a specific region).

8.2.8. Selective photocatalysis

8.2.8.1. Adsorption study: Prior to photocatalytic study, adsorption study should be conducted for 2 hr under dark using all TNFM samples dried at 100 °C to remove the error due to initial adsorption effect. Experiments were performed by stirring a mixture of 25 mL each of MB and MO solution with 0.1g of the catalyst. The entire TNFM sample adsorbs methylene blue and methyl orange in different proportion based on their charge and amorphous characteristics. TNFM0.5 and TNFM0.6 at 100 °C adsorb both methyl orange and methylene blue dyes in almost equal proportion due to the slight amorphous nature of the sample. TNFM0.3 adsorb more methylene blue dye molecule than methyl orange, whereas reverse adsorption is happened in the case of TNFM0.8 as shown in Figure 8.10. This preferential adsorption of both TNFM0.3 and TNFM0.8 is because of the negative and positive charges exist respectively on the surface of catalyst in addition to the amorphous nature of the catalysts. X-ray diffraction study account for the amorphous nature of the sample (Figure 8.1A) and zeta potential measurements support the charge on the surface of TiO_2 (Figure 8.11).

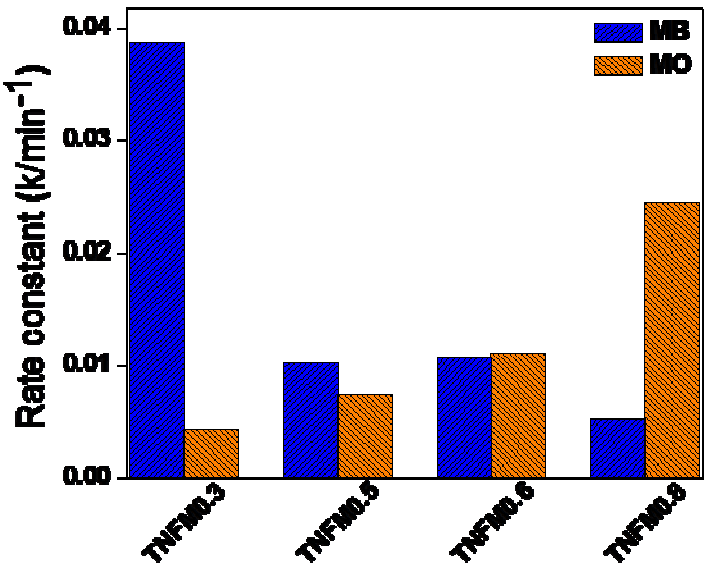

Figure 8.10: Adsorption characteristics of TNFM samples dried at 100 °C.

8.2.8.2. Selective photocatalysis

The enhanced visible light absorption features of the TNFM samples were electively utilized in selective photocatalysis. For this venture, the photodegradation of a mixture of anionic (MO) and cationic (MB) dyes were carried out with each TNFM photocatalyst. The degradation behavior of each TNFM sample is shown in Figure 8.13 (Scheme 8.1). TNFM0.3 selectively degraded the positively charged Methylene blue (cationic) dye whereas the TNFM0.8 selectively degraded the negatively charged Methyl orange (anionic) dye (Figure 8.13). However, selective photocatalysis is not much noticeable in TNFM0.5 (Figure 8.13B) and TNFM0.6 (Figure 8.13C). Similarly, for comparison photodegradation study of the dye mixture were carried

out on TC and TNF samples. TNF catalyst selectively degraded MB than MO (Figure 8.14), where as TC could degrade both MB and MO in equal rate (Figure 8.14).

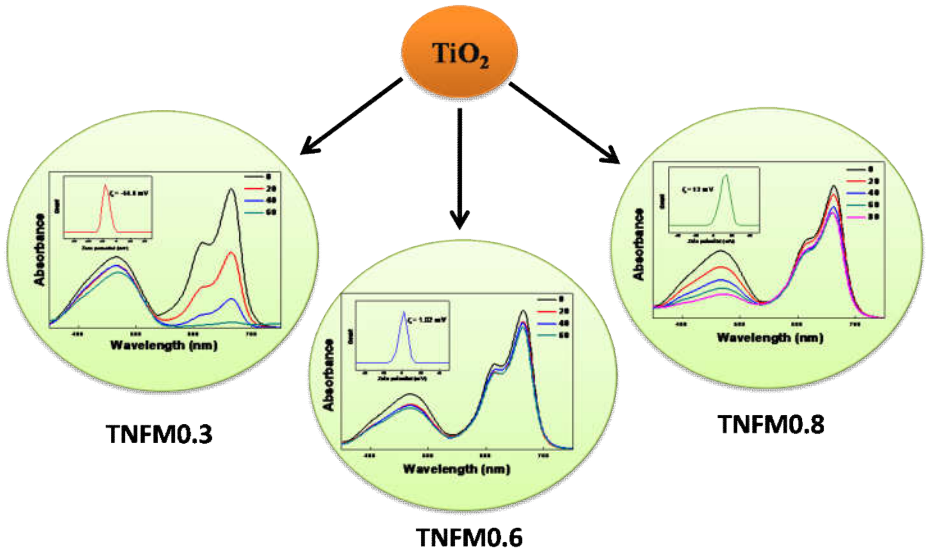

Scheme 8.1: Schematic representation of selectivity exhibited by TNFM samples

To have a better understanding on the selectivity of dye mixture, the surface charge existed on the photocatalyst surface were investigated through Zeta (ζ)–potential measurement. The (ξ) potential is the electrostatic potential that exists at the shear plane of a particle, which is related to both surface charge and the local environment of the particle.[28] Zeta potential graph of synthesized TNFM samples dried at 100 °C are shown in Figure 8.11. Inset of figure 8.11 shows the zeta potential value of TNF, TC and TM catalyst at same temperature. For

comparison, the ζ–potential value of all the synthesized photocatalyst at 100 and 500 °C was also plotted and pictorially represented in Figure 8.12. The zeta (ξ) potential measurement showed that TNFM0.3 (−14.8 mV) and TNFM0.5 (−4.97 mV) have negative surface charge whereas TNFM0.6 (+1.02 mV) and TNFM0.8 (+12 mV) showed positive surface charge. As the concentration of Mn^{2+} increases, there was a considerable decrease in the negative charge on the surface up to TNFM0.6 due to the neutralization of F^{-} ion by Mn^{2+}. Further addition of Mn^{2+} introduces more positive charge on the surface of TNFM0.8. This variation of negative and positive charge on the surface of TiO_2 is conducive for the selectivity in photocatalytic degradation activities of the synthesized photocatalysts.

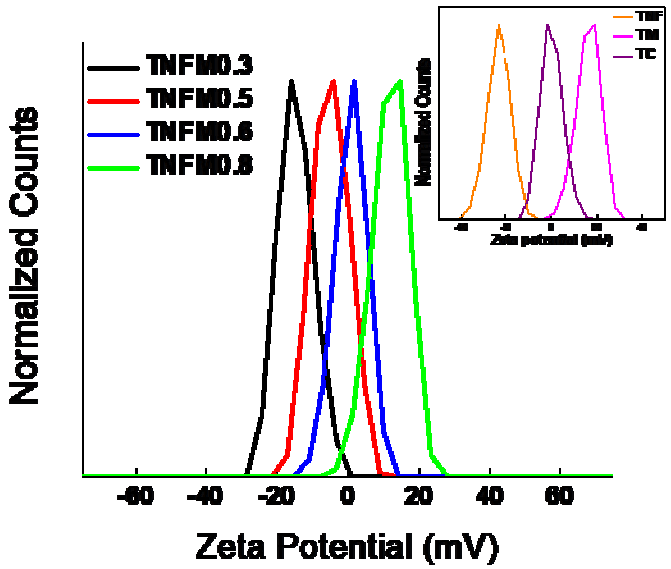

Figure 8.11: Zeta potential data of TNFM samples at 100 °C (Inset shows the zeta potential curve of TNF, TC and TM samples at 100 °C).

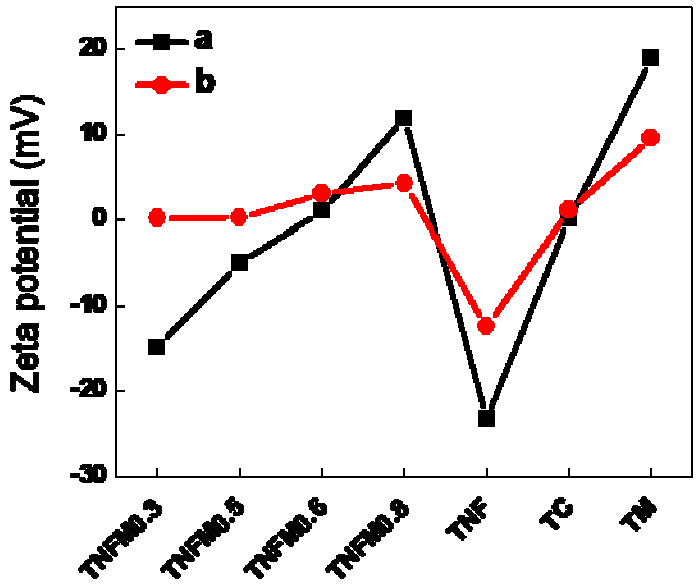

Figure 8.12: Zeta potential value of all the prepared samples at a) 100 and b) 500 °C.

ζ – Potential measurements uphold the existence of negative charge on TNF, positive charge on TM and almost zero charge on TC catalyst. Due to the negative charge on TNF catalyst, the adsorbed MB dye can easily degrade from the dye mixture than MO. Whereas the control sample TC, non-selectively degrade both MO and MB due to the absence of surface charge on TC. Liu et al. have reported that hydroxyl modified fluorine mediated photocatalyst can easily adsorb and degrade MB over MO from the dye mixture.[8] Similarly, the positively charged TM can simultaneously adsorb and degrade oppositely charged MO dyes than MB. The Zeta (ξ) potential measurements confirm that the charge on the surface of nanoparticle can be controlled by electrostatic attraction between oppositely charged dopants. Stability limit of nano particle is $-30\ mV \geq x \geq +30\ mV$, where x

represents the ζ-potential of colloidal suspension of TiO_2 nanoparticles. This stability is attained due to the electrostatic repulsion existing between particles adsorbed on the surface of TiO_2, which also prevent them from aggregating.[29,30] This is a good indication that there is a great degree of electrostatic attraction between oppositely charged dopants, since ξ potential values of TNFM samples exist within the range of −15 mV to +15 mV. In TNFM0.3 negative charge was originated on the surface of TiO_2 from the left-over F^- ion after neutralization with Mn^{2+} causing the adsorption of positively charged dye, methylene blue. The negatively charged dye methyl orange was adsorbed on the positively charged surface of TNFM0.8 as a result of the excess Mn^{2+} ion on its surface. Almost equal adsorption can be found in TNFM0.5 andTNFM0.6 due to complete neutralization of F^- and Mn^{2+} ions. Adsorption and corresponding degradation patterns in all the TNFM samples is due to surface charge present on TiO_2 nanomaterials as shown in Figure 8.12. The non-selectivity of TNFM0.5 and TNFM0.6 are the result of electrostatic charge neutralization of F^- and Mn^{2+} ions adsorbed on the surface of TiO_2. This charge neutrality was confirmed from ζ-potential measurements as shown in Figure 8.11. Here the selectivity was achieved in a single system just by varying the charge on the TiO_2 surface by simply changing the dopant concentration. Negative surface charge on TNFM0.3 and positive surface charge on TNFM0.8 respectively motivate the preferential adsorption of MB on TNFM0.3 and MO on TNFM0.8. This led to the selective degradation of adsorbed MB on TNFM0.3 and MO on TNFM0.8 from the mixture of dyes in a single system. Zeta potential of TNF is due to the respective adsorption of

anionic (F^-) dopant on the surface of TiO_2. The surface adsorption of F^- ion is confirmed from XPS technique as observed in Figure 8.9B. The non-selective nature of the control sample is because of the absence of charge on its surface and is obtained from zeta potential measurements.

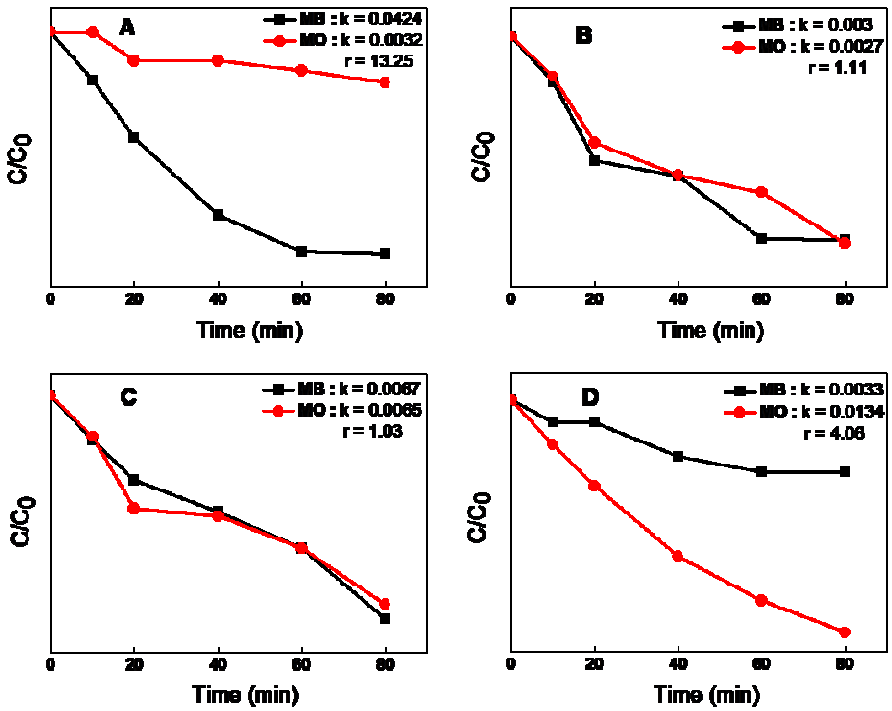

Figure 8.13. Concentration Vs time plot showing the degradation of MO and MB mixture with A) TNFM0.3, B) TNFM0.5, C) TNFM0.6 and D) TNFM0.8 (All the samples were dried at 100°C).

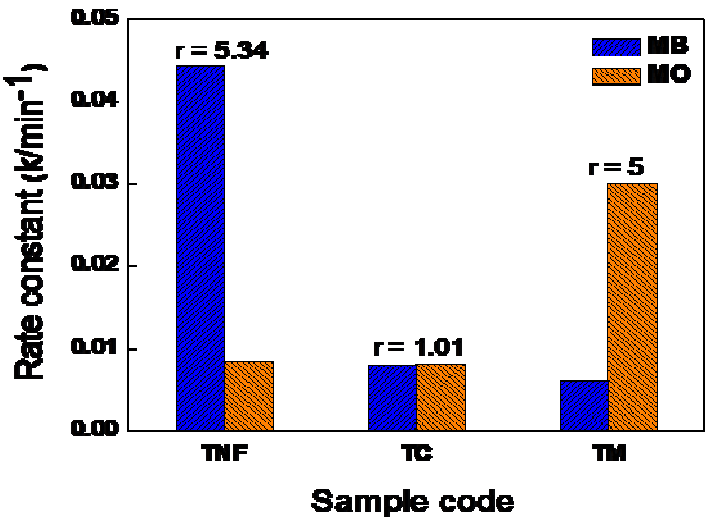

Figure 8.14: Rate constant value of TNF, TC and TM catalyst at 100 °C.

The selectivity of the prepared catalyst can also be expressed in terms of the ratio (r) of the rate constant for the degradation of MO and MB. The value of 'r' equal to one indicates non-selectivity and the value of 'r' exceeds one indicates increase in selectivity of the dyes by the photocatalyst. The corresponding 'r' value TNFM0.3 is ~13 showing higher selectivity compared TNFM0.8 having an 'r' value ~ 4 (Figure 8.13).

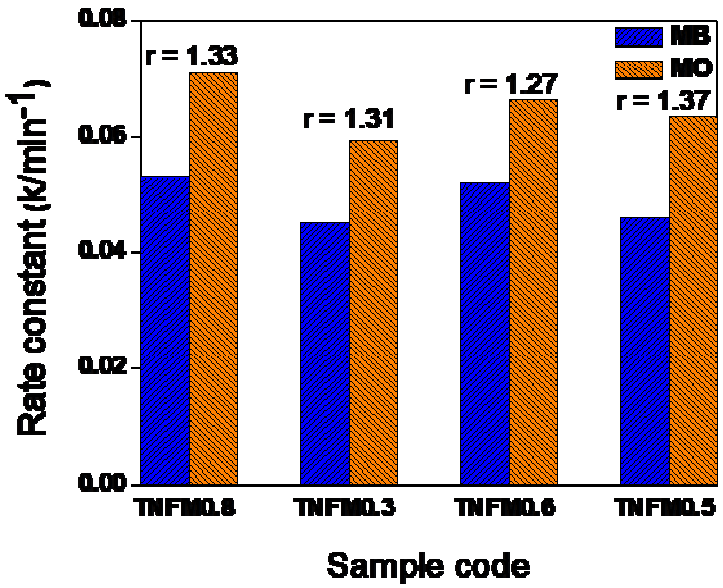

Figure 8.15: Rate of degradation of MB and MO by TNFM catalysts calcined at 500 °C.

Figure 8.15 shows the high temperature photocatalytic degradation of the mixture of MB and MO by TNFM catalyst. In the case of TNFM samples, calcination decrease or we can say almost lost the photocatalytic selectivity. This may be attributed due to the fact that calcination improve the crystalline nature as well as diminish the surface charge on TNFM samples. Higher crystalline substances have a tendency to degrade all the molecule that can degrade and does not take into account the charge and nature of the sample.[5]

8.3. Conclusions

Mesoporous nanocrystalline TiO_2 materials for selective photocatalysis were prepared using titanium isoporpoxide, ammonium fluoride and

manganous acetate. These TiO_2 nanomaterials were characterized by Powder X-ray diffraction (XRD), FTIR spectroscopy, BET surface area measurement, UV–Vis spectroscopy, SEM and TEM. These mesoporous nanocrystalline TiO_2 showed high selectivity towards dye degradation. Selective photocatalysis study showed that methylene blue was selectively degraded at lower concentration of Mn^{2+} whereas methyl orange was degraded at higher concentration. The selectivity exhibited by these TiO_2 nanomaterials has wide applications in the destruction of toxic substance from their valuable counterparts

References

[1] C. M. Teh and A. R. Mohamed, J. Alloys Comp., 2011, **509**, 1648.

[2] J. D. Jong, J. T. V. Buuren and J. P. A. Luiten, Water Sci. Technol., 1996, **34**, 9.

[3] W. Hung, S. H. Fu, J. J. Tseng, H. Chu and T. H. Ko, Chemosphere, 2007, **66**, 2142.

[4] R. M. Alberci and W. F. Jardim, Appl. Catal B: Environ., 1997, **14**, 55.

[5] M. A. Lazar and W. A. Daoud, RSC Adv., 2012, **2**, 447.

[6] D. Robert, A. Piscopo and J. V. Weber, Environ. Chem. Lett., 2004, **2**, 5.

[7] G. Zhang, W. Choi, S. H. Kim and S. B. Hong, J. Hazard. Mater., 2011, **188**, 198.

[8] S. Liu, J. Yu and M. Jaroniec, J. Am. Chem. Soc., 2010, **132**, 11914.

[9] J. H. Shen, Y. H. Zhu, X. L. Yang and C. Z. Li, J. Mater. Chem., 2012, **22**, 13341.

[10] S. G. Ullattil and P. Periyat, Nanoscale, 2015, **7**, 19184.

[11] S. G. Ullattil and P. Periyat, Sol. Energy, 2017, **147**, 99.

[12] Zhang, H., Banfield, B.J.H., J. Phys. Chem. B, 2000, **104**, 3481.

[13] L. G. Devi, S. G. Kumar, B. N. Murthy and N. Kottam, Catal. Commun., 2009, **10**, 794.

[14] L. G. Devi, N. Kottam, B. N. Murthy and S. G. Kumar, J. Mol. Catal. A: Chem., 2010, **328**, 44.

[15] Z. Ding, G. Q. Lu and P. F. Greenfield, J. Phys. Chem. B, 2000, **104**, 4815.

[16] D. Huang, S. Liao, S. Quan, L. Liu, Z. He, J. Wan and W. Zhou, J. Mater. Sci., 2007, **42**, 8193.

[17] D. Huang, S. Liao, S. Quan, L. Liu, Z. He, J. Wan and W. Zhou, J. Mater. Res., 2000, **22**, 2389.

[18] T. Matsumoto, N. Iyi, Y. Kaneko, K. Kitamura, S. Ishihara, Y. Takasu and Y. Murakami, Catal. Today, 2007, **120**, 226.

[19] Y. Li, C. Xie, S. Peng, G. Lu and S. Li, J. Mol. Catal. A: Chem., 2008, **282**, 117.

[20] R. Ullah and J. Dutta, J. Hazard. Mater., 2008, **156**, 194.

[21] P. Periyat, F. Lazar, S. A. M. Tofail and E. Magner, RSC Adv., 2011, **1**, 1794.

[22] S. J. Parikh and J. Chorover, Geomicrobiol. J., 2005, **22**, 207.

[23] J. C. Yu, J. Yu, W. Ho, Z. Jiang and L. Zhang, Chem. Mater., 2002, **14**, 3808.

[24] P. Periyat, S. C. Pillai, D. E. McCormack, J. Colreavy and S. J. Hinder, J. Phys. Chem. C, 2008, **112**, 7644.

[25] J. Choi, H. Park and M. R. Hoffmann, J. Mater. Res., 2010, **25**, 149.

[26] W. Zhang, W. Zhou, J. H. Wright, Y. N. Kim, D. Liu and X. Xiao, ACS Appl. Mater. Interfaces, 2014, **6**, 7292.

[27] M. Zhu, C. Zhai, L. Qiu, C. Lu, A. S. Paton, Y. Du and M. C. Goh, ACS Sustain. Chem. Eng., 2015, **3**, 3123.

[28] Y. Zhang, M. Yang, N. G. Portney, D. Cui, G. Budak, E. Ozbay, M. Ozkan and C. S. Ozkan, Biomed. Microdevice, 2008, **10**, 321.

[29] Y. Lu and J. Liu, Acc. Chem. Res., 2007, **40**, 315.

[30] K. Yoosaf, B. I. Ipe, C. H. Suresh and K. G. Thomas, J. Phys. Chem. C, 2007, **111**, 12839.

CHAPTER 9
CONCLUSIONS

This thesis work deals with the synthesis, characterization and application of various non-metal and metal modified TiO_2 nanomaterials for non-selective as well as selective removal of pollutants through photocatalytic reactions.

Chapter 1 gives a general introduction to titanium dioxide (TiO_2) and its applications as well as mentioned different synthesis technique, mainly concentrating on the sol-gel method giving step by step description of the sol-gel process. An introduction to the different modification techniques available on TiO_2 and factors that affect TiO_2photocatalysis are discussed concisely. Objectives and overview of the present work are also discussed in this chapter.

Chapter 2 explains the strategy adopted for the synthesis of nonmetal, metal co-doped TiO_2 systems. Sol-gel method and simple mechanical mixing (*via* stirring the dopant with TiO_2) were employed for the preparation of the co-doped TiO_2 system, where Ti $[OCH(CH3)_2]_4$, different N,S containing modifiers, NH_4F and manganous acetate were used as the sources for TiO_2, N and S, N and F, and Mn respectively. In all the co-doped systems, percentage of TiO_2 was taken as constant and varied the concentration of dopants. A brief explanation of physico-chemical techniques used for the characterization of the material was also presented in this chapter. This includes X-ray Diffraction (XRD), Raman Spectroscopy, FTIR analysis, Energy Dispersive X-ray Analysis (EDX), Scanning Electron Microscopy(SEM), UV-Visible Diffuse Reflectance Spectroscopy (UV-Vis DRS), Transmission Electron Microscopy (TEM), BET Surface Area Measurements and X-ray Photoelectron Spectroscopy (XPS).

Chapter 3 to 7 describes the results and discussion on modified TiO_2 nanomaterials samples in comparison with unmodified TiO_2 and its detailed photocatalytic activity study. The modifiers used are thiourea, explained in chapter 3, thiosemicarbazide explained in chapter 4, sulfanilic acid explained in chapter 5, cysteine explained in chapter 6 and ammonium fluoride explained in chapter 7. All these modified TiO_2 samples are well characterized using various physico-chemical characterization techniques and compared with unmodified TiO_2 and the prepared samples were successfully employed for the removal of a dye, methylene blue which can be considered as a model contaminant. The various physicochemical properties and corresponding photocatalytic efficiency of all the prepared systems in chapter 3 to 7 are summarized in Table 9.1.

Table 9.1: The various physicochemical properties and corresponding photocatalytic efficiency of samples studied in chapter 3 to 7.

Sample Shows maximum efficiency in each chapter	**Calcination temperature showing maximum efficiency**	**Crystallite size (nm)**	**Surface area (m^2/g)**	**Reaction rate constant for the degradation of MB**	
				UV light	**Direct solar light**
TC	500	13.6	34.54	0.038	0.030
TU2	700	15.45	31.29	0.064	0.088
TSC3	700	20.25	25.83	0.048	0.064
TSA2	500	11.08	75.79	0.088	0.103
TCS2	**700**	**21.6**	**49.93**	**0.101**	**0.108**
TNF2	500	12.02	82.35	0.075	0.105
TC	700	32.1	6.36	0.001	0.006

Generally photocatalytic degradation by TiO_2 follows free radical mechanism and which follows complete mineralization of pollutant non-selectively. Hence second major aim of this thesis work is to achieve selectivity in the photocatalytic activity of TiO_2. **Chapter 7** explains selective photocatalytic activity of N, F- codoped TiO_2 using NH4F as a modifier and its effect on the anatase to rutile transformation of TiO_2.NH_4F doped TiO_2 catalyst (TNF) exhibit fully selective degradation of cationic organic dye MB from a mixture of cationic (MB) and anionic (MO) dyes at lower and higher temperature.

Chapter 8 further explains the tuning of selective photocatalysis by modifying the as prepared NH_4F modified TiO_2 photocatalyst by using manganese and detailed how Mn^{2+} cation affect the selective photocatalytic behavior. Manganese ion tune the photocatalytic selectivity by varying the concentration of Mn^{2+} on ammonium fluoride doped TiO_2.Selective photocatalysis study showed that methylene blue was selectively degraded at lower concentration of Mn^{2+} whereas methyl orange was degraded at higher concentration.